The Potential Effect of Cirrus on Microwave Limb Sounder Retrievals

Stephen Thomas Bond

Doctor of Philosophy
The University of Edinburgh
1996

Declaration

I declare that this thesis was written by myself, and that the work it describes is my own except where otherwise stated.

To my parents

Acknowledgments

I would like to thank my supervisor, Robert Harwood, for his support and advice throughout the writing of this thesis, and for having faith in my ability even when I had none.

I am very grateful to Mark Filipiak for the great deal of help he has provided, and for answering innumerable questions, even when he was no longer working in this department.

Thanks also to Hugh Pumphrey and Gordon Peckham for their help in solving various problems along the way.

Special thanks to Charles Duncan, and to Andrew Longmore of the Royal Observatory of Edinburgh, for providing part-time employment when it was badly needed.

Thankyou to Andrew Thackrah and Sarah Fleming, and to all the other friends who have made the time I have spent in Edinburgh so enjoyable, especially Andrew Harrison, Steve McNally, Jonny Tedds, Irene Fleming, Miles Hopkinson, Fiona Gavin, Sarah Low, Freia Millar, Graham Smith, Alison Cringle, John Holland, Hannah Clark, Patrick Walder, Stephen Dodds, Alison Stirling and Jon Blenkin.

Finally, and most importantly, I thank my parents for their continuous support.

Abstract

A microwave limb sounder (MLS) is an instrument used to study the composition and temperature of the atmosphere by measuring the microwave radiation that is thermally emitted by atmospheric molecules. When such measurements are made in the upper troposphere, the extinction of radiation caused by cirrus clouds may affect the quality of the results obtained. The extent to which such extinction degrades the sensitivity of MLS measurements to tropospheric parameters has been estimated using computer simulations of radiative transfer in a cloudy atmosphere. Results have been derived specifically for the proposed EOS MLS instrument due to be launched in December 2002, but are applicable to microwave limb sounding in general.

To calculate the microwave emission spectrum of the atmosphere, a forward model was developed which represents the absorption properties of atmospheric molecules, and solves the equation of radiative transfer along a one-dimensional path through the atmosphere. A simple scattering model was developed using Mie theory to calculate scattering and extinction by a distribution of spherical particles, and was used to extend the capabilities of the forward model such that it was able to simulate radiative transfer through a cloudy atmosphere.

A review of existing literature on the microphysical structure of cirrus clouds has been conducted, allowing the parameterisation of their size distributions and a characterisation of their crystal shapes. Cirrus is composed of ice crystals which take a variety of non-spherical forms. Therefore in order to make use of the forward model described, a method was developed for converting the geometrical forms of the cirrus crystals into spheres of the same projected area, on the assumption that such spheres will have similar gross scattering properties to their non-spherical counterparts. This technique allowed the derived crystal distributions to be converted into distributions of spheres suitable for input to the forward model.

The results produced by the forward model were used to calculate the change in received radiance caused by the presence of a cirrus cloud of typical structure and height for the latitude under consideration. From this radiance change the resulting uncertainty in the estimated concentrations of water vapour and ozone was determined by an error analysis of the retrieval process. The results show that in certain cases the presence of cirrus, if unaccounted for, may cause an uncertainty of sufficient magnitude to render the estimated concentrations highly unreliable. Given that, on average, cirrus covers between 20% and 50% of the Earth, it appears that some consideration must be given to accounting for its effects if the retrieval of tropospheric species is to be feasible.

Contents

Chapter 1

Introduction

1.1 Aim of the Thesis

The aim of this thesis is to determine to what extent the tropospheric retrievals made using a microwave limb sounder (MLS), specifically that of the Earth Observing System (EOS), are impaired by the presence of cirrus cloud in the line of sight. An MLS is an instrument which measures the thermal microwave radiation naturally emitted by molecules in the Earth's atmosphere, and its measurements are used, via the *retrieval process*, to deduce the chemical composition of the atmosphere, as well as its vertical profiles of temperature and pressure. When the microwaves received by the MLS pass through cloud on their way to the instrument, they interact with the cloud particles and so the signal received by the MLS is altered. This means that the measurement of the physical quantity which is retrieved from the observation is also altered.

The principle of limb sounding is illustrated in figure 1.1. The MLS directs its antenna to look along a line of sight which passes through the Earth's atmosphere and out the other side without intercepting the surface. This means that, apart from the small contribution due to the cosmic microwave background (CMB), the signal received by the MLS originates entirely from the molecules of the atmosphere itself. Since the number density of molecules in the atmosphere increases exponentially with decreasing height, the intensity of radiation emitted by the atmosphere is correspondingly higher at lower altitudes. Therefore the majority of the radiation received along a limb sounding path originates from, and provides information about, a region around the *tangent point* T, where the line sight makes its closest approach to the surface.

At very low tangent heights, retrieval becomes impossible because the atmosphere is sufficiently opaque that the radiance received by the MLS originates primarily from the atmosphere between the instrument and the tangent point, not from the tangent point itself. In addition, the microwave signal is so large and

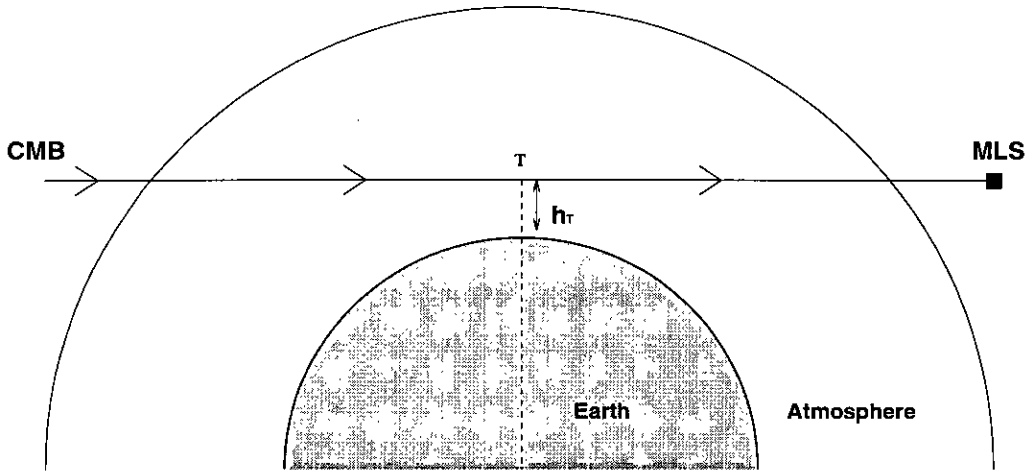

Figure 1.1: The geometry of limb sounding. 'CMB' represents the cosmic microwave background.

spread out in frequency at these altitudes that it obliterates the spectral lineshape information that is required to determine the species of molecule from which the radiation was emitted. This means that in general the low cloud types such as cumulus do not need to be taken into account. However, in the upper troposphere, a limited amount of retrieval *is* possible, and therefore high-altitude, cirriform cloud may affect results.

The presence of cloud in the line of sight means that the microwaves are incident on a number of small particles on their way to the MLS. These particles may remove radiation from the line of sight, either by absorbing it, or by scattering it into new directions. Such processes are dependent on the size of the particle compared to the wavelength of the radiation. For this reason, microwave observations are much less affected by the presence of cloud than are those made in the infrared or at shorter wavelengths. However, when cloud occupies a long section of the line of sight, the cumulative effect may be significant.

Cirrus cloud is composed of ice crystals of various shapes and sizes. At the lower end of the size range, the crystals are too small compared to the wavelengths used by an MLS to cause appreciable scattering, but this is not the case for the larger crystals. Therefore the potential degradation caused by a cirrus cloud depends on the nature of its particle size distribution.

The results presented in this thesis are specific to the EOS MLS. However, the work which has gone into producing these results, and the conclusions which may be drawn from them, are pertinent to microwave limb sounding in general.

The objectives of this thesis were achieved by the combination of radiative transfer calculations with the simulation of the microphysical structure of cirrus cloud. The process which was followed is outlined below.

1.1.1 Structure of the Thesis

The results presented in this thesis were produced by the incorporation of a cirrus scattering simulation into a *forward model*. The forward model is a computer simulation which calculates the microwave radiance, emitted by the molecules along the line of sight, which is measured by the MLS. This emission is due to quantum-mechanical processes which may be quantified. The theory which underpins the forward model, and the details of its practical implementation are described in chapter 2, including a description of the way in which the MLS instrument itself modifies the radiation which is incident on its antenna. The inclusion of multiple scattering processes into this model was achieved using the *Mie theory* of scattering for spheres, as demonstrated in chapter 3.

In chapter 4 the microphysical structure of cirrus clouds is examined in detail, and it is shown that the ice crystals of which such clouds are composed take a variety of non-spherical forms. Therefore the scattering theory of chapter 3 was found to be unsuitable as it stood for direct application to cirrus clouds, and in chapter 5 it is shown how this problem was overcome by the representation of complex ice crystal forms as *equivalent spheres*. The complete forward model, including cirrus scattering, was then used to produce the results presented in chapter 6, which demonstrate the effect of cirrus both on the MLS measurements themselves and on the physical quantities retrieved from those measurements. Finally, the principal findings of the thesis are summarised and discussed in chapter 7.

The remainder of this chapter is devoted to a description of the EOS MLS, in terms of its scientific objectives, the measurements it will make to fulfil those objectives, and the manner in which the measurements are made.

1.2 The EOS MLS

The Earth Observing System [Dozier 1990] is a collective name for a series of orbiting spacecraft due to be launched from 1998, as part of NASA's Mission to Planet Earth programme of Earth observation from space. Each of the EOS spacecraft will carry a suite of instruments designed to study large-scale environmental processes, with an emphasis on global climate change. The CHEM-1 spacecraft, due for launch in December 2002, is designed to study chemical species in the atmosphere, and it is this platform upon which the MLS will be mounted.

The EOS MLS will be constructed by the same consortium which was responsible for the MLS instrument on the Upper Atmosphere Research Satellite (UARS) [Reber *et al* 1993] which was launched in 1991. The UARS MLS employed radiometers operating at frequencies at or below 200 GHz to measure vertical profiles of water vapour, ozone, and chlorine monoxide. The EOS MLS will make use of considerable developments in microwave technology since the launch of UARS to significantly extend its capabilities over those of the UARS MLS. The EOS MLS incorporates radiometers operating at shorter wavelengths than the UARS MLS, in the submillimetre region where it is possible to measure a larger range of atmospheric constituents, and where certain species such as ClO have their strongest lines, allowing higher sensitivity for these measurements. The set of radiometer frequencies which will be used has been subject to frequent review, owing to the need to optimise the measurement capabilities of the MLS whilst keeping costs down. The final configuration is not yet finalised, but it seems probable that it will include radiometers operating at frequencies close to 200 GHz, 240 GHz, 640 GHz and 2.5 THz.

The objective of the EOS MLS is to monitor chemical processes in the atmosphere which are vital to global climate change research. The instrument will give continuous day-and-night coverage of the globe between 82°N and 82°S, with radiance profiles being measured approximately every 170 km along the orbit track [Heriot-Watt *et al* 1994]. The MLS measures each profile by changing the pointing direction of its antenna in steps down through the atmosphere from 80 km to the ground, integrating the received radiation for a period of 0.33 s on each step. The field of view of the measurements depends on the frequency; for the 640 GHz radiometer it is specified in the EOS Reference Handbook [NASA 1995] as 1.5 km in the vertical, 3 km cross-track, and 300 km along-track at the tangent point.

The areas of the atmosphere which will be studied are listed below, together with the chemical species which will be observed.

Chemistry of the Upper Troposphere: Concentrations of water vapour and ozone, for various reasons which are explained below.

Chemistry of the Lower Stratosphere: Concentrations of water vapour, ozone, chlorine monoxide, hydrochloric acid, nitric acid, nitrous oxide, and the hydroxyl radical, in order to determine their effects on the transformation of greenhouse gases, on radiative forcing of climate change, and on ozone depletion.

Chemistry of the Middle and Upper Stratosphere: Concentrations of the radicals involved in ozone destruction, and of their reservoirs and source gases.

Effect of Volcanic Plumes on Climate Change: Concentrations of sulphur dioxide as well as other gases in volcanic plumes in the lower stratosphere, to determine their effect on global warming.

Since cirrus is an upper-tropospheric cloud, its possible contamination effect would only apply to the first of the objectives listed above. Therefore in this section it is only the measurement of upper-tropospheric water vapour and ozone which is examined in detail. In the following sections the reasons why such measurements are required are examined, firstly for water vapour, and then for ozone.

1.2.1 The Need for Observations of Upper Tropospheric H_2O

There is a lack of data on the global distribution of upper-tropospheric water vapour (UTW). The conventional method of measuring this is by *radiosonde*, that is a balloon-borne instrument which transmits its results to a receiving station on the ground. However, such measurements can be unreliable in cold dry conditions, and so the H_2O climatology above the mid-troposphere derived from radiosondes is not well known [Elliott & Gaffen 1991]. In addition, the geographical distribution of radiosonde measurements is poor, especially over Africa and Asia [Van de Berg *et al* 1991]. To achieve global coverage satellite measurements are required, and to date there have not been a large number of such studies. Some of those that have been undertaken are the infrared measurements made by instruments on the GOES and METEOSAT satellites, which are highly affected by cloud contamination, and the solar occultation measurements of the Stratospheric Aerosol and Gas Experiment II (SAGE-II), which are limited to about 30 per day [Read *et al* 1995]. Therefore the EOS MLS, with its continuous global coverage, would provide a valuable contribution to the UTW climatology. The EOS MLS Review [RAL *et al* 1993] specifies the ability to measure UTW *in the presence of clouds* as a key scientific consideration underpinning the selection of the MLS for inclusion on CHEM-1.

There are several reasons why UTW is an important quantity to measure. These are listed below, followed by a more detailed discussion of the science involved in certain cases.

- Water vapour is the most important 'greenhouse gas', but the precise relationship between its concentration and the surface temperature of the Earth is not well understood.
- Cloud formation is also a crucial factor in global warming, and the abundance of high cloud is highly coupled to water vapour concentration.
- Accurate UTW concentrations are required to initialise and verify numerical weather prediction models.

- H_2O is a source of the hydroxyl (OH) radical, which is an important factor in tropospheric chemistry [Logan *et al* 1981], and which acts as a catalyst in the destruction of ozone [Rind *et al* 1993].
- Water can be used as a tracer for the study of stratosphere-troposphere exchange, and for determining atmospheric circulation patterns.

Of these properties, perhaps the most widely studied is the first. The greenhouse effect is defined by Raval and Ramanathan [1989] as the trapping of infrared radiation energy by atmospheric gases and clouds. Solar radiation which is incident on the Earth with little absorption by the intervening atmosphere is re-radiated in the infrared, which is more readily absorbed by the molecules of greenhouse gases in the atmosphere. These molecules re-radiate the absorbed energy in all directions, so there is a downward component of radiation which is incident on the surface, and which causes the equilibrium temperature to be higher than it would be if greenhouse gas concentrations were lower. Water vapour is the most important of the greenhouse gases because it absorbs well in the infrared, and because of its abundance in the troposphere.

Water is additionally important because of the possibility that there is a strong positive feedback between H_2O content and surface temperature. Surface temperatures may initially be increased by the enhanced greenhouse effect due to an influx of anthropogenic gases such as CO_2, and this will in turn lead to increased evaporation from the surface and the injection of more water vapour into the troposphere. Therefore the cycle would be self-sustaining. Rind *et al* [1991] present observational evidence from SAGE-II to support this picture. On the other hand, Lindzen [1990] argues that in the tropics, an increased surface temperature will cause moist air to be convected in cumulonimbus columns, and the consequent condensation and precipitation of the water content during the ascent will lead to the upper troposphere actually becoming drier rather than wetter. This would suggest a *negative* feedback process. In addition to these factors, the reflective properties of cirrus clouds also have an influence. Cirrus shields the Earth from incoming short-wavelength solar radiation [Ramanathan & Collins 1991], and since the formation of cirrus is highly dependent on water vapour content, this will also act as a negative feedback.

Clearly an accurate knowledge of the UTW content, and of long-term trends in this content, is required if such processes as those described above are to be successfully modelled. Most climate models include a positive H_2O feedback but because of the uncertainty in UTW there is great variation between the results of these models [Cess *et al* 1990]. In addition, the inter-hemispheric asymmetry of UTW content described by Kelly *et al* [1991] is not properly reproduced by most

models.

Certain other properties of UTW listed above are worthy of further discussion here. In numerical weather prediction, an accurate water vapour climatology is required to initiate and verify the models. Illari [1989] comments that individual profiles of water vapour provided by radiosondes are not adequate to provide the initialising humidity analysis for such models, and that satellite data are required to provide the necessary spatial and temporal resolution. Rind *et al* [1993] note that the uncertainty in the radiosonde-derived water vapour climatology limits the success of tropical forecasting to just 1 or 2 days ahead.

Finally, it has been noted that water vapour may be used as a tracer, allowing the mapping of circulation patterns. Van de Berg *et al* [1991] use patterns of mean monthly UTW derived from METEOSAT infrared measurements to characterise the geographical structure of Hadley cells. Given that a UTW climatology derived from microwave measurements is likely to be more reliable than that which is possible with infrared measurements, the EOS MLS would considerably aid such studies.

1.2.2 The Need for Observations of Upper-Tropospheric O_3

As well as water vapour, the EOS MLS is intended to retrieve ozone in the upper troposphere. The study of O_3 at such altitudes is not as vital a research area as is that of water vapour in the same region, or that of stratospheric ozone. However it still has an important part to play in our understanding of the atmosphere, for reasons explained below.

Ozone is a greenhouse gas, and while not as potent as water vapour, it is one of the most important of the trace gases in this respect. In the upper troposphere it is at its most effective, as demonstrated by Lacis *et al* [1990]. Its greenhouse properties are somewhat more complex than those of water vapour, because O_3 absorbs strongly both the incoming solar radiation in the ultraviolet as well as the re-radiated infrared radiation. Wang *et al* [1988] find that changes in the vertical distribution of ozone in the middle and upper troposphere due to the destructive effects of CFCs may trigger a negative feedback effect which would regulate the greenhouse effect of CFCs.

Ozone is also a strong oxidant, as well as being a source of other, more highly reactive oxidants [Schnell *et al* 1991], and as such it is important in tropospheric photochemistry. Penkett *et al* [1988] point out that ozone is the primary source of the hydroxyl radical in the troposphere, and that this radical is responsible for most of the chemical transformations which result in the removal of pollutants from the atmosphere.

Typically only 10% of the total column density of ozone resides in the tro-

posphere, and it is the stratospheric contribution which plays the major role in protecting life from the harmful effects of solar UV radiation. However, in order to predict future levels of stratospheric ozone, it will be necessary to understand the transport processes which govern ozone levels in the troposphere, and particularly the exchange of ozone across the tropopause [WMO 1985]. The work of Moody *et al* [1995], *inter alia*, suggests that there is also some transport of ozone from the upper troposphere to the surface. This would add considerable importance to upper tropospheric ozone measurements, since surface ozone in high enough concentrations can be toxic, and damages vegetation [Prinz 1988].

As with water vapour, the accumulated radiosonde measurements of upper-tropospheric ozone are very sparse, and of uneven quality [Lacis *et al* 1990], and as such are unsuitable for trend detection. Lacis *et al* point out that the verification of existing photochemical models of the troposphere requires a global database which can only be provided by satellite instruments. Some satellite studies have been made, including those provided by SAGE-II and by the Limb Infrared Monitor of the Stratosphere (LIMS), although the former has limited daily coverage (as explained previously) and the latter, being an infrared instrument, suffers from cloud contamination. Therefore it is clear that EOS MLS will have an important role to play if it can successfully retrieve ozone in the upper troposphere.

Chapter 2

The Forward Model

2.1 Introduction

The results of this thesis are based upon a simulation of the radiance which is observed by the microwave limb sounder. Such a simulation is an essential part of any radiometric sounding study, and the code that performs it is called a *forward model*. The forward model provides a calculated measurement which acts as a reference for the observation made by the MLS. In this capacity it is used before the observation is made in order to determine which spectral bands will provide sufficient information for an accurate retrieval of the atmospheric state, and is also used in conjunction with the chosen observation to make that retrieval.

The forward model described in this chapter was used to provide radiance data for a non-scattering atmosphere, to identify spectral bands which allow the retrieval of tropospheric species. Then the extent to which a cloud's presence degrades the sensitivity of these retrievals was determined by incorporating a scattering model into the forward model. The development of such a scattering model is the subject of the later chapters of this thesis.

In this chapter I will outline the physical basis upon which the forward model is constructed, and show how the calculations are implemented in practice. This description is in four sections:

1. Section 2.2: An introduction to the theory of radiative transfer, which sets out the basic problem which the forward model is designed to solve – the radiative transfer equation.

2. Section 2.3: A description of the absorption and emission of microwave radiation by molecules, and an explanation of the way in which the forward model quantitatively simulates these processes.

3. Section 2.4: The solution of the radiative transfer equation, including the numerical method used, and descriptions of the model atmosphere through

which the transfer takes place, and the geometry of the solution path with respect to this atmosphere.

4. Section 2.5: The simulation of the microwave limb sounder's processing of the signal which arrives at its main antenna.

In section 2.6 there is a discussion of the model's validation by comparison with similar models developed independently by other researchers. A summary of what the work described in this chapter has achieved is presented in section 2.7.

The development of the forward model (without scattering) as described in this chapter does not represent all my own work. The model was adapted from an early version of the EOS MLS forward model developed by Mark Filipiak of the Department of Meteorology, University of Edinburgh. In the following sections I have indicated where necessary when a part of the forward model was already extant in the Filipiak model, and when the work described is my own alteration or addition to the original.

2.2 Thermal Radiation

To develop a theory of how radiation is emitted and absorbed by molecules, we start by considering an idealised *blackbody*. This is defined as a material which absorbs all the radiation incident upon it, at all frequencies. According to Planck's law, a blackbody radiates isotropically with a spectral radiance given by

$$B_\nu = \frac{2h\nu^3}{c^2}\left[\frac{1}{\exp(h\nu/kT)-1}\right] \tag{2.1}$$

where ν is the frequency and T the temperature. The spectral radiance B_ν has SI units of $\mathrm{Wm^{-2}sr^{-1}Hz^{-1}}$.

When $h\nu \ll kT$, the Planck function reduces to the *Rayleigh-Jeans Law*. This is done by expanding the exponential term as a power series and neglecting powers higher than 1, so that $\exp(h\nu/kT) \simeq 1 + (h\nu/kT)$. Then the Planck function becomes

$$B_\nu = \frac{2kT\nu^2}{c^2} \tag{2.2}$$

At atmospheric temperatures and a frequency of 600 GHz, the Rayleigh- Jeans law differs from the Planck function by about 5 to 10%, so the latter is used in preference to the former in the forward model. However, equation 2.2 may be inverted to define the *brightness temperature* T_B as follows:

$$T_B = \frac{c^2}{2k\nu^2} I_\nu \tag{2.3}$$

where I_ν is any spectral radiance. The brightness temperature is commonly used quantity in microwave radiometry because it is proportional to the received spectral

power P_ν, as shown by Ulaby *et al* [1981, p.200]. Therefore, although it is derived from the Rayleigh-Jeans law, its use is not restricted to the Rayleigh-Jeans limit[1].

Real bodies are non-blackbodies which do not absorb all the radiation incident upon them, nor do they emit as much radiation (summed over all frequencies) as a blackbody. However, when in thermal equilibrium, a body obeys *Kirchhoff's Law*, which states that a body which absorbs a fraction a_ν of the radiation incident upon it will emit an isotropic spectral radiance $a_\nu B_\nu$, where B_ν is the Planck function as defined in equation 2.1. The quantity a_ν is called the spectral absorptivity. The assumption of thermal equilibrium is discussed later.

Consider a radiance I_ν which is incident on a particular gas. The gas is composed of particles of number density n, each with an absorption cross-section C_a, which is to say that each particle absorbs the radiance falling upon the area C_a. The total absorption cross-section per unit volume is known as the *volume absorption coefficient*, γ_a. Therefore, in a homogeneous volume ΔV, the spectral power per unit solid angle absorbed by the gas is $I_\nu \gamma_a \Delta V$. Now if ΔV is a box of length Δx in the direction of propagation of I_ν, with area ΔA normal to that direction, then the absorbed spectral power per unit solid angle may also be expressed as $I_\nu a_\nu \Delta A$. Therefore the spectral absorptivity is expressed in terms of the volume absorption coefficient by $a_\nu = \gamma_a \Delta x$, or if γ_a is a function of x, $a_\nu = \int \gamma_a dx$. For a given path $x_1 \rightarrow x_2$ through a gas, the spectral absorptivity is called the *optical path*[2] and is written $\tau(x_1, x_2)$.

Kirchhoff's law now leads to a derivation of the equation of radiative transfer in a gas. Across an elemental length dx, the change in the radiance I_ν due to absorption is given by

$$(dI_\nu)_{\text{ABS}} = -I_\nu \gamma_a dx \tag{2.4}$$

while that due to emission is

$$(dI_\nu)_{\text{EM}} = B_\nu \gamma_a dx \tag{2.5}$$

So combining these two parts gives the basic formula of radiative transfer, called the *Schwarzschild equation*:

$$\frac{dI_\nu}{dx} = \gamma_a [B_\nu - I_\nu] \tag{2.6}$$

where γ_a and I_ν are functions of x, and B_ν is a function of T, which is in turn a function of x.

[1] The brightness temperature as defined here does not have the same physical significance as the *equivalent blackbody temperature*, which is obtained by inverting the Planck function, giving the temperature of a blackbody that would produce the given radiance at that frequency. In infrared studies, however, the brightness temperature is often defined as the equivalent blackbody temperature.

[2] Also known as the *opacity*.

The Schwarzschild equation is an ordinary differential equation which may be converted to an integral form called the *Chandrasekhar equation*:

$$I_\nu(L) = I_\nu(0)\exp[-\tau_\nu(0,L)] + \int_0^L B_\nu \exp[-\tau_\nu(x,L)]\gamma_a \, dx \qquad (2.7)$$

where $I_\nu(0)$ is the radiance incident on the gas at $x = 0$ and $I_\nu(L)$ is the emergent radiance at $x = L$.

In this form the physical meaning of the equation is apparent: the first term on the right hand side is the incident radiation, attenuated through the whole path length L, and the second term is the sum of the contributions to thermal emission from each point in the gas, also attenuated by the intervening gas.

From equation 2.3, the brightness temperature T_B is proportional to I_ν, so it can be substituted into the Schwarzschild equation – provided B_ν is also transformed by setting $I_\nu = B_\nu$ in equation 2.3, to give a 'Planck brightness temperature', T_B^*. Outside the Rayleigh-Jeans limit the Planck brightness temperature will be close to, but not equal to, the physical temperature. The resulting Schwarzschild equation for brightness temperature is as follows

$$\frac{dT_B}{dx} = \gamma_a(T_B^* - T_B) \qquad (2.8)$$

This is the equation which is solved by the forward model to yield the brightness temperature along a given path through a non-scattering atmosphere. Details of the method used to solve the equation are given in section 2.4.1.

2.3 Molecular Emission and Absorption

2.3.1 Introduction

The solution of the Schwarzschild equation requires the calculation of the absorption coefficient γ_a, which is determined by the physics of the interaction between the molecules in the atmosphere and the radiation incident upon them. This section is a description of the quantum mechanical process by which molecules absorb and emit radiation. This will involve consideration of the rotational dynamics of molecules, and therefore the rules governing angular momentum of quantum systems will be discussed and applied to the rotation of a molecule. This will be followed by a derivation of an expression for the absorption coefficient, and a description of how the calculation is performed in the forward model. Finally the *broadening* of spectral lines is considered, and various methods of accounting for its effect in the model are presented.

2.3.2 Quantum Energy Levels

According to quantum theory, the dynamic properties of particles, such as their energies and momenta, are quantised such that they can only take certain discrete values. Each species of molecule therefore has its own characteristic set of internal energy levels, or *states*. The internal energy is the sum of individual contributions arising from the different modes of motion within the molecule, such as vibration, rotation, and the orbits of its electrons.

When a molecule changes between states, energy is conserved by the emission or absorption of a photon (the quantum of radiation) with an energy equal to the difference between the states. Since photon energy is given by the Planck-Einstein relation $E = h\nu$, an energy level transition has a characteristic frequency of radiation, ν, and so the transition gives rise to a spectral line of absorption or emission at that frequency. Such emission or absorption is known as *resonant*, because the photon has to resonate with (i.e. have the same frequency as) the energy gap.

Each mode of motion within the molecule has energy levels which are spaced on different scales, and therefore the resulting spectral lines occupy different regions of the spectrum. Transitions between electron energy levels give rise to radiative effects in the visible and ultraviolet, while vibrational transitions appear in the infrared, and rotational transitions in the microwave and millimetre-wave region. In microwave limb sounding it is the radiation due to rotational transitions in molecules that we are attempting to measure.

The JPL Spectral Line Catalogue [Pickett *et al* 1992] contains the physical parameters which describe the rotational transitions of all the significant gases in the Earth's atmosphere. Additional data were also taken from the HITRAN 1991 Catalogue [Rothman *et al* 1992], and added to the JPL data by Mark Filipiak. Details of the contents of the resulting combined database are discussed later.

A gas at a given temperature T will contain molecules which occupy a range of energy states above the ground state, according to the rate of excitation and de-excitation which occurs as a result of thermal agitation. The distribution of state occupancies is described by the *Boltzmann distribution*, which gives the number density of molecules in a given state l as

$$n_l = \frac{g_l \exp(-E_l/kT)}{Q} n \tag{2.9}$$

where n is the total number density of the gas, and E_l is the energy of state l. The denominator Q is a factorising term called the *partition function* which is defined

by the following sum over all states l:

$$Q = \sum_l g_l \exp(-E_l/kT) \tag{2.10}$$

The term g_l in equations 2.9 and 2.10 is the *degeneracy*, which represents the number of states of equal energy E_l in which a molecule may lie. It is fully defined later.

The Boltzmann distribution accurately represents the behaviour of all real gases, except for those composed of a few of the lightest atoms at very low temperatures [Dickerson 1969, p.32]. As such it is suitable for use in the Earth's atmosphere. In full thermal equilibrium, this Boltzmann distribution is maintained independently by both radiative effects and collisions. If there is a net radiation gain or loss, the Boltzmann distribution is not maintained in radiative processes, but it may still be maintained overall by collisions. This requires that the rate of collisional excitation and relaxation is sufficiently high that it dominates the radiative processes. Such conditions are described as *local thermodynamic equilibrium* (LTE) [Houghton 1986, p.70]. The assumption of LTE allows the application of Kirchhoff's Law and therefore the use of the Planck function as the source function in the equation of radiative transfer.

LTE will fail, and the source function will begin to differ significantly from the Planck function, when there is a significant net radiative energy change *and* the rate of transitions due to collision becomes comparable to that due to radiative processes. This only occurs at an altitude of $\sim$ 80km [Houghton 1986, p.74], when there is significant heat loss to space, and the pressure (and therefore the collisional frequency) is very low.

2.3.3 Rotational Angular Momentum

Angular momentum is a dynamic property, so it is quantised, and can be represented by a positive integer called the quantum number of angular momentum. For example, the orbital angular momentum L of an electron bound in an atom is given by the equation

$$L^2 = l(l+1)\hbar^2 \tag{2.11}$$

where l is the quantum number.

Particles may also possess an intrinsic angular momentum called *spin*. The spin quantum number s is distinct from l in that it may take half-integer values; for example, the spin of an electron is $s = 1/2$. This is an intrinsic property of the electron which puts it in a class of particles called the *fermions*. Particles with integral values of spin are called *bosons*.

To a good approximation, a molecule can be considered a rigid rotator, such that the equilibrium separation between its component atoms is effectively fixed. The ro-

tational angular momentum of such a molecule is given by the total orbital[3] angular momentum of its atoms, and is quantised with a quantum number N. The rotational energy of the molecule depends on its angular momentum, and so the energy transitions observed by microwave limb sounding are those due to changes in N. The spacing of the resulting rotational energy levels is similar to the fine structure splitting of electronic spectral lines in atoms [French & Taylor 1978, p.426,492].

The total angular momentum of a molecule is the sum of its rotational angular momentum, the orbital and spin angular momenta of its electrons, and the spin of its nuclei. This total angular momentum is itself independently quantised, and is represented by the quantum number J. For a given J there exist $2J + 1$ separate states which have the same energy. Such states are called *degenerate*, and the value $g = 2J + 1$ is the degeneracy for that total angular momentum.

2.3.4 Molecular Radiation

Given the above description of the angular momentum states of molecules, the radiation which results from transitions between those states can now be discussed. Any such transition is constrained by a *selection rule* which is a manifestation of the conservation of angular momentum. The photon which is emitted or absorbed is a boson with a spin angular momentum of one. Therefore in order to conserve angular momentum, the total angular momentum of the molecule must change by one in the course of a single transition, and so the selection rule is $\Delta J = \pm 1$.

The existence of an energy gap between two states is not sufficient in itself to cause a transition to occur. In order to absorb or emit a photon, there must also be some interaction between the molecule and the electromagnetic field of the radiation. Usually this takes place when the molecule has a permanent electric dipole moment, which will be the case when there is a mean asymmetry in its electron charge distribution. When such a dipole moment is present, the emission of a photon is the result of an oscillation of the charge distribution, which is equivalent to the oscillation of the charges of a classical electric dipole[4]. The oscillation of the molecule's charge distribution arises from the harmonic time dependence of the overall electron wavefunction as the transition takes place. Herzberg [1945] provides a detailed explanation of this process.

When a molecule has no permanent electric dipole moment, radiation may still occur if instead there is an electric quadrupole moment, or a magnetic dipole moment as in the case of the oxygen molecule described later. In both cases the probability of a transition occurring is considerably less than when it happens through

[3] Orbital in the sense that the component atoms are orbiting about their common centre of mass.

[4] The classical electric, or *Hertzian* dipole is described by Grant & Phillips [1975, p.427].

an electric dipole, by a factor of 10^6 for the electric quadrupole, and 10^4 for the magnetic dipole [French & Taylor 1978, p.610,611]. For this reason such transitions are known as 'forbidden', although they do in fact occur.

The interaction between the radiation and the molecule, however it is achieved, may take one of the following three forms:

- Absorption, which occurs when the incident radiation resonates with an energy gap.
- Spontaneous Emission, which occurs because states higher than the ground state are occupied, and there is a probability of the molecule dropping down a state.
- Stimulated Emission, which occurs when the transition to a lower state is stimulated by the incidence of a photon of the same frequency.

The net effect of these three processes manifests itself as the overall emission or absorption of the gas, and is represented in the Schwarzschild equation (2.6) by the volume absorption coefficient, γ_a. Waters [1990] formulates the following expression for the absorption coefficient at frequency ν due to an electric dipole:

$$\gamma_a = \frac{2\pi^2 n g_l g_u |\mu_{ul}|^2 \nu f(\nu, \nu_{ul})[\exp(-E_l/kT) - \exp(-E_u/kT)]}{3\epsilon_o c Q h} \tag{2.12}$$

where ν_{ul} is the line centre frequency, g_l and g_u are the degeneracies of the lower and upper states respectively, E_l and E_u are the energies of those states, $|\mu_{ul}|$ is the magnitude of the electric dipole vector, and $f(\nu, \nu_{ul})$ is the lineshape function, which is defined and discussed in section 2.3.5.

The calculation of the absorption coefficient in the forward model using equation 2.12 did not require the determination of each of the individual physical quantities it includes. Considerable effort was saved by the use of a spectroscopic database, as described below.

Calculation of the Absorption Coefficient in the Forward Model

In the JPL spectral line catalogue [Pickett *et al* 1992] a value is listed, for each microwave transition, of the 'line intensity' W_{ul}, which incorporates many of the terms involved in the definition of the absorption coefficient. The line intensity in units of m^2Hz is defined by Waters [1990] as[5]:

$$W_{ul} = 10^{12} \frac{2\pi^2 g_l g_u |\mu_{ul}|^2 \nu_{ul}}{3\epsilon_o c h} \left[\frac{\exp(-E_l/kT) - \exp(-E_u/kT)}{Q_{rs}}\right]_{300\,\mathrm{K}} \tag{2.13}$$

[5] This expression differs from that given by Pickett *et al* [1992] in that the factor $g_l g_u |\mu_{ul}|^2$ is replaced by ${}^x S_{ul} \mu_x^2$, where μ_x is the electric dipole moment in the x-direction, and ${}^x S_{ul}$ is called the 'line strength'. Waters [1990] demonstrates that $g_l g_u |\mu_{ul}|^2 = {}^x S_{ul} \mu_x^2$, so there is no need to introduce these new terms here. There is also a difference of a factor $(4\pi\epsilon_o)^{-1}$, which arises from the use of Gaussian units in the definition of line intensity.

Although the line intensity is defined for an electric dipole transition, the values listed in the catalogue include those for molecules which do not have an electric dipole moment. In these instances the line intensity is defined with an equivalent electric dipole vector magnitude $|\mu_{ul}|$, which gives the same results as the electric quadrupole or magnetic dipole it represents.

Q_{rs} is the *rotation-spin* partition function. This is the partition function defined by equation 2.10, but summed only over the states j which arise from transitions in either rotational energy, or spin-rotation coupling energy. The total partition function Q is the product of the rotation-spin partition function and the corresponding partition function for electronic and vibrational transitions, Q_{ev}. According to Waters [1990], Q_{ev} can be considered approximately equal to 1 for submillimetre and millimetre lines. Therefore we assume $Q = Q_{rs}$. Values of Q_{rs} are listed for each molecule in the JPL catalogue at temperatures of 300 K, 225 K and 150 K, which covers the range of atmospheric temperatures. Waters [1976] shows that in general $Q_{rs} \propto T^n$ where n depends on the type of molecule, so the value of Q_{rs} for a given temperature may be obtained from the catalogued values by logarithmic interpolation.

So, substituting the line intensity into the absorption coefficient equation 2.12, we get the equation which is used in the forward model itself

$$\gamma_a = 10^{-12} n f(\nu, \nu_{ul}) W_{ul} \frac{\nu}{\nu_{ul}} \frac{\exp(-E_l/kT)[1-\exp(-h\nu_{ul}/kT)]}{\exp(-E_l/300k)[1-\exp(-h\nu_{ul}/300k)]} \frac{Q_{rs}(300\text{ K})}{Q_{rs}(T)} \tag{2.14}$$

The lower state energies E_l are also listed for each transition in the JPL catalogue. The lineshape function $f(\nu, \nu_{ul})$ is defined in section 2.3.5. Equation 2.14 is the expression for the absorption coefficient used by Filipiak, and is inherited by my model.

Examples of Important Atmospheric Molecules

Some of the ideas developed in this section are best illustrated by reference to particular molecules. The discussion below centres on three of the most important molecules for microwave limb sounding: water, oxygen and ozone.

The water molecule, shown in figure 2.1 is an *asymmetric top*, meaning that it has a different moment of inertia about each of its axes. For this reason there are a large number of different rotational transitions which may occur and a correspondingly wide rotational spectrum which extends from a wavelength of 10 μm to about 1 cm [Schanda 1986, p.53]. Furthermore, the asymmetry of the molecule's nuclear arrangement means that the electron charge distribution is similarly asymmetric, and therefore it has a large electric dipole moment. From equation 2.12 it may be

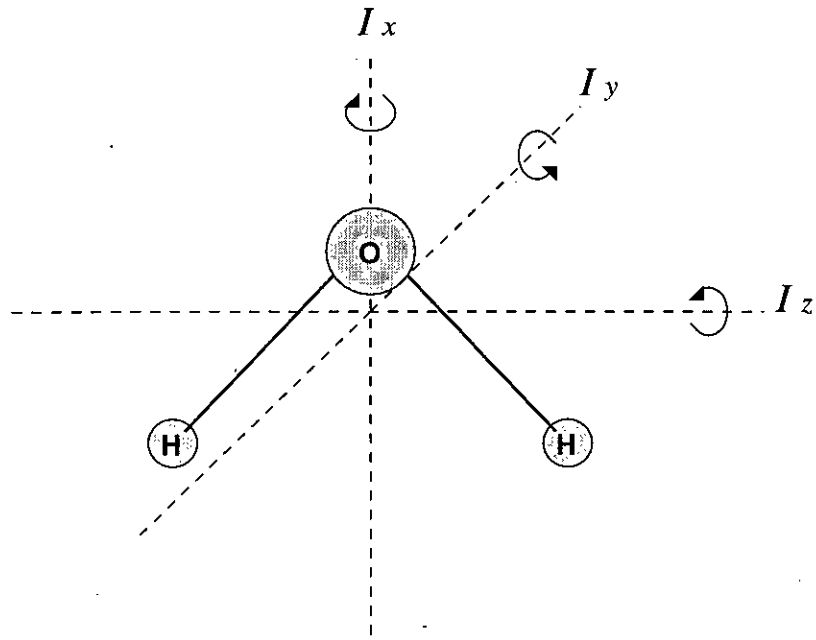

Figure 2.1: Modes of rotation of the H_2O molecule.

seen that this results in a large absorption coefficient, and it is this, coupled with the relative abundance of water vapour in the lower atmosphere, that gives water a very strong microwave emission spectrum in the troposphere.

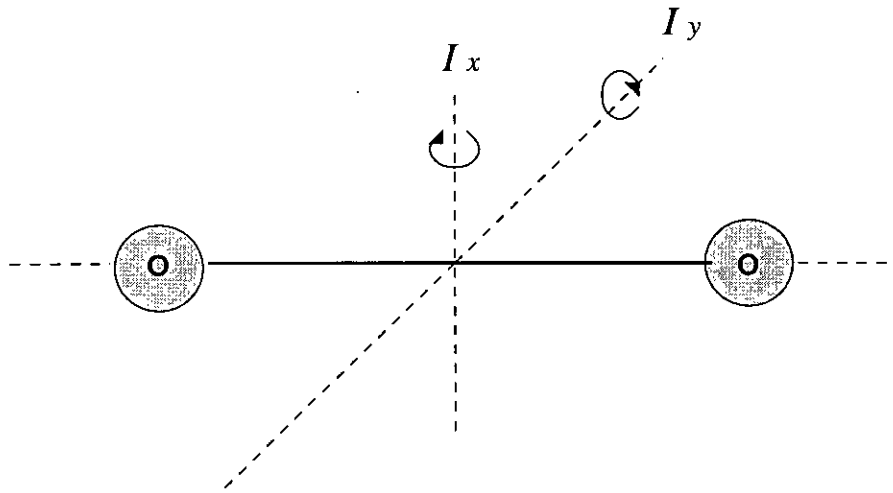

Figure 2.2: Modes of rotation of the O_2 molecule.

The oxygen molecule O_2, shown in figure 2.2, has only two degrees of rotational freedom, and significantly has no electric dipole moment because of its symmetry. The same is true of other homonuclear diatomic molecules such as N_2. In the case of N_2, this means that there is no rotational spectrum because the molecule is unable to interact with radiation, but O_2 is able to interact by way of its *magnetic* dipole

moment.

This magnetic moment is due to the electronic structure of the molecule. The ground state of O_2 is denoted by the molecular term symbol $^3\Sigma$, which denotes its overall angular momentum state. The Σ is analogous to the atomic term symbol S, in that it signifies a total orbital angular momentum of zero, which occurs when pairs of electrons orbit the molecule in opposite directions. Therefore the outermost two electrons of the molecule, being in different orbital states, may both adopt the same spin state without violating the Pauli exclusion principle, which requires that no two electrons share the same set of quantum numbers. The electrons may in fact be spin-paired, but the resulting molecular state has a higher energy and is therefore not the ground state. Therefore the total spin of the molecule in its ground state is one.

The magnetic moment of a molecule arises from its spin state, so the non-zero spin of the O_2 molecule in its ground state is the source of the permanent magnetic dipole moment which allows the oxygen molecule to interact with radiation. Since magnetic dipole transitions are considerably less probable than those due to electric dipoles, the absorption coefficient of an O_2 rotational transition is very much smaller than that of other molecules. However, the great abundance of oxygen in the Earth's atmosphere means that the resulting spectrum is strong and may be easily measured.

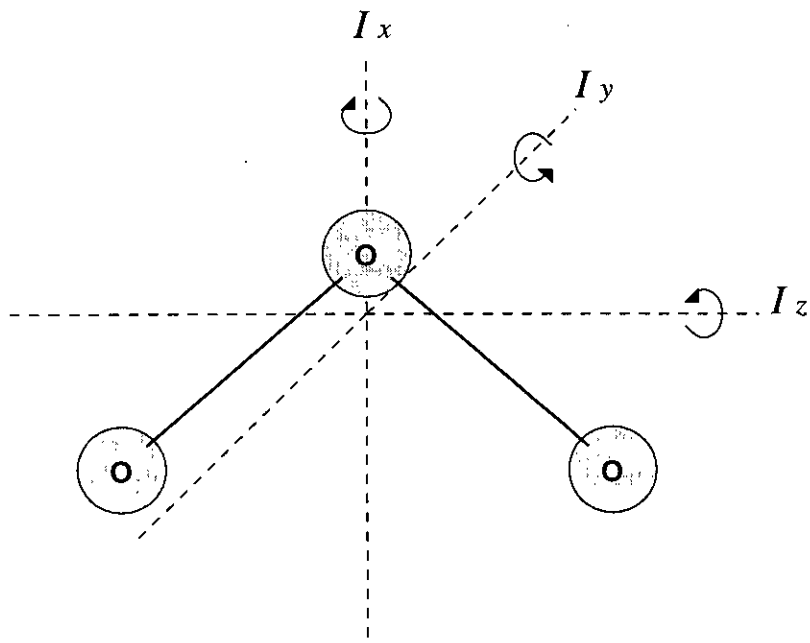

Figure 2.3: Modes of rotation of the O_3 molecule.

The ozone molecule (figure 2.3), like water, is an asymmetric top, and it shares

some of water's characteristics. It has a strong electric dipole moment owing to its asymmetry (although not as strong as that of water), so it has strong absorption lines. Like water, its three degrees of rotational freedom, each with a different moment of inertia, lead to a wide range of spectral lines. However, whereas water is most abundant in the lower troposphere, ozone reaches its maximum concentration at $\sim$ 25 km [Schanda 1986, p.61], where it may be observed without being swamped by the stronger water vapour spectrum.

2.3.5 Lineshapes

The spectral lines described so far have been entirely monochromatic. In nature this is not the case since there are various processes of line broadening which give an emission or absorption feature a finite frequency width. The mathematical form of a broadening process is expressed as the *lineshape function* $f(\nu, \nu_{ul})$, which is the remaining undefined term in equation 2.14 for the calculation of the absorption coefficient. The lineshape function is normalised such that its integral over all frequencies is unity.

The most fundamental form of broadening is called the *natural width* of the line, which arises because of the Heisenberg energy-time uncertainty principle. In the atmosphere however, this form of broadening is absolutely negligible compared with other broadening processes.

In the troposphere and stratosphere *collisional broadening* (also called pressure broadening) is the most significant process. The thermal agitation of the molecules in the gas means that they continually collide with one another, and such collisions disturb the interaction between radiation and the dynamical states of the molecule (i.e. its vibration and rotation). This can stimulate a transition and thus shorten the lifetime of such a state, and consequently the line is broadened.

A third process is *Doppler broadening*. The molecules in a gas have a Gaussian distribution of velocities; when the velocity of a molecule is towards the observer, the Doppler effect means that its emitted radiation appears shifted up in frequency. At the same time, the molecule is moving in the same sense as the radiation incident upon it in the direction of the observer, so it absorbs at a lower frequency. The velocity distribution is symmetrical, so the net effect on the observed radiance from the gas is also symmetrical.

In the following sections, formulae are presented for calculating both collisional and Doppler broadening, and for a combination of the two. The choice of which formula to use is dependent on the way in which the contribution due to water vapour is evaluated, as will become clear.

Collisional Broadening

The lineshape function for collisional broadening may take various forms according to the theoretical model used to describe the collision. The simplest form used is the *Lorentz* lineshape given by the formula

$$f_{\text{L}}(\nu, \nu_{ul}) = \frac{1}{\pi} \frac{\Delta\nu}{(\nu_{ul} - \nu)^2 + \Delta\nu^2} \tag{2.15}$$

where ν_{ul} is the frequency of the transition (the line centre frequency), and $\Delta\nu$ is the *linewidth parameter*, which is the half-width at half-maximum of the line.

The linewidth parameter is proportional to the frequency of collisions, and so it is a function of pressure and temperature, and Waters [1976] gives the function as $\Delta\nu \propto pT^{-x}$, where x depends on the way in which the intermolecular force varies with separation[6]. Values of x are listed for each line in the HITRAN catalogue [Rothman *et al* 1992], as are values $\Delta\nu_0$ of the linewidth parameter for each line, measured at a standard temperature and pressure of $T_0 = 300$ K, $p_0 = 1$ hPa. Therefore the linewidth parameter at any (T, p) can be obtained by:

$$\Delta\nu(T, p) = \left(\frac{\Delta\nu_0}{300^{-x}}\right) pT^{-x} \tag{2.16}$$

The Lorentz lineshape is a good approximation only when $\Delta\nu \ll \nu_{ul}$, which is the case when the pressure is low; however for the high pressure of the lower atmosphere this is not so. A more realistic treatment of the collision process yields the lineshape derived by Van Vleck and Weisskopf [1945] (abbreviated hereafter to the VVW line), which takes the form

$$f_{\text{VVW}}(\nu, \nu_{ul}) = \frac{1}{\pi}\left(\frac{\nu}{\nu_{ul}}\right)\left[\frac{\Delta\nu}{(\nu_{ul} - \nu)^2 + \Delta\nu^2} + \frac{\Delta\nu}{(\nu_{ul} + \nu)^2 + \Delta\nu^2}\right]. \tag{2.17}$$

This function is generally thought to be a better representation of collisional broadening than the Lorentz line. However, the factor (ν/ν_{ul}), whilst introducing a necessary asymmetry at frequencies close to the line centre, begins to dominate the function when $\nu \gg \nu_{ul}$, and therefore tends to overstate the far upper wing of the line. This may lead to excess absorption at high MLS frequencies caused by the wings of strong, broad lines at longer wavelengths (e.g. $0 \rightarrow 100$ GHz). Ulaby *et al* [1981, p.269] report significant deviations of the VVW from observations in the far wings.

A third collisional broadening form is the *Gross* or *kinetic* lineshape, defined as

$$f_{\text{G}}(\nu, \nu_{ul}) = \left(\frac{1}{\pi}\right) \frac{4\nu\nu_{ul}\Delta\nu}{(\nu_{ul}^2 - \nu^2)^2 + 4\nu^2\Delta\nu^2} \tag{2.18}$$

[6] This function appears counter-intuitive, since we would expect the linewidth to have a positive dependence on the temperature. However, according to the ideal gas law the pressure p is also a function of the temperature, and given that $|x| < 1$, the overall temperature dependence of the linewidth is therefore positive.

which fits the observations better than the VVW in the far wings according to Hall [1967], who fitted the lineshape to the measured spectrum in the far infrared due to water vapour lines centred on millimetre wavelengths.

Although the VVW and Gross lines better represent the collision processes which occur in nature than does the Lorentz, it is the latter which was eventually used in the forward model. To understand why, it will first be necessary to introduce the concept of excess water-vapour absorption.

Excess Water-Vapour Absorption and Choice of Lineshape

When the spectrum of water vapour absorption is calculated using the methods described above, there is a discrepancy between the results and experimentally measured values, which is known as excess water-vapour absorption (EWA). This was investigated by Gaut and Reifenstein [1971], who used the Gross line shape to calculate the spectrum for water vapour between 10 GHz and 1000 GHz, and found that the EWA that remained between their calculations and an observed spectrum could be fitted by a correction term proportional to ν^2. The expression they present is in units of dB/km; the same expression in m^{-1} is given by

$$\Delta\gamma_a = 1.08 \times 10^{-29} \rho \left(\frac{300}{T}\right)^{2.1} p\nu^2 \tag{2.19}$$

where all terms are in SI units.

At least part of the EWA is thought to be due to the cumulative effect of imperfectly-modelled far wings of strong water lines at low frequencies [Burch & Gryvnak 1980, Ma & Tipping 1990]. The Gross lineshape used by Gaut and Reifenstein predicts weaker absorption in the far wings than does the VVW line, and since the Lorentz line behaves similarly to the Gross line in the far upper wing [Ulaby *et al* 1981, p.268], I have chosen to use the Lorentz in the forward model, rather than the VVW lineshape.

The Lorentz line was chosen in favour of the Gross line because the former may be readily combined with the effects of Doppler broadening, as described below, in those regions of the atmosphere where both are important. I recognise in retrospect that it would have been better to use the Gross lineshape, with no consideration given to Doppler broadening, since the aim of this thesis is the modelling of tropospheric retrievals, and it will be seen that Doppler broadening is not significant at such low altitudes.

Doppler Broadening and the Voigt Line

The Doppler lineshape is derived directly from the velocity distribution of the molecules, so it is Gaussian in form. The normalised Doppler lineshape is expressed

as follows [Schanda 1986, p.48]

$$f_{\mathrm{D}}(\nu,\nu_{ul}) = \frac{1}{\Delta\nu_{\mathrm{D}}}\left(\frac{\ln 2}{\pi}\right)^{\frac{1}{2}} \exp\left[-\ln 2\left(\frac{\nu-\nu_{ul}}{\Delta\nu_{\mathrm{D}}}\right)^2\right] \tag{2.20}$$

where $\Delta\nu_{\mathrm{D}}$ is the Doppler linewidth parameter, defined as the half-width at half maximum of $f_{\mathrm{D}}(\nu,\nu_{ul})$, and given by:

$$\Delta\nu_{\mathrm{D}} = \frac{\nu_{ul}}{c}\left(\frac{2kT}{m}\ln 2\right)^{\frac{1}{2}} \tag{2.21}$$

where m is the molecular mass.

Doppler broadening becomes comparable in magnitude to collisional broadening above $\sim$ 50 km in the atmosphere. When both types of broadening are significant, the lineshape function is obtained by the convolution over frequency of the Doppler line with whichever collisional lineshape is being used. If the Lorentz line is used, the resulting Doppler-convolved function is the *Voigt* line, given by Armstrong and Nicholls [1972, p.218] as

$$f_{\mathrm{V}}(\nu,\nu_{ul}) = \frac{1}{\Delta\nu_{\mathrm{D}}}\left(\frac{\ln 2}{\pi}\right)^{\frac{1}{2}} K(x,y) \tag{2.22}$$

where $K(x,y)$ is the *Voigt function*, defined by

$$K(x,y) = \frac{y}{\pi}\int_{-\infty}^{\infty}\frac{\exp(-t^2)}{y^2+(x-t)^2}\,dt \tag{2.23}$$

and

$$x = \frac{(\ln 2)^{\frac{1}{2}}}{\Delta\nu_{\mathrm{D}}}(\nu-\nu_{ul}) \tag{2.24}$$

$$y = (\ln 2)^{\frac{1}{2}}\left(\frac{\Delta\nu_{\mathrm{P}}}{\Delta\nu_{\mathrm{D}}}\right) \tag{2.25}$$

where $\Delta\nu_{\mathrm{P}}$ is the collisional (or pressure) broadening linewidth parameter, as defined in equation 2.16. The terms involving $\Delta\nu_{\mathrm{D}}$ in the above expressions differ from those used by Armstrong and Nicholls because they use an alternative definition of the Doppler linewidth parameter which differs from $\Delta\nu_{\mathrm{D}}$ by a factor $(\ln 2)^{1/2}$.

The integral in equation 2.23 has to be evaluated numerically, and this is done in the model using the fast routine developed by Drayson [1975]. In this way the processing time required to compute the Voigt function is kept low enough to allow the repeated calculations of absorption coefficients which the forward model must perform.

The Voigt line is only required when the Doppler linewidth is a significant fraction of the collisional linewidth. Where possible it is preferable to replace it with one of the pure lineshape functions in order to save processing time. Figure 2.4 shows the relative difference between the Voigt line function and, respectively, the

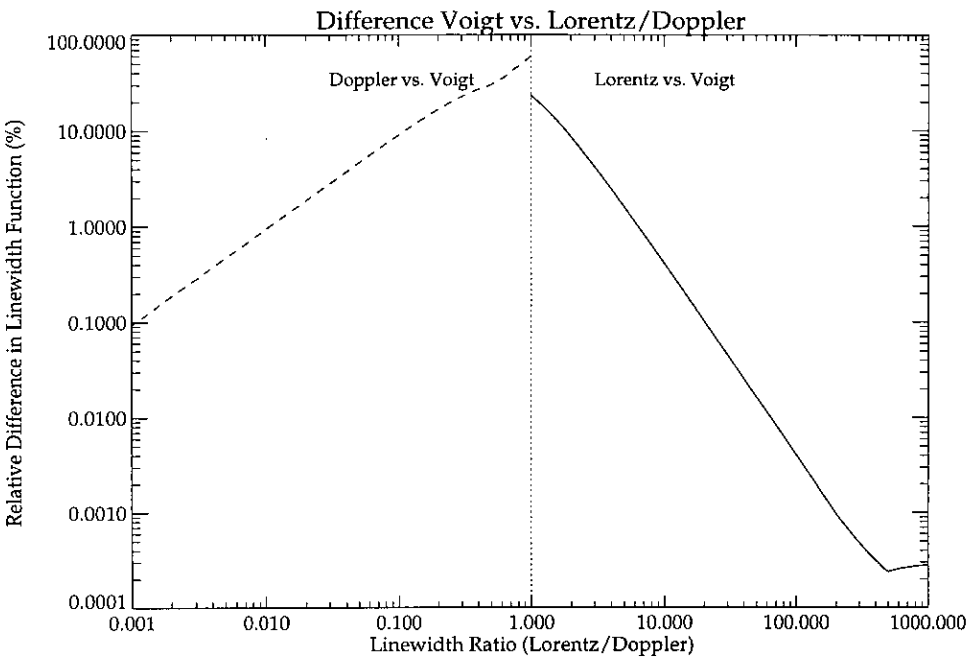

Figure 2.4: Mean error in unconvolved lineshape functions compared with the Voigt line.

Lorentz and Doppler lines, averaged across the width of the line. The variable on the abscissa is the ratio of the linewidths $\Delta\nu_{\text{P}}/\Delta\nu_{\text{D}}$. If an inaccuracy of 0.1% in the pure lineshape compared to the Voigt is considered acceptable, figure 2.4 indicates that the Voigt need only be used when the linewidth ratio lies in the range $10^{-3} \rightarrow 10$. For water molecules, which have a molecular mass $m \simeq 3 \times 10^{-26}$ kg, the linewidth ratio at a frequency of 200 GHz drops below 10 above ~ 50 km, but remains above 10^{-3} even at 100 km. Therefore, with the above condition controlling the use of Voigt line, the pure Doppler lineshape is seldom used in the forward model.

Other Absorption Effects

A final contribution to the absorption arises from the continuum due to collision-induced absorption (CIA) by N_2 molecules [Dagg *et al* 1985]. This was included as an additive term to the total absorption coefficient according to the following formula devised by Bill Read [personal communication]

$$\Delta\gamma_a = 8.42 \times 10^{-20}\nu^2 p^2 \left(\frac{300}{T}\right)^{3.63} \exp[-1.85 \times 10^{-12}\nu^2] \qquad (2.26)$$

where ν is in MHz, p is the pressure in hPa, and T is in K. Read derives his formula by fitting a semi-empirical function to a set of measurements at 70 GHz, 140 GHz and 452 GHz, taken from the papers by Dagg *et al* [1974, 1975, 1978,

1985], Urbaniak *et al* [1977] and Stone *et al* [1984].

Consideration was also given to the possibility of *interference* between spectral lines. When there are a large number of identical molecules in a gas, such as in the atmosphere, they are well-separated and the interaction of any one molecule with a photon can be considered independent of the neighbouring molecules. Therefore the combined radiative effect of all the energy transitions across the gas is simply given by the sum of the individual contributions. There is an exception to this rule when several spectral lines are very close together. For example, the closely spaced O_2 lines between 50 GHz and 70 GHz which result from the $\Delta N = 0, \Delta J = \pm 1$ transitions can interfere with each other, causing non-Lorentzian variations in lineshape [Rosenkranz 1988]. This has the effect of increasing absorption near the centre of the band, but reducing it in the wings. Rosenkranz describes a modification to the VVW lineshape which accounts for this effect. In the forward model, it is only the wings of this band which are relevant, since the EOS MLS radiometers will all operate at higher frequencies than this. This being so, I have chosen not to include Rosenkranz's corrections, since the forward model uses the Lorentz lineshape which has a reduced wing contribution compared to the VVW anyway.

2.4 Solution of the Radiative Transfer Equation

2.4.1 Numerical Method

The two forms of the radiative transfer equation require different methods of solution. The Chandrasekhar equation (2.7) is an integration, whereas the Schwarzschild equation (2.6) requires the solution of an ordinary differential equation (ODE). Integration has the benefit that it is explicit, meaning that the incremental radiance at each step of a numerical solution is independent of previous steps, and so the solution is stable. However, the Chandrasekhar equation contains terms in τ_ν, the optical path, which must itself be calculated by integration. This increases both the processing time and the error in the solution.

In the case of the Schwarzschild equation, the change in radiance at each step of a numerical solution is a function of the radiance at that step, so inaccuracies may compound themselves over successive steps. The extent to which this does or does not occur is called the *stability* of the solution. The Schwarzschild equation is chosen for use in the forward model because it may be solved by *Runge-Kutta* methods, which have the advantage that they allow the numerical error to be estimated at each step of the solution, and therefore controlled. A Runge-Kutta method is based upon the Euler method, which is itself merely the use of the derivative in the differential equation, multiplied by the step-size, to estimate the value of the

function at the next step. A Runge-Kutta method is an extension of this technique which calculates intermediate values of the derivative within the step, to prevent the solution straying from the true value.

The *order* of a Runge-Kutta method is the same as the order of a Taylor method with an equivalent truncation error. If a function $y(x)$ is known at $x = x_o$, then the value at $x = x_o + \delta x$ can be approximated by a Taylor expansion as follows:

$$y(x_o + \delta x) \simeq y(x_o) + \left.\frac{dy}{dx}\right|_{x_o} \delta x + \left.\frac{d^2y}{dx^2}\right|_{x_o} \frac{\delta x^2}{2!} + \ldots + \left.\frac{d^Ny}{dx^N}\right|_{x_o} \frac{\delta x^N}{N!} \qquad (2.27)$$

The error in this approximation results from the truncation of the series at order N, and will therefore be of order δx^{N+1}. As part of a solution requiring many steps, the error due to this one step is called the *local truncation error* (abbreviated as 'local TE'). In the same way, a Runge-Kutta method of order N will also have a local TE of $O(\delta x^{N+1})$ [Mathews 1987, p.423][7].

When such an approximation is applied repeatedly over a large number of steps, the local TE due to one step becomes the error in the initial value of $y(x)$ for the next step. This will cause a deviation of the solution from the true $y(x)$, and the resulting deviation of the overall solution from the true value is called the *global* truncation error, which is not necessarily the sum of all the individual local TEs. Whether the global TE is larger or smaller than this sum depends on the stability of the differential equation. An unstable equation exhibits positive feedback, and results will quickly deviate from the true value. It is clear, however, that the Schwarzschild equation is stable, since the change in radiance over a step is negatively related to the radiance itself.

The global TE for Nth order Taylor or Runge-Kutta solutions is $O(\delta x^N)$ [Mathews 1987, p.417], so although it is not equal to the sum of the local TEs, such a sum gives a result of the correct order (since the number of steps will depend on $1/\delta x$).

When solving the differential equation, the step-size is of extreme importance. Since the global TE is $O(\delta x^N)$, a step-size reduction of a half, say, will reduce the overall error by a factor 2^N, which can be very significant for high N. However, the step-size cannot be too small because the processing time would be prohibitively high. Therefore the most efficient method is to monitor the local TE as it varies along the path, and continually adjust the step-size to keep the error close to a predetermined tolerance. Such a procedure is called an *adaptive step-size* technique.

The adaptive step-size technique which was used in the forward model was the *Runge-Kutta-Fehlberg*. Fehlberg discovered a set of six functions, evaluated at intermediate points in a step δx, which could be combined in two different ways

[7] The $O()$ notation is used here to represent "order".

to produce either a fifth-order or fourth-order solution. The two combinations are known as *embedded* formulae. The details of the formulae are given by Press *et al* [1992, p.710,711].

It may be shown rigorously that the difference between the solutions provided by the two orders is a good estimate of the local TE [Johnson & Riess 1982, p.374], but intuitively one can see that if the error in the 5th-order solution y_{n+1} is an order of magnitude smaller than that of the fourth-order solution y^*_{n+1}, then $|y_{n+1} - y^*_{n+1}|$ is expected to be a reasonable estimate of the error in y^*_{n+1}. There is no way, using this method, of estimating the error in y_{n+1} itself, but $|y_{n+1} - y^*_{n+1}|$ may be taken as a maximum value for this error.

So, for a given step-size h_1, the local TE when using the fifth-order solution, $\Delta_1 = |y_{n+1} - y^*_{n+1}|$, is $O(h_1^5)$. Therefore if we define a *desired* error tolerance Δ_2, which occurs when the step length is h_2, then:

$$\frac{\Delta_1}{\Delta_2} = \left(\frac{h_1}{h_2}\right)^5 \tag{2.28}$$

For a given solution of the differential equation (i.e. the Schwarzschild equation) a desired global error tolerance is specified, below which the global TE is to be kept. Dividing this tolerance by the length of the path over which the equation is solved gives the error tolerance per unit step[8], ϵ, such that $\Delta_2 = \epsilon h_2$. Then equation 2.28 may be rearranged to give the adaptive step-size formula

$$h_2 = h_1 \left[\frac{\epsilon}{\Delta_1/h_1}\right]^{\frac{1}{4}} \tag{2.29}$$

This formula should give the step-size required to ensure that the error on the next step is approximately equal to the specified tolerance. When the local TE is large, the routine reduces the step-size to compensate, and vice versa when the local TE is small. However, since equation 2.29 is approximate, and because the error characteristics will change slightly for the next step along the path, it is prudent to introduce an extra 'safety factor', to ensure that h_2 is not slightly too large. The usual choice for this factor is given by Burden & Faires [1989, p.253] as $2^{-0.25}$. If, despite all this, the error should be too large, the step is just repeated with a newly-calculated step-size.

Error Weighting

In the upper atmosphere, where the molecules are sparse and the errors in the radiative transfer calculation are correspondingly small, the steps become large. The reverse is true in the lower atmosphere, and at very low altitudes the steps

[8] In doing this the assumption is being made that the sum of the local TEs is a good approximation for the global TE.

may become so small that the computation is impractically slow. An effort was made to speed up the calculation at low altitudes by *error weighting*, although as explained below, this was unsuccessful.

The allowed error for any given step is proportional to the length of that step – clearly if it were 'weighted' so that more of the global error tolerance was allotted to steps in the lower atmosphere, then the computation would proceed more quickly at those altitudes. Of course, this would mean restricting the allowed error in the upper regions, but the errors in this part of the computation are so low that in the unweighted case the step size can often grow to its maximum permissible size. This leads to the error in each step being a long way below the allowed threshold, which is inefficient since the adaptive step routine cannot increase the step size any further.

The weighting scheme was put in place by calculating the absorption coefficient at 30 equally spaced points along the line of sight.[9] The size of the absorption coefficient at a given height in the atmosphere acts as a rough guide to the magnitude of the error that can be expected when evaluating the Schwarzschild equation over a step at that height. Then this crude profile is used to give each allowed error a fractional weight of $w_2 h_2 / W$, where h_2 is the size of the next step, w_2 is the weight interpolated from the absorption coefficient profile at the midpoint of h_2, and W is the area under the whole profile. When the weighting is applied to the adaptive step equation 2.29, the result is:

$$h_2 = h_1 \left(\frac{\tau w_2 h_1 / W}{\Delta_1} \right)^{\frac{1}{4}} \tag{2.30}$$

where h_1 and Δ_1 are the size and error of the current step, and τ is the allowed brightness temperature error for the whole path, equal to ϵ times the path length.

Since w_n depends on h_n, which is not yet known, I err on the side of safety by using the smallest possible value of w_n, which will be the minimum value from the midpoints of the largest and smallest permissible steps.

Unfortunately the gain in speed from this refinement was limited. That is to say, for an allowed global error τ the weighted model was much faster, but the actual global TE it produced was equivalent to the unweighted model running at a much higher allowed global error, which would take about the same time to run. This is because the weighted version is using its allowed error more efficiently, whereas the unweighted model always undercompensates. To produce the results in this thesis the unweighted model was used, in conjunction with the pre-calculated absorption coefficient profile described below.

[9] This weighting scheme was developed before the introduction of the fixed-grid absorption coefficient profile (described later), and was in fact rendered obsolete by it.

Fixed Grid Absorption Coefficient Profile

The solution of the radiative transfer equation originally used by Filipiak calculated the absorption coefficient, using equation 2.14, at each step of the path, a method referred to hereafter as '*in situ*' calculation. There are two reasons why this is not the most efficient method for solution. Firstly, as noted in the previous section, the step-size tends to become small when the absorption coefficient is high. This occurs in practice in the lower atmosphere when water-vapour absorption is dominant, and where the path will be near its tangent point. Therefore the absorption coefficient changes very little between steps in this region, and yet the model is recalculating it for each step. Secondly, it will become clear later in this thesis that we need to solve the Schwarzschild equation for a number of paths at different tangent heights in a single atmosphere.

Therefore it is more efficient to calculate a fixed, high vertical-resolution grid of absorption coefficients for a particular atmosphere, before beginning the solution, and to interpolate the required absorption coefficient at each point on the path from this grid. The grid used has a resolution of 0.25 km and extends from the ground to the top of the model atmosphere (the latter is defined in the next section).

Figure 2.5 shows a profile of the absorption coefficient at 242.4 GHz. The absorption coefficient is plotted logarithmically, so the plot indicates that the decrease of absorption with altitude is exponential in the troposphere. The forward model interpolates linearly between the 0.25 km steps of the absorption coefficient grid, whereas the form of figure 2.5 suggests that logarithmic interpolation would be more appropriate. In the event, the fine spacing of the levels means that the difference between the two methods of interpolation is negligible. For example, when calculating the midpoint of the two lowest grid levels shown in figure 2.5, the difference between the linear and logarithmic results is less than 0.1%.

The gain in processing speed was tested by running both the original *in situ* calculation model, and the modified fixed-grid model, on the same model atmosphere for an MLS path at a tangent height of 5 km. The fixed-grid model completed the calculation in less than half the time taken by the *in situ* calculation version. In addition, the majority of the time taken by the fixed-grid model was used in the initial calculation of the absorption coefficient profile, so subsequent limb paths in the same model atmosphere and at the same frequency required only a small extra processing time.

2.4.2 The Model Atmosphere

The model atmosphere referred to previously must be an approximately realistic representation of the pressure and temperature structure of the Earth's atmosphere,

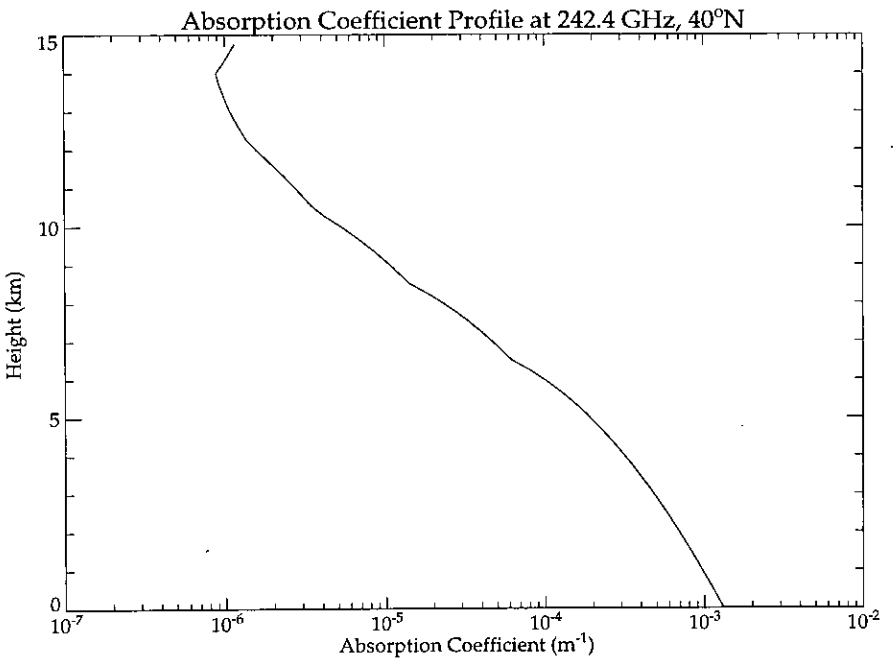

Figure 2.5: Vertical profile of absorption coefficient for 40°N at 242.4 GHz.

and of its chemical composition. This requires an independent set of atmospheric parameters (the *climatology*), which may be based either on measurements or on modelling studies. The climatology used by Filipiak and therefore by my model is that produced by the Cambridge-Edinburgh 2D model, known as CAMED [Harwood *et al* 1993]. This consists of vertical profiles of *volume mixing ratio*[10] for the 28 most abundant molecular species in the atmosphere, as well as temperature profiles. Each profile is defined for three separate latitude-season cases, being: Equator-March, 40°N-March and 70°N-December. The profiles are vertically indexed according to pressure rather than height, by the definition of *pressure height*, z^*, defined as

$$z^* = 16(3 - \log_{10} p) \tag{2.31}$$

where p is in hPa and z^* is in km. The pressure height approximates the geometric height, but the latter depends on the temperature structure of the atmosphere, and on the local gravitational field. In the CAMED climatology, the mixing ratios and temperatures are given for 31 levels, which correspond to 2 km steps between the ground and 60 km. In addition to these data, the climatology was extended by Filipiak to include two extra levels at $z^* = 80$ km, 100 km, using profiles from Shimazaki [1985].

In order to relate pressure to geometric height, two simplifying approximations

[10] Volume mixing ratio is the number density of a given molecular species as a proportion of the total air number density.

must be made. The first of these is the assumption of hydrostatic equilibrium. On synoptic scales, vertical accelerations of air are totally insignificant compared to the gravitational acceleration [Gedzelman 1985, p.8], which means that the vertical component of the equations of motion for the atmosphere reduces to the simple form of the hydrostatic equation:

$$dp = -g\rho\, dz \tag{2.32}$$

where p =pressure, ρ =density, g =gravitational acceleration and z =height. This equation represents the equilibrium between the forces due to gravity and those due to the pressure gradient on a layer of air (of thickness dz).

The second approximation made is the use of the ideal gas equation $p = nkT$, where n is the number density, k is Boltzmann's constant, and T is the temperature. The pressure of a real gas deviates from this expression as number density increases and temperature decreases, as described by Zemansky and Dittman [1981, p.102]. However, for the Earth's atmosphere it may be shown that the deviation is very small, and so the ideal gas equation may be safely used.

By combining the ideal gas equation with the hydrostatic equation, and applying the CAMED temperature profile, the pressure may be related to height (see appendix A).

Viewing Geometry

Filipiak's original model solved the radiative transfer equation along a limb path only, that is, along a line of sight such as that shown in figure 1.1. In my modified version of the forward model, the geometry was made more general to allow a line of sight at any angle, with a receiver placed anywhere within or outside the atmosphere, as shown in figure 2.6. This would allow the simulation of aircraft-based measurements, or of ground-based receivers. In this study the generalised geometry permits the calculation of *augmentation* by scattering, which is described in chapter 3.

The initial radiance I_ν with which the radiative transfer calculation is begun depends on the geometry of the measurement. For a limb view, the line of sight from the satellite is looking at space, so the initial radiance is the cosmic microwave background, which is a black-body spectrum of T_o = 2.7 K [Raychaudhuri *et al* 1992, p.224]. This is converted to an initial brightness temperature by substitution into equations 2.1 and 2.3. The same initial condition is applied to the more general lines of sight marked A and B in figure 2.6.

Alternatively, if the line of sight intercepts the Earth, as is the case for ray C in figure 2.6, the initial brightness temperature will depend on the temperature of

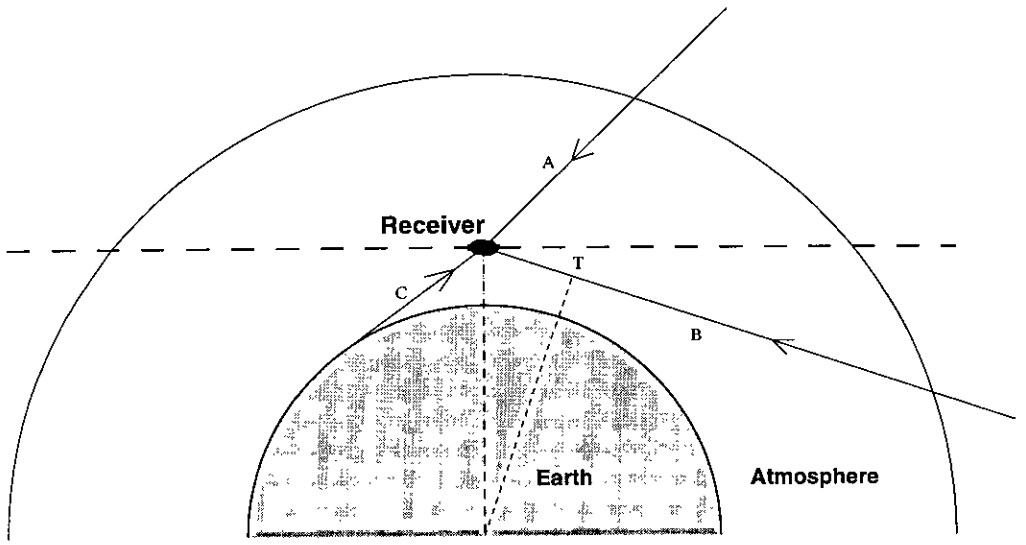

Figure 2.6: The geometry of a receiver's line of sight for an arbitrary view.

the Earth's surface. In addition there will be a reflected component which depends on the total incident radiation at the point of interception, and on the albedo of the Earth at that point. This would be very awkward to model, but in practice the lower troposphere is so opaque that the radiance emerging from it may be assumed to be independent of its value at the surface. To test this assumption, the model was used to calculate the brightness temperature at 204 GHz observed from a receiver placed at a height of 10 km, looking at an angle of $-50°$ below the horizontal (i.e. towards the Earth's surface). Two cases were considered, with the Earth's surface as a black-body radiating firstly at 0.1 K, and secondly at 300 K (the surface temperature). The observed brightness temperatures varied by only $\sim 1\%$. Therefore the initial brightness temperature for Earth-intercepting rays is set to the black-body value for an arbitrary surface temperature of 300 K.

2.5 Microwave Radiometry

The forward model described so far simulates the radiance (brightness temperature) which arrives at the receiver at a given frequency. The radiance which is actually measured is the incident radiance after it has passed through the components of the measurement system. The action of these components must therefore also be simulated by the forward model.

A simplified block diagram of the EOS MLS is shown in figure 2.7. Each of the sections labelled *Antenna*, *Radiometer* and *Spectrometer* is a set of components which modify the received radiance. These sections are presented below with a

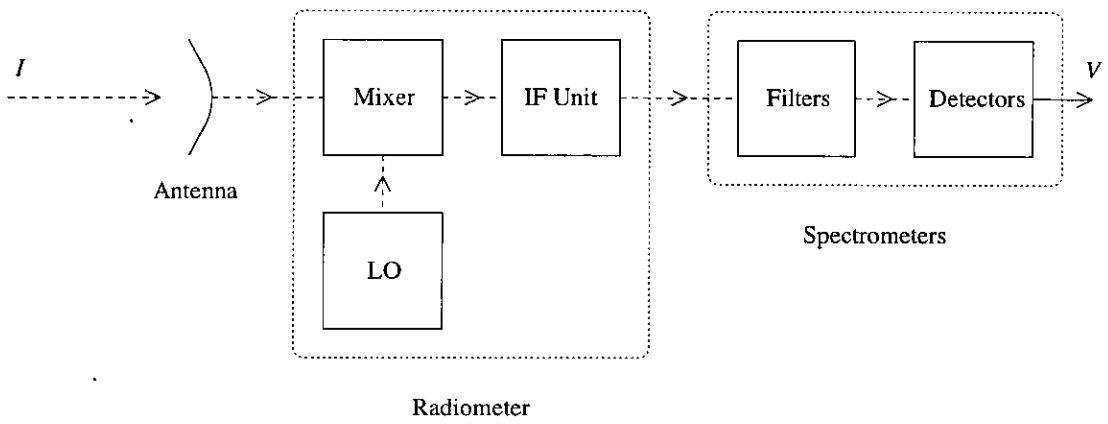

Figure 2.7: The EOS Microwave Limb Sounder.

description of their effect on the radiance in each case.

The Antenna

The antenna system comprises a parabolic main antenna, and then a hyperbolic secondary mirror to flatten the incoming wavefront, and a tertiary mirror to redirect the radiation into the radiometer. Radiation is incident on the main antenna from all directions in its forward-pointing hemisphere, and the efficiency with which the antenna absorbs the radiation at a given angle to the central axis is expressed as the *antenna function*.

Every antenna has its own characteristic function, which in addition depends on the frequency of the radiation it receives. For the EOS MLS, the proposed antenna system (at the time of writing) has the same physical dimensions as that used for the UARS MLS. The main antenna is elliptical with a major axis of 1.6 m and a minor axis of 0.8 m. The exact antenna function was experimentally determined for UARS MLS by Jarnot and Cofield [1991, p.43] for the frequencies of its three radiometers: 63 GHz, 183 GHz, and 205 GHz. The antenna function for 183 GHz is shown as a logarithmic plot in figure 2.8.

The main lobe of the antenna function shown in figure 2.8 is replotted in figure 2.9 on a linear vertical axis. It is clear that the majority of the area under the antenna function is contained within this main lobe, so in the forward model the actual function is represented simply by a Gaussian function of an equivalent width to the main lobe. The dotted line in figure 2.9 shows a Gaussian fit to the measured data. There is a slight offset because the peak of the measured antenna function is slightly off-centre.

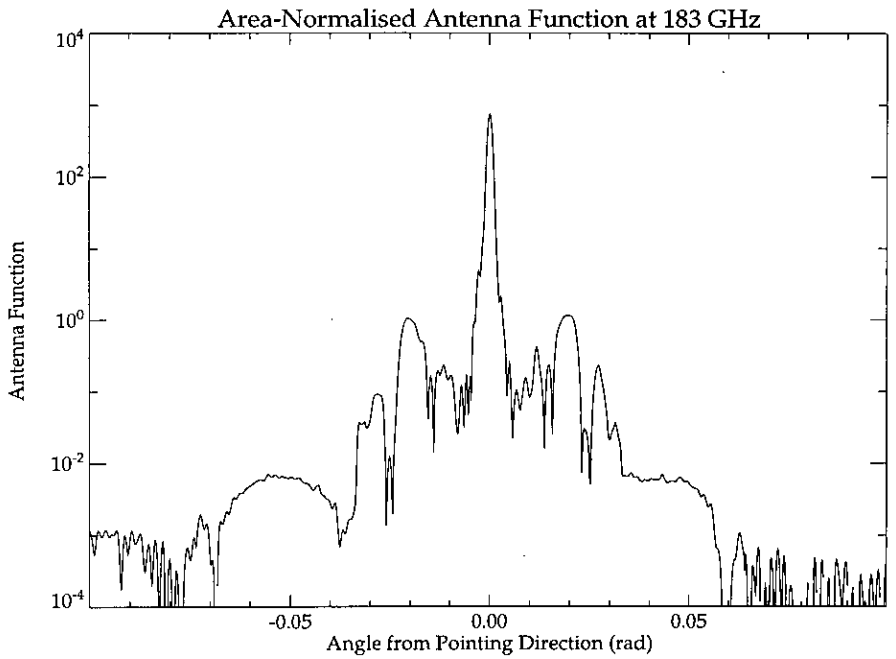

Figure 2.8: Logarithmic plot of the measured antenna function for the UARS MLS at 183 GHz.

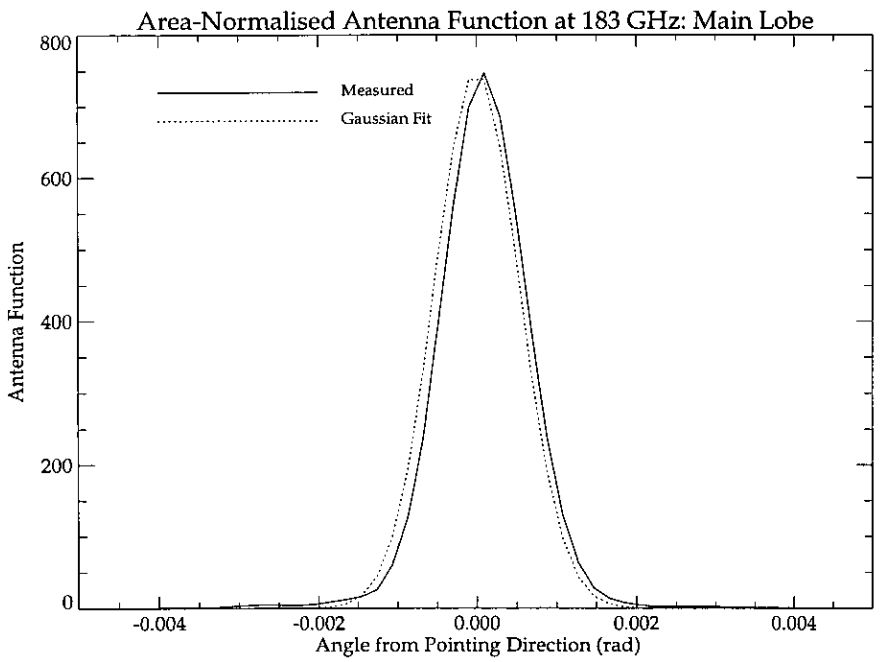

Figure 2.9: Main lobe of the measured antenna function for the UARS MLS at 183 GHz, with a Gaussian fit superimposed.

The Gaussian antenna function is given by

$$A(\theta) = \frac{1}{\sigma\sqrt{2\pi}} \exp\left(\frac{-\theta^2}{2\sigma^2}\right) \tag{2.33}$$

where θ is the angle from the pointing direction, and σ is the width of the Gaussian. This is related to γ, the full width at half maximum (FWHM), by $\gamma = 2\sigma\sqrt{2\ln 2}$.

The width of an antenna function's main lobe is inversely proportional to the frequency of the radiation it receives. This may be demonstrated for circular and rectangular antennae [Ulaby *et al* 1981, p.131], and may equally be applied to the elliptical MLS antenna. Therefore when using the Gaussian approximation above, a spectral width constant may be defined as the product of the FWHM and the frequency, and this can be used to determine the width at some frequency other than that at which the constant is defined. For example, for the UARS MLS antenna function described above, the spectral width constant is $\gamma_{183} \times 183$ GHz, which may be divided by an arbitrary frequency ν to obtain $\gamma(\nu)$. The spectral width constant used for EOS MLS is described later.

The antenna function is convolved with the incoming brightness temperature distribution to give the antenna temperature, T_A. Now the antenna function has been described so far as a function of a single angle, θ, but in fact this only describes its vertical response; in the horizontal there is a Gaussian response of a different width, and so the antenna function is properly represented as $A(\theta, \phi)$.

The area covered by the main lobe of the antenna function is small enough that the curvature of the Earth's atmosphere may be neglected. In this case the lobe is projected onto an xz-plane, where x is the horizontal and z the vertical. For a spherically symmetric atmosphere the brightness temperature is a function of z only. Therefore the convolution looks like this:

$$T_A = \frac{\int\int T_B(z)A(x,z)\,dx\,dz}{\int\int A(x,z)\,dx\,dz} \tag{2.34}$$

The antenna function is separable into independent exponential factors in x and z (corresponding to θ and ϕ), and the normalisation integral on the denominator of the above expression means that the terms in x cancel out. Therefore the convolution reduces to a one-dimensional integral in height as follows

$$T_A = \frac{\int T_B(z)A(z)\,dz}{\int A(z)\,dz} \tag{2.35}$$

Therefore the only spectral width constant required is that in the vertical direction. Although the EOS MLS antenna is dimensionally the same as that used by the UARS MLS, its reflective properties differ. In the forward model a Gaussian fit is used as an approximation to the actual antenna function, with a vertical spectral width constant (i.e. FWHM$\times\nu$) of 1140 km GHz [Filipiak, personal communication, 1996]. This corresponds to a Gaussian spectral width constant of $\sigma = 484$ km GHz.

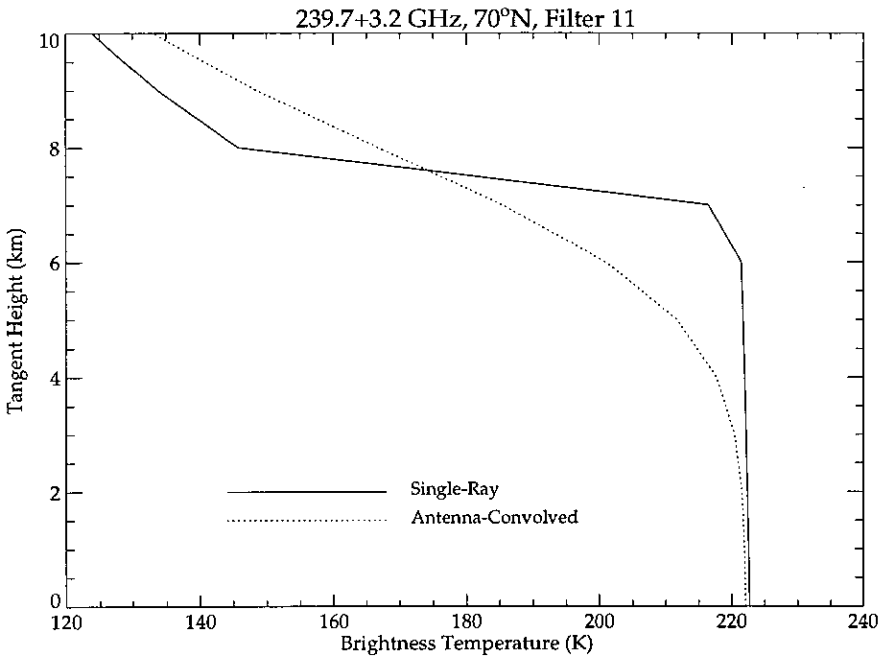

Figure 2.10: Profiles of single-ray calculated brightness temperatures and convolved antenna temperatures, at 242.9 GHz, 70°N.

Figure 2.10 demonstrates the smoothing effect of the antenna function on the received radiance. The brightness temperature profile shown by the solid line is that calculated for single lines of sight at the tangent heights indicated, whereas the dotted line is the profile for the antenna temperature when its pointing direction is at the tangent heights indicated.

The Radiometer

The radiation received by the antenna is divided by an optical multiplexer into separate beams for each of the MLS radiometers. The microwave radiation enters each of these radiometers through a feed horn, and passes into the *mixer*. Here it interacts with a second signal produced by a *local oscillator* (LO) operating at a fixed frequency (the radiometer centre frequency). The resulting superposition of waves leads to the production of beat frequencies $(\nu_{IN} + \nu_{LO})$ and $|\nu_{IN} - \nu_{LO}|$, where ν_{IN} is the incoming frequency and ν_{LO} is the local oscillator frequency.

In the case of the frequency subtraction, a beat frequency ν_B may be produced by an input frequency of either $\nu_{LO} + \nu_B$ or $\nu_{LO} - \nu_B$. Therefore the resulting spectrum which is output from the mixer is the folded superposition of the spectra on either side of the radiometer centre frequency.

The down-converted radiation then passes to the IF (*intermediate frequency*) unit, which amplifies the signal, and filters out all frequencies except those within

the required bandwidth, which is centred on the intermediate frequency. The filtering process removes the higher beat frequency produced by the mixer. The frequency band which is output from the IF unit is composed of the two folded contributions of the input spectrum from either side of the radiometer centre frequency. These contributions are separately referred to as the *sidebands*. The superheterodyne method of spectroscopy produces double-sideband measurements, in which each sideband carries approximately equal weight. In general, measurements are designed such that one sideband includes a spectral line of interest, while the other is as spectrally flat as possible to avoid contamination of the signal. However, for tropospheric measurements, both sidebands can often provide useful information when the spectral feature being observed is either a continuum or a line wing which covers a wide frequency range.

The Spectrometer

The radiation from the IF unit passes into the spectrometers, where it is averaged across each of 21 contiguous fixed-bandwidth filters, or *channels*. The filters ideally have a 'top-hat' response, i.e. they are equally sensitive at all frequencies across their bandwidth. In reality there will be some 'wiggle' of the filter sensitivity across the band, which must be experimentally determined. The forward model used in this study assumes idealised top-hat filters, and so the incoming radiance is averaged into 21 channels accordingly. The channel widths of the EOS MLS filter bank are symmetrically arranged about a central 6 MHz filter in the following sequence from the centre: 8 MHz, 16 MHz, 32 MHz, 48 MHz and 6×64 MHz on either side, making a total bandwidth of 982 MHz per sideband. The filters are illustrated in figure 2.11, which shows a brightness temperature spectrum centred on an ozone emission line at 235.7 GHz. The continuous spectrum is depicted by the dotted line, and the horizontal bars show the same spectrum filtered into the 21 channels.

Each filter output signal is amplified again to compensate for losses inherent in the filtering process, and the signal is finally converted by diodes into a DC voltage for each channel. This final conversion is known as square-law detection, because the output voltage is directly proportional to the power of the input signal (and therefore to the brightness temperature as explained in section 2.2).

2.6 Model Validation

The results produced by the forward model described in this chapter were verified in the course of steps 2 and 3 of the European Space Agency's Intercomparison Campaign of Forward Calculations [IFE 1995]. The campaign ran from 1993 to

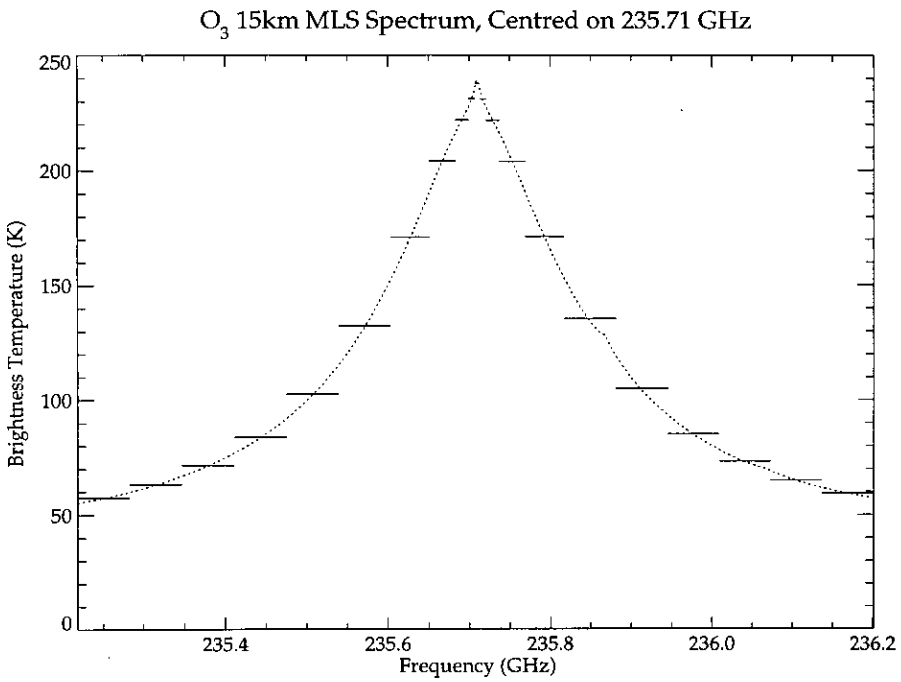

Figure 2.11: Example of a brightness temperature spectrum (dotted line) filtered through the EOS MLS spectrometers (horizontal bars).

early 1995, with the aim of gathering and comparing the results produced from a variety of forward models designed by European researchers. There were three steps to the campaign. Step 1 had been an attempt to gather absorption coefficients, optical paths, and brightness temperatures, for three given spectral bands, along limb paths at various tangent heights. However, misunderstandings concerning the input data for this process meant that the results obtained were of limited value, so step 2 of the campaign was started, at which point my version of the model was entered into the campaign. Step 2 was a repeat of the first step, but with a larger number of the input parameters predefined by the IFE (the Institute of Remote Sensing at the University of Bremen, Germany).

The spectral bands for the campaign were each 250 MHz wide, and centred on the ozone lines at 206 GHz, 648 GHz and 949 GHz. A set of spectroscopic parameters for these lines was defined by the IFE, consisting of the line centre frequency, the line intensity (as defined in equation 2.13 above), the lower state energy, and the pressure broadening parameters $\Delta\nu_0$ and x (as defined in equation 2.16). The partition function for ozone at atmospheric temperatures was also provided by the IFE, leaving the lineshape function $f(\nu, \nu_{ul})$ as the only unconstrained spectroscopic parameter in the forward model calculation of the absorption coefficient (equation 2.14). In addition to the spectroscopic data, the IFE also provided profiles of atmospheric temperature and pressure, and of the ozone mixing ratio.

The results submitted to the IFE took the form of brightness temperature spectra for each band, measured at tangent heights from 5 km to 70 km in steps of 5 km. In addition, spectra of the absorption coefficient were calculated at each of these heights.

Step 3 of the campaign aimed to investigate the differences between the models due solely to the numerical solution of the radiative transfer equation. Therefore a standard set of absorption coefficient spectra was provided by the IFE in the same format as that described above, and these were used to produce a new set of brightness temperature spectra for each band.

The results of the step 3 intercomparison showed that there was a group of models, including the IFE's own contribution, which were closely consistent. The brightness temperatures produced by my model varied by at most 0.2 K from those of this group, indicating a good level of consistency between the method of radiative transfer used in my model, and those used by the other contributors. Also, the comparison of absorption coefficients performed in step 2 also showed a good correspondence between my calculations and those to which they are compared in the report [IFE 1994], with the differences between the two generally less than 1%.

The only model used in the intercomparison which has been widely used outside its originating institute is the GENLN2 model [IFE 1995] developed at Oxford University, and held under copyright by the National Center for Atmospheric Research (NCAR) in Boulder, Colorado. This model was one of those included in the group referred to above for which the step 3 brightness temperatures were consistent, and to which my model corresponded well. There is some literature which describes comparisons of the GENLN2 output with observations, for example Kilsby *et al* [1992] and Rudman *et al* [1994], but both of these studies are conducted in the infrared at 10–12 μm, and are principally concerned with excess water-vapour absorption at these wavelengths.

Therefore I have not obtained direct evidence that the output produced by the forward model described in this chapter is consistent with observations of the Earth's atmosphere. However, it is consistent with similar models developed independently by other researchers, and as such I am confident of its accuracy.

2.7 Chapter Summary

This chapter has laid out the physical theory behind the propagation of microwaves through an atmosphere composed of absorbing and emitting molecules. The radiative transfer equation (2.8) shows that the molecular absorption coefficient γ_a is the factor controlling this propagation, and an expression has been given (equa-

tion 2.14) which allows the calculation of this coefficient. It has been shown how the forward model uses a numerical method to solve the radiative transfer equation along a given path, giving the brightness temperature which would be observed along that line of sight. The MLS instrument itself has also been described, and the effects of its various components on the incoming radiance have been evaluated.

The result is a forward model which, when given a model atmosphere and a direction in which to look, will return the brightness temperature measured in each channel of the EOS MLS. The model's results have been checked against those of similar models and were found to be consistent. The next stage is to introduce scattering into the model and determine its effect on the forward model's results. In the next chapter I begin the discussion of how the scattering process is to be modelled.

Chapter 3

The Scattering Model

3.1 Introduction

The forward model described in the previous chapter simulates the propagation of microwave radiation through the atmosphere under the influence of absorption and emission from gases. In the real atmosphere this radiation is also influenced by its interaction with suspended aerosols. The aerosols remove radiation from the line of sight both by scattering it into new directions, and by absorbing it. The combination of these two effects is known as *extinction*.

The atmosphere is full of aerosols, most visibly in the form of clouds. The water or ice particles which make up clouds are collectively known as *hydrometeors*. If the scattering effects of hydrometeors result in the removal of significant amounts of radiation from the line of sight of the MLS, the accuracy of the retrieved state may be diminished. In order to evaluate the extent of the problem, it is necessary to incorporate a scattering mechanism into the forward model. In the following sections a practical method of doing this is developed, which begins by considering the scattering properties of a single sphere. From this basis a model for a cloud composed of a *dispersion*[1] of particles of various sizes is developed in section 3.3. In section 3.4 the effect of multiple scattering on the radiative properties of such a dispersion is considered. At each stage the practicalities of applying the theory to the forward model are discussed.

The aim is to construct an enhanced forward model which can account for scattering by a distribution of spheres within a specified region in the model atmosphere. This is the basis from which I shall go on to simulate the scattering effect of realistic clouds.

Note: When reference is made in this chapter to 'the model', this means the scattering extension to the forward model rather than the forward model itself.

[1] 'Dispersion' is the name given in scattering theory to any collection of large numbers of particles.

3.2 Single Particle Scattering

When an electromagnetic wave is incident on a particle, it may be transmitted or absorbed, or scattered with a particular directionality. The scattering effect is a combination of the optical phenomena of reflection, refraction and diffraction, but it is only in the case of particles which are very large compared with the wavelength that these three are distinguished. In the formulation below, scattering is regarded as a single phenomenon.

To quantify the scattering due to a particle, we define a *scattering cross-section*, C_s, which is defined as the area across which the energy of the incident wave is equal to the total scattered energy. If this area is divided by the geometrical cross-sectional area of the scattering particle, the resulting dimensionless quantity is called the *scattering efficiency*, ξ_s. In the case of a sphere this is straightforward and leads to the expression

$$\xi_s = \frac{C_s}{\pi r^2} \tag{3.1}$$

where r is the radius of the sphere. In the case of non-spherical particles both the scattering and geometrical cross-sections depend upon the orientation of the particle.

In the same way, the total energy absorbed by the particle is equal to the incident energy across an area C_a, the *absorption cross-section*, with a corresponding absorption efficiency $\xi_a = C_a/\pi r^2$.

The *extinction* energy is defined as the sum of the absorbed and scattered energies, and so it follows that we have an extinction efficiency ξ_e defined thus:

$$\xi_e = \xi_s + \xi_a \tag{3.2}$$

These three terms are referred to collectively as the *Mie efficiencies*.

The intensity of the scattered light in a given direction depends on the angle which that direction makes with the incident direction. This angle is called the *scattering angle*, θ, and the plane in which it lies is the *scattering plane*. The angular distribution of the scattered light is represented by a dimensionless quantity called the *phase function*[2], $p(\theta)$. The phase function is normalised such that its integral over all directions is 4π, so

$$\oint p(\theta) d\Omega = 4\pi \tag{3.3}$$

where $d\Omega$ is the element of solid angle. For example, an isotropic phase function normalised according to this condition would have the form $p(\theta) \equiv 1$. By expansion into spherical coordinates equation 3.3 becomes

$$\frac{1}{4\pi} \int_{-\pi}^{\pi} \int_{0}^{\pi} p(\theta) \sin\theta \, d\theta \, d\phi = 1 \tag{3.4}$$

[2]Note that the word 'phase' in this context has nothing to do with the phase of the wave.

where the azimuth angle ϕ lies in the xy plane if z is the direction of the incident radiation.

The overall shape of the phase function is often expressed as a single value known as the *asymmetry factor* g, which is defined by Twomey [1977, p.243] as

$$g = \frac{\int_{-1}^{1} p(\theta) \cos\theta d(\cos\theta)}{\int_{-1}^{1} p(\theta) d(\cos\theta)} \tag{3.5}$$

By making the substitution $d(\cos\theta) = -\sin\theta d\theta$ in equation 3.4, the denominator of the above expression is shown to be equal to 2 for a normalised phase function.

The asymmetry factor is a measure of a bias towards either forward or backward scattering. In the case of isotropic scattering, or in Rayleigh scattering where light is scattered equally forwards and backwards, the asymmetry factor is zero. The limiting values are $g = -1$ where $p(\theta)$ is a delta function at $\theta = 180°$, and $g = 1$ for the same situation at $\theta = 0°$.

The efficiencies and the phase function described above may be calculated exactly for a given situation using Maxwell's equations. The solution of these equations for light scattered from a homogeneous sphere is known as the *Mie* solution. The treatment of scattering by Mie theory is absolutely general, but there are also approximate methods valid in the high and low particle radius limits which can be preferable.

The size of the sphere compared to the wavelength is expressed in terms of a dimensionless quantity χ known as the *Mie parameter* or the *size parameter*, defined as the ratio of the sphere's circumference to the wavelength, so

$$\chi = \frac{2\pi r}{\lambda} \tag{3.6}$$

where λ is the wavelength in air.

When χ is small, the Rayleigh approximation to the Mie solution is valid. The approximation is described in section 3.2.2, where it will be seen that it is considerably simpler than the full Mie calculation. Conversely, when χ is large the problem becomes one of geometrical optics, where the effect of scattering may be separated into its three components of reflection, refraction and diffraction. However, it transpires that the range of χ considered in this study does not extend into the geometrical-optical regime. Since the wavelengths I will be considering range approximately from 0.5 mm to 1.5 mm, and the particle sizes can be anything up to the order of millimetres, χ is expected to range from 0 to order 10.

The scattering properties of a sphere depend not only on its size but also on its dielectric properties, which are expressed in the form of its complex refractive index. For a non-absorbing sphere, the refractive index m would be real, but in

the general case where there is absorption, the refractive index includes a negative imaginary component. Thus we have:

$$m = n' - jn'' \tag{3.7}$$

where m is the complex refractive index. The imaginary part is related to the volume absorption coefficient γ_a of the sphere by the equation, given by van de Hulst [1981, p.267], below

$$\gamma_a = \frac{4\pi n''}{\lambda} \tag{3.8}$$

3.2.1 Mie Theory

In this section the mathematical formulation of the Mie solution for the *far-field* of the scattered electromagnetic wave is presented. The far-field condition requires that we consider the scattered wave only at distances $\gg \lambda$. This is a reasonable assumption since the wavelength is the order of millimetres and the dispersions of particles which will be discussed later are expected to be much more widely separated than this.

Scattering and Extinction Efficiencies

The Mie solution leads to equations 3.9 and 3.10 below for the scattering and extinction efficiencies, as presented by Ulaby *et al* [1981, p.290]. They are functions of the complex *Mie coefficients* a_i and b_i. These coefficients are used to characterise the wave equations for the scattered electromagnetic field outside the sphere, as formulated by van de Hulst [1981, p.122].

$$\xi_s(n, \chi) = \frac{2}{\chi^2} \sum_{i=1}^{\infty} (2i + 1)(|a_i|^2 + |b_i|^2) \tag{3.9}$$

$$\xi_e(m, \chi) = \frac{2}{\chi^2} \sum_{i=1}^{\infty} (2i + 1)\mathrm{Re}\{a_i + b_i\} \tag{3.10}$$

where Re signifies the real part of a complex quantity.

These series are convergent, so in the model they are built up iteratively until the next step is considered negligible in proportion to the total. This requires a predefined threshold of negligibility, which I set to 0.1% after some experimentation. This appears to yield a comparable order of accuracy in the final output.

The Mie coefficients are formally defined in terms of the Riccati-Bessel functions and their derivatives, as shown by van de Hulst [1981, p.123]. However, the recursive procedure below, developed by Deirmendjian [1969, p.14–19], is more suitable for the computation of a_i and b_i and involves no approximations, and so it was used in

this study.

$$a_i = \frac{\left(\frac{A_i}{m} + \frac{i}{\chi}\right) \mathrm{Re}\{W_i\} - \mathrm{Re}\{W_{i-1}\}}{\left(\frac{A_i}{m} + \frac{i}{\chi}\right) W_i - W_{i-1}} \tag{3.11}$$

$$b_i = \frac{\left(mA_i + \frac{i}{\chi}\right) \mathrm{Re}\{W_i\} - \mathrm{Re}\{W_{i-1}\}}{\left(mA_i + \frac{i}{\chi}\right) W_i - W_{i-1}} \tag{3.12}$$

The value i is the same as the index of summation in equations 3.9 and 3.10. The formulae above are explicitly functions of m and χ, but also implicitly through the additional parameters W_i and A_i. These parameters are calculated iteratively as follows:

$$W_i = \left(\frac{2i-1}{\chi}\right) W_{i-1} - W_{i-2} \tag{3.13}$$

where

$$\begin{aligned} W_0 &= \sin\chi + j\cos\chi \\ W_{-1} &= \cos\chi - j\sin\chi \end{aligned} \tag{3.14}$$

And for A_i:

$$A_i = -\frac{i}{m\chi} + \left[\frac{i}{m\chi} - A_{i-1}\right]^{-1} \tag{3.15}$$

where

$$A_0 = \cot m\chi \tag{3.16}$$

The equations 3.11 through 3.16 give the Mie coefficients at each step of the summations of equations 3.9 and 3.10, so the iteration required to find A_i and W_i need only be continued until the point of convergence of these sums.

Figures 3.1 and 3.2 show the Mie scattering and extinction efficiencies plotted against the size parameter χ, for spheres made of ice and of *nitric acid trihydrate* (NAT) respectively. The asymmetry parameter is also plotted in each case as a dashed line, and this will be discussed later. The calculations for ice use a refractive index of $1.78 - 5.6 \times 10^{-3}j$, which is approximately the value tabulated by Warren [1984] at a temperature of $-60°$C and a frequency of 600 GHz. These values are typical of those used later in the model.

NAT is thought to be the primary constituent of Type I polar stratospheric clouds[3]. The refractive index used here is $2.17 - 0.3j$, the value given by Toon *et al* [1994] for the low-temperature crystalline form of NAT known as α-NAT, at a temperature of $-92°$C and a frequency of 14.4 THz. I was unable to find published data for frequencies lower than an order of 10 THz, which is well above the MLS frequency range; nevertheless in this case it is used merely as an example of scattering under a different refractive index. The larger imaginary component

[3] See Chapter 4.

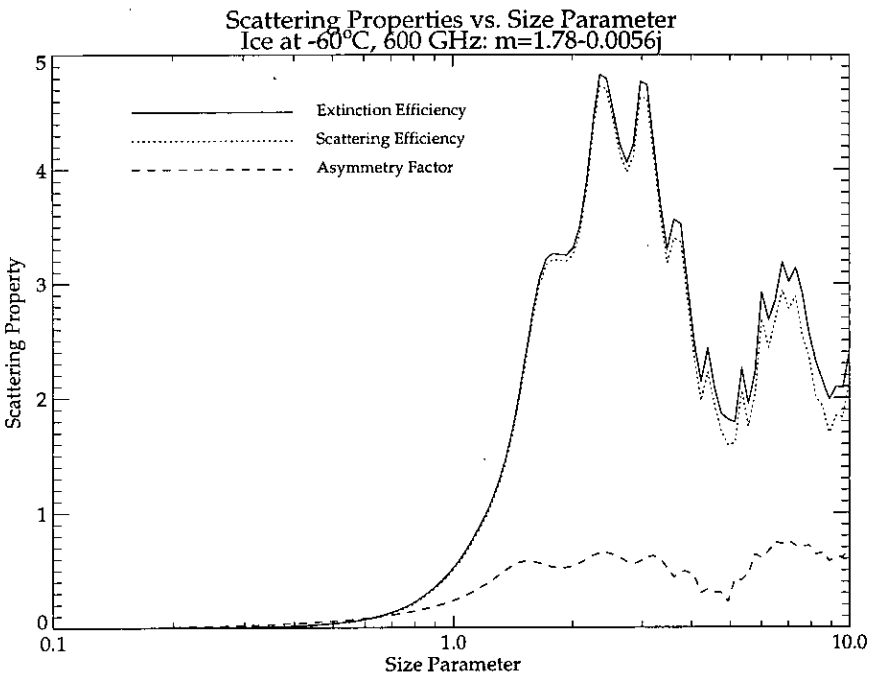

Figure 3.1: Mie efficiencies and asymmetry factor against size parameter for ice at $-60°C$ and 600 GHz. Quantities on both axes are dimensionless.

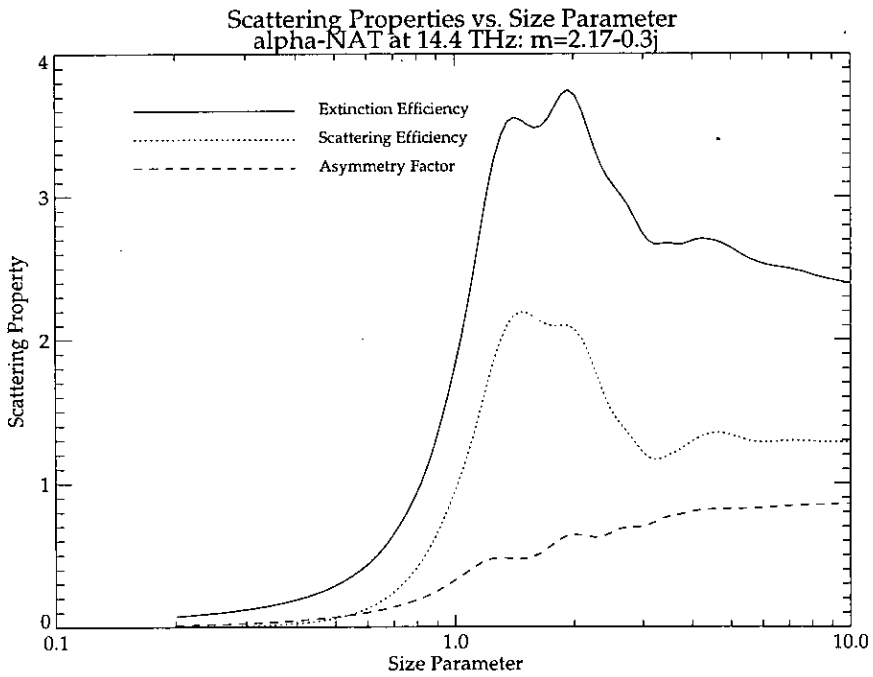

Figure 3.2: Mie efficiencies and asymmetry factor against size parameter for α-NAT at $-92°C$ and 14.4 THz. Quantities on both axes are dimensionless.

of the refractive index means that a larger proportion of the extinction is due to absorption, so in figure 3.2 we see that the scattering efficiency is substantially less than the extinction efficiency.

Phase Function

The calculation of the phase function $p(\theta)$ employs the *amplitude function* $S(\theta, \phi)$, which is the angular term in the wave equation of the scattered light. In the most general case there are actually four separate amplitude functions, representing the two components of polarisation in each of the θ and ϕ directions. For spherical particles however, symmetry reduces the problem to two functions: $S_1(\theta)$ and $S_2(\theta)$, these being respectively the amplitude functions for the electric fields perpendicular to, and parallel with, the plane of scattering. Therefore, given that intensity is proportional to the square of electric field, the intensity of the scattered radiation has an angular dependence of $(|S_1(\theta)|^2 + |S_2(\theta)|^2)$. The phase function itself is a normalised version of this angular pattern, such that:

$$p(\theta) \propto (|S_1(\theta)|^2 + |S_2(\theta)|^2) \tag{3.17}$$

with the constant of proportionality defined by the normalisation condition 3.4. The amplitude functions are the fundamental expressions which describe the scattered wave, and are used in the derivation of the earlier equations 3.9 and 3.10 for the scattering and extinction efficiencies.

The Mie solution for the amplitude functions $S_1(\theta)$ and $S_2(\theta)$ is given by Lenoble [1985, p.187] as follows:

$$S_1(\theta) = \sum_{i=1}^{\infty} \frac{2i+1}{i(i+1)} \left(a_i \frac{dP_i^1}{d\theta} + b_i \frac{P_i^1}{\sin\theta} \right) \tag{3.18}$$

$$S_2(\theta) = \sum_{i=1}^{\infty} \frac{2i+1}{i(i+1)} \left(a_i \frac{P_i^1}{\sin\theta} + b_i \frac{dP_i^1}{d\theta} \right) \tag{3.19}$$

where a_i and b_i are the Mie coefficients defined in the previous section, and the quantities P_i^1 are *associated Legendre polynomials*. These are functions of θ which are the solutions of the associated Legendre equation, itself an ordinary differential equation which represents the θ component of the general wave equation. The notation used for the associated Legendre polynomial is P_i^h, where h and i are integer indices greater than zero. The polynomials are awkward to calculate directly, but may be more conveniently derived by means of the recurrence relations provided by Arfken [1985, p.669]. These relations work by expressing the required polynomial as a function of the indices h and i, and of two previous polynomials in the series. Since equations 3.18 and 3.19 involve only the $h = 1$ associated Legendre

polynomials, the recurrence relations applicable in this case are, for the polynomial itself:

$$P_i^1 = \left(\frac{2i-1}{i-1}\right) P_{i-1}^1 \cos\theta - \left(\frac{i}{i-1}\right) P_{i-2}^1 \tag{3.20}$$

and for its derivative with respect to θ:

$$\frac{dP_i^1}{d\theta} = \left(\frac{2i-1}{i-1}\right)\left(\cos\theta \frac{dP_{i-1}^1}{d\theta} - P_{i-1}^1 \sin\theta\right) - \left(\frac{i}{i-1}\right)\frac{dP_{i-2}^1}{d\theta} \tag{3.21}$$

Therefore, given that the initial values in this series (tabulated by Arfken [1985]) are $P_1^1 = \sin\theta$ and $P_2^1 = 3\cos\theta\sin\theta$, the corresponding derivatives can be found, and all subsequent $h = 1$ associated Legendre polynomials may be derived.

The Mie coefficients in equations 3.18 and 3.19 are obtained as before from equations (3.11) and (3.12). The summations in this case are convergent, as was the case for the scattering and extinction efficiencies, so again successive contributions are added until the next contribution is negligible. Note however that these sums may require a higher order of Mie coefficients than did those in equations 3.9 and 3.10. Therefore the calculated W_i and A_i parameters are retained when the first pair of sums has converged, so that the iteration of equations 3.13 and 3.15 may be continued if necessary for the second pair.

In figures 3.3 and 3.4 the normalised phase function is plotted as a polar diagram for low and high values of the size parameter respectively. In each case the corresponding asymmetry factor is printed at the top of the plot. The refractive index is set to that used for α-NAT previously, $2.17 - 0.3j$. In the first case, $\chi = 0.2$, the particle scatters radiation in nearly equal quantities forwards and backwards, so the asymmetry factor is close to zero. However in the second plot where $\chi = 4.0$, the radiation is heavily concentrated in a narrow forward lobe and the asymmetry factor is correspondingly very high. Note that the axes of the second plot cover a very much larger range than do those of the first.

The variation of the asymmetry factor with the size parameter was plotted in the previous section in figures 3.1 and 3.2, where it can be seen that there is a general increase of asymmetry with increasing size parameter. Note that the asymmetry factor has a maximum possible value of one, so at the high-χ end of these plots it is approaching its maximum.

Polarisation

In the case of spheres, van de Hulst [1981, p.36,126] demonstrates that the amplitude functions $S_1(\theta)$ and $S_2(\theta)$, and therefore the scattering properties which are derived from them, are independent of the state of polarisation of the incident light. However, for general (non-spherical) particles, this is not the case.

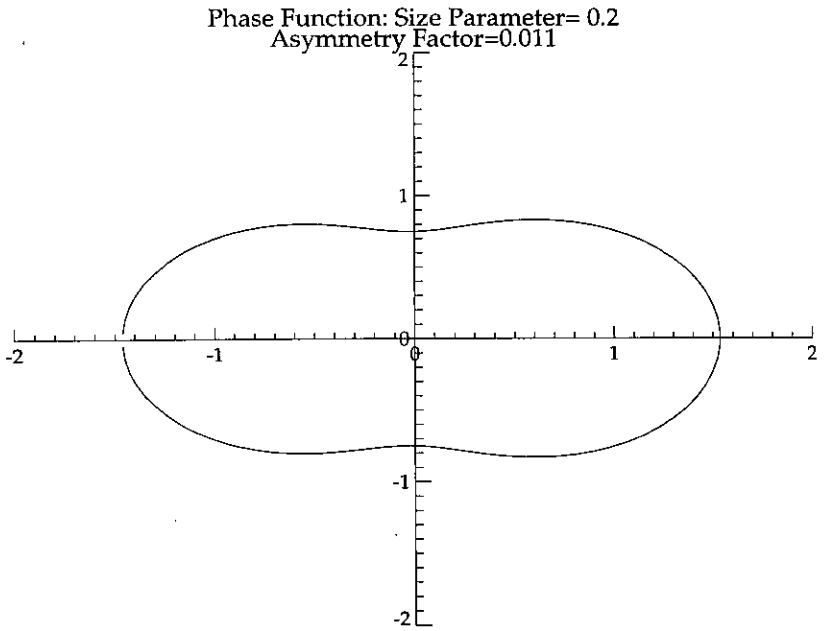

Figure 3.3: Phase function for a $\chi = 0.2$ sphere of α-NAT. The refractive index is $2.17 - 0.3j$.

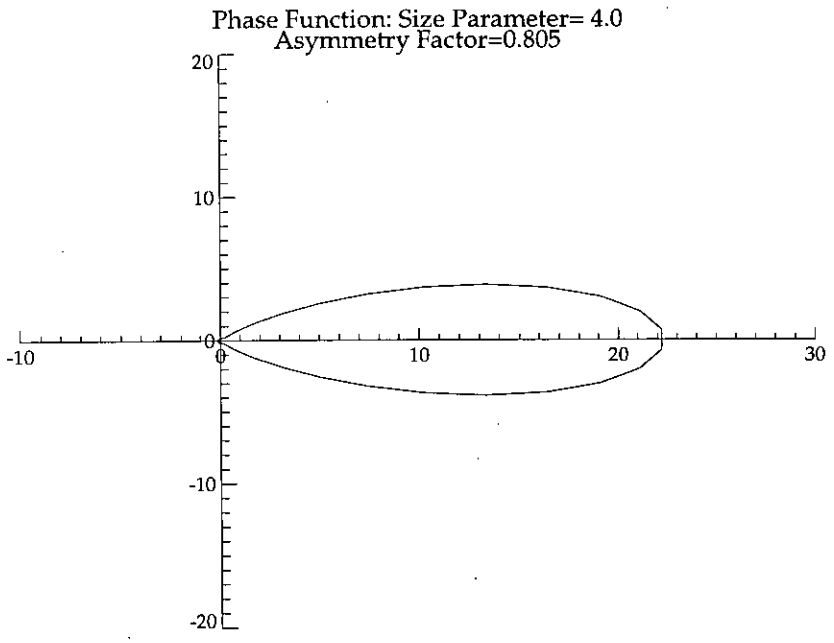

Figure 3.4: Phase function for a $\chi = 4$ sphere of α-NAT. The refractive index is $2.17 - 0.3j$.

Asymmetrical particles produce scattering effects which are dependent on the polarisation of the incident radiation, and therefore a bulk distribution of such particles may exhibit optical phenomena such as *birefringence* and *dichroism*.

The former effect is when the refractive index of the medium depends on the direction of the electric field vector of the incident radiation with respect to an *optical axis*. This axis is inherent in the scattering medium. In this case the light is separated into two separate rays, the 'ordinary' ray which is linearly polarised perpendicular to the optical axis, and an 'extraordinary' ray with parallel polarisation. This is linear birefringence; there is also circular birefringence, also known as *optical activity*, in which the refractive index depends on the type of circular polarisation of the incident light. Circular polarisation is the condition where one component of the radiation's electric field is $\pi/2$ out of phase timewise with the other, so that the electric field vector rotates about the direction of propagation. Circularly polarised light may be 'left-handed' or 'right-handed' depending on the direction of this rotation, and it is this distinction to which the refractive index of an optically active medium is sensitive.

Dichroism is a similar phenomenon where the scattering medium absorbs light in one direction but transmits it in another. Since absorption is an aspect of the complex refractive index (equation 3.7), dichroism is really a subset of birefringence. Circular dichroism, analogous to circular birefringence, is also possible.

With such effects in mind, van de Hulst [1981, p.46–59] discusses the scattering properties with respect to polarisation of a hypothetical cloud of identical (or mirror-image) arbitrary particles, under various symmetry conditions governing particle orientation. The condition most applicable to the clouds I will be considering is where there is a dispersion of asymmetric particles, with an equal number of mirror-image particles. This is equivalent to a more realistic situation where the particles have one plane of symmetry, in which case they are their own mirror-images. If such a dispersion is randomly orientated, there is no birefringence or dichroism, and the propagation of the light is called *scalar*.

So to summarise, one may neglect the effect of polarised incident radiation on the scattering due to a dispersion of particles if they are spheres, or if they are non-spherical but symmetrical and randomly orientated.

In the event that the above assumptions are not valid, it is still probable that the incident radiation itself will be unpolarised. The molecular emission spectrum originates from a large number of independent rotational transitions, and therefore we can expect it to have random polarisation[4] [Grant & Phillips 1975, p.368]. In addition, radiation which has been scattered from other particles will be polarised

[4] 'Randomly polarised' light is the same as unpolarised light.

with respect to the orientation of those particles and the direction of the incident radiation upon them. In the case of randomly oriented cloud particles, the net effect is unpolarised radiation.

It is possible that there will be regions of similarly-oriented crystals in a cirrus cloud due to the tendency of free-falling objects to assume a position of maximum air-resistance, in which case the effects of polarisation might not be entirely negligible. However such situations have not been investigated in this study. The microphysics of ice crystal clouds is discussed in detail in chapter 4.

Practical Limitations

While the Mie solution is in theory general to all particle sizes (to all χ), it is not always practical. The formulae described above involve complicated and time-consuming summations of complex parameters, and in the case of the phase function, this must be done over a range of angular steps. The recursive nature of such calculations means that errors due to the accumulated imprecisions of computer arithmetic can build up, and this can cause the Mie theory to become unreliable in practice at high χ. Deirmendjian [1969, p.19] notes that this problem occurs at $\chi \sim 30$.

To investigate the behaviour of my model at large size parameters, I calculated the Mie efficiencies and the asymmetry factor over the range $10 < \chi < 90$, for two types of particle: the α-NAT sphere at 14.4 THz, as described earlier in this section, and a sphere of iron at a visual wavelength of 395 nm, where its refractive index is $1.16 - 1.27j$ [van de Hulst 1981, p.273]. Figure 3.5 shows the variation of the scattering properties with size parameter for the iron sphere, and figure 3.6 is the equivalent plot for the α-NAT sphere. Note that figure 3.6 is an extension of the plot presented previously in figure 3.2.

In the case of the iron sphere, the efficiencies appear stable and consistent up to a size parameter of about 35, where some oscillation begins to set in. This may or may not be realistic, but the behaviour beyond $\chi = 45$, where the scattering efficiency exceeds the extinction efficiency, is unphysical. A corresponding oscillation in the asymmetry factor is also evident beyond $\chi = 50$. However there is no evidence of failure in the α-NAT case until the size parameter exceeds 90. The iron example serves to illustrate the potential fallibility of the recursive Mie method at high size parameters, but the α-NAT results show that this fallibility is highly dependent on the refractive index. The equivalent results for ice, not shown are here, indicate a similar effectiveness at high-χ to those of the α-NAT.

Where the recursive Mie method does fail for very large χ, a method involving geometrical optics is required. This is feasible to model, but it turns out not to be

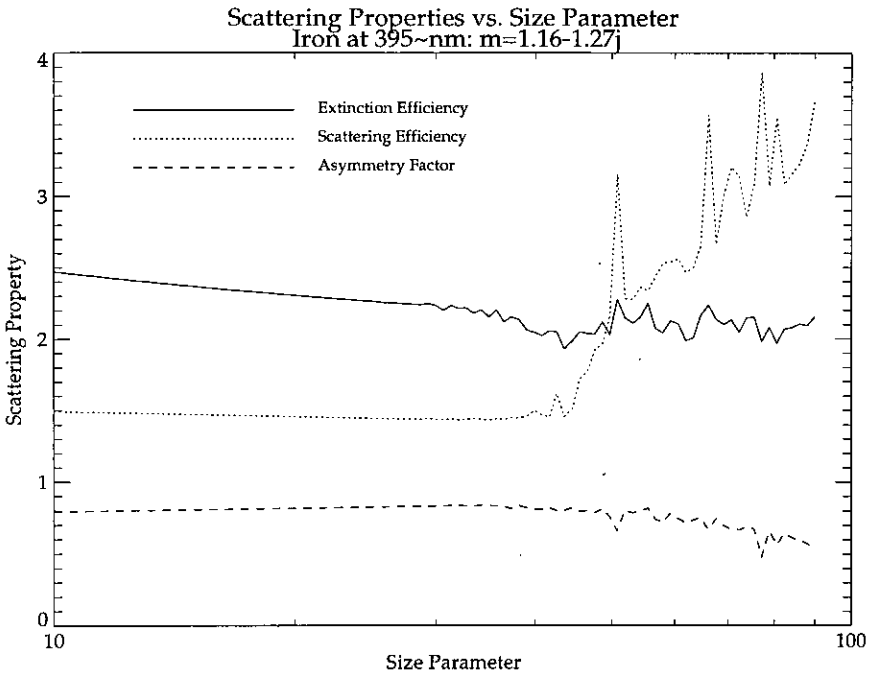

Figure 3.5: Mie efficiencies and asymmetry factor at large size parameters for an iron sphere at 395 nm.

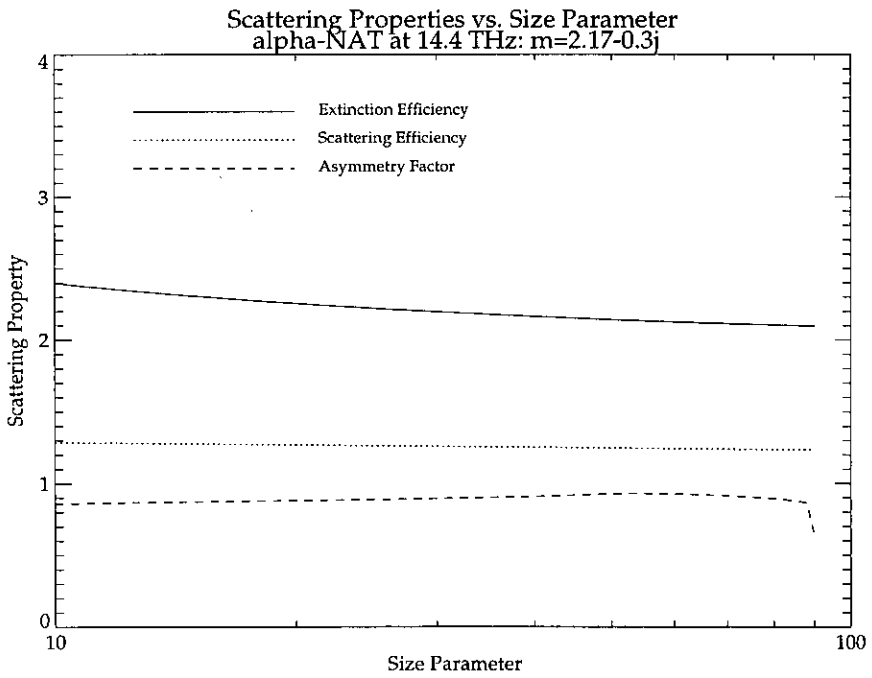

Figure 3.6: Mie efficiencies and asymmetry factor at large size parameters for α-NAT at $-92°$C and 14.4 THz.

necessary. A size parameter of 30 implies a sphere radius of at least 2 mm at the frequencies considered here, and it will be shown in chapter 5 that this limit was not exceeded in the sphere distributions used.

On the other hand, when χ is small, about the order of 0.1 (depending on m), the W_i parameter, which has an inverse relationship with χ (equation 3.13), grows so fast with the iteration that it exceeds the capacity of the computer (effectively becomes infinite) before the current element of summation can be considered negligible. In this situation, the elements of summation show little or no sign or diminishing relative to the total. This problem becomes especially pronounced when calculating the phase function when the angle is near $\pm\pi/2$. The problem can be alleviated to some extent by increasing the threshold below which the relative contribution of the next step must fall in order to halt the summation, but it does not have a great effect. Therefore this provides an effective lower limit to the Mie regime below which I am obliged to use the Rayleigh approximation.

3.2.2 The Rayleigh Approximation

When a particle is small compared to the wavelength of the incident radiation, it scatters in much the same way as a molecule does. The oscillating electric field of the radiation induces a corresponding Hertzian dipole across the particle. Rayleigh scattering describes the radiation from such a dipole.

The induced dipole $\mathbf{p}$ is related to the incident electric field $\mathbf{E}$ by the polarisability, α, of the particle, such that $\mathbf{p} = \alpha\mathbf{E}$. The polarisability is a complex value. For Rayleigh scattering it is assumed that the polarisability is isotropic, and since it is a function of the dielectric properties of the particle, this is equivalent to assuming that the particle is non-birefringent.

The intensity I of the far-field[5] dipole radiation at polar coordinates (R, θ) with respect to the particle is derived by van de Hulst [1981, p.64] and is as follows:

$$I = \frac{(1 + \cos^2\theta)k^4|\alpha|^2}{2R^2} I_0 \tag{3.22}$$

where k is the wavenumber ($k = 2\pi/\lambda$), and I_0 the intensity, of the incident radiation. This radiation must be unpolarised for the above equation to be valid.

The factor $(1 + \cos^2\theta)$ in equation 3.22 is the sum of the squared amplitude functions $S_1(\theta) \equiv 1$ and $S_2(\theta) = \cos\theta$, which describe the two components of polarisation of the scattered field: S_1 represents the radiation polarised perpendicular to the scattering plane, and the S_2 part is polarised parallel to the plane (but perpendicular to the direction of propagation).

[5] At a distance of several wavelengths from the particle.

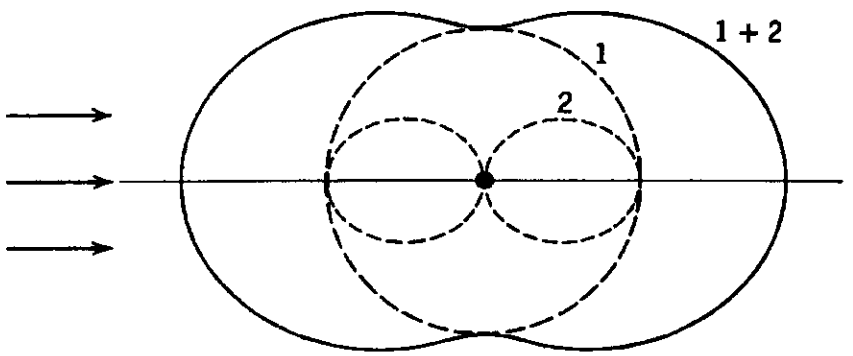

Rayleigh scattering: polar diagram of scattered intensity if incident radiation is unpolarized, 1 = polarized with electric vector ⊥ plane of drawing, 2 = polarized with electric vector in plane of drawing, 1 + 2 = total.

Figure 3.7: Angular distribution of Rayleigh-scattered intensity (from van de Hulst [1981, p.65]).

Figure 3.7 shows the angular distribution of the scattered radiation, in total and as each of its two polarised components. At 90° to the direction of propagation, the intensity of the parallel-polarised component drops to zero, so the radiation is 100% linearly polarised perpendicular to the scattering plane. The shape of the overall angular distribution is the symmetrical form approached by the low-χ phase function of figure 3.3, and the asymmetry factor $g = 0$.

The scattering and absorption cross-sections for Rayleigh scattering are derived by van de Hulst [1981, p.70] and are as follows

$$C_s = \frac{8}{3}\pi k^4 |\alpha|^2 \tag{3.23}$$

$$C_a = -4\pi k \,\mathrm{Im}(\alpha) \tag{3.24}$$

where Im signifies the imaginary part of a complex quantity.

The polarisability is defined in terms of the refractive index by the *Lorentz relation*:

$$\alpha = \left(\frac{m^2 - 1}{m^2 + 2}\right) r^3 \tag{3.25}$$

where r is the particle radius and m is the complex refractive index as defined in equation 3.7. So substituting this into equations 3.23 and 3.24 above, and dividing by πr^2, we get the scattering and absorption efficiencies as follows:

$$\xi_s = \frac{8}{3}\chi^4 \left|\frac{m^2 - 1}{m^2 + 2}\right|^2 \tag{3.26}$$

$$\xi_a = -4\chi \,\mathrm{Im}\left(\frac{m^2 - 1}{m^2 + 2}\right) \tag{3.27}$$

These formulae for Rayleigh scattering may be reproduced from the Mie solution by expanding the Bessel functions used in the solution as power series of χ. Then these expansions can in turn be used to expand the Mie coefficients a_i and b_i, and the scattering and extinction efficiencies, all as power series of χ. Then in the low χ case applicable to Rayleigh scattering, the high powers of χ drop out. The results of such an expansion for the scattering and extinction efficiencies are given by van de Hulst [1981, p.297–271] as follows:

$$\xi_e = -\mathrm{Im}\left\{4\chi\frac{m^2-1}{m^2+2} + \frac{4\chi^3}{15}\left(\frac{m^2-1}{m^2+2}\right)^2\left(\frac{m^4+27m^2+38}{2m^2+3}\right)\right\} \tag{3.28}$$
$$+\chi^4\mathrm{Re}\left\{\frac{8}{3}\left(\frac{m^2-1}{m^2+2}\right)^2\right\} + \cdots$$

$$\xi_s = \frac{8\chi^4}{3}\left|\frac{m^2-1}{m^2+2}\right|^2 + \cdots \tag{3.29}$$

Equation 3.29 is identical to the Rayleigh scattering result, equation 3.26, and the first term on the right-hand side of equation 3.28 is the Rayleigh absorption term from equation 3.27. All powers of χ of 4 or less have been retained, which makes the expression for the extinction efficiency more complicated than the sum of the Rayleigh scattering and absorption efficiencies. This extra complexity does not cause any significant computational delay, so it is used in preference to the standard Rayleigh formula in the model.

The phase function is proportional to the angular terms in equation 3.22 if the incident radiation is unpolarised. The form of the phase function can also be obtained by substituting the amplitude functions into the general formula 3.17. Then the exact constant of proportionality of the Rayleigh phase function can be found by analytically evaluating equation 3.4, leading to the following expression:

$$p(\theta) = \frac{3}{4}(1+\cos^2\theta) \tag{3.30}$$

The Mie-Rayleigh Changeover

The Rayleigh approximation diverges from the full Mie solution as the size parameter increases, and therefore it is used for small values of χ, up to a changeover value beyond which the Mie solution is computed. The changeover size parameter is chosen to be as high as possible without compromising the accuracy of results, so that the simplicity of the Rayleigh approximation is used to its full advantage. The changeover for the calculation of the phase function may take place at a different χ, because its characteristics are different.

The error associated with the use of the Rayleigh approximation to calculate the Mie efficiencies is plotted in figure 3.8, for ice at the same temperature and

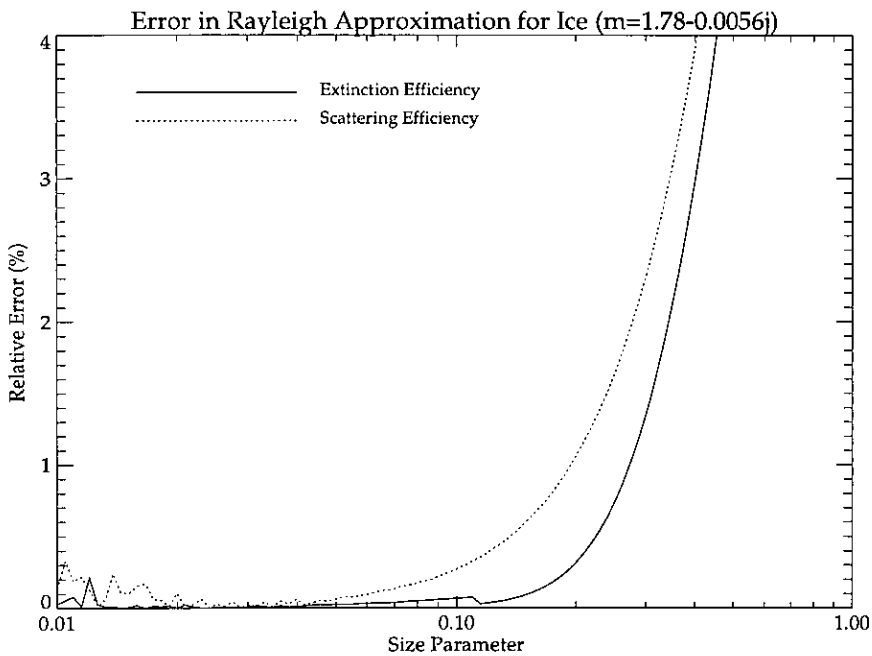

Figure 3.8: Relative deviation of the Rayleigh approximation from the Mie solution, for ice at $-60°$, 600 GHz.

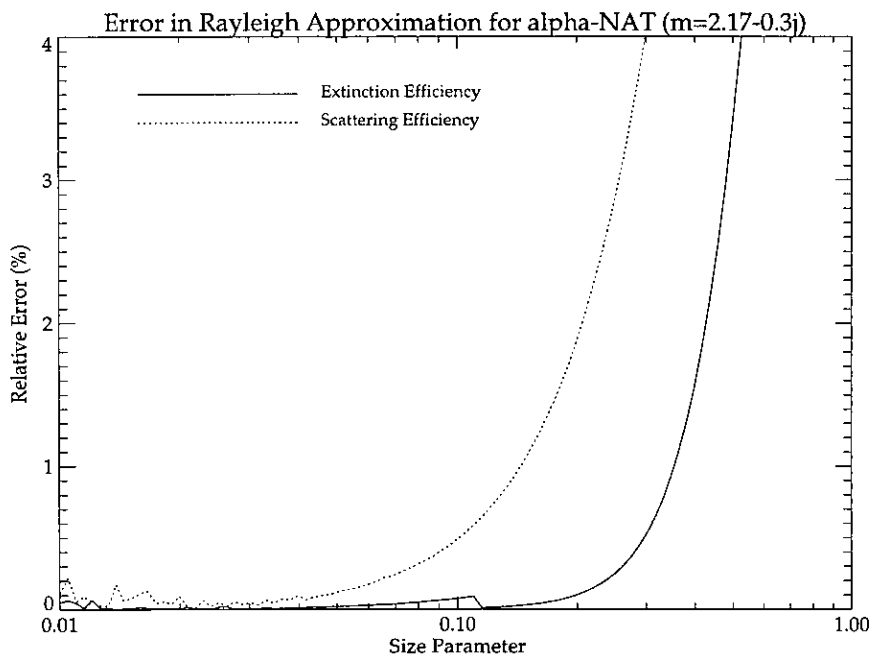

Figure 3.9: Relative deviation of the Rayleigh approximation from the Mie solution, for α-NAT at $-92°$, 14.4 THz.

frequency as before. The 'relative error' is the difference between the Rayleigh result and the Mie solution, as a percentage of the Mie solution. The error between $\chi = 0.01$ and $\chi = 0.05$ looks noisy, and this is probably due to numerical noise in the Mie solution, since we would expect the Rayleigh results to be stable.

If an error of 1% in either efficiency is considered acceptable, then a changeover point of $\chi = 0.2$ would be suitable. However, the corresponding plot for α-NAT shows that the scattering efficiency error rises more quickly with χ, reaching $\sim 2\%$ at $\chi = 0.2$. Therefore to be on the safe side the changeover point is set to be at $\chi = 0.1$.

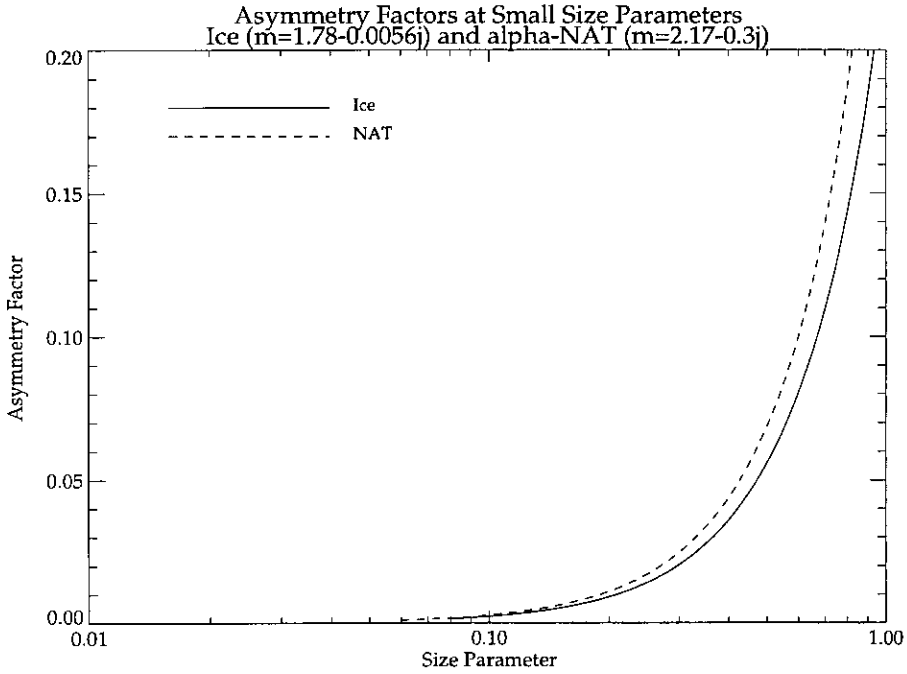

Figure 3.10: Asymmetry factors at low size parameters, for α-NAT at $-92°$, 14.4 THz, and for ice at $-60°$, 600 GHz.

Figure 3.10 is a plot of the asymmetry factors, calculated from the Mie solution for ice and for α-NAT, against small values of the size parameter. The ideal Rayleigh asymmetry factor which follows from equation 3.30 is zero, so when g rises to a significant value we can be deduce that the Rayleigh phase function is no longer a suitable approximation. The asymmetry factors for both substances are very low at the previously defined changeover point of $\chi = 0.1$, so the Rayleigh phase function is evidently reliable at this point. However, the recursive Mie routine can fail at size parameters about 0.1 when calculating the phase function at angles near $\pm\pi/2$. For example, the asymmetry plots in figure 3.10 stop at $\chi = 0.08$ in the case of ice, and $\chi = 0.06$ for the NAT, because the routine failed for these refractive indices at size parameters below these respective limits. Therefore the changeover point for

the phase function calculation is set to $\chi = 0.2$ instead. The asymmetry factors at this point are still only ~ 0.01, so the Rayleigh approximation is still safe.

3.3 Polydispersions

A scattering dispersion may be one of two types:

- A *monodispersion*, in which all the particles are identical.
- A *polydispersion* in which there is a range of particle sizes described by a size distribution $n(r)$, where $n(r)dr$ is the number density of particles with radii between r and $r + dr$. Therefore the total number density, N, of a polydispersion is given by

$$N = \int_0^\infty n(r)dr \tag{3.31}$$

Clouds in the Earth's atmosphere are polydispersions of hydrometeors, and so in order to model their scattering properties, the single-particle scattering theory described in the previous section must be extended to dispersions. To begin, consider a monodispersion of spheres of radius r_o, with number density N. We define a *volume extinction coefficient* γ_{ce} as the extinction cross-section per unit volume[6] [Deirmendjian 1969, p.74]. This is analogous to the volume absorption coefficient for thermal radiation defined in chapter 2. From the definition of extinction efficiency in section 3.2, the volume extinction coefficient (referred to hereafter simply as 'extinction coefficient') for the monodispersion is given by

$$\gamma_{ce}(N, r_o) = N\pi r_o^2 \xi_e(r_o) \tag{3.32}$$

This formula relies on the assumption of *independent scattering* [van de Hulst 1981, p.4; Ulaby *et al* 1981, p.305]. The scattered field from a particle has the same wavelength as the incident radiation, so there will be interference between the fields from different particles, but in the case of independent scattering there is no systematic relation between the phases. Constructive and destructive interferences are equally weighted, and the scattering appears incoherent, allowing the simple summation of intensities (and therefore of cross-sections). For independent scattering to be a valid assumption, the particles must be separated by several radii, which is the case for even the densest of atmospheric dispersions. This also means that the shadowing of one particle by another can be considered negligible.

The formula 3.32 for a monodispersion is extended to a polydispersion by substituting for N from equation 3.31, to give

$$\gamma_{ce} = \pi \int_0^\infty n(r) r^2 \xi_e(r) dr \tag{3.33}$$

[6] The subscript '*ce*' represents 'cloud extinction'.

In the same way the scattering coefficient γ_{cs} of the polydispersion can be calculated from the scattering efficiencies $\xi_s(r)$.

The overall phase function of the polydispersion is obtained by integrating the individual phase functions, weighted by the scattering cross-section, over the size distribution as follows [Lenoble 1985, p.188]

$$P(\theta) = \frac{\pi}{\gamma_{cs}} \int_0^\infty n(r) r^2 \xi_s(r) p(\theta, r)\, dr \tag{3.34}$$

where $P(\theta)$ is the overall phase function.

In practice the integrals (3.33) and (3.34) are evaluated between upper and lower limits of r, outside which there is not a significant contribution. This range of r will straddle the Mie and Rayleigh regimes.

3.3.1 The Modified Equation of Transfer

To incorporate the scattering properties of a polydispersion into the forward model requires modification of the equation of transfer. The familiar Schwarzschild equation for one-dimensional transfer in a non-scattering atmosphere was given in chapter 2 and is repeated here:

$$\frac{\partial I_\nu}{\partial x} = -\gamma_a [I_\nu - B_\nu(T)] \tag{3.35}$$

where γ_a is the molecular absorption coefficient.

The extension of equation 3.35 to a scattering atmosphere requires consideration of the two components of the equation individually. The first term, $-\gamma_a I_\nu$ is the differential fall in radiance due to molecular absorption. In the scattering atmosphere the extinction due to scattering is added, so that the total extinction coefficient is $(\gamma_a + \gamma_{ce})$.

The second term is the source function. The contribution due to molecular emission is unchanged, but there are two new components due to the presence of the polydispersion. One of these is the contribution to brightness temperature caused by the scattering of radiation from other directions into the line of sight, which I call *augmentation*. This process is described fully in section 3.4; for the moment the source function due to augmentation is referred to by J_a.

In addition there is emission from the scattering particles themselves; if they are absorbing radiation, then they must also be emitting the same amount if they are to remain in local thermodynamic equilibrium. Therefore there is a contribution of $\gamma_{ca} B_\nu(T)$ to the source function, where γ_{ca} is the volume absorption coefficient of the polydispersion, given by $\gamma_{ca} = \gamma_{ce} - \gamma_{cs}$.

Therefore the modified equation of transfer is:

$$\frac{\partial I_\nu}{\partial x} = -(\gamma_a + \gamma_{ce}) I_\nu + [(\gamma_a + \gamma_{ca}) B_\nu(T) + J_a] \tag{3.36}$$

which is solved in the same way as described in chapter 2.

The polydispersion is put into the model atmosphere of the forward model as a homogeneous, isothermal layer between predefined heights for the base and top. This is illustrated in figure 3.11, where the layer base and top are at heights h_{cb} and h_{ct} respectively. The volume scattering properties of the layer are calculated independently of the forward model, and are passed to it as input parameters. Then, as the equation of transfer is solved along the path (the line of sight), the additional scattering terms γ_{ce}, γ_{ca} and J_a in equation 3.36 are 'turned on' when the path lies within the layer, and set to zero when it does not. The adaptive steps along the path are constrained such that they do not straddle the edges of the layer, so that the scattering terms contribute over the correct in-layer path length.

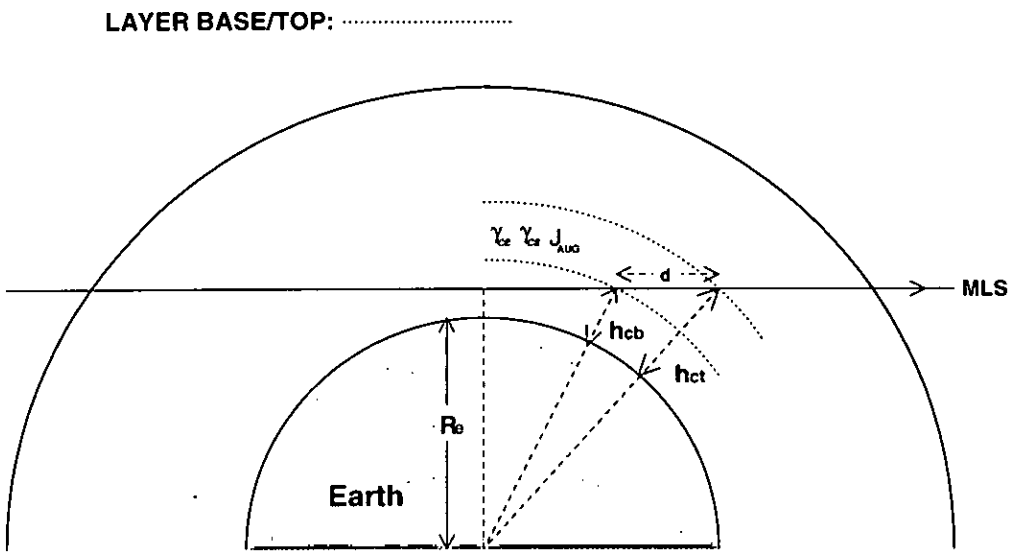

Figure 3.11: Limb path through a model atmosphere including a polydisperse scattering layer.

3.4 Augmentation

3.4.1 Source Function

As shown above, the source function is the positive component of the equation of transfer. It comprises the thermal emission from molecules and aerosols, and also the enhancement due to light scattered into the line of sight from other directions. The part of the source function due to the latter effect is called the augmentation, J_a.

Consider the volume element M of a scattering medium shown in figure 3.12. The line of sight along which the MLS is looking, in other words the direction of

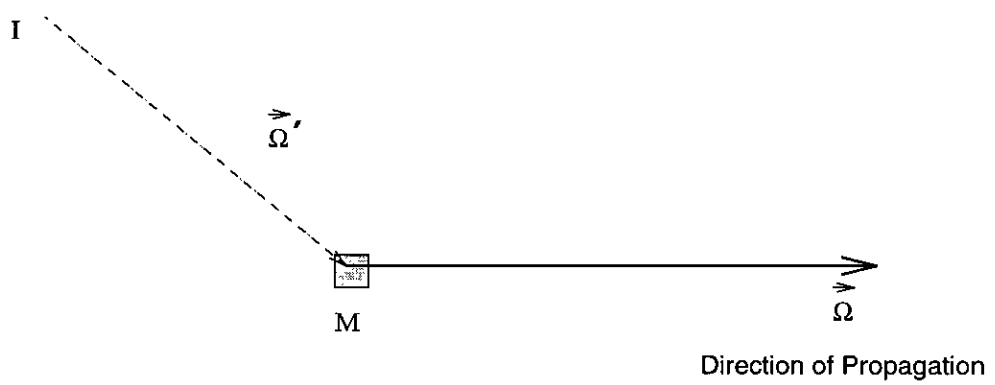

Figure 3.12: Scattering from a single incident ray into the line of sight.

propagation of the radiation I in the equation of transfer, is denoted by the vector $\mathbf{\Omega}$. The direction of an incident ray on M is denoted by $\mathbf{\Omega}'$. Therefore a component proportional to $\gamma_{cs} p(\mathbf{\Omega}, \mathbf{\Omega}') I(\mathbf{\Omega}')$ is scattered into the line of sight, if γ_{cs} is the scattering coefficient of M. The phase function $p(\mathbf{\Omega}, \mathbf{\Omega}')$ is expressible in terms of the scattering angle θ, where θ is the angle between $\mathbf{\Omega}$ and $\mathbf{\Omega}'$. The calculation of θ is described later.

For a continuous incident field on M, we treat the incident ray as an incident pencil of light across a solid angle $d\Omega'$. Then the total contribution from scattered light is obtained by integration over all directions, giving the following formula[7]:

$$J_a(\mathbf{\Omega}) = \gamma_{cs} \frac{\iint_{4\pi} p(\mathbf{\Omega}, \mathbf{\Omega}') I(\mathbf{\Omega}') d\Omega'}{\iint_{4\pi} p(\mathbf{\Omega}, \mathbf{\Omega}') d\Omega'} \tag{3.37}$$

The denominator normalises the source function due to augmentation, and will equal 4π if the phase function is normalised according to equation 3.3.

Calculating the Scattering Angle

Figure 3.13 shows a frame of reference (x, y, z) in the atmosphere, where the z axis is the projection of a radius of the Earth, and the xy plane is tangential to the Earth's curvature. The origin is a point within a layer of polydisperse scattering particles. All the solid lines lie in the yz plane. LOS is the line of sight of the MLS measurement, passing through the scattering layer. This line is at an angle ψ to the y-axis.

In a spherically symmetric atmosphere, the incident radiance at the origin is constant for a given zenith angle – therefore the conic surface shown, with the z-axis as its central axis, represents a set of rays all of radiance I. These rays make

[7] Adapted from Lenoble [1985, p.8].

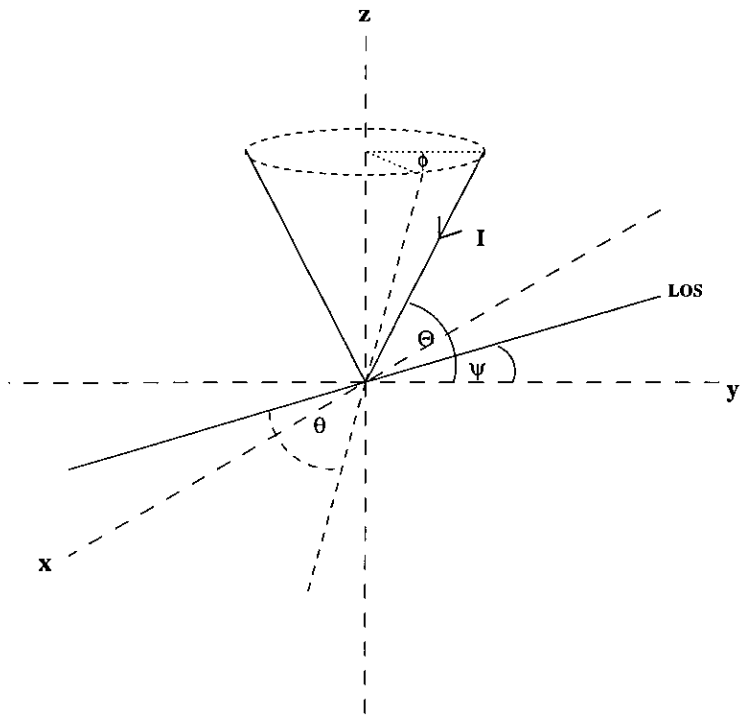

Figure 3.13: Scattering angle made by rays in a cone of constant zenith angle.

an angle Θ with the xy plane, such that the zenith angle is $(\pi/2 - \Theta)$. Any given ray in this set is defined by its azimuth angle ϕ about the the z-axis, where $\phi = 0, \pi$ when the incident ray is in the yz plane (as shown by the two solid lines).

A given incident ray makes an angle θ with the LOS, and this angle will be the scattering angle which is required for the incident radiation to be scattered into the line of sight. The scattering angle is expressed in terms of the other angles by spherical geometry. In general, for two lines $\mathbf{P}$ and $\mathbf{P}'$ which meet at the origin, the angle θ between them is given by the equation [Gow 1960, p.352]:

$$\cos\theta = ll' + mm' + nn' \tag{3.38}$$

where l, m, and n are the *direction cosines* of the line $\mathbf{P}$, and l', m', and n' are those of the line $\mathbf{P}'$. The direction cosines of a line are defined as the lengths of the projections of a unit-length segment of that line onto each of the three orthogonal axes. In this case the line $\mathbf{P}$ is the line of sight, so its direction cosines are $l = 0$, $m = \cos\psi$ and $n = \sin\psi$. The line $\mathbf{P}'$ is the incident augmentation ray, and its direction cosines are $l' = \cos\Theta\sin\phi$, $m' = \cos\Theta\cos\phi$ and $n' = \sin\Theta$. Therefore equation 3.38 becomes:

$$\cos\theta = \cos\psi\cos\Theta\cos\phi + \sin\psi\sin\Theta \tag{3.39}$$

bearing in mind that the angle Θ is the *complement* of the zenith angle. This expression satisfies the boundary conditions that when $\phi = 0, \pi$, the scattering

angle should be $\theta = (\Theta - \psi)$ and $\theta = (\pi - \psi - \Theta)$ respectively, which is apparent from figure 3.13.

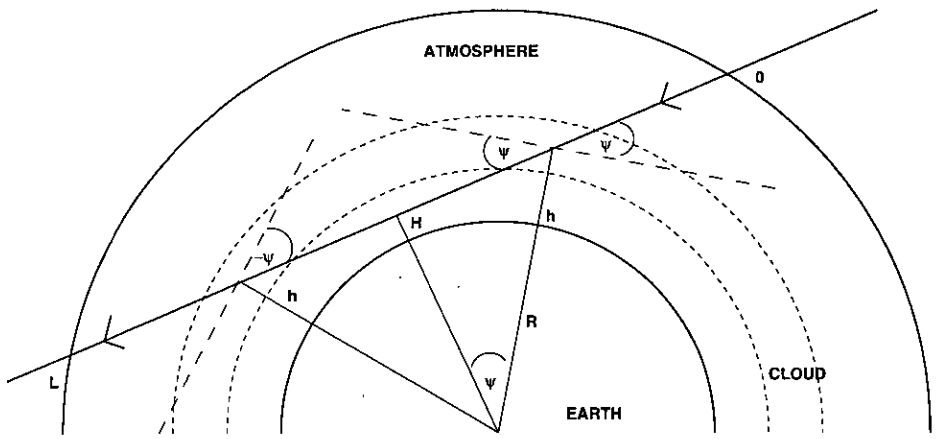

Figure 3.14: Twin scattering points on an MLS line of sight.

The angle of the LOS, ψ, is assumed in equation 3.39 to be as shown in figure 3.13, such that the direction of propagation is descending. In the case of an MLS line of sight which passes through and below an aerosol layer, as in figure 3.14, there are two scattering segments along the line, one with the LOS ascending in the atmosphere frame, and one with it descending. In the ascending case, the geometry of equation 3.39 still applies, but ψ is negative. The sign of ψ must be distinguished because of the $\sin\psi$ term in equation 3.39. From figure 3.14 it can be seen that

$$\psi = \pm \cos^{-1}\left[\frac{H+R}{h+R}\right]. \tag{3.40}$$

If the aerosol layer is of more limited horizontal extent, there may be only one scattering segment on the line of sight. In this case it is always assumed in the forward model that the aerosol lies on the near side of the tangent point with respect to the satellite.

To calculate the source function due to augmentation in practice, equation 3.37 needs to be converted to a double integral in spherical coordinates. The integration over the zenith angle is converted into an integration over its complement, Θ, leading to the following expression:

$$J_a = \gamma_{cs} \frac{\int_{-\pi}^{\pi}\int_{-\pi/2}^{\pi/2} p(\theta) I(\Theta)\cos\Theta \, d\Theta \, d\phi}{\int_{-\pi}^{\pi}\int_{-\pi/2}^{\pi/2} p(\theta)\cos\Theta \, d\Theta \, d\phi} \tag{3.41}$$

The integrals are calculated using trapezoidal integration, with the scattering angle at each integral step calculated from equation 3.39. Note that the scattering

angle is calculated in terms of its cosine, so there are two values of θ in the range $-\pi$ to π which satisfy the equation at any given time. However, these solutions for θ are symmetrical about $\theta = 0$, as is the phase function, so no confusion arises.

3.4.2 Practical Considerations

Incident Augmentation Radiation

Calculation of the source function due to augmentation by equation 3.41 requires that the incident radiation function $I(\Theta)$ be known. $I(\Theta)$ itself must be calculated by the forward model. This was achieved using the generalised viewing geometry of the forward model described in section 2.4.2.

The function $I(\Theta)$ is measured from a single point within the scattering layer, known as the *augmentation point*, which is generally chosen to be the vertical midpoint of the layer. Then the forward model is used to calculate the brightness temperatures along lines of sight radiating from the augmentation point, as if there were an aircraft-borne sounder located at that point. Time limits the number of rays that can be calculated, so a representative set of incident rays is needed, from which intermediate rays can be interpolated with reasonable accuracy. These 'preliminary' runs of the forward model to calculate the incident radiances at the augmentation point precede the 'main run', which is the solution of the radiative transfer equation along the required MLS line of sight, with the source function due to augmentation included.

The angular distribution of brightness temperature at 227 GHz, measured from three different augmentation heights, is shown in figure 3.15 where it is seen that there is a very sharp change in brightness temperature about the horizontal. This means that an evenly spaced set of incident rays may not be a good basis for interpolation, and so a finer angular resolution is needed about the horizontal than at other angles.

At each augmentation height, the brightness temperature is approximately constant for those rays which intercept the Earth's surface (i.e. those below about $-3°$), so the lowest ray I use is one which grazes the Earth's surface. Then a further four rays are set at regular intervals up to an angle of 1° above the horizontal, as shown in figure 3.16. This fine resolution covers the angular range in which the sharp change is expected to occur. The angle at which this change occurs and its gradient will depend on the height of the augmentation point, as shown by figure 3.15, and on the nature of the atmosphere, so it is not possible to know in advance how to optimally arrange the incident rays. The method described here is an attempt to cover all possibilities to a reasonable degree.

The rays above 1° are spaced logarithmically, reflecting the diminishing gradient

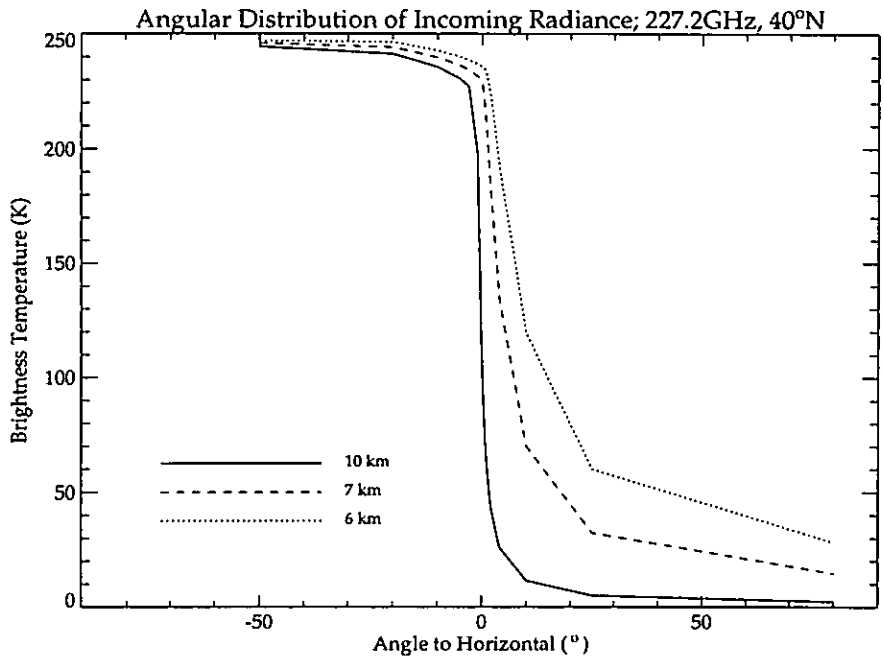

Figure 3.15: Angular distribution of incident radiance at typical cirrus cloud heights.

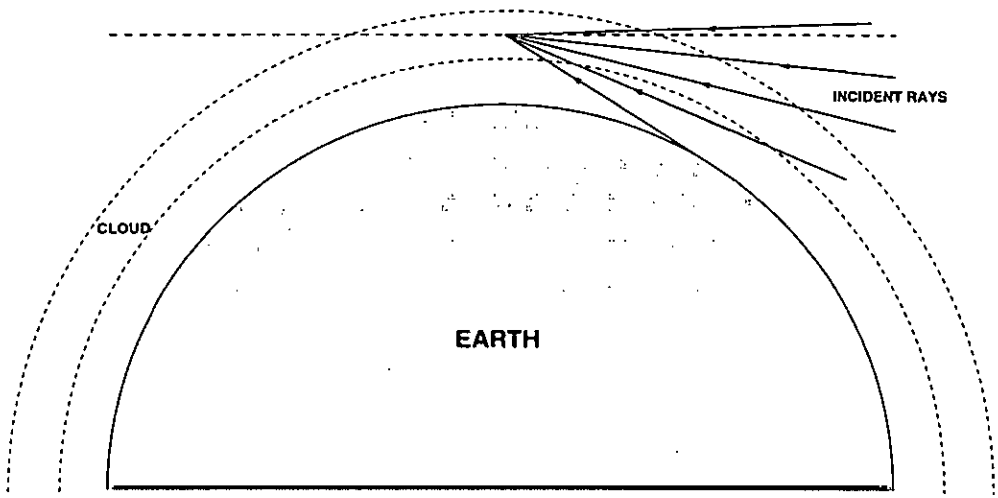

Figure 3.16: Angular resolution of incident augmentation rays near or below the horizontal. The cloud is represented as a continuous layer lying between the base and top altitudes.

of the brightness temperature profile with increasing angle, especially in the case of the lower augmentation heights. The first of these rays is at 2°, and subsequent rays are at angles which increase in powers of 2.5° up to a maximum of 78°; thus there are 10 augmentation rays altogether.

Angular Resolution of Integrations

The trapezoidal integrations in equation 3.41 were initially calculated using a uniform step size of $\pi/12$ in both cases. The model was tested using double this resolution, which did not lead to a significant difference in results. However, given the variable resolution of the incident ray set, it is probably more appropriate to use a similarly variable resolution for the integration over the complement of the zenith angle, Θ.

This was done by retaining 12 steps in the zenith loop, but spacing them logarithmically, so that each step covers half the angle of the previous one as the horizontal is approached. The average change in output from the model as a result of this modification is less than 0.5%, but there is no extra computation time associated with its use, so it was adopted anyway.

Solar Contribution

The ten augmentation rays calculated by the forward model describe the incident radiation $I(\Theta)$ due to molecular emission from the atmosphere. The contribution from the sun, which has a proportion of its radiance scattered into the line of sight, should also be considered, but as shown below it proves to be insignificant.

The solar irradiance arriving at the edge of Earth's atmosphere approximately fits the Planck function for a black-body at 5900K [Schanda 1986, p.56]. The corresponding brightness temperature (the *solar equivalent brightness temperature*) is given by the Planck function at a frequency ν:

$$T_B(\nu, T) = \left(\frac{h\nu}{k}\right) \frac{1}{\exp\left(\frac{h\nu}{kT}\right) - 1} \tag{3.42}$$

In the microwave region this function varies very little with frequency; over a frequency range of 100 GHz to 1 THz, the solar equivalent brightness temperature varies between $\sim$ 5900 K and 5875 K.

The solar radiation arriving at the cloud has passed through the atmosphere and so will be attenuated by the molecular absorption of the intervening atmosphere. Therefore to include this contribution properly the forward model would have to be run along another line of sight from the augmentation point in the direction of the sun. However, it can be shown by approximation that this is unnecessary. The angular diameter of the sun, $\theta_\odot$, given by Houghton [1986, p.224], is 31.99′ of an

arc, or 1.861×10^{-2} radians. If the sun is regarded as a circle on the surface of the celestial sphere, which is itself regarded as being locally flat over the small angular diameter covered by the sun, then the solid angle of the sun may be approximated as $\Omega_\odot = \pi(\theta_\odot/2)^2 = 2.72 \times 10^{-4}$ sr.

If, for the purposes of this approximation, scattering is assumed to be isotropic[8], then from equation 3.37 we see that the contribution from the sun will be proportional to its brightness temperature multiplied by the solid angle it subtends. Therefore, taking the unattenuated brightness temperature 5900 K as a maximum:

$$T_B(\text{sun})\Omega_\odot \simeq 1.60 \text{ K sr}$$

The same calculation for the rest of the sky can be simplified by reference to figure 3.15. This shows that the incident radiance at the cloud from the atmosphere may be crudely represented by a two layer system, where the radiance is zero above the horizontal, and $\sim$ 200 K below the horizontal. The total solid angle of the sub-horizontal hemisphere is 2π, so

$$2\pi T_B(\text{sky}) \simeq 1260 \text{ K sr}$$

Therefore the solar contribution to augmentation is at most only 0.13% of the contribution from the rest of the sky, and as such it can be safely neglected.

3.4.3 Higher-Order Scattering

The model described so far has used single-scattering, of which the two components are:

- Scattering out of the line of sight, causing attenuation of the observed radiance.
- Scattering into the line of sight from other incident rays, causing augmentation of the observed radiance.

The brightness temperatures of the incident rays at the augmentation point are calculated first by the forward model as described at the start of section 3.4.2, and their intensities are reduced by extinction over the short distance for which they are within the cloud. However, the incident rays are themselves subject to the same augmentation processes as the ray along the line of sight, and so the results can be made more representative by processing these rays twice.

This process is illustrated in figure 3.17. The preliminary runs of the forward model yield a set of single-scattered radiances I_1 which define the incident radiation

[8] In practice the solar contribution to augmentation will depend on the asymmetry factor, and the angle between the MLS line of sight and the direction of the sun.

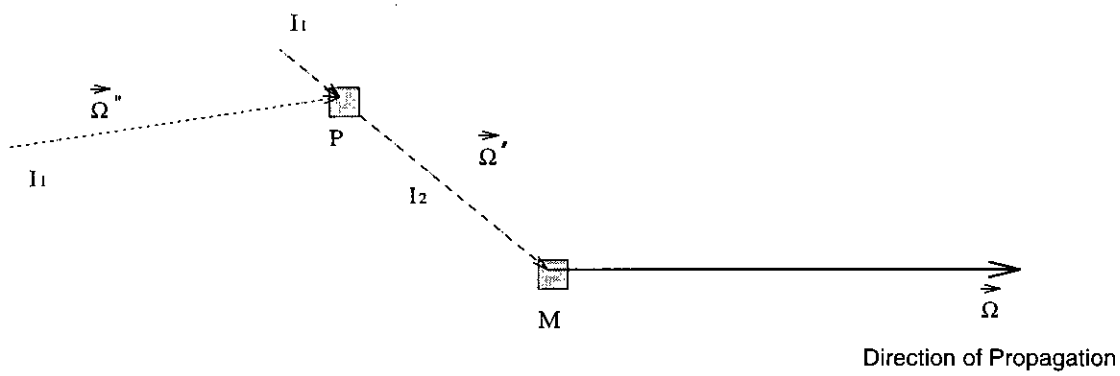

Figure 3.17: Double-scattering: Augmentation of the augmentation ray.

on M that augments the line of sight. Then a second set of preliminary runs is performed, using the first set of radiances I_1 to determine the source function due to augmentation, as shown at point P. This results in a new set of augmented incident rays, I_2, which are then used to define the incident radiation field $I(\Theta)$ which augments the radiance along the MLS line of sight. The final result is therefore doubly-scattered.

This process may be repeated indefinitely, and with each such successive reprocessing of the incident ray set, the resulting brightness temperature approaches an ideal multiple-scattering value. Therefore an order of scattering must be chosen which yields sufficiently accurate results without requiring excessive computation time.

The forward model was run using both the single-scattering and the double-scattering methods, and the resulting brightness temperature differences are presented in table 3.1. The measurements at 215.8 ± 11.4 GHz and 310.5 ± 4.7 GHz are bands which were, at the time these results were produced, proposed for use as tropospheric retrievals on EOS MLS. For each band the forward model was run under two cloud conditions, based upon cirrus data presented by Stackhouse and Stephens [1991] for a latitude of 45°N. The 'standard' cloud lies between 8.7 km and 10.8 km, and has a midpoint temperature of −47°C and a mean ice water content of 0.007 gm^{-3}. These characteristics are about average for this latitude, as will be seen in chapter 5. The 'thick' cloud is an extreme example of cirrus which lies between 7.7 km and 11.9 km, with a midpoint temperature of −45°C and an IWC of 0.022 gm^{-3}. The microphysical characteristics of the cirrus polydispersions in each case were represented using techniques which will be described in chapters 4 and 5 of this thesis. Results were produced for MLS tangent heights of 7 km and 10 km, which are respectively below and within both the standard and thick

clouds. Each tabulated value is the difference between the single-scattered and the double-scattered brightness temperatures[9], as a percentage of the double-scattered value.

	Standard Cloud		Thick Cloud	
	7 km	10 km	7 km	10 km
215.8 ± 11.4GHz	0.70%	1.25%	7.60%	10.45%
310.5 ± 4.7GHz	0.88%	1.19%	8.67%	10.10%

Table 3.1: Relative differences between single- and double-scatter brightness temperatures.

Clearly in the case of the thick cloud there is a significant difference in brightness temperature as a result of the extra scatter, so the same comparison was made between the double-scatter results and those from a *triple*-scattering model. These results are shown in table 3.2, for the thick cloud only.

	Thick Cloud	
	7 km	10 km
215.8 ± 11.4GHz	1.68%	2.31%
310.5 ± 4.7GHz	2.22%	2.59%

Table 3.2: Relative differences between double- and triple-scatter brightness temperatures.

The inclusion of the third scatter leads to a considerable increase in processing time, which is probably unwarranted for the sake of an improvement in accuracy of the order of a few percent. However, there may be some advantage in using a triple-scatter method with a reduced number of augmentation rays. Table 3.3 shows the effects on the triple-scatter results of a reduction of the augmentation ray resolution from the 10 rays specified in section 3.4.2 to only 5 rays. The 5 ray set is arranged as follows: a ray which just grazes the earth, a ray at 1° above the horizontal, a third ray which bisects the other two, and then two more rays at 8° and 78°. Table 3.3 gives the differences between the 5-ray and 10-ray methods, again for the thick cloud only.

So, in tables 3.2 and 3.3 we have comparisons of an 'ideal' method, the 10-ray triple-scattering model, with two inferior methods. Each of the inferior methods differs from the ideal by about the same amount, so they may be considered approximately equivalent in terms of accuracy. However, the 5-ray triple-scattering method

[9] Averaged across all 21 filters.

	Thick Cloud	
	7 km	10 km
215.8 ± 11.4GHz	1.36%	1.89%
310.5 ± 4.7GHz	2.07%	2.44%

Table 3.3: Relative differences between triple-scatter brightness temperatures for 5-ray and 10-ray sets.

requires only 15 augmentation ray calculations, while the 10-ray double-scattering method calculates 20, so the former technique was used to reduce processing time.

3.5 Chapter Summary

In this chapter I have described a method of modelling the scattering and extinction due to a cloud of spherical particles. The scattering properties of a single sphere were shown to be expressible in terms of of the Mie efficiencies and the phase function, and it was explained how the Mie solution was applied in practice to calculate these quantities, using the Rayleigh approximation where appropriate.

The single sphere theory was then extended to model scattering by a collection of spheres covering a range of sizes, so as to form a first approximation to a cloud scattering model. I have shown how such an idealised cloud was incorporated into the forward model described in chapter 2. It was also shown how the effects of multiple scattering in the cloud were approximately simulated by the addition of the augmentation source function to the equation of transfer.

This has resulted in a forward model in which a cloud of spherical particles may be placed in the form of a layer between fixed heights in the model atmosphere. Therefore the effect of such a cloud on the radiances measured by the MLS may be determined. In the next chapter it will be shown how this idealised layer was made to represent the scattering behaviour expected of a real cloud in the Earth's atmosphere.

Chapter 4

Cirrus Microphysics

4.1 Introduction

The idealised polydispersion of particles described in the previous chapter is intended to represent a naturally occurring distribution of atmospheric aerosols. The aim of this thesis is to determine the effect of such distributions on the EOS MLS retrievals, and so it is first necessary to decide which forms of distribution need to be studied. Various forms of scattering polydispersion occur in nature, the majority of which are clouds of one form or another. In ascending order of height in the atmosphere, they may be broadly classified as follows:

- Rainfall. Precipitation from clouds in the lower troposphere takes the form of quasi-spherical droplets of liquid water, with diameters ranging from 100 μm to 10 mm [Schanda 1986]. These have a considerable scattering effect on long-wavelength radiation, as demonstrated by the use of radar to track rainfall patterns.

- Cumuliform Clouds. These occur mostly in the lower troposphere below 2 km, although altocumulus can reach as high as 7 km. They are formed from spherical drops of liquid water with diameters between 1 μm and 100 μm, and typical number concentrations are of order 10^8 m^{-3}, though lower than this in altocumulus [UKMO 1972].

- Cirrus Clouds. This classification is used in this chapter to include all ice clouds occurring in the upper troposphere. The crystals which comprise such clouds have a wide variety of shapes. Typical number concentrations are of order 10^5 m^{-3}, considerably less than in cumulus [UKMO 1972].

- PSCs. *Polar stratospheric clouds* are found from the tropopause up to about 30 km, and are divided into two types. Type I are composed of droplets

of nitric acid trihydrate ($HNO_3.3H_2O$), usually abbreviated to NAT[1]. They are thought to be generally spherical, although the larger particles in this group (sometimes called type I_a) may be more aspherical [Torres *et al* 1992]. The droplets are of order 1 μm in radius. Type II PSCs are thought to be composed predominantly of particles of water ice in crystalline form, similar to cirrus. The crystals are larger than the type I droplets, of order 10 μm [Kinne *et al* 1989], but their concentrations are lower, so their visible optical depth is considerably less than that of type I [Toon *et al* 1989], and their microwave extinction is not expected to be significant.

- Stratospheric Sulphate Aerosol. There is a layer of sulphate aerosol which ranges from the tropopause up to about 30 km. In general the particles are spherical droplets of supercooled sulphuric acid and water in the proportions 75% H_2SO_4, 25% H_2O [Deshler *et al* 1992]. From the data of Deshler *et al* [1992,1993] and Stone *et al* [1993], their diameters are in the range 0.1 μm to 0.5 μm. These aerosols act as the condensation nuclei for PSCs.

Of these polydispersions, the stratospheric forms are generally composed of particles which are small enough not to be likely to cause a significant scattering problem at millimetre wavelengths. The cumuliform clouds and raindrops occur low in the troposphere, at levels which are not suitable for MLS retrievals because of the high water vapour extinction. However, the cirrus clouds in the upper troposphere lie in the height range in which we hope to be able to make tropospheric retrievals of ozone and water vapour with the EOS MLS. It is necessary to be able to simulate such clouds, with a view to determining their detrimental effect on tropospheric retrieval.

The scattering model developed in chapter 3 applies to a known distribution $n(r)$ of *spherical* scatterers, of known refractive index m. The purpose of the present chapter is to apply this model to cirrus clouds, so there are three requirements to be satisfied:

1. Define the size distribution[2] $n(r)$ for the cloud. A distribution of crystal concentration with respect to size can be estimated using the results of aircraft studies of cirrus, and several such studies have been conducted. The distributions I have chosen are described below in sections 4.3.1 and 4.4.1.

2. Find the refractive index m of the crystals. Warren [1984] tabulates the refractive index of ice for wavelengths from the ultraviolet to radio, and at

[1] Recent research, for example Disselkamp *et al* [1996], suggests that nitric acid dihydrate (NAD) may also be involved.

[2] A note on terminology: Such size distributions are often referred to as *particle spectra* in the literature. In this chapter the term 'distribution' is used exclusively.

temperatures of −1°C, −5°C, −20°C and −60°C. The values used for the cirrus simulation were interpolated with respect to temperature and wavelength between the values tabulated by Warren. Linear interpolation was appropriate for the real part of the refractive index, and logarithmic interpolation for the imaginary part.

3. Represent the crystals as spheres. This is clearly a problem. The ice crystals in cirrus clouds are far from spherical, as will be seen in sections 4.3.2 and 4.4.2 below.

This chapter deals primarily with the first item in the above list, the construction of a realistic size distribution of the crystals in a particular cirrus cloud. In addition to this, the distribution of crystal shapes in the cloud will also be required, so that in the next chapter an attempt may be made to represent these crystals as spherical equivalents, as required by the last item in the above list.

In the next section, cirrus cloud is divided into two distinct types, frontal and convective, according to the manner in which they are formed. Then in sections 4.3 and 4.4, results from the body of published literature on cirrus microphysics are used to determine appropriate number distributions, and expected distributions of crystal shape, for each type of cirrus cloud.

4.2 Formation of Cirrus

In this chapter I have divided cirrus clouds into two major types according to the way in which they are formed: either through mesoscale convection in the tropics, or at fronts in the middle and high latitudes. Each type has different micro- and macrophysical characteristics, although some cirrus belongs to both categories, being produced in the anvils of frontal cumulonimbus clouds, but sharing the physical characteristics of the tropical convective form.

The processes which lead to cirrus formation in each case are described in detail below. The formation of cirrus from frontal cumulonimbus is dealt with in the discussion of frontal cirrus.

4.2.1 Convective Cirrus

Convective cirrus is formed in the glaciated anvil head of a cumulonimbus cloud. In the tropics such clouds arise as the result of surface warming, which initiates the convective warming of the mid-troposphere. The resulting positive temperature anomaly will push the pressure surfaces upwards, as illustrated in part (a) of figure 4.1, creating a pressure gradient in the upper troposphere which drives a divergent upper-level wind. This process removes air from the column above the

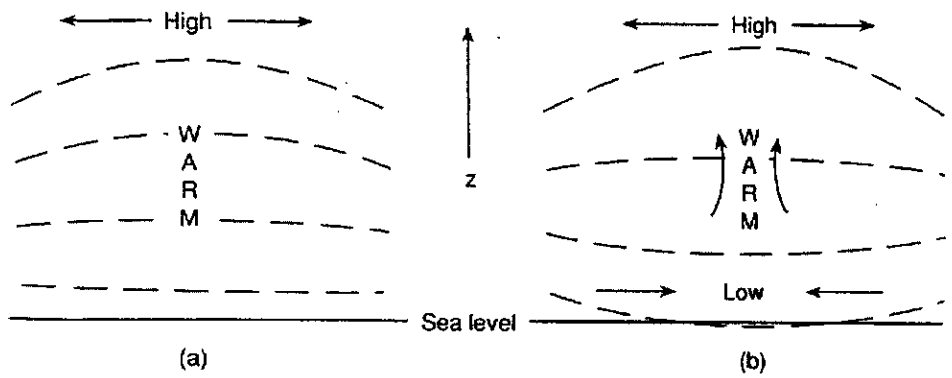

Figure 4.1: Convection caused by midtropospheric warming, from Holton [1992, p.81]. Dashed lines are isobars, and arrows denote movement of air.

anomaly and so generates a surface pressure low. Therefore there is also a pressure gradient at the surface, which causes air to converge at lower levels, and to be forced upwards into a vertical circulation which compensates the upper-level divergence, as shown in part (b) of figure 4.1.

The extent to which this process continues depends on the strength of the surface warming, the moistness of the air, and the depth of the moist layer. As the air is transported upward, the condensation of the water vapour into cloud droplets and precipitation leads to a release of latent heat energy, which maintains the mid-tropospheric temperature anomaly and so drives further convection. When the convection reaches the upper troposphere, the cloud particles which are formed are predominantly ice crystals, and the divergence of air at this level causes the familiar anvil shape of the cirriform head [Barton 1983]. These anvils are temporary, but as the largest ice particles settle out, the small remaining particles are dispersed by wind and diffusion, and the cirrus spreads out into a layer covering hundreds of kilometres, far beyond the convective region [Prabhakara *et al* 1988].

The convection required for the formation of these cumulonimbus clouds occurs most extensively in a tropical latitude band called the ITCZ (InterTropical Convergence Zone). This region, understood on a basic level, is the meeting point of two Hadley circulation cells, such that the air converges at lower levels, is forced upwards, and then diverges at the tropopause to carry heat back towards the pole. However, in practice the ascent stage is not a straightforward large-scale vertical motion, but instead is a mean zonal ascent which takes place in many separate convective clusters [Holton 1992, p.372]. The Hadley circulation provides the low-level convergence of moist air which charges the tropical lower troposphere with water vapour, making it unstable and leading to vigorous cumulus convection.

The strength of the north and south Hadley cells at the equator vary with season, and so the location of the ITCZ also changes. In addition, the latitude of the ITCZ varies with longitude, because of the localised effects of *monsoon* circulations (discussed further below). During the northern hemisphere summer the convection zone lies at latitudes between 5°N over the Atlantic, to 20°N over the Western Pacific, whereas during the northern hemisphere winter its extremes are 5°N over the Eastern Pacific, and 15°S over Australia [McIntosh & Thom 1969, p.188-189].

The ITCZ is not occupied by a continuous band of cumulonimbus convection, but rather by a series of clusters, each a few hundred kilometres across, separated by regions of relatively clear sky. The clusters are transient phenomena which propagate westwards at a speed of about 10 ms^{-1} [Holton 1992, p.373]. This is because they are associated with westwards-propagating equatorial waves. The latent heat released by condensation in the convective clusters acts to drive the equatorial waves, which in turn maintain the low-level convergence that feeds the convection.

The cumulus convection is particularly effective where there is a *monsoon* circulation. A monsoon is defined as any seasonally-reversing circulation, and by far the most extensive of these is the tropical Asian monsoon. This causes a warm wet summer and a dry cool winter in the Indian subcontinent. It is driven by the contrast between the thermal properties of the land and the sea. Intense surface warming of the land during summer leads to cumulus convection and latent heat release which warms the whole troposphere and creates a thermal low. As explained above, this is accompanied by high-level divergence and low-level convergence, the latter making conditions more favourable for cumulus convection.

The winter monsoon is the same effect in reverse, so that the convection occurs over the warm oceans. In this case the convection is strengthened by the *Walker circulation*. This is a longitudinal atmospheric circulation caused by the fact that sea surface temperatures are greater in the western Pacific than they are in the east. It leads to a pressure gradient, and therefore a mean surface wind in a westward direction which is stronger than the zonal mean [Holton 1992, p.381]. Therefore there is a horizontal transport of water vapour into the western Pacific which enhances the convection in that region.

4.2.2 Frontal Cirrus

The classical picture of frontal cirrus formation is that the cloud is produced at a warm front, when warm air pushes up over a wedge of cold air, as shown in figure 4.2. The decrease in pressure with altitude causes cooling by adiabatic expansion, which in turn causes water vapour to condense, producing clouds. The first clouds that

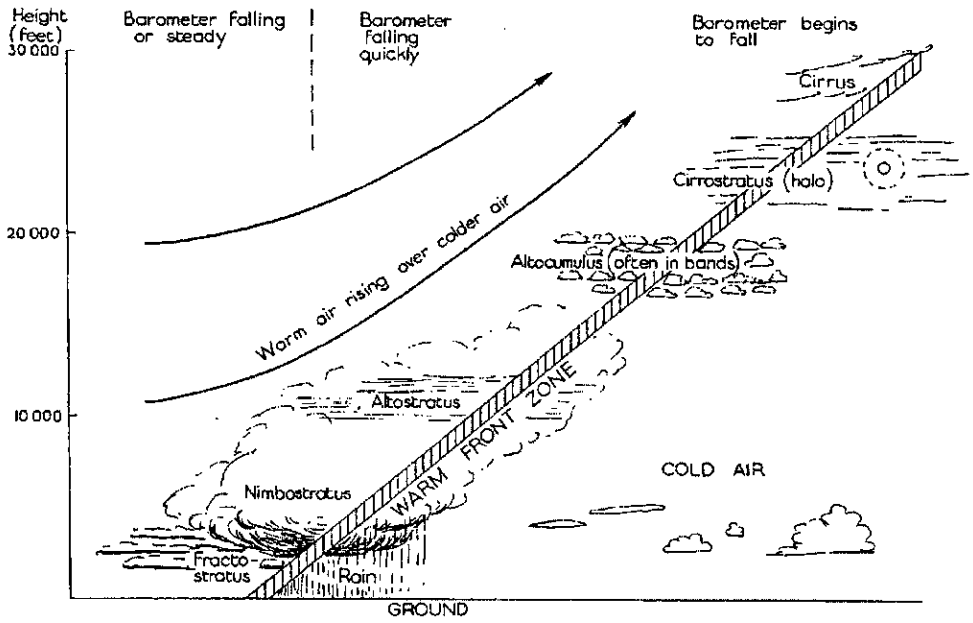

Figure 4.2: Classical picture of cloud formation at a warm front (from Pilsbury [1969, p.19]).

appear to an observer on the ground as the surface front approaches are the cirrus, followed by a denser layer of cirrostratus. To a lesser extent, a cold front may also produce cirrus as a by-product of the anvils of the cumulonimbus clouds associated with the front, in the same way that the anvils of the tropical convective complexes described above disperse to form cirrus. A cold front has a gradient two or three times greater than that of a warm front, as shown in figure 4.3, and this steepness causes a deep and rapid uplift of the moist warm air ahead of the cold front, leading to convective processes similar to those described in the previous section[3].

A recent study conducted as part of FIRE (First ISCCP[4] Regional Experiment) presents a more complicated theory of warm front cirrus production than that described above. Starr and Wylie [1988] find that warm front cirrus is always associated with an 'upper-level short wave', in other words a Rossby wave in the upper troposphere, of about 1000 km to 2000 km from trough to crest. Following the pattern of the Rossby wave is the *jet stream*, a narrow belt of high wind speeds just below the tropopause, of a few hundred kilometres in width and a few kilometres in depth. Starr and Wylie [1988] find that cirrus forms as a shield across the crest of the wave's ridge, with a sharp northern boundary defined by the jet stream. This

[3] A front producing such activity is known as an *ana* cold front. The *kata* cold front is also observed, which is characterised by descent of the warm air close to the frontal surface, and this results in weaker cloud formation.

[4] International Satellite Cloud Climatology Project.

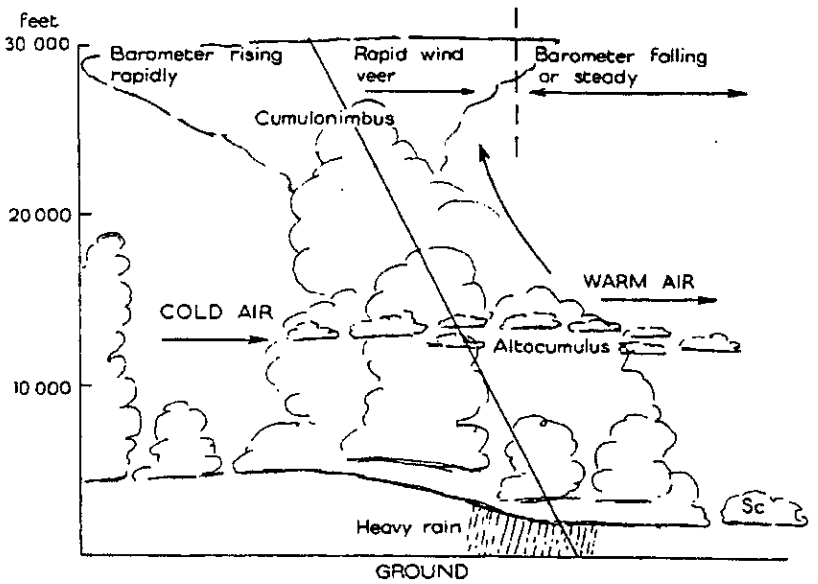

Figure 4.3: Cloud formation at a steep cold front (from Pilsbury [1969, p.21]).

is shown in figure 4.4, where the short Rossby wave in the upper troposphere lies above a surface low with associated warm and cold fronts. It may be seen that the shield extends back upstream of the surface warm front, contrary to the classical picture of figure 4.2. Often middle-level cloud develops as well, and the pattern of its development is consistent with the classic model, but the high-level cloud appears to develop independently, and its spatial pattern does not fit the classic theory. Given the absence of any frontal origin for the cirrus, its formation is likely to be due to a large-scale ascent of moist air [Sassen *et al* 1989].

Cirrus formation also occurs at a cold front, not only as the cumulonimbus anvil remnant described by the classical picture, but also as a larger-scale phenomenon. When a long Rossby wave forms (of about 3000 km to 5000 km from trough to crest), the boundary between the polar and tropical air masses (the *polar-frontal zone*) runs along the length of the wave between the trough and the crest, northeastward for the ascending part of the wave. The polar-frontal zone is a narrow region of strong temperature gradients, which means that the jet-stream axis tends to lie along it [Holton 1992, p.148]. Figure 4.5 shows an infrared satellite image of this type of jet-stream cirrus. The brightest areas correspond to the cold cirrus, and it can be seen that the cloud forms as a long swathe with the jet stream (denoted by arrows) as a northern edge. As the Rossby wave propagates slowly eastwards[5], the air mass boundary has a corresponding south-easterly progression, and so viewed on a large scale, it is a cold front. Typically the cloud will stretch for more than 3000 km, while the width is $\sim$ 500 km [Starr and Wylie 1988].

[5] Holton [1992, p.216] shows that the propagation of a Rossby wave pattern is westward, but this is relative to the air flow, so when the jet stream has a strong eastward component, the movement of the Rossby wave pattern relative to the Earth is also eastward.

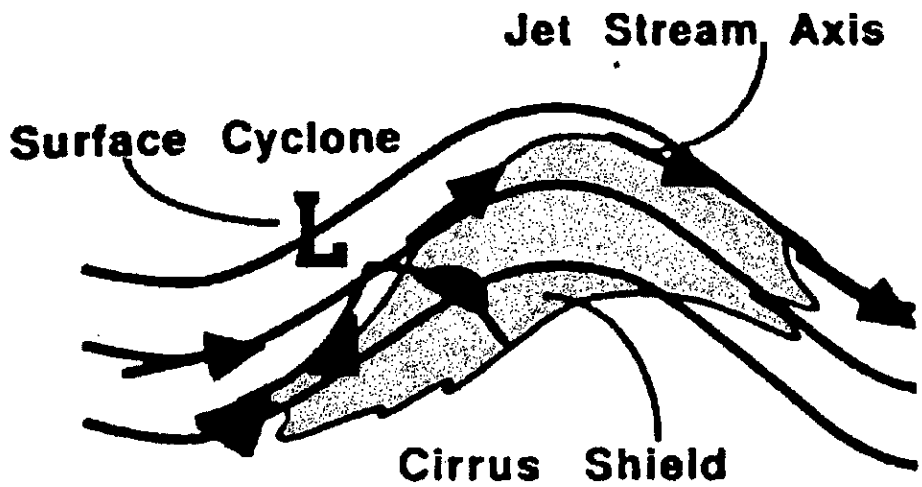

Figure 4.4: Warm front cirrus production not related to frontal upglide (from Starr and Wylie [1988]). Solid lines are upper-troposphere isobars. Surface fronts are shown, radiating from the centre of the surface low **L**.

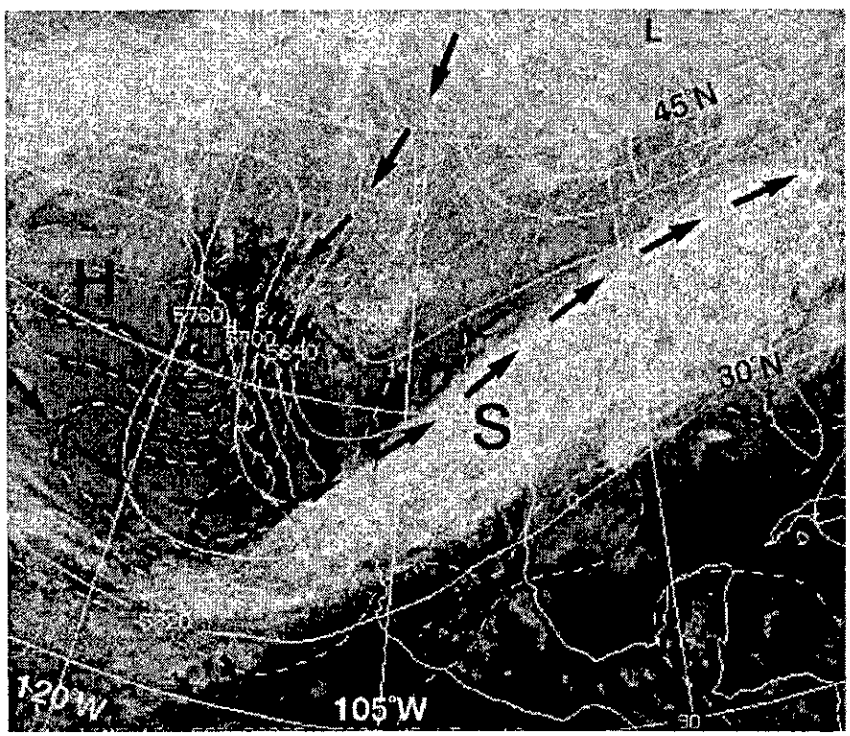

Figure 4.5: Infrared Satellite Image from Bader *et al* [1995], showing a band of cirrus cloud (brightest areas, labelled S) which has formed along the polar-frontal jet (black arrows) over North America.

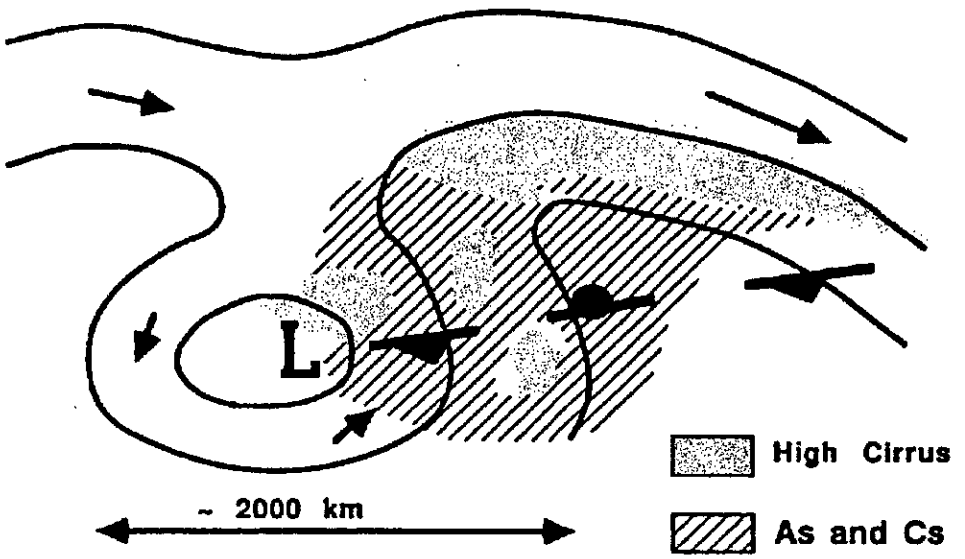

Figure 4.6: Cirrus cloud formation over a closed low aloft (Starr and Wylie [1988]).

A third type of mid-latitudinal cirrus, 'closed low' cloud, is described by Starr and Wylie. A low pressure region in the upper tropopause which cuts off from the main wave pattern, as shown in figure 4.6, is called a 'closed low aloft'. Often there are no clearly defined surface features corresponding to this situation, although there may be weak surface fronts such as those shown in the diagram, and these may indicate more well-defined fronts higher in the troposphere. High cirrus develops over the exit ridge of the low and extends downstream, in much the same way as the short wave cirrus described above. Altostratus and cirrostratus may also form, possibly due to classical formation of cloud on an upper-level warm front.

4.3 Microphysics of Frontal Cirrus

This section and the next are concerned with the microphysical description of cirrus cloud for firstly frontal, then convective systems. This microphysical description consists of the size distribution of the cirrus crystals, and the shapes that the crystals take. For each cirrus type, the microphysical data set is parameterised in terms of temperature, and in the frontal case, in terms of ice water content as well. Chapter 5 will explain how the data are converted into a form which is consistent with the scattering theory of chapter 3.

4.3.1 Parameterisation of Crystal Size Distributions

The size distribution for frontal cirrus was produced using the parameterisation of Heymsfield and Platt [1984], which is based on aircraft measurements made in uniform winter and springtime cirrus clouds associated with synoptic depressions. The complete data set used in the parameterisation is the product of 8 separate

flights over the Northern United States and Canada, comprising about 50 separate sampling passes through cirrus cloud.

Heymsfield and Platt grouped the measured size distributions into temperature bands of 5°C interval, from −20°C to −60°C, and averaged all the distributions within each band. Average ice water contents (IWC) for each band were also found, to an accuracy of 20%. The authors then fitted two-part power-law functions to each average distribution according to the formulae:

$$N = A_1(T)D^{B_1(T)} * \text{IWC} \qquad \text{for } D \leq D_o \tag{4.1}$$

$$N = A_2(T)D^{B_2(T)} * \text{IWC} \qquad \text{for } D \geq D_o \tag{4.2}$$

where N=concentration ($\text{m}^{-3}\ \mu\text{m}^{-1}$), D=maximum dimension of the crystal (μm), and IWC is the ice water content in gm^{-3}. The parameters $A(T)$ and $B(T)$ are constants for each temperature band, and the dimension D_o (μm) is the changeover point between the two parts of the fitted function.

Heymsfield and Platt tabulate, for each temperature band, the averaged IWCs, the B parameters for the 2 curves, and the particle concentrations at dimensions of 100 μm and 1000 μm (N_{100} and N_{1000} respectively). In the case of temperatures < -40°C, a single curve is sufficient to fit the average distributions, so there is only one B parameter. In this case, B (the slope), may be obtained directly from the values of N_{100} and N_{1000} by the formula:

$$B = \log_{10}(N_{1000}) - \log_{10}(N_{100}) \tag{4.3}$$

This gives a different value of B from that tabulated by Heymsfield and Platt in three of the four cases, and in the case of curve 8, the slope calculated by equation 4.3 is a whole 1.0 higher than the value given by the authors. Figure 4.7 (right) shows a diagram taken from Heymsfield and Platt's paper, which shows the fitted functions for each of the 8 temperature bands, plotted on logarithmic axes[6]. The N_{100} and N_{1000} values read from this plot are consistent with those tabulated by Heymsfield and Platt, so I accept these as correct, and use the values of B calculated from equation 4.3 in each case in place of the values given by the authors. Correspondence with the authors has confirmed that there are typographical errors in the tabulated values of B [Andrew Heymsfield, personal communication].

For bands 1–4, there can be no independent check of B since there are two values, so the only method of verification in this case is to overlay the fitted curves onto the plots of the average measured size distributions given in the paper. These distributions are reproduced as figure 4.7 (left). The fits defined by Heymsfield and

[6]Note that the lowest value on the concentration axis is 10^{-4}: I believe this to be a typographical error as it is inconsistent with the scale on that axis. The label should read 10^{-3}.

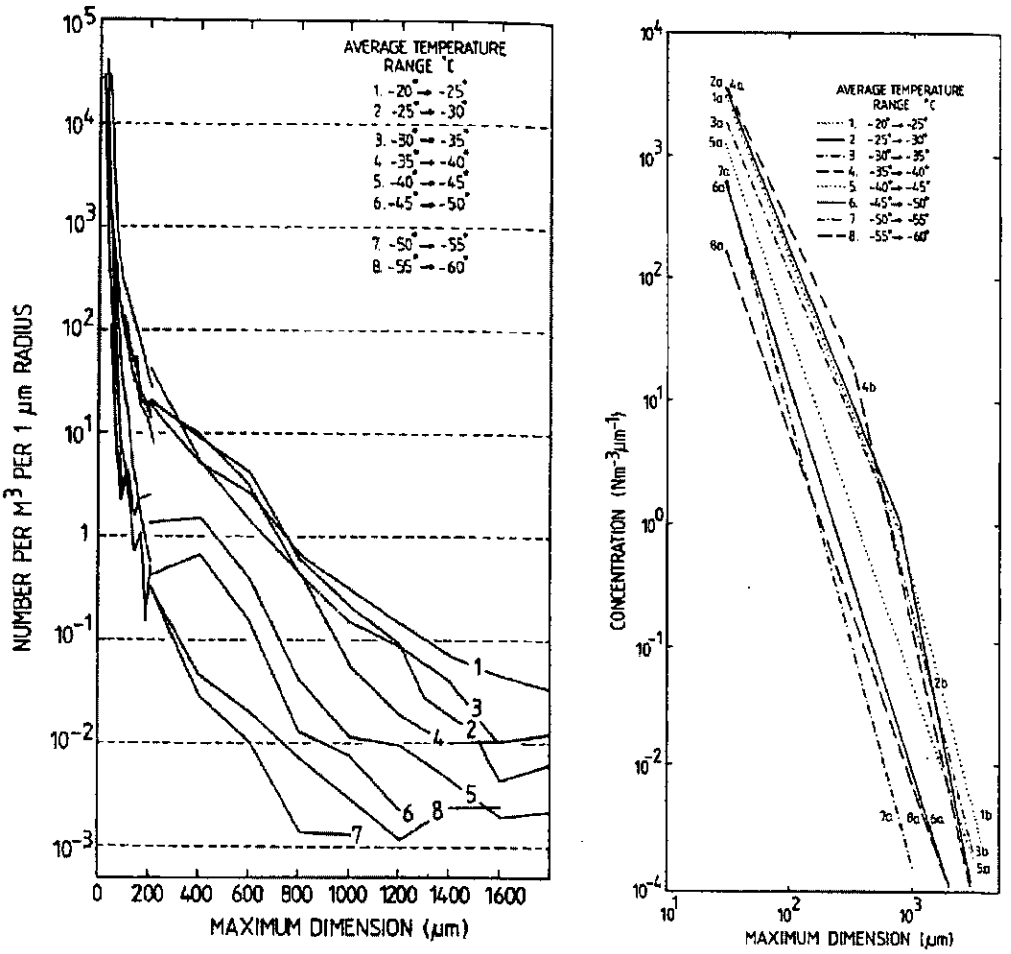

Figure 4.7: Left: Averaged measured size distributions for each temperature range; Right: Functions fitted to the average size distributions in each temperature range; both from Heymsfield and Platt [1984].

Platt's parameters for temperature bands 1–4 are reasonable, so I have accepted the authors values in these cases.

Table 4.1 shows the complete set of parameters for the fitted functions, with the B parameter changed for curves 5, 7, and 8, for the reasons given above. The other temperature-dependent parameter in equations 4.1 and 4.2 is A, and this may be calculated as follows:

$$A_1 = \frac{1}{\text{IWC}} \cdot \frac{N_{100}}{(100)^{B_1}} \tag{4.4}$$

and

$$A_2 = \frac{1}{\text{IWC}} \cdot \frac{N_{1000}}{(1000)^{B_2}} \tag{4.5}$$

Finally, the crystal dimension D_o, at which the two parts meet for each of the

Curve	T (°C)	$\overline{\text{IWC}}$ (gm^{-3})	N_{100} ($\text{m}^{-3}\ \mu\text{m}^{-1}$)	N_{1000} ($\text{m}^{-3}\ \mu\text{m}^{-1}$)
1	$-20 \rightarrow -25$	0.027	140	0.325
2	$-25 \rightarrow -30$	0.025	175	0.260
3	$-30 \rightarrow -35$	0.0175	130	0.240
4	$-35 \rightarrow -40$	0.0126	250	0.130
5	$-40 \rightarrow -45$	0.0034	25.5	0.017
6	$-45 \rightarrow -50$	0.0025	14.0	0.010
7	$-50 \rightarrow -55$	0.0018	7.00	0.00155
8	$-55 \rightarrow -60$	0.0009	5.02	0.00725

Curve	A_1 (g^{-1}m^3)	B_1	A_2 (g^{-1}m^3)	B_2	D_o (μm)
1	$6.84 * 10^8$	-2.56	$2.00 * 10^{12}$	-3.74	865
2	$7.33 * 10^8$	-2.51	$3.07 * 10^{14}$	-4.49	691
3	$1.95 * 10^8$	-2.21	$9.06 * 10^{12}$	-3.94	499
4	$7.54 * 10^8$	-2.29	$1.33 * 10^{14}$	-4.37	333
5	$1.69 * 10^{10}$	-3.18	–	–	–
6	$1.10 * 10^{10}$	-3.15	–	–	–
7	$7.93 * 10^{10}$	-3.65	–	–	–
8	$2.67 * 10^9$	-2.84	–	–	–

Table 4.1: Parameters for constructing ice crystal size distributions for frontal cirrus, from Heymsfield and Platt [1984], with modifications as described in the text.

curves 1–4, is given by

$$D_o = \left(\frac{A_2}{A_1}\right)^{\frac{1}{B_1 - B_2}} \tag{4.6}$$

The range of crystal sizes used in Heymsfield and Platt's study, and therefore the maximum range of validity of the fitted functions, is from 20 μm to 2600 μm. In practice I used the parameterisation as described above only up to a maximum dimension of 2 mm. The details of how the distribution was extended to include larger crystals are discussed in section 5.3.

Very Small Crystals

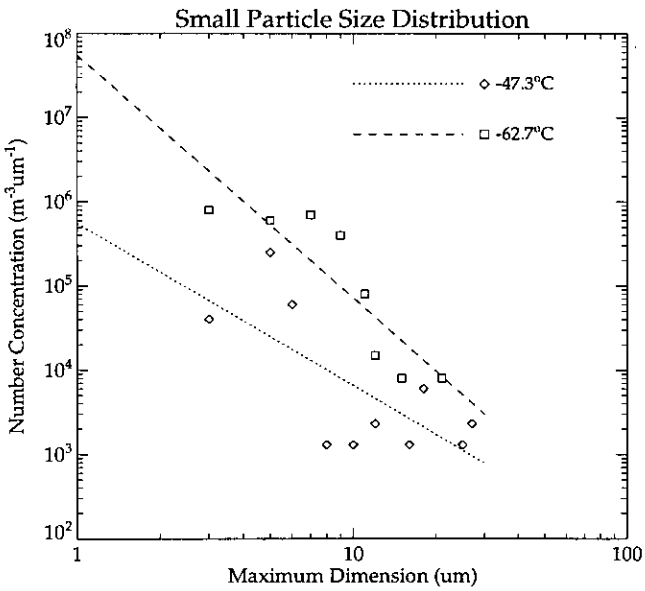

Figure 4.8: Concentrations for particles < 30 μm in size, after Platt *et al* [1989].

To represent ice crystals smaller than 20 μm, the results of Platt *et al* [1989] are used. Their study consists of a series of aircraft-based observations through frontal cirrus clouds over NW Missouri (40°N), during which they found high concentrations of such small crystals. The authors plot particle concentrations over the range 1 μm to 30 μm for two temperatures: -62.7°C and -47.3°C. These data are represented in figure 4.8 by the squares and diamonds respectively. For each temperature I have fitted a power-law function to the data of Platt *et al*, and these fits are represented by straight lines on the logarithmic axes of figure 4.8, with the dashed line fitted to the -62.7°C points, and the dotted line fitted to the -47.3°C points.

The spread of the data points means that the fit is subject to large uncertainties; in fact the authors state that the data points themselves are subject to large errors, varying from underestimates of order 2 to overestimates of order 2–5. Therefore only broad order-of-magnitude estimates are possible.

Therefore, in this study, the representation of small crystals in the size distribution is limited to just two points, one at 1 μm and one at 10 μm, with concentrations given approximately by the fitted functions. The two temperatures for which Platt *et al* provide data are matched with appropriate temperature bands corresponding to those used in the Heymsfield and Platt parameterisation, so $T > -50$°C is represented by the -47.3°C data; -55°C $> T > -60$°C is represented by the -62.7°C data; and concentrations in the -50°C $> T > -55$°C band are estimated by a logarithmic interpolation between the two sets of data. The resulting concentrations are shown in table 4.2. Then these two points are added to the start of the Heymsfield

and Platt parameterisation, which begin at 20 μm.

	$n(1\ \mu\text{m})$	$n(10\ \mu\text{m})$
$T > -50°\text{C}$	$10^6\ \text{m}^{-3}\ \mu\text{m}^{-1}$	$10^4\ \text{m}^{-3}\ \mu\text{m}^{-1}$
$-50°\text{C} > T > -55°\text{C}$	$10^7\ \text{m}^{-3}\ \mu\text{m}^{-1}$	$3 \times 10^4\ \text{m}^{-3}\ \mu\text{m}^{-1}$
$-55°\text{C} > T > -60°\text{C}$	$10^8\ \text{m}^{-3}\ \mu\text{m}^{-1}$	$10^5\ \text{m}^{-3}\ \mu\text{m}^{-1}$

Table 4.2: Concentrations of small frontal cirrus crystals, derived from Platt *et al* [1989].

The high concentrations of 1 μm crystals predicted by this data are relatively insignificant in terms of the effect they have on the cloud's extinction, as will be seen in section 5.3, because of the extremely steep reduction of the single-sphere scattering efficiency with decreasing size[7].

Very Large Crystals

Heymsfield and Platt's results are applied only as far as a maximum dimension of 2000 μm, but when the contribution of crystals of this size to the extinction coefficient is calculated[8] it is still found to be significant. Therefore it is desirable to extend the distribution to greater dimensions. There seems to be no information available about the concentrations of such large crystals. Heymsfield [1977] says that the largest crystals found are between 5 mm and 6 mm, but this is because concentrations at larger sizes are so low that finding one in the sampling volume becomes highly improbable. There is no real limit to the size of ice crystals in a cloud; while such crystals do fall faster, if updrafts are strong enough they will remain in the cloud [Peter Jonas, personal communication].

Therefore I extend the parameterisation up to a dimension at which there is negligible contribution to the extinction coefficient from larger crystals. This upper limit is chosen to be 6 mm; the method for determining this is described in section 5.3, where it is seen that the form of the distribution above 2 mm requires modification. Rather fortuitously, the maximum sphere radius that the Mie routine can cope with without crashing is at least 2 mm (as shown in section 3.2.1), which corresponds to a crystal maximum dimension just over 6 mm (for the plate rosette crystal defined in section 5.2), so no problems should be encountered here.

[7] At these sizes there is Rayleigh scattering, so from equation 3.26 the scattering efficiency $\xi_{cs} \propto r^4$, where r is the radius of the sphere.

[8] This will be done in section 5.3.

4.3.2 Crystal Habits

The crystals in a cirrus cloud occur in a variety of shapes, or 'habits'. However, Mie scattering theory only properly applies to spherical particles. Therefore the various crystal shapes are substituted in the size distribution by spheres which present an equivalent projected area to the radiation. To do this it is first necessary to know the relative abundances of each habit at a given temperature and size.

The types of habit and their relative abundance vary according to the type of cirrus in which they occur. In the case of frontal cirrus which I am considering here, the habits which are found may be classified as follows:

- Columns. These are prisms with bases which are regular hexagons. The diameter (i.e. the width of the base corner-to-corner) is less than the length. They may be hollow or solid.

- Bullets. These are hexagonal columns, but with one end tapering to a point. Various examples of both the bullet and column forms are documented by Magono and Lee [1966].

- Plates. These are generally hexagonal in shape, but vary in form between solid, stellar and dendritic (fern-like) types. The thickness (height) of the plate is less than the diameter of the base. Again, Magono and Lee [1966] present a wide range of examples.

- Bullet Rosettes. These are spatial forms, composed of several bullet crystals radiating from a common centre at which the tapered ends meet. The number of arms may vary from two to ten or sometimes more. Iaquinta *et al* [1995] provide a review of this crystal form.

- Side Planes. These are referred to frequently in the literature, but are only defined in Magono & Lee's paper [1966], as "columnar crystals with extended side planes". Their schematic diagram depicts a rosette of thin columns, with plate-like attachments along the axes of the arms. The microphotographs of the crystals show that the planes are like half hexagonal plates, attached by their longest side along the length of the columns. There appear to be two planes per column, one on each side.

- Radiating Assemblages of Plates. These are schematically represented by Magono & Lee [1966] as clusters of hexagonal plates joined at the centre along their edges. The microphotographs look as though the plates are joined at their points, and show that in some cases several plates join end to end to form extended arms.

- Aggregates. These are the largest crystals found in cirrus, and are haphazard clusters of several smaller crystal types. Any combination of habits may aggregate. Hobbs *et al* [1974] and Krupp [1991] provide some discussion of the aggregate form.

Another classification referred to in the literature is 'spatial'. This group includes any of the more complex radiating forms, such as the bullet rosettes and side planes, and is generally used where the exact nature of the crystal cannot be readily determined with the equipment available, such as in the results of Heymsfield *et al* [1990]. Often authors assume that such spatials are predominantly bullet rosettes, but it is more probable that they are a mixture of different habits, together with aggregates. The latter cannot be geometrically modelled, since they are completely irregular.

To deal with such indeterminate crystal shapes, their total abundance was divided half-and-half between bullet rosettes and 'plate rosettes', these being two idealised crystal forms which will be defined in section 5.2.

4.3.3 Habit Fractions

The relative abundances of the different habits within the cloud depend on the temperature, the size of the crystals, and the amount of convection (i.e. the updraught velocities). In the discussion below I consider separately each of four temperature bands, which appear to characterise distinct temperature regimes of crystal structure.

In certain papers on cirrus cloud microphysics, such as Heymsfield and Platt [1984], a distinction is made between the stable and convective regions of frontal clouds. This is not large-scale convection in the cumulonimbal sense, but refers to convective cells of cirrus, such as the cirrus uncinus cloud [Heymsfield 1975], or convective cells within a cirrus layer [Heymsfield 1977]. Most studies include samples of both the convective and the stable parts of the cloud, and only some discriminate between the two. The contents of this section are derived from general data for frontal cirrus, and those which are specific to a particular type of cloud are highlighted to allow the construction of two separate tables of data where possible. However, the majority of the results presented in this chapter which concern frontal cirrus are based upon the stable form. In section 5.5.2 some consideration will be given to the expected differences in the radiative properties of the stable and convective forms of frontal cirrus.

When a study of cirrus crystal shape is made, the reliability of the results depends on the technique used in a given study to identify the crystal shapes. The

instruments which are used in the majority of experiments described in the literature are as follows:

- Replicators. Such devices are described in detail by Sassen *et al* [1994]. They basically consist of a glass slide coated with a viscous transparent oil, which is introduced into the airstream from an aircraft flying through a cirrus cloud. The ice crystals impact with and adhere to the slide, which is then stored in a dry, low temperature environment until the crystals can be microphotographed. This allows almost unambiguous identification.

- 2D Probes. As described in detail by Bennetts and Ouldridge [1984], the 2D probe consists of an array of photodiodes illuminated by a laser source. The diodes measure the shadowing effect of ice crystals passing through the probe. The resolution of such images is restricted to the spacing between diodes which is typically about 25 μm [Heymsfield *et al* 1990, Bennetts and Ouldridge 1984].

- Holography. In this technique, cloudy air passes through a chamber mounted on an aircraft, and diffuse laser light is shone through the air onto a photographic film. Interference between the undisturbed light and that scattered by the ice crystals causes the hologram to form on the film. Objects as small as 10 μm may be detected by this method, but the shape is only resolvable for objects larger than 30 μm [Bennetts and Ouldridge 1984].

The remainder of this section is divided into four parts, representing the four temperature bands. In each part there is a review of the literature on crystal habits pertaining to that temperature range, and a tabulated set of habit fractions based on the review. The review is structured in each case so that the most reliable habit identifications, according to the instrumentation used by the authors, are presented first.

The temperature ranges studied by other authors do not always fit conveniently into the arbitrary divisions made here, so in some cases the results discussed in a given section may not be contained entirely within the corresponding temperature band.

Temperature: $T > -25°C$

The replicator data of Heymsfield [1977] is the most specific to this temperature range, giving habits between $-17°C$ and $-22°C$. These are categorised as bullet rosettes, capped columns, and plates. At higher temperatures there are higher plate concentrations. Heymsfield also says that no aggregates are found until much

higher temperatures. However, this does not tally with the work of Krupp [1991], whose holographic data for $-26°C$ suggests aggregates are prevalent, and that the simple shapes only occur at small sizes (< 50 μm). Krupp found few plates, and they were very small.

Heymsfield and Platt's [1984] replicator data for the temperature range $-15°C$ to $-40°C$ is relevant to this section. At these temperatures they do not discriminate between the convective and stable regions of clouds, as they do elsewhere. They found mostly the indistinct 'spatial' forms described in section 4.3.2 above. There were also some columns and plates.

The above literature summary is expressed as approximate habit fractions in table 4.3.

Stable *and* Convective Cirrus	
Size	Approximate Habit Fractions
$D < 50$ μm	50% bullet rosettes, 30% columns, 20% plates
50 μm$< D < 200$ μm	40% bullet rosettes, 40% spatial, 20% columns
$D > 200$ μm	100% aggregates/spatial

Table 4.3: Habit fractions for frontal cirrus at $T > -25°C$.

Temperature: $-25°C > T > -40°C$

Krupp [1991] analysed holograms of cirrus to determine habits. This method allows precise identification of the crystals but is hampered by the limited volume which can be analysed over a long period of time (in this case 2.8 litres in four weeks). His measurements are at three different temperatures spanning the $-25°C > T > -40°C$ range. I have used the highest and lowest temperatures as supplementary data for the adjoining temperature ranges, and the middle temperature to characterise the present range.

At the middle temperature, $-34°C$, there was a large variety of habits, but specifically bullet rosettes were present, both singly and stuck together, as well as the simpler crystal forms, although no plates were found. The largest crystal was about 600 μm. At all temperatures Krupp found that nearly all the crystals larger than 200 μm were combinations of smaller crystals.

The same replicator data from Heymsfield and Platt [1984] applies again here, that is mostly spatial forms, with some columns and plates. Their spatials possibly correspond to Krupp's irregular particles. This broadly supports Krupp's data and suggests that perhaps there are more than a negligible number of plates.

The replicator data of Heymsfield [1977] for temperatures below $-22°C$ apply to

Stable Cirrus	
Size	Approximate Habit Fractions
$D < 200$ μm	50% bullet rosettes, 35% columns, 15% plates
$D > 200$ μm	100% aggregates
Convective Cirrus	
Size	Approximate Habit Fractions
$D < 200$ μm	60% bullet rosettes, 40% columns
$D > 200$ μm	100% aggregate

Table 4.4: Habit fractions for frontal cirrus at $-25°C > T > -40°C$.

this temperature range, and are dependent on the updraught velocity (i.e. whether the cloud is convective or stable). For stable cloud Heymsfield says columns and thick plates are the most common forms at this temperature – although this contradicts the general findings from the other papers, it does suggest that these simple forms are not negligible. For convective cirrus he has bullet rosettes and hollow columns as the primary forms.

Heymsfield's [1975] replicator data are based on studies of a number of clouds, the majority of which display some convection. He found that the primary crystal forms were, in decreasing order of abundance, bullet rosettes, bullets, columns, and plates.

Finally, the 2D probe data of Heymsfield *et al* [1990], which can only reliably resolve crystal habits at sizes above 150 μm, has 20% of the crystals as bullet rosettes, with the rest as other types of undefined spatial, but no simple columns or plates. Some of these spatials will probably also be rosettes which could not be properly resolved as such. Above 500 μm, all the crystals are aggregates, and this is borne out by Sassen *et al* [1989] who found that all crystals larger than 200 μm were spatial forms.

The habit fractions deduced from the above discussion are presented in table 4.4.

Temperature: $-40°C > T > -50°C$

This temperature range is characterised by a change in the general form of habit from single crystalline forms at lower temperatures to more complex spatial forms at higher temperatures. This is noted by Heymsfield and Platt [1984], and also by Sassen *et al* [1989], who place the transition at about $-45°C$. In addition Platt and Dilley [1981] found that there was an abrupt change in the ratio of backscatter to extinction of their 0.694 μm lidar measurements, which they attribute to the change in habit noted above.

Arnott *et al* [1994] present replicator data which show that most of the particles larger than 200 μm are bullet rosettes, which ties in with Heymsfield and Platt's [1984] findings that the convective regions of frontal cirrus clouds contain mostly spatial forms at this temperature, and suggests that the data of Arnott *et al* was taken from convective regions. Conversely, for stable clouds Heymsfield and Platt found predominantly hollow columns. The majority of the particles smaller than 50 μm, according to Arnott *et al*, are simple hexagonal plates.

Krupp's [1991] holographic data at $-39°$C shows that most of the particles were irregular, seeming to be composed of several columnar crystals. Possibly this means that a bullet rosette model will suffice for such crystals. There were also some individual columns and bullets. The largest crystal was 230 μm.

The 2D probe results from Heymsfield *et al* [1990] are limited by the instrument's resolution to dimensions greater than 150 μm, where there were spatials and columns present in uncertain proportions. Above 225 μm they state more specifically that there were about 80% bullet rosettes and 20% other spatials. Particles larger than 500 μm were mostly aggregates.

The habit fractions derived from the above data are given in table 4.5.

Stable Cirrus	
Size	Approximate Habit Fractions
$D < 50$ μm	50% plates, 50% columns
50 μm$< D < 200$ μm	60% columns, 20% bullet rosettes, 20% plates
200 μm$< D < 500$ μm	60% bullet rosettes, 40% columns
$D > 500$ μm	100% aggregate/spatials
Convective Cirrus	
Size	Approximate Habit Fractions
$D < 50$ μm	75% plates, 25% columns
50 μm$< D < 200$ μm	50% bullet rosettes, 30% columns, 20% plates
200 μm$< D < 500$ μm	80% bullet rosettes, 20% other spatials
$D > 500$ μm	100% aggregate/spatials

Table 4.5: Habit fractions for frontal cirrus at $-40°$C$> T > -50°$C.

Temperature: $T < -50°$C

The only replicator data available for such low temperatures comes from Heymsfield and Platt [1984], who find that the crystals are mostly columns, with some plates. There are generally fewer plates at sizes above about 200 μm. These results apply equally to both the convective and stable regions of cirrus.

Other available data come from the low resolution 2D probes, and so are restricted to crystal dimensions greater than 150 μm. At these sizes, Heymsfield *et al* [1990] found evidence of spatial crystals, as well as columns and plates. At sizes greater than 225 μm there were roughly equal proportions of bullet rosettes, of other types of spatial, and of columns. However, Sassen *et al* [1989] found mostly columns at such sizes from their 2D probe data. Based on this, and from the replicator data, I expect there to be a large proportion of columns even at relatively large sizes. However Heymsfield *et al* [1990] are clear that at above 500 μm most of the crystals are aggregates, with clearly defined multiple centres of mass.

The habit fraction summary for this temperature range is therefore as given in table 4.6.

Stable *and* Convective Cirrus	
Size	Approximate Habit Fractions
$D < 200$ μm	90% columns, 10% plates
200 μm$< D <$ 500 μm	50% columns, 20% bullet rosettes 20% other spatials, 10% plates
$D > 500$ μm	80% aggregates, 20% bullet rosettes

Table 4.6: Habit fractions for frontal cirrus at $T < -50°$C.

4.4 Microphysics of Tropical Cirrus

The work described in the previous section has provided a description of the microphysical structure of frontal cirrus cloud, by the evaluation of a size distribution, and the approximation of the habit distribution. The same procedure is now followed in this section to describe the microphysics of tropical cirrus.

The predominant cirrus type produced in tropical regions is that which originates from the anvils of large-scale cumulonimbus complexes as described in section 4.2.1. There seems to be no reason to distinguish the microphysical properties of cirrus produced by tropical convective complexes from those of continental and maritime cumulonimbus anvil cirrus at mid- and high-latitudes. Heymsfield's [1993] general discussion of anvil cirrus makes no such distinction between the types. There are differences in the observed size distributions, but these may well be due to the difference in temperature, since tropical cumulonimbus reaches to a higher tropopause, and has a correspondingly colder anvil, than its mid-latitudinal equivalent. In both cases the cirrus is produced in the same way, the crystals growing on condensation nuclei in the moist air which has been forced up into the cold air by the convective turret. Knollenberg *et al* [1993] found much larger crystals in mid-latitudinal cirrus

(up to 1 mm) than in tropical cirrus, but the mid-latitudinal anvil is lower and warmer (−53°C to −57°C compared with −72°C to −85°C). The overall number densities are approximately the same for both. In addition, Knollenberg *et al* [1982] found particles as large as 1 mm in a tropical anvil at −68°C to −78°C. Although this latter evidence is from a small sample, while a larger sample in the same paper finds a maximum crystal dimension of 150 μm, it serves to demonstrate that the differences between individual studies of tropical cirrus can be as great as the differences between tropical and mid-latitudinal anvil cirrus.

Similarly, there is evidence of tropical cirrus which is *not* related to convective storms, and which has characteristics more relevant to frontal cirrus than convective anvils. This is known as *in situ* cirrus, which has formed in the same location it is found because the atmospheric conditions are suitable at that point, as opposed to the convective cirrus which has begun as an anvil and then migrated to form a layer. Heymsfield [1986a] describes the former type over the Marshall Islands, noting that there is no convective activity whatsoever in the area, which strongly suggests that the cloud has formed *in situ*. The cloud is uniformly stratiform, with no cellular structure. Knollenberg *et al* [1982] report that the occurrences of cumulonimbus anvils which they studied were always accompanied by at least a thin shield of 'deck' cirrus at heights of 12 km to 15 km, well below the tropopause and the anvil. This deck cirrus has a maximum observed crystal size of 1 mm, while the anvil above it is the one described in the previous paragraph, with a maximum crystal dimension of 150 μm. Griffith *et al* [1980] also appear to find both types of tropical cirrus, referring to clouds ranging "from a very tenuous, patchy layer to a dense cirrus anvil outflow from an active cumulonimbus cell". The lack of a reference to any nearby convection in the case of the patchy layer perhaps suggests that it formed *in situ*.

The one major difference between tropical and non-tropical anvil cirrus is its temporal extent. Since convective activity is more or less continuous in the tropics, the cirrus which forms is often replenished by new anvils, whereas the continental storms at mid-latitudes are short-lived phenomena. In the same way, dispersed anvil cirrus from convective storms will link up in the tropics to create very wide sheets. Horizontal extents for individual cumulonimbus events range from about 13 km for Bennetts and Ouldridge's [1984] example to about 150 km for Heymsfield's [1986b] severe thunderstorm. By way of contrast, the *in situ* cloud observed by Heymsfield [1986a] extends for over 350 km, although it is very thin (IWC $\sim 10^{-4}\mathrm{gm}^{-3}$).

4.4.1 Anvil Cirrus Size Distributions

Tropical Anvils

The most comprehensive study of the microphysics of tropical anvils is that of Knollenberg *et al* [1993], who present size distributions measured in the anvils of tropical cumulonimbus complexes over Darwin, Australia. Darwin is at a latitude of about 12°S, and the clouds investigated in the study were found between 10°S and 20°S. This region is in the tropical convective region associated with the Asian monsoon as described in section 4.2.1. The authors present results corresponding to three separate aircraft passes through anvils on different dates in January and February 1987. The ice water content of the measurements varies along the path of the flight as the aircraft passes in and out of cloud, and the size distribution taken is one which corresponds to the region of highest IWC (called 'strong' cloud), because the data for such regions is generally more complete than in the weaker cloud regions. Conditions for each data set are shown in table 4.7. Note that the ice water contents tabulated are maximum values. The IWC varies rapidly throughout the strong cloud regions themselves and so the average IWC value will be somewhat lower.

Flight no.	Date	Temperature	Altitude	Max. IWC
1	31/1/87	$-78°C \rightarrow -83°C$	15.5 km	0.06 gm^{-3}
2	4/2/87	$-72°C$	14.5 km	0.04 gm^{-3}
3	8/2/87	$-85°C$	17.5 km	0.05 gm^{-3}

Table 4.7: Cirrus conditions for the tropical observations of Knollenberg *et al* [1993].

During the first flight, the aircraft passed through a distinct cell of strong cloud which was about 120 km across. The second flight had an entire cloud path of about 500 km, for most of which the IWC was higher than about $3 \times 10^{-3} gm^{-3}$. The peak values, above $10^{-2} gm^{-3}$, comprised about half the total path, $\sim$ 250 km. In the third flight, the peak IWC values were confined to a small region, while the size distribution is based on the measurements over a larger region for which the average ice water content was of order $2 \times 10^{-3} gm^{-3}$. Knollenberg *et al* do not quote the path length of this flight, but the flight path is marked on an infra-red satellite image, and appears to follow the meridian for about 10% of the distance between the 10°S and 20°S lines of latitude. If the Earth is treated a sphere of radius 6371 km, then the flight path through the strong cloud region was about 110 km, similar to the first flight.

The size distribution data were extracted by eye from the distributions plotted

by Knollenberg *et al* [1993]. The raw data points thus extracted are shown in figure 4.9, with a different symbol for each flight: diamonds for flight 1, triangles for flight 2 and squares for flight 3.

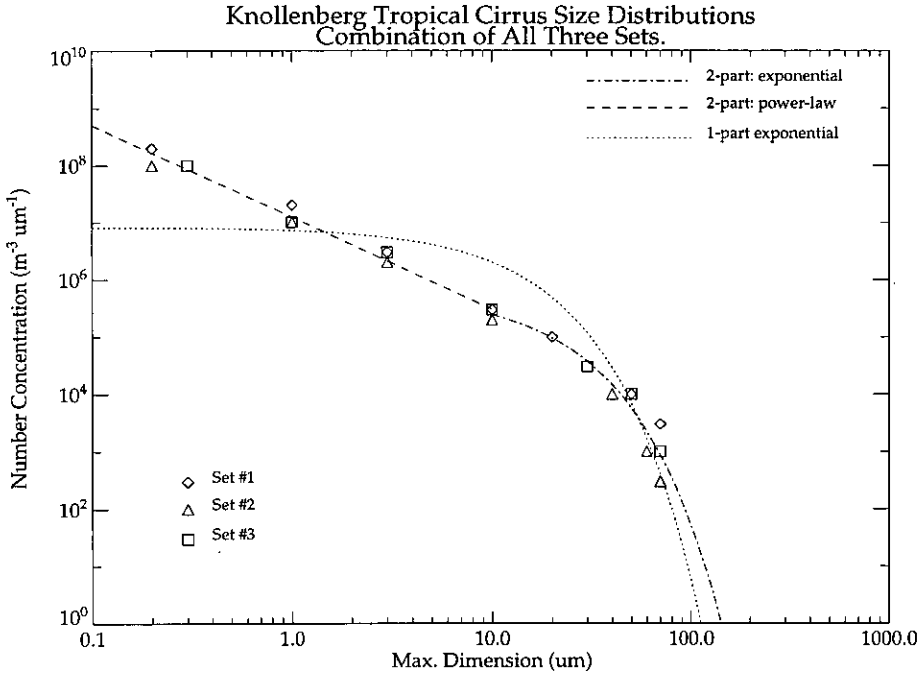

Figure 4.9: Combined size distributions for tropical cirrus at −80°C, from Knollenberg *et al* [1993].

The three separate data sets are not sufficiently distinct to allow their form to be parameterised in the way that the results of Heymsfield and Platt [1984] were for frontal cirrus. Although each set displays a distinctive trend at high maximum dimension (D), this behaviour is unrelated to the temperature of the cloud in each case, and the ice water content does not vary enough between sets to be considered a parameter. It is more likely that the differences between the sets are due to the particular atmospheric conditions which prevailed at the time of the observations, rather than being rigidly dependent on temperature and IWC. This being the case, I have combined the measurements from all three flights into a single data set, which is used as the basis of a generalised size distribution.

The distribution is formed by fitting a functional form to the combined data set. A simple power law distribution (a straight line on figure 4.9) was ruled out because the observed concentrations clearly drop off more quickly than this at high D. An exponential fit would be more appropriate, but a single exponential function fitted to the data gives a very poor fit (shown by the dotted line), and it seems clear that the data at low D *does* follow a power law. Therefore I opt for a two-part fit, with a power law up to $D = 10$ μm (the dashed line in figure 4.9), and an exponential

at larger dimensions (the dot-dashed line). The equations for the functions, fitted by linear regression, are:

$$\begin{aligned} N &= 2.608 \times 10^3 \times D^{-1.613} && \text{for } D < 10\ \mu\text{m} \\ N &= 6.267 \times 10^{11} \times \exp(-9.401 \times 10^4 \times D) && \text{for } D > 10\ \mu\text{m} \end{aligned} \tag{4.7}$$

Knollenberg *et al* [1993] record no crystals larger than 100 μm, perhaps because above such sizes the concentrations were too low for their instrumentation to register. The studies of Knollenberg *et al* [1982] of tropical cirrus over Panama reveal maximum crystal sizes of 1 mm, suggesting that crystals much larger than 100 μm may have been present in the clouds observed by Knollenberg *et al* [1993]. To try to account for this possibility I extrapolated the exponential part of the distribution beyond 100 μm. However, it will be shown in section 5.4 that the contribution of crystals larger than 100 μm to the total scattering and extinction coefficients is small.

The temperature range of the individual measurements was −72°C to −85°C, which gives a rough range of validity for the generalised distribution. This corresponds to temperatures near the tropical tropopause, so the combined size distribution defined by equations 4.7 is appropriate for high tropical convective cirrus. The other form of tropical cirrus mentioned in section 4.4, that which is formed *in situ*, might have been considered analogous to the mid-latitudinal frontal cirrus and parameterised accordingly for temperatures below ∼ −60°C. However, such a method was not used in the present study, and so the results presented in this thesis for tropical cirrus apply to the convective form only.

Extratropical Anvils

It was stated in section 4.4 that tropical convective cirrus would not be distinguished in this study from its extratropical equivalent. Therefore published data on the microphysics of cumulonimbus anvils at middle and high latitudes may also be collected to form a supplementary set of statistics for convective cirrus. The extratropical tropopause is warmer than at the equator (as shown in figure 5.26 later in this chapter), so the data assembled may be representative of cirrus found lower in the tropical troposphere than that already discussed.

Microphysical data for extratropical cumulonimbus anvils were obtained from two independent sources. Knollenberg *et al* [1993] have two size distributions from separate flights on consecutive days through cumulonimbus anvils over Arizona (35°N)[9], at temperatures from −53°C to −57°C; while Heymsfield [1986b] presents

[9] Knollenberg *et al* [1993] refer to these clouds as *continental* cumulonimbus, meaning that they are associated with a large continental landmass, as opposed to the Darwin measurements which are associated with the ocean north of Australia.

size distributions for two altitudes, 8.0 km and 9.3 km, through a severe thunderstorm over Montana (45°N).

The two Knollenberg *et al* [1993] distributions, being the coldest of the above examples, are most likely to be representative of tropical anvils at lower altitudes. Each distribution is at roughly the same temperature, −55°C, so data were extracted by eye from each plot and combined into one set. The resulting superset of points is displayed as the diamonds and triangles in figure 4.10. The familiar power law distribution is observed at low D, but an attempt to fit an exponential to the high-D points, shown by the dotted line, is not good. The solid line representing a power law function is a better fit but fails to represent the obvious exponential component of the data. The observations of Heymsfield [1986b] for maximum dimensions above 1 mm indicate a clear exponential distribution, and so it seems reasonable that as the distribution changes from power law to exponential with increasing size, it must pass through a transitory stage where both functional forms are evident. This is represented in figure 4.11, where the dotted line shows a curve composed in equal logarithmic parts of the power law and exponential best fit functions.

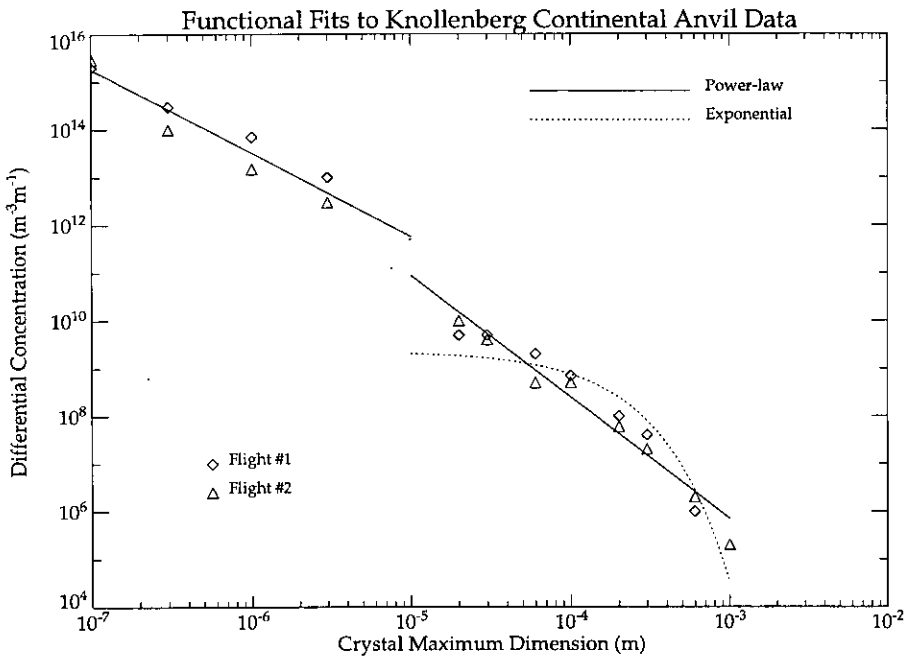

Figure 4.10: Combined size distributions for continental cirrus at −55°C, from Knollenberg *et al* [1993].

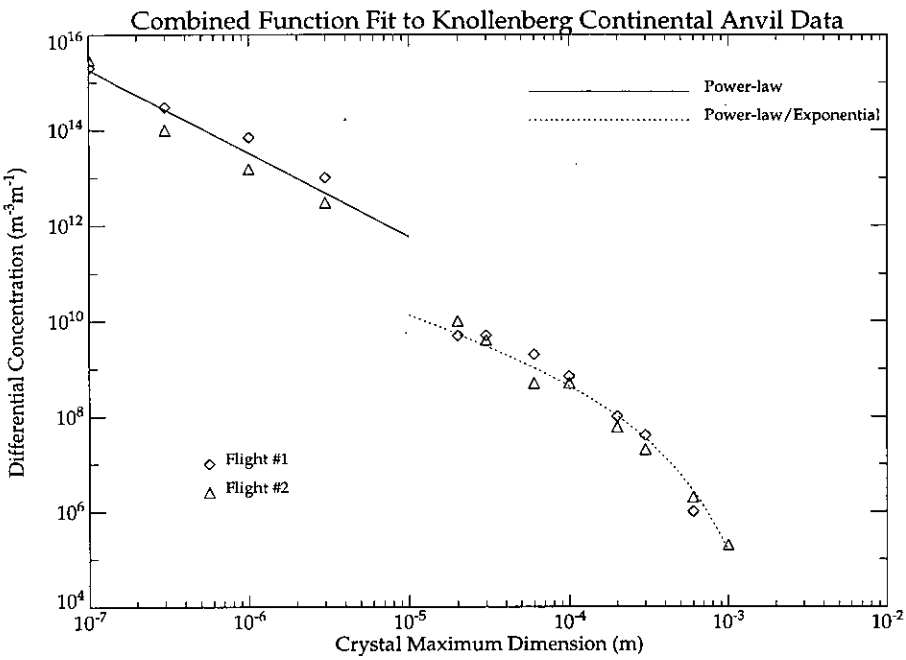

Figure 4.11: As previous figure, with a combined exponential/power law function fitted at large crystal sizes.

Therefore the function fitted to the data is represented by the two equations:

$$\begin{aligned} N &= 1.033 \times 10^3 \times D^{-1.750} && \text{for } D < 10\ \mu\text{m} \\ N &= [3.545 \times 10^7 \times D^{-2.552} \times \exp(-1.120 \times 10^4 \times D)]^{1/2} && \text{for } D > 10\ \mu\text{m} \end{aligned} \tag{4.8}$$

To recap this section, two size distributions have been defined in functional forms represented by the equation pairs 4.7 and 4.8. The former pair are used to simulate the size distribution of a 'cold' cumulonimbus anvil of temperature $\sim -80°$C, and the latter pair to simulate a 'warm' anvil, at a temperature of $\sim -55°$C. In practice, for a given situation, the distribution will be selected which is closest in temperature to the temperature of the cloud being considered.

4.4.2 Tropical Crystal Habits

Having obtained size distributions for the tropical cumulonimbus anvil, the habit fractions must now be approximated. The set of crystal habits which occur in anvils is the same as that defined in sections 4.3.2 for frontal cirrus, except that there is an additional form, the *trigonal plate*. This is defined by Yamashita [1973] as an ice crystal plate with the basal face of a regular triangle, and such habits are observed by Heymsfield [1986a].

The information available concerning crystal habits for anvil cirrus is again divided into the tropical and mid-latitudinal cases, and as before I shall make no dis-

tinction between these types except on the basis of temperature. In the same way as was done for frontal cirrus in section 4.3.3, the following description is a review of the available literature on anvil habits, separated into two parts corresponding to the 'cold' and 'warm' anvils defined in the previous section. The reviewed work is presented in each case in order of the quality of the habit identification, according to the instrumentation used by the researchers. Finally the information is grouped according to temperature and presented as a set of approximate habit fractions in table 4.8.

'Cold' Anvils

The tropical cirrus studied is all at temperatures below −80°C. The only replicator data available for this temperature come from Heymsfield [1986a], who studied thin tropical cirrus, although he claims it is likely to have formed *in situ* rather than having spread from a convective turret. The temperature is a fairly uniform −83°C, and the habits are divided half-and-half between columns and trigonal plates, with dimensions between 5 μm and 50 μm. There are also a few bullet rosettes and hexagonal plates. Heymsfield notes that no trigonal plates occur naturally above −65°C. Although at the beginning of section 4.4 it was noted that *in situ* cirrus forms in a very different way to anvil cirrus, nevertheless the appearance of the trigonal form seems to be primarily a function of temperature, and it is therefore likely that they will also be found in cold anvils.

Knollenberg *et al* [1982] provide results for stratospheric cirrus produced by tropical thunderstorms, for temperatures about −80°C. Their data are from a 2D probe, and so the limited resolution means that only particles larger than about 200 μm can be resolved. The primary habits are column aggregates and rosettes at sizes of a few hundred microns, and the larger particles, up to 1000 μm, are aggregates of intact single crystals, rather than fragments.

Knollenberg *et al* [1993] also examine tropical cirrus with a 2D probe, at temperatures below −80°C, but find no particles larger than 100 μm and therefore cannot resolve their habit.

From the first two references I infer that the column/trigonal mix for small particles is typical of crystal formation at these temperatures, whereas the larger rosettes are more specific to convective systems.

'Warm' Anvils

For habit information at warmer temperatures I reverted to extratropical anvil observations. Bennetts and Ouldridge [1984] present holographic data for a maritime cumulonimbus anvil, at temperatures between −20°C and −32°C. Particles larger

than 30 μm could be resolved, which the authors found to be either columns or aggregates of columns. They use the bullet rosette as a model for these aggregates.

Knollenberg *et al*'s [1993] 2D probe data for temperatures about $-55°C$ show that for particles larger than 100 μm, the majority appear to be plates of low aspect ratio[10], with limited numbers of larger, more complex forms.

Finally, Heymsfield [1986b] also presents 2D probe data, between $-25°C$ and $-36°C$. Habit assignment was limited to particles larger than 1500 μm, of which the majority were spatial forms, with some columns and plates also present. All the particles he observed that were larger than 3000 μm were aggregates.

Approximation of Habit Fractions

Table 4.8 represents the combination of the various sources of information reviewed above. There are large spaces between the temperature ranges covered by the papers discussed where there is no information available. In the case of temperatures between $-36°C$ and $-55°C$ I have chosen $-45°C$ as a natural dividing point, since it was seen in section 4.3.3 that with the frontal cirrus this temperature corresponds to a sudden shift in the general habit type.

The primary characteristic of the lowest temperature habits is the emergence of the trigonal form, and given that these do not occur naturally above $-65°C$, a dividing point of $-70°C$ seems sensible. This is also an appropriate dividing point between the cold and warm size distributions. It is difficult to reconcile the apparent abundance of plates larger than 100 μm found at $-55°C$ by Knollenberg *et al* [1993] with the finding of Knollenberg *et al* [1982] that at $-80°C$ the particles larger than 200 μm are primarily spatial forms. In both cases these conclusions are drawn from the rather vague images obtained from a 2D probe, and given the weight of evidence already presented in previous sections that larger particles tend to be complex spatial forms, I have biased the $-55°C$ habits to contain more spatial forms than Knollenberg *et al* [1993] suggest.

4.5 Chapter Summary

The review which has been presented in this chapter has provided a comprehensive set of statistics on the structure of various types of cirrus cloud. Using these data it is now possible to reconstruct, for a given temperature (and ice water content), a model of the microphysical form of a cirrus cloud. There is great variation between the individual clouds from which the data are garnered, and so the description presented here is not expected to accurately represent any one particular cloud.

[10] The ratio of depth to width.

$-20°C > T > -45°C$	
Size	Approximate Habit Fractions
$D < 1000$ μm	50% bullet rosettes, 50% columns
1000 μm$< D < 3000$ μm	90% spatials, 10% columns
$D > 3000$ μm	100% aggregates
$-45°C > T > -70°C$	
Size	Approximate Habit Fractions
$D < 1000$ μm	50% plates, 50% spatials
$D > 1000$ μm	20% plates, 80% spatials
$T < -70°C$	
Size	Approximate Habit Fractions
$D < 100$ μm	50% trigonal plates, 50% columns
$D > 100$ μm	100% spatials

Table 4.8: Habit fractions for convective cirrus.

However, it does represent a set of the typical characteristics of cirrus clouds of each type and at each temperature, and will therefore provide a reasonable basis upon which to build a simulation of the scattering effect of cirrus.

There now remains a gap between the idealised scattering model of chapter 3, and the less than ideal structure of the real cirrus clouds that have been described. The next chapter is an attempt to bridge that gap, and to incorporate the scattering due to cirrus into the forward model.

Chapter 5

Cirrus Simulation

5.1 Introduction

The techniques for modelling scattering which were developed in chapter 3 are applicable only to spherical particles. In chapter 4 the microphysical structure of cirrus cloud was investigated and it was found that cirrus crystals are highly non-spherical. Therefore in this chapter a method is developed to convert the cirrus crystal shapes into spheres with approximately equivalent scattering properties. Such a conversion is difficult to achieve effectively. The method used in this study was to estimate the likely geometrical forms of the crystals, and calculate the projected area which such shapes present to a plane wave of radiation. Then a sphere of the same projected area is used to represent the more complex crystal, in the hope that the extinction coefficient will be of the same order. The validity of such an approximation may be assessed by comparison with the methods of other authors.

A number of authors have contented themselves with the direct use of spheres in place of the crystals in a distribution, for example Wu [1987], Weinman [1988], Vivekanandan *et al* [1991], Matrosov *et al* [1992] and Intrieri *et al* [1993]. In most cases a standard functional form is used for the size distribution of the crystals, and this size is used as the diameter of the sphere. Intrieri *et al* [1993] claim that the uncertainty in the actual shapes of cirrus crystals means that a more complicated theory would probably not be any more appropriate for the modelling of their scattering properties. Their observations in the microwave and infrared, used in conjunction with a simple sphere model for scattering, allowed them to estimate an effective radius[1] for a cirrus cloud which compared well with the value measured *in situ*.

A higher level of complexity is the use of equivalent spheres to represent the actual crystal shapes, by replacing each crystal with a sphere of either equal volume

[1] *Effective radius* is defined as the mean particle volume divided by the mean particle projected area.

or equal projected area. The latter method is the one I have used, and is also used by Wielicki *et al* [1990] and by Sun and Shine [1994], although in both cases in the visible and infrared only. The equal volume method has been used by Mugnai and Smith [1988] and by Muller *et al* [1994] in the microwave.

There are ways of exactly modelling scattering by geometrically complex ice crystals, for example the infrared and visible methods for hexagonal columns described by Takano and Liou [1989], or that for bullet rosettes in the visible given by Iaquinta and Personne [1992] and Iaquinta *et al* [1995]. In addition, an approximate method for modelling the microwave scattering properties of cirrus crystals is that given by Evans and Stephens [1995a], which is described in detail in section 5.6. However, it is not clear that the idealised shapes which are used for these models are realistic. As has been shown, naturally-occurring forms are often extremely irregular, as a result of the aggregation of simple crystal forms into larger crystals. Significantly, these larger particles are those that cause the majority of the extinction, as will be demonstrated in section 5.3.

Pollack and Cuzzi [1980] provide a straightforward summary of the scattering properties of non-spherical particles which are of a similar size to the wavelength. They define a fixed size parameter[2] χ_o which divides two regimes of scattering behaviour. The value of χ_o depends on the shape of the particles, and must be determined by experimentation, but typically $\chi_o \simeq 5$ (corresponding to spheres of diameter between 0.8 mm and 2.4 mm at EOS MLS frequencies). For particles with $\chi < \chi_o$, they find that all the scattering properties of non-spherical particles may be well represented by *equivalent-volume* spheres. For large particles with $\chi > \chi_o$, the absorption is still well represented by equivalent-volume spheres, but for the scattering part equivalent-area spheres give better results. It is clear from figure 3.1 that for ice at microwave frequencies, the scattering efficiency comprises the major part of the extinction efficiency. Pollack and Cuzzi find that the phase function is well represented by the equivalent-volume spheres only at small scattering angles ($< 60°$); for large angles the observed phase function deviates considerably from that predicted by Mie theory. This last point reflects similar findings in the infrared studies cited above. In addition, Evans & Stephens [1995a] note that scattering from non-spherical crystals leads to polarisation of the scattered light, which is not represented by an equivalent-spheres method.

If Mie theory is to be used, it appears from the above review that in most cases the best way of treating cirrus crystals is to convert each to a sphere of equal volume, although the equivalent-area method is valid for the scattering part of large crystals, and indeed in most cases the extinction is dominated by scattering from the largest

[2] As defined in section 3.2.

crystals in the cloud. The equivalent-area approach was naïvely adopted at an early stage of the research, and it has not been modified. Therefore sensitivity tests were required to assess the likely difference in the results between the methods. These are described in section 5.5.

Although the equivalent-area method is crude, a more rigorous modelling of the scattering properties of irregular crystals might not be justified given the wide variations in shape which occur in nature. My method uses idealised crystal shapes, but it is hoped that their projected areas will act as best estimates for the projected areas of the natural crystals they represent. A limitation of this method is that the results are highly dependent on the relative concentrations of crystals of each shape or *habit*. The sources of information which were used in sections 4.3.3 and 4.4.2 to estimate these habit proportions are vague and often contradictory owing to the experimental difficulty of accurately identifying crystal habits. The proportions chosen are compromises between the various data sources according to their relative reliability, and as such are subject to large uncertainties.

In the next section the process of converting the complex cirrus crystal shapes into equivalent-area spheres is described in detail, and then in sections 5.3 and 5.4, the results are combined with the microphysical data from chapter 4 to produce equivalent-sphere distributions for frontal and tropical cirrus, which may be operated on by the scattering model of chapter 3. In section 5.5, the sensitivity of the calculated scattering properties to variations in uncertain parameters is investigated, and then in section 5.6 the model results are compared with those produced by the more complex methods of Evans and Stephens [1995a], in order to determine the suitability of the assumptions which have been made. Finally, in section 5.7, I present a review of average cirrus statistics and use them to create a set of parameters which can be used as inputs to the cirrus simulation to represent a 'typical' cirrus cloud for each of three latitude bands.

5.2 Representation of Crystal Habits as Equivalent Spheres

The maximum crystal dimension distributions which were defined in chapter 4 have to be converted into distributions of spheres with equivalent mean projected areas. Therefore, for each crystal habit, a relationship is required between the crystal's maximum dimension, and the radius of a sphere with the same projected area.

To find the equivalent sphere radius it is first necessary to calculate the mean projected area of the crystal in random orientation. The expressions derived in this section are based upon Cauchy's theorem (proved by Vouk [1948]), which states that

the mean projected area of a convex body is equal to 1/4 of its total surface area. The condition of convexity is not fulfilled in two of the cases given below, and it is recognised that the expressions derived in these cases are likely to be overestimates.

The only size data available for the crystals are their maximum dimensions, but the dimensions of cirrus ice crystals are interrelated, so there are functional relationships between the maximum dimension and the other dimensions of the crystal, and therefore it is possible to calculate the total area.

Now each of the idealised shapes intended to represent the habits found in cirrus are presented in turn, based upon the habits described in sections 4.3.2 and 4.4.2, and formulae are defined in each case to convert maximum crystal dimensions into equivalent-area sphere radii. In each formula, the dimensions and radii are measured in μm, and the areas in μm^2.

5.2.1 Hexagonal Columns

The idealised hexagonal column is used in the model to represent both hollow and solid columns, and also bullets.

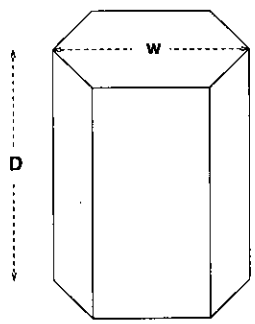

Figure 5.1: Model representation of a hexagonal column.

Figure 5.1 shows the simple geometrical version of a column used by the model. This is a hexagonal prism, of width w between the corners of the base, and of length D (the maximum dimension). The study by Auer and Veal [1970] provides empirical relationships between w and D, and in addition, Mitchell and Arnott [1994] provide an improved fit to the Auer and Veal data for $D < 1000$ μm. This gives the following set of relations:

$$\begin{aligned} w &= 0.7D && \text{for } 20\ \mu\text{m} < D < 100\ \mu\text{m} \\ w &= 6.96D^{0.5} && \text{for } 100\ \mu\text{m} < D < 1000\ \mu\text{m} \\ w &= 12.6D^{0.414} && \text{for } D > 1000\ \mu\text{m} \end{aligned} \tag{5.1}$$

where the factor of 12.6 in the final expression differs from the 11.3 used by Auer and

Veal because I have constrained the last two equations to be equal at $D = 1000\ \mu$m.

According to Cauchy's theorem, the projected area of a randomly oriented hexagonal column with a $w - D$ relation of the form $w = aD^b$ is given by:

$$P_{\text{col}} = \frac{3\sqrt{3}\,a^2 D^{2b}}{16} + \frac{3aD^{b+1}}{4} \tag{5.2}$$

So, using the formulae in 5.1, the radius r_{col} of a sphere of equivalent projected area, given by $P_{\text{col}} = \pi r_{\text{col}}^2$, is:

$$\begin{aligned} r_{\text{col}} &= 0.467D && \text{for } 20\ \mu\text{m} < D < 100\ \mu\text{m} \\ r_{\text{col}} &= \sqrt{(1.66D^{1.5} + 5.00D)} && \text{for } 100\ \mu\text{m} < D < 1000\ \mu\text{m} \\ r_{\text{col}} &= \sqrt{(3.01D^{1.414} + 16.4D^{0.828})} && \text{for } D > 1000\ \mu\text{m} \end{aligned} \tag{5.3}$$

5.2.2 Hexagonal Plates

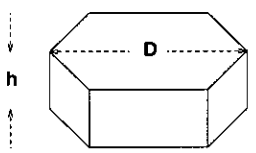

Figure 5.2: Model representation of a hexagonal plate.

The theory here is the same as for hexagonal columns, except that the maximum dimension is the width of the plate, and so instead of the $w - D$ relation of the columns there is an $h - D$ relation where h is the height of the plate, as shown in figure 5.2. Auer and Veal [1970] provide the following empirical relation for various forms of flat hexagonal plate:

$$h = 2.02D^{0.449} \qquad \text{for } D > 20\ \mu\text{m} \tag{5.4}$$

Now that D refers to a different dimension of the crystal, the projected area formula 5.2 is rewritten in the following form, for an $h - D$ relation of the form $h = \alpha D^\beta$:

$$P_{\text{pla}} = \frac{3\sqrt{3}\,D^2}{16} + \frac{3\alpha D^{\beta+1}}{4} \tag{5.5}$$

Consequently the radius of the equivalent sphere is given by:

$$r_{\text{pla}} = \sqrt{0.103D^2 + 0.482D^{1.449}} \qquad \text{for } D > 20\ \mu\text{m} \tag{5.6}$$

5.2.3 Bullet/Column Rosettes

Arnott *et al* [1994] provide an empirical relation for the projected area of ice crystals taken from a sample almost entirely composed of bullet rosettes. This empirical

relation is also quoted, to a higher precision, by Mitchell and Arnott [1994] as follows:

$$P_{\text{ros}} = 28.185 D^{1.268} \qquad \text{for } 200\ \mu\text{m} < D < 500\ \mu\text{m} \tag{5.7}$$

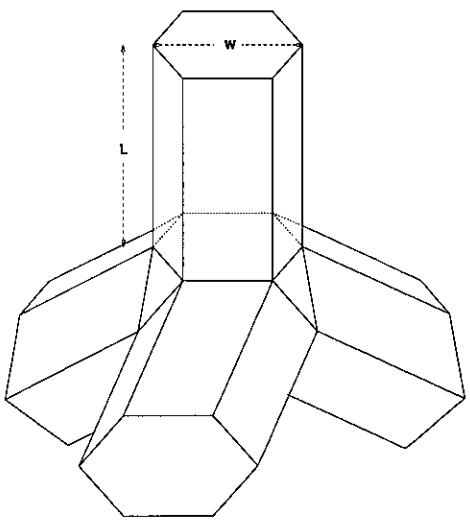

Figure 5.3: Model representation of a bullet rosette.

This expression may be considered highly representative of actual bullet rosette areas because it is not based on any idealised model; however, it is only valid across a limited size range. Outside this range it is necessary to use a theoretical formula based on an idealised model of a bullet rosette, known as a *rosette construct*. As shown in figure 5.3, the rosette construct is composed of a number of columnar branches, each of length L, radiating from a common centre. The bullet rosette crystal grows outwards in this form, so the branches are not necessarily to be regarded as having the same aspect ratio function as individual columns of the same size. This is reflected in the functional forms presented by Mitchell [1994] for the width versus the length of rosette branches, which are distinct from the corresponding relations for individual columns. These width-length relations are as follows:

$$\left.\begin{array}{rcll} w & = & 2.31 L^{0.63} & \text{for } T = -42°\text{C} \\ w & = & 0.701 L^{0.88} & \text{for } T = -32°\text{C} \end{array}\right\} 100\ \mu\text{m} < L < 500\ \mu\text{m} \tag{5.8}$$

These relations are applied to equation 5.2 to obtain the projected area of a single branch. Then this area can be multiplied by the number of branches, N, to obtain an area for the whole rosette, so

$$P_{\text{ros}} = N P_{\text{col}} \tag{5.9}$$

In practice this will be an overestimate, because some branches may shadow others; in addition, the ends of the branches which meet at the centre ought not to bbe

counted. Typically the maximum dimension D will be the length of two branches, $2L$, and so given the range of validity of equations 5.8, the calculation will be valid for 200 μm $< D <$ 1000 μm. Therefore the size range 500 μm $< D <$ 1000 μm is covered by this method.

Mitchell and Arnott [1994] investigate this method and compare it to the empirical formula (equation 5.7), finding that the projected area given by the latter corresponds to that calculated for a 6-branch rosette construct at $D = 200\mu$m. However, the slope of the construct curves is steeper than that of the empirical formula, so as D increases, the empirical formula corresponds to constructs of fewer branches. This does not tally with the findings of Arnott *et al* [1994], that rosettes in this size range have on average 7 or 8 branches, and this discrepancy may be due to the shadowing effect. The equations 5.8 show a sub-linear relationship between the width and the length of the branches, which implies an inverse relationship between the aspect ratio and the length. It may be seen intuitively that branches of a lower aspect ratio will be more prone to shadowing effects.

At present the model does not account for shadowing, and so the number of branches is fixed by determining the value of N which gives the same projected area as the empirical formula at $D = 500$ μm. This will mean a non-integer value for N, but this is not a problem if it is accepted that the rosette construct is not truly representative of a real rosette. The best that can be expected of this method is that the functional form of the construct area is not too divergent from that of the projected area of a real rosette.

	$T = -42°$C	$T = -32°$C
$D <$ 200 μm	3.41	
200 μm$< D <$ 500 μm	—	—
500 μm$< D <$ 1000 μm	4.72	3.80
$D >$ 1000 μm	3.39	4.08

Table 5.1: Numbers of branches in rosette crystal constructs. These are non-integer values to make the projected area of the construct consistent with mean measured values.

Below 200 μm and above 1000 μm, equations 5.8 are not valid, so here there is a choice of extrapolating these formulae outside of their range, or reverting to the Auer and Veal formulae (equations 5.1) for single columns. The latter was chosen because it appears preferable to use formulae which are appropriate for the size range in question, if not for the way in which the crystal is formed. It is doubtful whether these formulae accurately represent rosette branches, but they are the best available. Again, the number of branches N is chosen to make the curves meet at

$D = 200$ μm and $D = 1000$ μm. This will mean different values of N from those used in the 500 μm $< D <$ 1000 μm range. The values of N which fit each range are given in table 5.1.

The combination of all these elements leads to the final set of equations for the equivalent radius $r_{\rm ros}$:

$$
\begin{aligned}
r_{\rm ros} &= 0.43D && \text{for } D < 200\ \mu\text{m} \\
r_{\rm ros} &= 3.0D^{0.634} && \text{for } 200\ \mu\text{m} < D < 500\ \mu\text{m} \\
r_{\rm ros} &= \sqrt{0.84D^{1.63} + 1.1D^{1.26}} && \text{for } 500\ \mu\text{m} < D < 1000\ \mu\text{m} \\
r_{\rm ros} &= \sqrt{8.5D + 2.0D^{1.5}} && \text{for } 1000\ \mu\text{m} < D < 2000\ \mu\text{m} \\
r_{\rm ros} &= \sqrt{31D^{0.828} + 3.8D^{1.414}} && \text{for } D > 2000\ \mu\text{m} \qquad \Big\} T < -37^\circ\text{C} \\
r_{\rm ros} &= \sqrt{0.17D^{1.88} + 0.057D^{1.76}} && \text{for } 500\ \mu\text{m} < D < 1000\ \mu\text{m} \\
r_{\rm ros} &= \sqrt{10D + 2.4D^{1.5}} && \text{for } 1000\ \mu\text{m} < D < 2000\ \mu\text{m} \\
r_{\rm ros} &= \sqrt{38D^{0.828} + 4.6D^{1.414}} && \text{for } D > 2000\ \mu\text{m} \qquad \Big\} T > -37^\circ\text{C}
\end{aligned}
\tag{5.10}
$$

5.2.4 Plate Rosettes

The plate rosette, shown in figure 5.4, is an idealised form consisting of a number of hexagonal plate crystals joined at their points. It is intended to model both the radiating assemblages of plates *and* side planes crystals described in section 4.3.2. In the case of the former, a rosette of hexagonal plates is a simple way of modelling the assemblage which fits that description. In the case of the side planes crystal, the bulk of the projected area comes from the planes themselves, since the columnar arms are thin. Therefore my model ignores the actual width of the arm and regards it merely as an axis for the plates. For each arm there are two half-hexagonal plates, and if these are considered symmetric, the idealised side planes crystal becomes an assemblage of hexagonal plates joined by their points. In this way the side planes crystal and the radiating assemblage of plates have the same modelled form.

The method used here is equivalent to that used for bullet rosettes, except that the component crystals are plates. Using equations 5.4 and 5.5 the projected area of a randomly oriented plate of width w is given by:

$$P_{\rm pla} = \frac{3\sqrt{3}\,w^2}{16} + \frac{6.06w^{1.449}}{4} \tag{5.11}$$

As for the bullet rosettes, it is assumed that the maximum dimension of the plate rosette is twice the maximum dimension of its component plates, i.e. $w = D/2$. The projected area of the plate rosette is calculated as the sum of the projected areas of its component plates, so given that N is the number of plates in the rosette, the equivalent radius will be given by

$$r_{\rm pr} = \left(\frac{N}{\pi}\right)^{\frac{1}{2}} \left(0.0813D^2 + 0.555D^{1.449}\right)^{\frac{1}{2}} \tag{5.12}$$

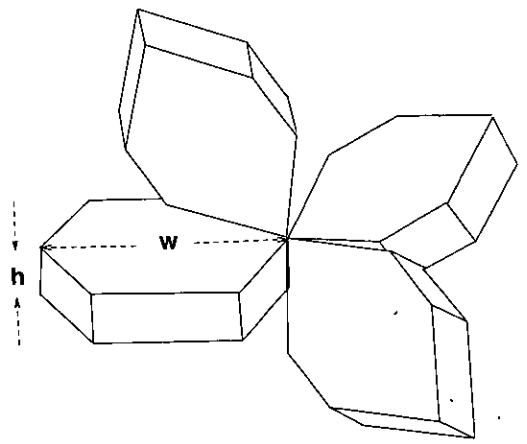

Figure 5.4: Model representation of a plate rosette.

There is no empirical data set for these crystals with which this equation may be compared in order to choose a suitable number of plates per rosette. Moreover, there is very little in the literature to indicate a typical number of arms for a side planes crystal, or the number of plates in a radiating assemblage. The microphotographs of Magono and Lee [1966] show side planes crystals with between two and five arms. The radiating assemblages appear to be composed of seven or more plates. The bullet rosette model described previously had between 3 and 5 arms, as shown in table 5.1. Any choice would therefore appear to be rather arbitrary; for this study a 4-plate rosette was used. Therefore the equivalent-sphere radius from equation 5.12 becomes:

$$r_{\mathrm{pr}} = \left(0.104D^2 + 0.707D^{1.449}\right)^{\frac{1}{2}} \tag{5.13}$$

5.2.5 Trigonal Plates

Yamashita's [1973] definition of the trigonal plate given in section 4.4.2 suggests a triangular prism, the height of which is less than its width, as illustrated in figure 5.5. In nature more complicated forms occur, such as elongated dendritic trigonals, but in this study a single, simple form is retained.

Using Cauchy's theorem, for a trigonal plate with an equilateral cross-section of side D and a height h, the projected area is

$$P_{\mathrm{tri}} = \frac{1}{4}\left(\frac{D^2\sqrt{3}}{2} + 3Dh\right) \tag{5.14}$$

Therefore, if the height of the plate is related to the maximum dimension by the relation $h = \alpha D^{\beta}$, this becomes

$$P_{\mathrm{tri}} = \frac{1}{4}\left(\frac{D^2\sqrt{3}}{2} + 3\alpha D^{\beta+1}\right) \tag{5.15}$$

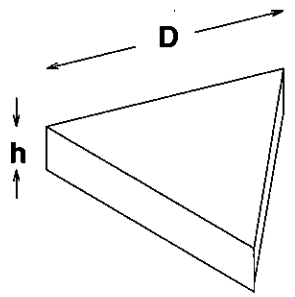

Figure 5.5: Model representation of a trigonal plate.

The actual relationship between height and width is not clear. Heymsfield [1986a] says that the axial ratio of thickness (height) to diameter is close to unity at small sizes (< 20 μm), but that it decreases at larger sizes. Auer and Veal's [1970] formula for the thickness of hexagonal plates with respect to diameter gives $h = 2.02D^{0.449}$. I have combined these two sets of information so that $h = D$ (i.e. $\alpha = 1$, $\beta = 1$) at sizes below 20 μm, and then $h \propto D^{0.449}$ at larger sizes. The constant of proportionality is chosen to make the two functions equal at $D = 20\mu$m, which means that $\alpha = 5.210$ and $\beta = 0.449$ above 20 μm. Substituting into equation 5.15:

$$\begin{array}{lcll} P_{\text{tri}} & = & 0.967D^2 & \text{for } D < 20\ \mu\text{m} \\ P_{\text{tri}} & = & 0.217D^2 + 3.908D^{1.449} & \text{for } D > 20\ \mu\text{m} \end{array} \tag{5.16}$$

And so the radius of a sphere of equivalent projected area is given by

$$\begin{array}{lcll} r_{\text{tri}} & = & 0.555D & \text{for } D < 20\ \mu\text{m} \\ r_{\text{tri}} & = & \sqrt{0.0689D^2 + 1.244D^{1.449}} & \text{for } D > 20\ \mu\text{m} \end{array} \tag{5.17}$$

Although it appears to be an overgeneralisation to represent all crystals larger than 20 μm by the same equation, the largest trigonals are smaller than 100 μm, so the upper size range is not excessively wide.

5.3 Equivalent Sphere Distributions for Frontal Cirrus

The sets of equations 5.3, 5.6, 5.10, 5.13 and 5.17 defined above allow the conversion of all the crystals in the model cirrus cloud into spheres of equivalent projected area. The frontal case is considered first, for which all the equations except 5.17 will be required.

The process used for conversion of the distributions is as follows. First the concentration at each crystal dimension of the raw size distribution is divided between

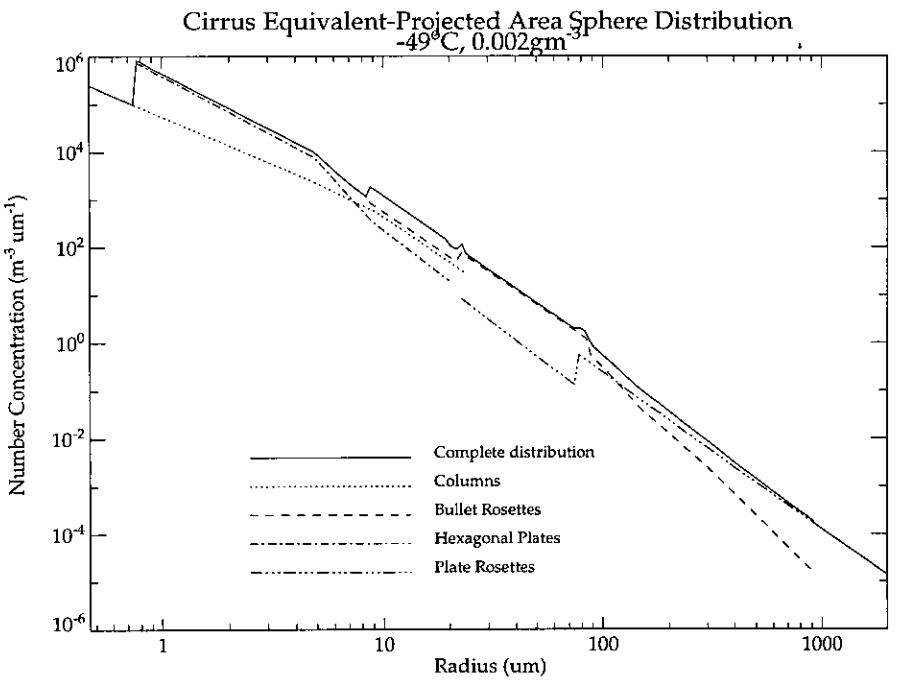

Figure 5.6: Equivalent-area sphere distribution for frontal cirrus at -49°C, IWC=0.002.

the habit fractions appropriate for that dimension and temperature. Then the appropriate expression from section 5.2 is used to convert the crystal's maximum dimension into the radius of an equivalent sphere for each habit. The fractional concentration of a given habit is then stored at the equivalent sphere radius. In this way a separate equivalent sphere distribution is created for each habit. These distributions are then superimposed to create an overall distribution for the cloud.

The scattering properties of the resulting distribution of spheres can then be dealt with using the scattering theory developed in chapter 3. Figure 5.6 shows an equivalent-area sphere distribution for a frontal cirrus cloud at $-49°C$, with an IWC of 0.002 gm^{-3}. The individual contributions from each habit type are also shown.

Examination of the scattering properties of this distribution reveal a problem with the extension of the Heymsfield and Platt power law beyond the 2 mm limit which was imposed in section 4.3.1. Figure 5.7 is a plot of the marginal contribution to the extinction coefficient (or scattering coefficient in the case of the dotted line), at 200 GHz, per unit radius of the equivalent sphere distribution shown in figure 5.6. As such it indicates the size range which contributes most to the coefficient. The area under the marginal contribution function is equal to the total coefficient.

The largest equivalent-sphere radius of a crystal of maximum dimension 2 mm is that of a plate rosette, $\sim 700\ \mu$m. In figure 5.7 there is still a significant contribution

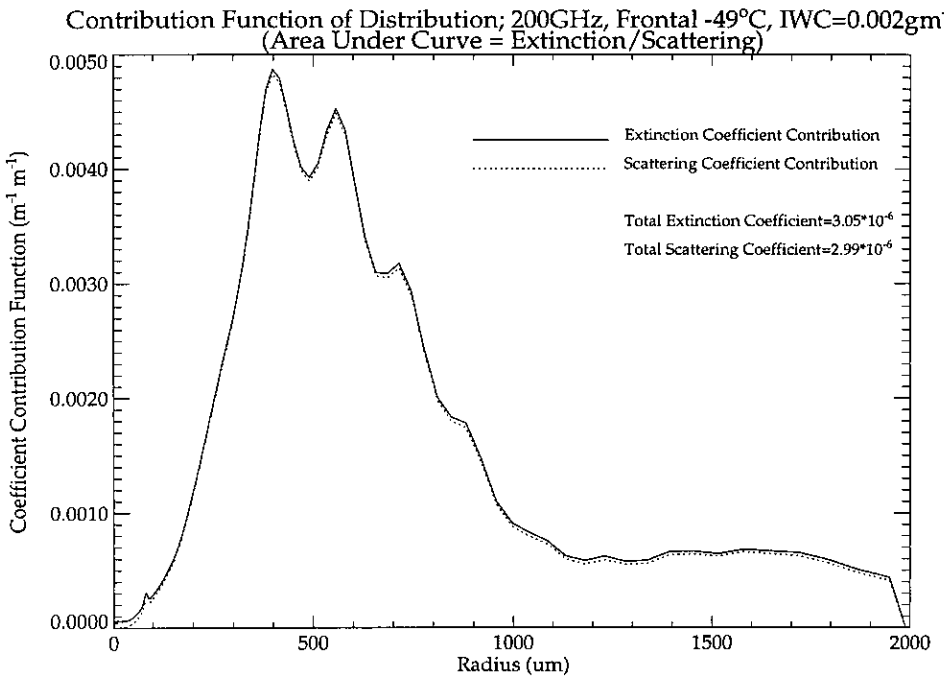

Figure 5.7: Marginal contribution functions at 200 GHz for frontal cirrus at −49°C, IWC=0.002. Power law size distribution beyond 2 mm.

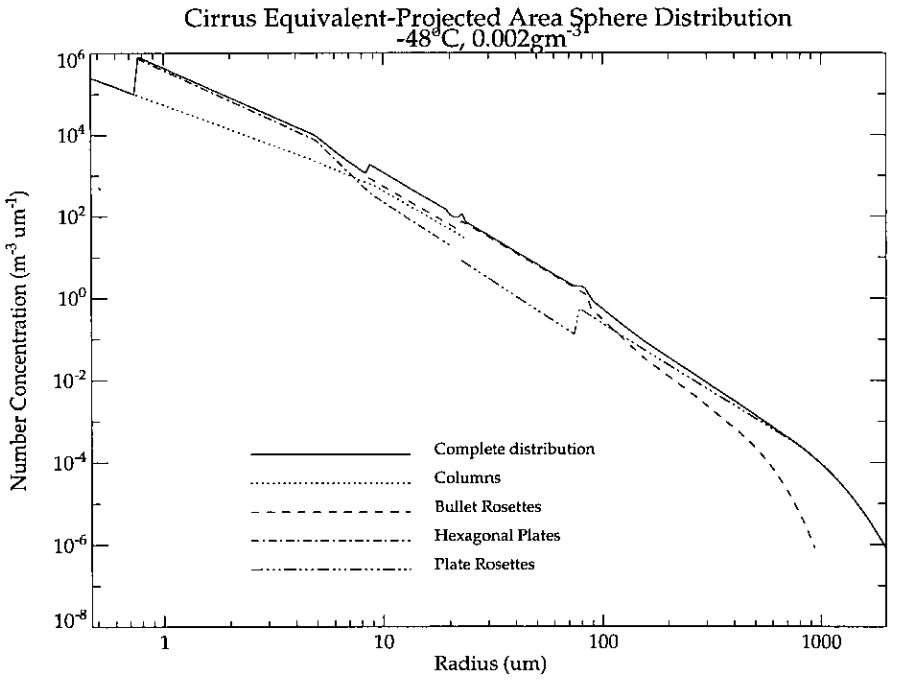

Figure 5.8: Equivalent-area sphere distribution for frontal cirrus at −49°C, IWC=0.002.

to be added to the scattering and extinction coefficients beyond this radius, and so the distribution clearly needs to extend beyond this point. However, the marginal contribution of the power law distribution beyond an equivalent radius of about 1 mm ceases to decline, and only finally drops to zero at a radius of 2 mm, which corresponds to the 6 mm cut-off of the original size distribution.

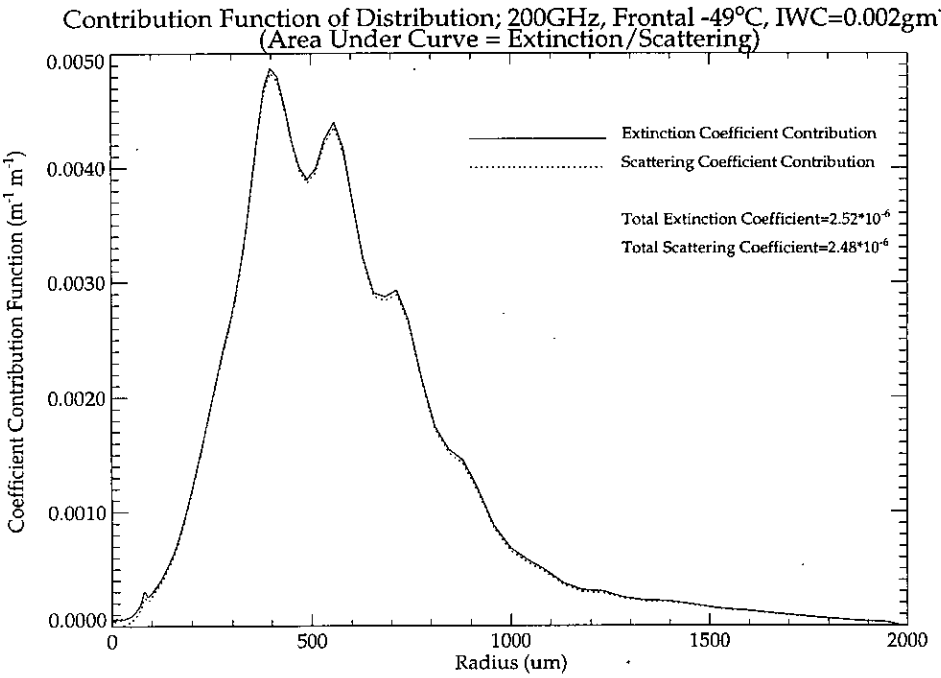

Figure 5.9: Marginal contribution functions at 200 GHz for frontal cirrus at −49°C, IWC=0.002. Exponential size distribution beyond 2 mm.

Therefore the continuation of the power law distribution beyond 2 mm is not satisfactory. As was shown in section 4.4.1, there is evidence that in the case of cumulonimbus anvil cirrus, the size distribution for large (millimetre-sized) crystals is exponential. This is most evident in the severe thunderstorm recorded by Heymsfield [1986b], for which he presents an exponential distribution up to ~ 6 mm. It seems likely that frontal cirrus will behave similarly at high dimensions, so the power law beyond 2 mm was replaced by an exponential.

In the absence of data to which to fit the exponential, instead it was made consistent with the existing data, by matching the concentration and the gradient of the power law distribution at 2 mm. Therefore, if the exponential is of the form $N = \alpha \exp(\beta D)$, and the power law is as given by equation 4.2, the parameters of the fitted exponential are given by

$$\alpha = \mathrm{IWC} \times A_2 \exp(-B_2)(2000)^{B_2} \tag{5.18}$$

$$\beta = B_2/2000 \tag{5.19}$$

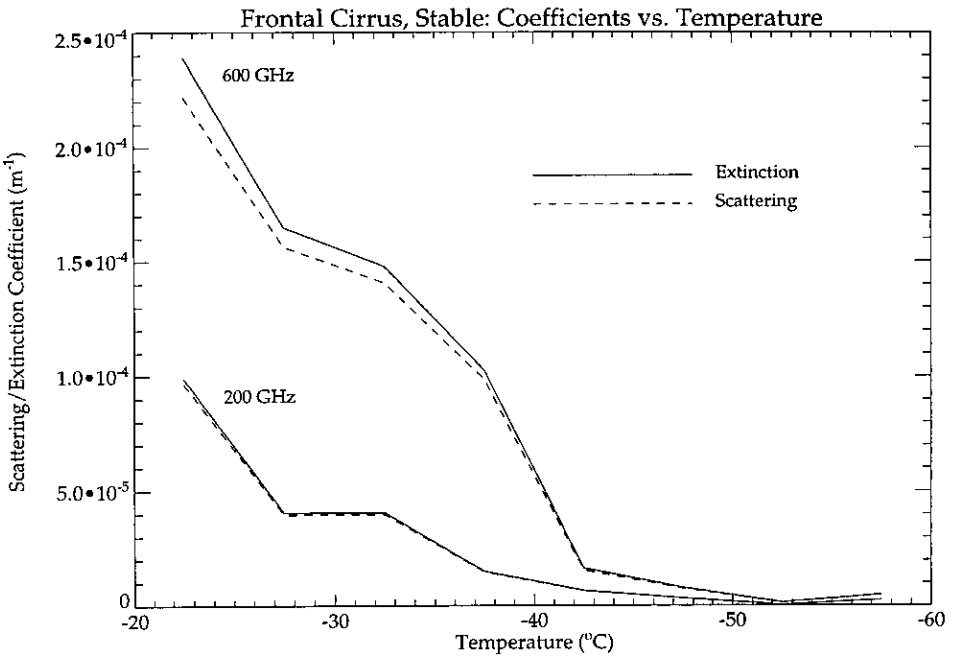

Figure 5.10: Variation of typical scattering and extinction coefficients with temperature in frontal cirrus.

where A_2 and B_2 are the temperature-dependent parameters of the fit as defined in section 4.3.1.

The result of this change to the equivalent sphere distribution, as shown in figure 5.8, does not appear dramatic compared with the unmodified distribution shown in figure 5.6, but the effect on the marginal contribution function in figure 5.9 is significant when compared with figure 5.7. The marginal contribution now tapers off to zero without the need for truncation, allowing greater confidence in the values of the coefficients.

The equivalent sphere distribution depends on the original size distribution from which it is derived, and on the habit fractions. In turn, these factors are dependent on the temperature and the IWC. In section 5.7.4 it will be shown that the IWC is, on average, related to the temperature, and an expression linking the two quantities is given in equation 5.26. Therefore a crude relationship between the scattering properties and the temperature of the distribution may be obtained, and this is shown in figure 5.10, where the scattering and extinction coefficients are plotted against temperature. Two sets of coefficients are plotted, the upper pair being those calculated at 600 GHz, and the lower pair those for 200 GHz. These frequencies represent the lower and upper reaches of the EOS MLS frequency range used in this thesis. It is clear from these plots that it is the warmer (i.e. lower) cirrus clouds which are expected to have the greatest scattering effect.

5.4 Equivalent Sphere Distributions for Tropical Cirrus

The same process as that described in the previous section, for converting raw frontal size distributions into equivalent sphere distributions, was also applied to the tropical cirrus, and the results are described below.

In figure 5.11 the equivalent sphere distribution for a tropical 'cold' anvil (as defined in section 4.4.1) at −80°C is shown. The contributions of the individual habit types to the overall distribution are shown by the broken lines.

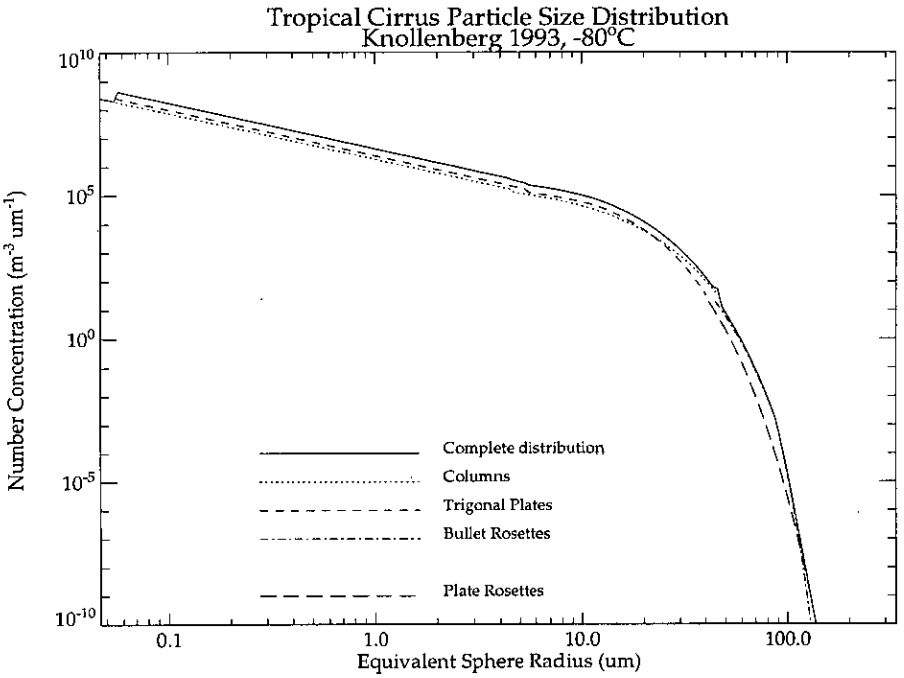

Figure 5.11: Equivalent sphere size distribution for the 'cold' tropical anvil at −80°C.

In the same way as for the frontal cloud, scattering theory is applied to the distributions to ascertain the appropriateness of the functions fitted to the data; in this case it allows investigation of the importance of crystals larger than 100 μm, which are extrapolated from the data of Knollenberg *et al* [1993] by the exponential fit shown in figure 4.9. In figure 5.12 the marginal contribution function of the scattering and extinction coefficients of the −80°C anvil is shown for a typical MLS frequency of 200 GHz. The radius plotted as the abscissa is the equivalent-sphere radius, as plotted in figure 5.11. From equations 5.10 and 5.13, which give the equivalent sphere radii for bullet rosette and plate rosette crystals respectively, it can be determined that at a maximum dimension of 100 μm, the equivalent-sphere radius in both cases is of order 40 μm. Figure 5.12 shows that above this radius

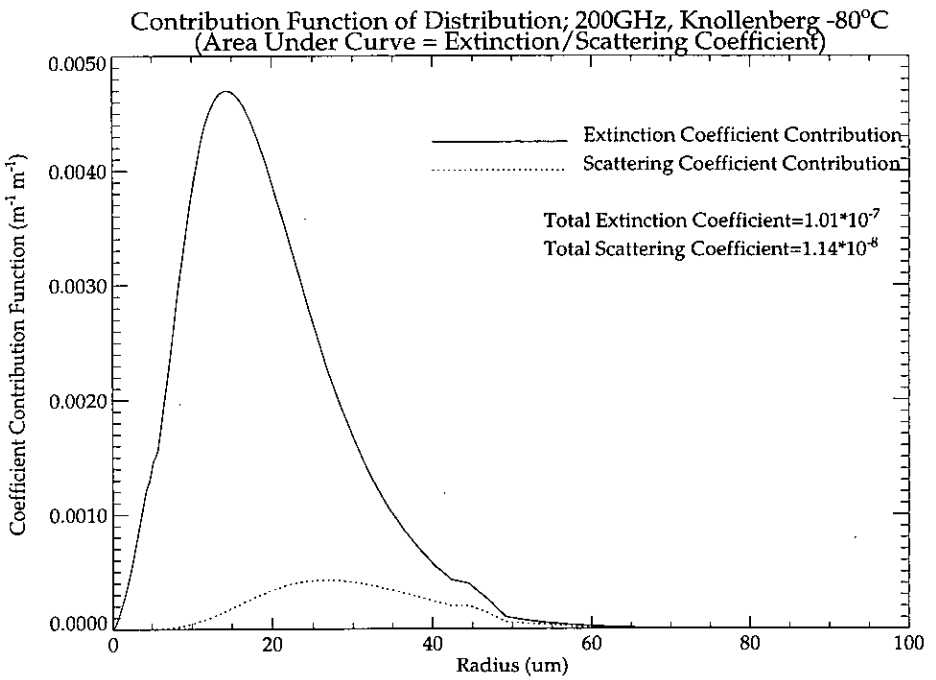

Figure 5.12: Marginal contribution functions at 200 GHz for the 'cold' tropical anvil at $-80°C$.

the contribution to both coefficients is small. This is because the concentration, declining exponentially with increasing radius, is falling off at a greater rate than that at which the single-sphere scattering and extinction coefficients are increasing.

Figure 5.12 also gives the total extinction and scattering coefficients as the area under each marginal contribution function. The scattering coefficient is an order of magnitude lower than the extinction, which implies that the majority of the extinction is due to absorption rather than scattering, in contrast to the frontal cirrus distributions, which have similar scattering and extinction coefficients, and consequently very little absorption. This is because the cold tropical distribution, whilst having higher crystal concentrations than the frontal in general, has many fewer large crystals (> 100 μm), and so the scattering properties of the cloud tend towards those characteristic of small particles, for which a greater part of the extinction is due to absorption.

The same process was repeated at 600 GHz, to test the high-frequency end of the EOS MLS spectrum. The total scattering and extinction coefficients were of course higher, but the contribution function is much the same, with a slightly increased, but still very small, contribution from particles larger than 100 μm.

The same treatment was given to the 'warm' anvil distribution which was shown in figure 4.11. The distribution in this case diminishes less rapidly than an exponential, because it is a combined power law/exponential fit (given by the second

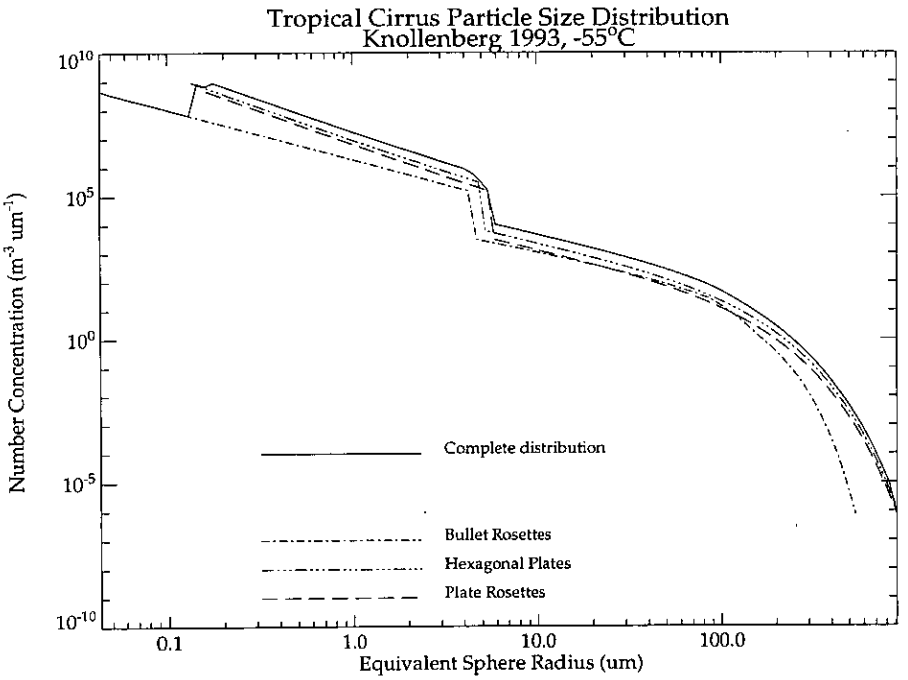

Figure 5.13: Equivalent sphere size distribution for the 'warm' tropical anvil at −55°C.

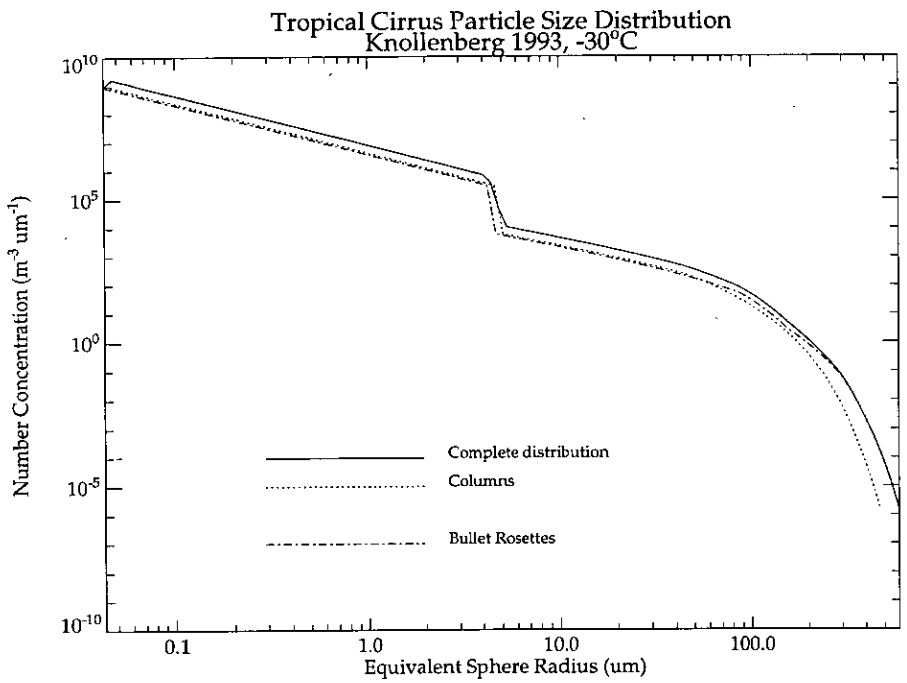

Figure 5.14: Equivalent sphere size distribution for the 'warm' tropical anvil at −30°C.

of equations 4.8). It will be demonstrated presently that this causes the cloud to have a significant extinction effect at much larger crystal dimensions than was the case for the 'cold' anvil. Therefore the distributions in this case were extended to maximum dimensions of 3 mm.

In figures 5.13 and 5.14 the equivalent-sphere size distributions for warm anvils at $-55°C$ and $-30°C$ are shown, these temperatures being representative of the two warmest habit regimes shown in table 4.8.

It is interesting to note the large difference between the scattering properties of these two distributions, which results entirely from their differing habit characteristics. Figures 5.15 and 5.16 show the marginal contribution functions at 200 GHz which correspond to the size distributions in figures 5.13 and 5.14. In the $-55°C$ case, the marginal contribution function extends to much larger equivalent radii than in the $-30°C$ case. This is because in the warmer case the crystals are predominantly columns and bullet rosettes, which present a smaller mean area at large maximum dimensions than do the plate and plate rosette crystals. This can be seen in figure 5.13, where the bullet rosette contribution to the total of equivalent spheres drops off faster than that of the planar crystals.

These contribution functions also demonstrate the need to extend the warm anvil distributions to maximum dimensions beyond 1 mm. For example, the plate rosette crystal, which presents the largest area for a given maximum dimension, has an equivalent-sphere radius at 1 mm of 350 μm. In figure 5.15, it is clear that truncation of the distribution at 1 mm would exclude the significant proportions of the scattering and extinction coefficients which occur above a radius of 350 μm. Therefore as stated above, 3 mm was chosen as the upper limit, which ensures that the total coefficient calculated reaches its convergent maximum.

As in the case of the cold anvil, the contribution functions for these distributions calculated at 600 GHz take the same general form as those at 200 GHz, except that the total values of the coefficients are higher.

The tropical distributions are distinguished by means of temperature only (not by IWC), and so the correlation of scattering properties and temperatures is simpler than it was for the frontal cloud. Figure 5.17 shows the extinction and scattering coefficients, plotted at three temperatures which represent the three temperature bands of the habit fractions, and which also separate the two distinct 'warm' and 'cold' size distributions. This figure is equivalent to figure 5.10 for frontal cloud, and as in that case, results are presented at 200 GHz and at 600 GHz. The pattern seems very unlike that of the frontal cloud, although with only three points in the plot, it is difficult to determine what that pattern is.

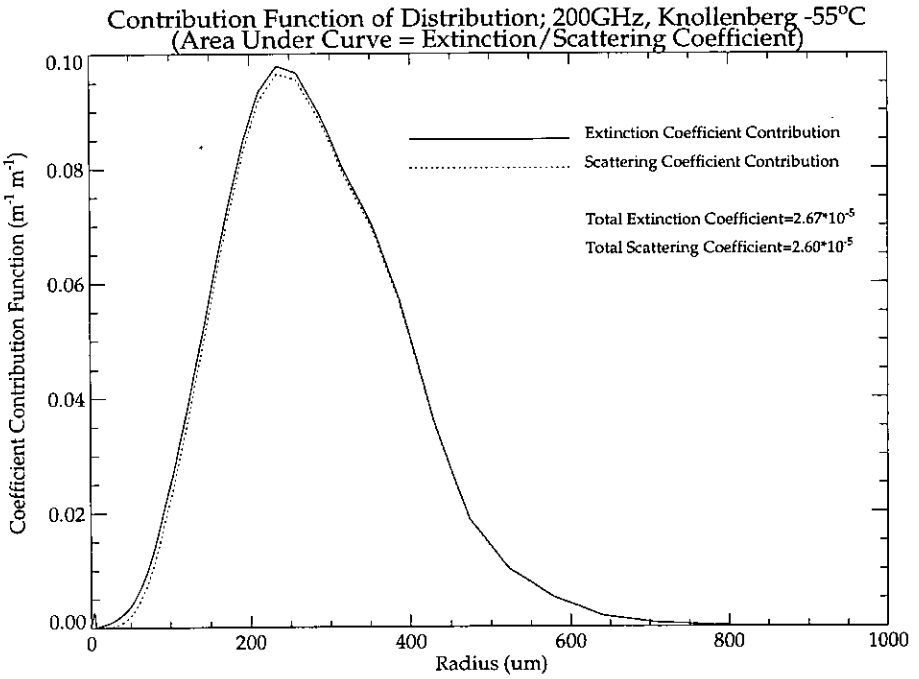

Figure 5.15: Marginal contribution functions at 200 GHz for the 'warm' tropical anvil at −55°C.

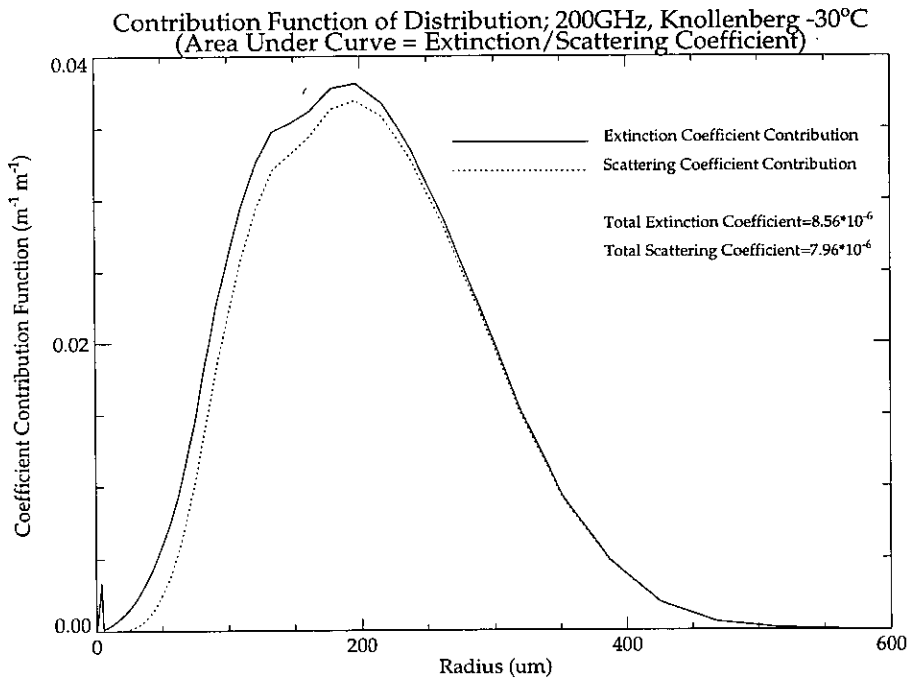

Figure 5.16: Marginal contribution functions at 200 GHz for the 'warm' tropical anvil at −30°C.

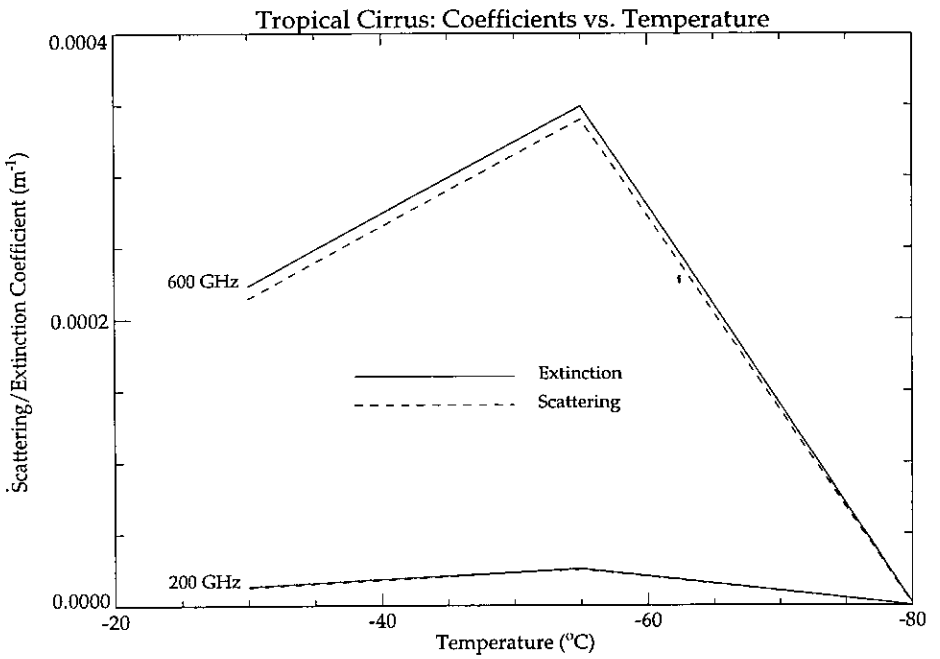

Figure 5.17: Variation of typical scattering and extinction coefficients with temperature in tropical anvils.

5.5 Sensitivity of Scattering Properties to Variations in Simulation Parameters

The simulation of the scattering properties of cirrus which has been described relies on broad approximations and uncertain microphysical data. In this section a set of results are presented which demonstrate the extent to which the calculated scattering properties are affected by variations in particular characteristics of the scattering model. First, the equivalent-area method is compared with the equivalent-volume method, showing the difference in the values of extinction calculated in each case. Secondly, the sensitivity of the results to changes in the habit distribution of the cloud is evaluated by comparing results for the stable form of frontal cirrus with those for the convective form, which has different habit characteristics. Such a comparison means that the change in habit distribution which is used for the sensitivity test reflects the extent of the variation which may occur in nature.

5.5.1 Equivalent Area vs. Equivalent Volume

It was stated in section 5.1 that the equivalent-volume method is likely to be a more suitable technique than the equivalent-area method for modelling the extinction of microwave radiation by cirrus crystals. Therefore an estimate was made of the difference between the scattering properties calculated by the equivalent area and

equivalent volume approximations respectively. Rather than recalculating all results using an equivalent-volume method, a single column crystal was used as a model to get an idea of the order of the difference between the methods.

The radius of a sphere of equivalent surface area to a column is given by equations 5.3 in section 5.2.1 for each of three size regimes. To find the corresponding formulae for equivalent-volume spheres, the volume of a hexagonal column must be formulated. For a column of length D and corner-to-corner width w, as shown in figure 5.1, the volume is expressed as follows

$$V_{\text{col}} = \frac{3\sqrt{3}w^2 D}{8} \tag{5.20}$$

The same $w - D$ relations, given by equations 5.1, that were used to calculate the equivalent-area radii may be used here. The column volume evaluated in each case in terms of D is then equated to the volume of a sphere of radius r_{col}, to give the following formulae:

$$\begin{aligned} r_{\text{col}} &= 0.424D && \text{for } 20\ \mu\text{m} < D < 100\ \mu\text{m} \\ r_{\text{col}} &= 1.958D^{0.67} && \text{for } 100\ \mu\text{m} < D < 1000\ \mu\text{m} \\ r_{\text{col}} &= 2.909D^{0.61} && \text{for } D > 1000\ \mu\text{m} \end{aligned} \tag{5.21}$$

Figure 5.18 shows an intercomparison between the extinction efficiencies calculated for equivalent-volume and equivalent-area spheres respectively. The extinction efficiency is plotted against the length of the column crystal, and results are given for 200 GHz and 600 GHz. The plot demonstrates that in general the equivalent-volume technique results in lower values of the extinction efficiency. The exception to this occurs for large column crystals at 600 GHz, where it is seen that the extinction efficiency for equivalent-volume spheres exceeds that of the equivalent-area spheres.

If the equivalent-volume method is in fact the more accurate technique, then figure 5.18 shows that the use of the equivalent-area method in this thesis has resulted in an overestimate of the extinction caused by clouds at 200 GHz. At a column length of 2 mm, this overestimate is approximately a factor of 3. Although this is large, it means the two methods yield results of the same order of magnitude.

At 600 GHz it is likely that there is considerably less overestimation, or even none, due to the equivalent-area method. The equivalent-volume extinction efficiency exceeds the equivalent-area value when the crystal size is about 1 mm, and it is crystals of this size and above which contribute the majority of the overall extinction coefficient of a cirrus cloud, as was demonstrated in section 5.3.

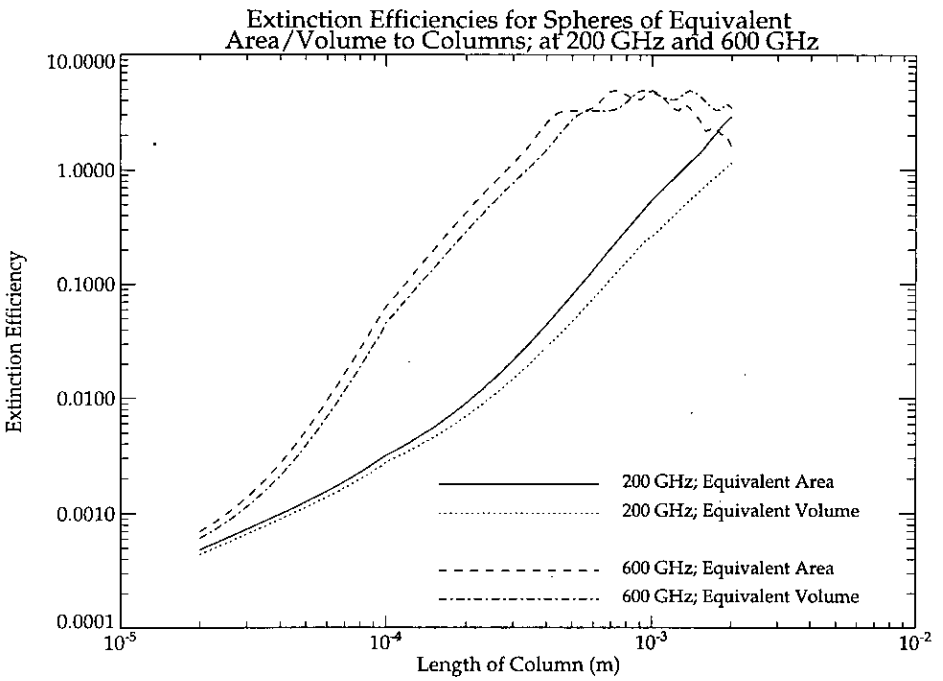

Figure 5.18: Comparison of extinction efficiencies calculated for column crystals, using spheres of equivalent area and equivalent volume.

5.5.2 Stable vs. Convective Frontal Cirrus

In section 4.3.3 a distinction was drawn between the stable, stratified forms of frontal cirrus, and those forms which exhibit internal convection. In two of the temperature bands defined in that section, the distribution of habits is different according to whether the cloud is stable or convective. The results which have been produced for frontal cloud in this chapter have been obtained using the stable cirrus habit fractions. Therefore in this section the difference which results from the use of the convective cirrus habit fractions is investigated.

The temperature range for which the habit distributions are distinct for each type of frontal cirrus is from $-25°C$ to $-50°C$. Therefore a set of five temperatures were chosen, representing each of the Heymsfield and Platt [1984] temperature bands within this range. For each temperature, an appropriate ice water content was chosen in the manner described in section 5.3 for the production of figure 5.10. Thus, with the temperature and IWC defined, the cirrus simulation was used to generate model clouds representative of each temperature, for the stable and convective cases respectively. The scattering model was then applied to each cloud, to produce the comparative plots of extinction coefficient shown in figure 5.19.

The plot shows two pairs of curves, the upper pair being the extinction coefficients at a frequency of 600 GHz, and the lower pair those at 200 GHz. The solid

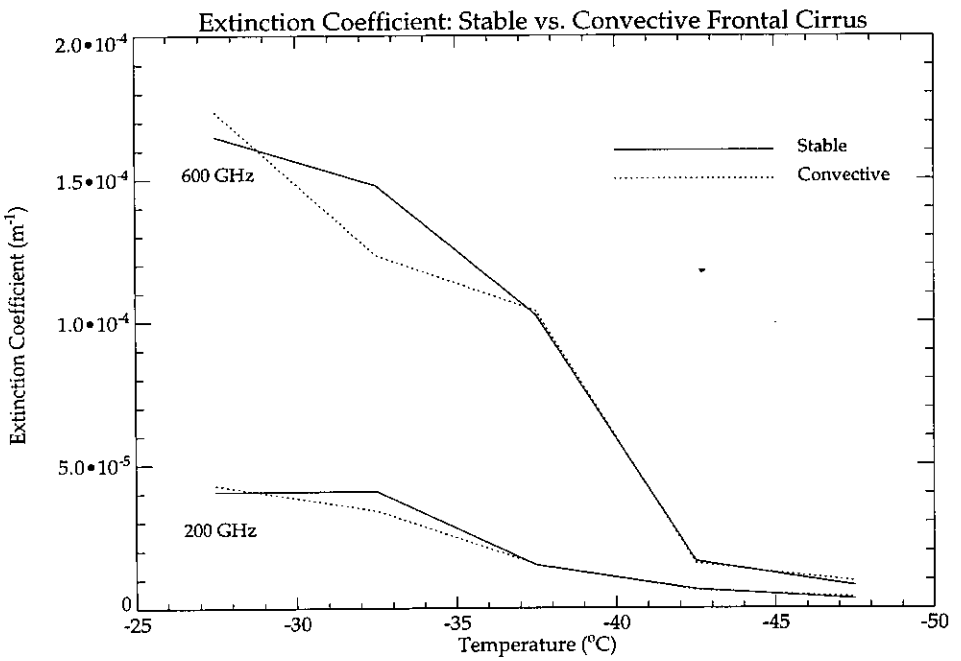

Figure 5.19: Comparison of extinction efficiencies calculated for stable and convective frontal cirrus clouds.

lines represent results for the stable form of cirrus, and the dotted line those for frontal cirrus which displays internal convection. The solid lines are therefore subsets of the curves plotted in figure 5.10. The largest difference between the types occurs at a temperature between $-30°C$ and $-35°C$, while at other temperatures the difference is negligible. This suggests that at temperatures in the sensitive range, the use of stable frontal cirrus which has been made in this thesis may constitute an overestimate of the likely extinction when frontal cirrus is of a more convective nature. However, the overestimate is confined to a narrow temperature range, which is not included in the set of examples which are defined in section 5.7 for use in chapter 6 to produce the principal results of this thesis.

5.6 Comparison with Other Models

Studies of the scattering effect of cirrus crystals at microwave frequencies have been made, with varying degrees of complexity, by Gunn & East [1954], Weinman [1988], Mugnai & Smith [1988] and Muller *et al* [1994], the latter three of which have been briefly discussed in section 5.1. However, by far the most detailed study is that of Evans and Stephens [1995a, 1995b]. They use a technique called the 'discrete dipole approximation' (DDA) to attempt to represent realistically the scattering properties of complex crystal shapes. The idea behind the DDA is to divide the

crystal into a number of identical cubic subunits whose size is small compared to the wavelength. The scattered field of the crystal can then be estimated by calculating the total, mutually scattered field from the ensemble of these units. In this section an intercomparison is presented, between the results from the equivalent-area sphere method which has been described, and those from the DDA.

Evans and Stephens [1995a] consider five different habits: spheres, solid and hollow columns, hexagonal plates and bullet rosettes. The columns are represented by cylinders in both cases, and the bullet rosette is represented by four cylinders meeting at right angles at a common centre. Rather than assuming completely random orientation as I have done, the authors take account of the observation originally made by Ono [1969], that elongated crystals fall with their long axes horizontal as a result of the air resistance acting upon them. In addition, they consider a nadir view of these crystals.

The spheres used by Evans and Stephens are intended to represent spatial crystals of high aspect ratio, whose density decreases with increasing size. To this end, a spatial crystal of maximum dimension D is replaced in their model by a sphere of volume V, where

$$V = \frac{\pi D^3}{6} \left(\frac{D}{10\ \mu\text{m}} \right)^{-1/2} \tag{5.22}$$

Evans and Stephens calculated the extinction coefficients of monodispersions of each habit shape, over a range of crystal sizes from 30 μm to 2000 μm. The concentration of each monodispersion was 10 m^{-3}. The results are reproduced in figures 5.20 and 5.22, for 85 GHz and 340 GHz respectively. These results may be compared with results for the same conditions from the cirrus simulation which has been described in this thesis. The model was used to produce extinction coefficients for monodispersions, at concentration 10 m^{-3}, of column, plate and bullet rosette crystals. In addition, equation 5.22 was used to produce results for spheres equivalent to those used by Evans and Stephens. The results are plotted in figures 5.21 and 5.23 using the same units, and on the same scale, as the plots of Evans and Stephens. All the habits plotted by Evans and Stephens are represented here, with the exception of hollow columns, for which no modelling technique has been developed.

A comparison of these results with those of Evans and Stephens shows that the extinction coefficients calculated for the spheres appear identical, as would be expected. For the 85 GHz plots, there is considerable difference between the results for large non-spherical crystals, where the extinction due to plates and rosettes calculated with the equivalent-area model is an order of magnitude higher than that found by the DDA; conversely, the equivalent-area model predicts an extinction due to solid columns which is an order of magnitude lower than that calculated by Evans

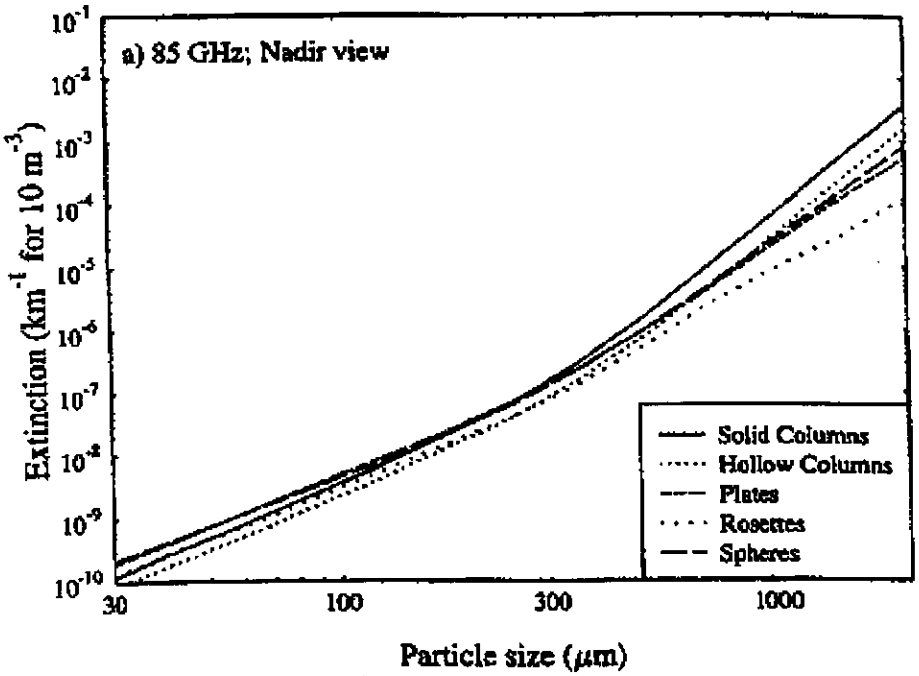

Figure 5.20: Extinction coefficients at 85 GHz, for monodispersions of cirrus crystals at 10 m^{-3} concentration, calculated by the discrete dipole approximation of Evans and Stephens [1995a].

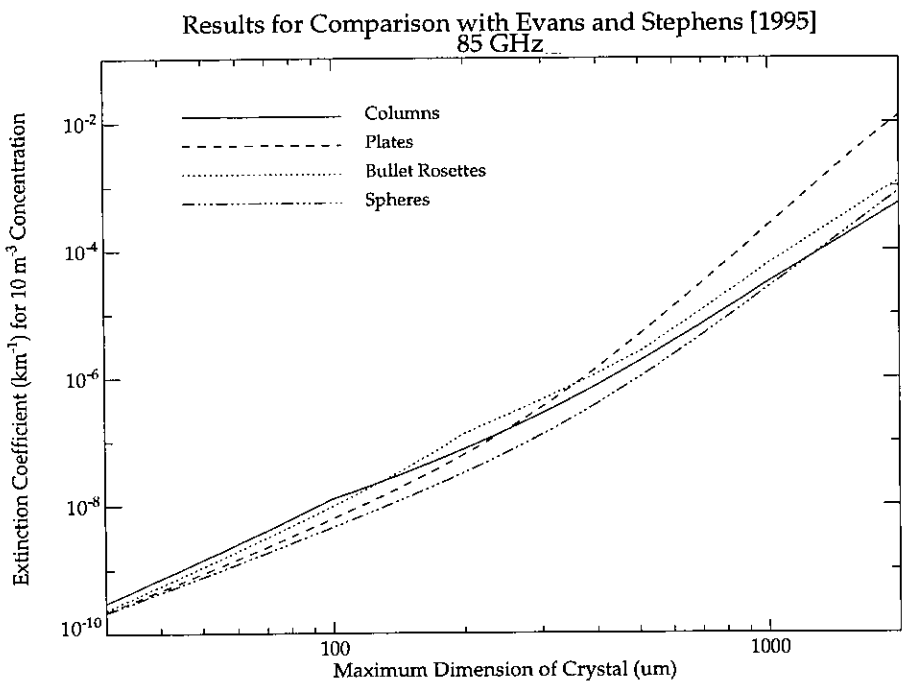

Figure 5.21: Extinction coefficients at 85 GHz, for monodispersions of cirrus crystals at 10 m^{-3} concentration, calculated by the equivalent-area sphere method used in this thesis.

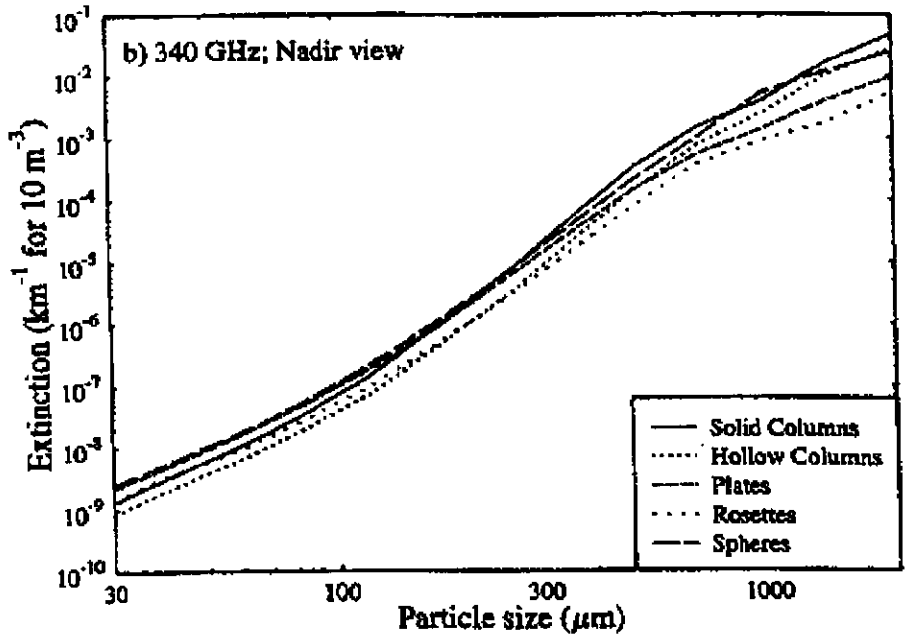

Figure 5.22: Extinction coefficients at 340 GHz, for monodispersions of cirrus crystals at 10 m^{-3} concentration, calculated by the discrete dipole approximation of Evans and Stephens [1995a].

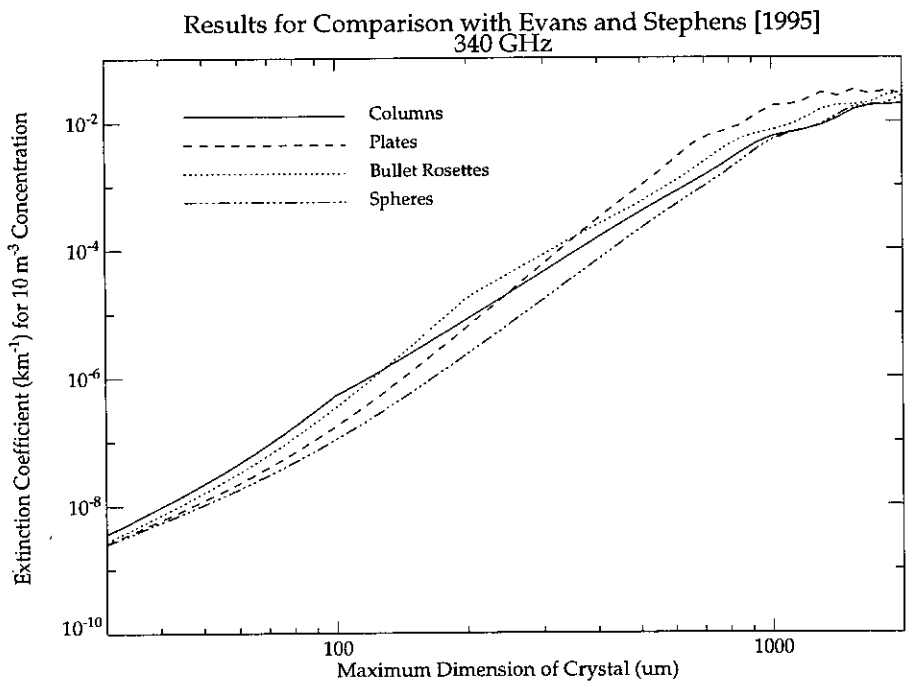

Figure 5.23: Extinction coefficients at 340 GHz, for monodispersions of cirrus crystals at 10 m^{-3} concentration, calculated by the equivalent-area sphere method used in this thesis.

and Stephens.

At 340 GHz there is less difference between the methods. The equivalent-area model again predicts an extinction due to bullet rosettes which is an order of magnitude higher than that found by the DDA, but the other habits differ by a factor of 2 or 3, similar to the difference which was found between the equivalent-area and equivalent-volume methods in section 5.5.

Therefore, if Evans and Stephens' method is indeed more representative of the extinction due to complex crystal shapes, it seems likely that the use of the equivalent-area sphere technique is leading to an overestimation of the extinction caused by cirrus. The significance of this overestimate to the results will be discussed when they are presented in chapter 6.

5.7 Parameters for Modelling Typical Cirrus Cloud

So far in this chapter I have described methods of representing the microphysical structure of a cirrus cloud as a dispersion of spheres. This simulated cloud may be added to the atmosphere of the forward model according to the method described in section 3.3.1. The model (that is, the forward model incorporating the scattering model) may then be used to determine the extent to which microwave observations of the atmosphere will be affected by the cloud. In order to perform such an experiment, a set of parameters will be needed to define the cloud, such as temperature, base and top heights, and ice water content. In this section the available cirrus climatology is examined to determine a set of average cirrus parameters which may be used to represent a typical cirrus cloud in the model.

In order simplify the process of obtaining a set of average cirrus statistics, various properties of the cirrus may be related to one another. In the following sections, relationships are given for cirrus top height against latitude, cirrus depth against latitude, temperature against ice water content, and temperature against height and latitude. A discussion of horizontal cloud extent is also included. Then finally in section 5.7.5, all the inter-relationships are brought together to define the 'typical' cirrus cloud for each latitude.

5.7.1 Cirrus Altitudes

Cloud top heights decrease with increasing latitude, consistent with the decrease in height of the tropopause. Dowling and Radke [1990] suggest that the typical cloud-centre height is about three-quarters of the height of the tropopause.

Comprehensive statistics for cloud top heights are available from the strato-

spheric aerosol and gas experiment (SAGE), from which McCormick [1987] (as reproduced by Dowling and Radke [1990]) produces a summary of mean cirrus top altitudes over an 11-month period. These data are given below in table 5.2.

Latitude	Mean Cloud Top Altitude	Latitude	Mean Cloud Top Altitude
65°N	7.0 km	65°S	7.0 km
55°N	8.2 km	55°S	8.2 km
45°N	9.5 km	45°S	8.7 km
35°N	9.7 km	35°S	9.6 km
25°N	10.9 km	25°S	10.3 km
15°N	13.0 km	15°S	12.0 km
5°N	13.3 km	5°S	13.5 km

Table 5.2: Cirrus top altitudes as measured by SAGE, from Dowling and Radke [1990].

In table 5.3 the height of the tropopause is tabulated against latitude (in either hemisphere) [Wang *et al* 1995]. Comparison of these heights with the contents of table 5.2 shows a broad agreement with the three-quarters rule of Dowling and Radke[3].

Latitude (N or S)	Tropopause Height
70°	9.0 km
60°	9.5 km
50°	10.5 km
40°	12.0 km
30°	14.5 km
20°	16.5 km
10°	17.0 km
0°	17.0 km

Table 5.3: Tropopause heights, from Wang *et al* [1995].

Borovikov *et al* [1963] comment that the altitude of cirrus varies with season, with higher clouds in summer than in winter. However, the amplitude of variation is only about 0.5 to 1.0 km.

[3]Note that Dowling and Radke's result is for cloud midpoints, rather than tops. However, as the next section will show, cirrus clouds are generally not more than a couple of km in depth.

5.7.2 Cirrus Depths

Dowling and Radke [1990] quote a mean depth of 1.5 km, obtained from a weighted mean of three different data sets, as being typical for cirrus, but point out that depths as great as 8 km may be found under certain conditions. In general they estimate that cirrus will occupy a range from 70% to 80% of the height of the tropopause – this ties in with their suggestion of mean cloud centre height described in the previous section. The depth of 1.5 km corresponds well with a figure of 1.7 km quoted by Liou [1986] in his discussion of cirrus climatology.

Borovikov *et al* [1963] discuss the variation of cloud base heights with latitude and conclude that the variation is much the same for bases as for tops, suggesting that cloud depths are relatively latitude-independent. Therefore a depth of 1.5 km was used at all latitudes to represent typical cirrus.

5.7.3 Horizontal Extent

The purpose of this section is to determine whether we can expect that cirrus cloud, when present, will occupy the full path length of the MLS line of sight as it passes between the altitudes of the cloud base and cloud top. The longest in-cloud path length occurs, for a given cloud base and top, when the tangent point is coincident with the base of the cloud, as shown in figure 5.24. The path length, L, is then given by:

$$L = 2[(R_e + h_{ct})^2 - (R_e + h_{cb})^2]^{\frac{1}{2}} \tag{5.23}$$

where h_{cb} and h_{ct} are the cloud base and top heights respectively.

For a cloud of the typical 1.5 km depth, at 40°N, table 5.2 gives cloud top and base heights as, respectively, $h_{ct} = 9.6$ km and $h_{cb} = 8.1$ km. The corresponding path length L from equation 5.23 is about 280 km. In the case of frontal cirrus it seems clear that cirrus sheets may extend for distances of this order and above. Dowling & Radke [1990] note that sheets of jetstream cirrus may cross entire continents almost unbroken, and an example of this is provided by Starr & Wylie [1988], who describe jetstream cirrus associated with a cold front extending 3000 km along the front, with a width of about 500 km. They also present observations, previously described in section 4.2.2, of a cirrus shield associated with a closed low which spans about 2000 km. Similarly, Heymsfield and Jahnsen [1974] report their observation, on several occasions, of a cirrus layer over the continental United States extending for over a thousand miles (1600 km).

In a more general sense, Borovikov *et al* [1963] quote statistics for the extent of frontal cirrus along a normal to the generating front, by giving frequencies of occurrence in 200 km bins from 0 km to 1000 km. The most frequent extent is

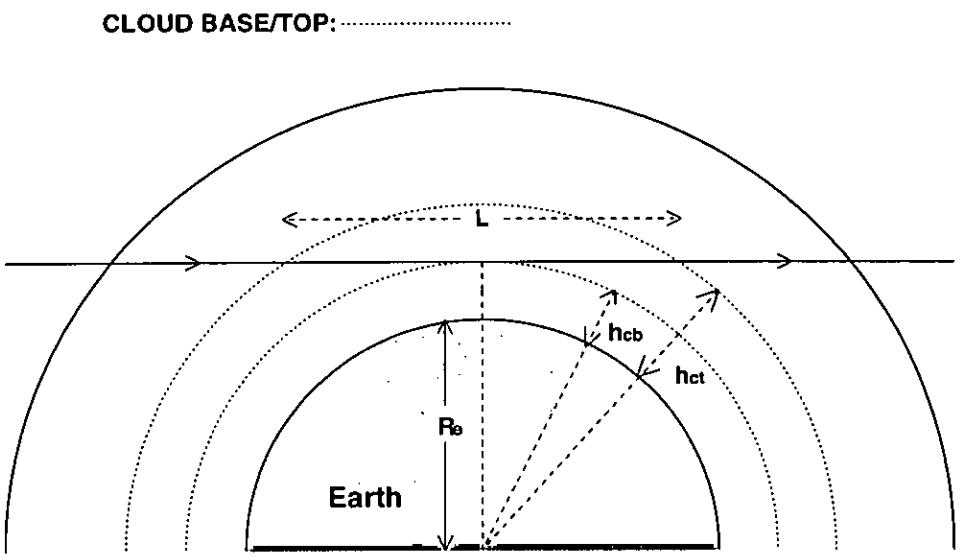

Figure 5.24: Geometry of a path with tangent height at cloud base.

about 400 km. Along the front, the authors note that the cloud may extend the entire length of the front, which may be 1000 km or more. It seems reasonable to assume that when frontal cirrus is present it occupies the entire path length of the line of sight between the appropriate altitudes.

In the case of anvil cirrus the situation is less straightforward. Horizontal extents documented in the literature for the anvils themselves range from the severe thunderstorm anvil described by Heymsfield [1986b], which extends for over 150 km, to the maritime winter cumulonimbus anvil described by Bennetts and Ouldridge [1984], which appears to cover only $\sim$ 13 km. However, in the tropical case, although the convective clusters themselves tend to be restricted to about 100 km across, the anvils are continually generated and spread out with time to cover hundreds of kilometres, as described in section 4.2.1.

To summarise, in the case of frontal cirrus, the horizontal extent of the cloud is likely to be such that the entire path length between the cloud base altitude and the cloud top altitude will be occupied by cirrus. In the case of tropical cirrus, the complete path length will not necessarily be within the cloud. There is no mechanism in the forward model at the time of writing to account for cirrus layers of limited horizontal extent, and so subsequent results for the tropical regions should be treated as a worst-case scenario.

5.7.4 Variation of IWC with Temperature

The parameterisation described in section 4.3.1 which provides the frontal cirrus size distribution requires the temperature of the cloud and its ice water content as inputs. Temperature is the more readily available parameter of the two, and so for the purposes of defining the typical cloud parameters, I have sought to find the IWC from the temperature using empirical relationships between the two. The tropical anvil particle size distributions which are used in the model are not parameterised according to ice water content, so a relationship between temperature and IWC is not required. Therefore the following discussion concerns frontal cirrus only.

Examination of the literature yields three independent data sets relating the ice water content to the temperature of the frontal cirrus cloud. Two of these are reported by Heymsfield [1993], who provides empirical relationships fitted to the data. The first expression is derived from data obtained by the Environmental Definition Programme (E.D.P.) in cirrus and cirrostratus over the U.S.A. Further details of the source of these data were not available[4]. The IWCs obtained are averages over about 20 km distances, and the temperatures sampled range from $-15°C$ to $-55°C$. The formula derived by Heymsfield is

$$\ln(\text{IWC}) = 0.558 + 0.0667T - 0.0016T^2 \tag{5.24}$$

where IWC is measured in gm^{-3} and T in °C.

The second set of results reported by Heymsfield [1993] comes from the First ISCCP Regional Experiment (FIRE), for cirrus and cirrostratus over Wisconsin.[5] The data given cover a temperature range of $-15°C > T > -45°C$, and are based on a much larger number of measurement points, averaged over about 0.5 km each. The resulting empirical fit is significantly different from that previously given by the E.D.P. data (see figure 5.25 later).

$$\ln(\text{IWC}) = -4.25 - 0.0044T - 0.00036T^2 \tag{5.25}$$

with units as for equation 5.24.

A third relation can be derived from the data given by Heymsfield and Platt [1984] (the same data used for the parameterisation of section 4.3.1). They provide mean IWC values for each set of measurements within a 5°C temperature band. Stephens *et al* [1990] provide an empirical fit to these data, but the expression they

[4] Heymsfield refers to a 1977 paper of his own in connection with this study, but the reference given is to Heymsfield [1978], which is a study of graupel in cumulus clouds, and appears to bear no relation either to this data set or to the E.D.P. in general.

[5] Heymsfield [1993] refers to Heymsfield *et al* [1990] in relation to these data, but this is a reference to FIRE in general rather than to the source of the data. Heymsfield *et al* [1990] do provide graphs of IWC against altitude, and temperature against altitude, but it seems clear that this does not represent the same set of data given by Heymsfield [1993].

give is incorrect; substitution of temperature into their expression gives the correct IWC at $-60°$, where their effective origin of temperature is located, but the value at $-20°$C is a straight factor of 10 out. Therefore the corrected expression below was used in place of that given by Stephens *et al.*

$$\text{IWC} = 0.0007 \exp[0.102(T + 60)] \tag{5.26}$$

where IWC and T are again measured in gm^{-3} and °C respectively.

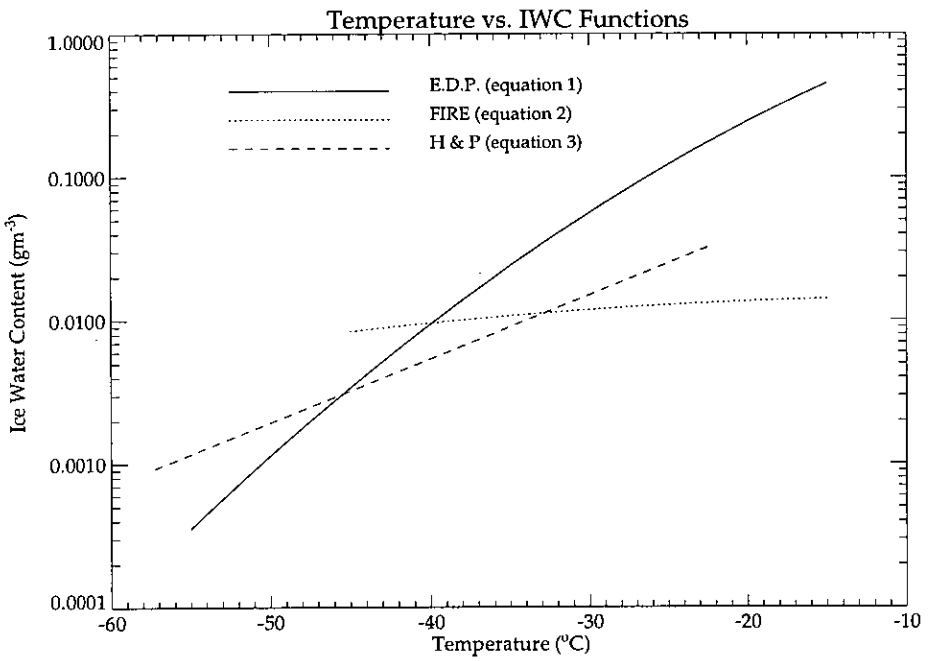

Figure 5.25: Empirical Functions of Temperature vs. IWC.

Graphical representation (figure 5.25) of these three expressions reveals that they are seriously inconsistent. However, the object of this exercise is only to gain an idea of the parameters for a typical cloud at a given latitude. Equation 5.26 is derived from Heymsfield and Platt's data set, which is the only one for which details of the original observations are available, allowing us to be sure of the nature of the measurements. Therefore it is this expression which is used to define the typical cirrus cloud's ice water content.

5.7.5 Typical Cloud Parameters

The information assembled in this section is sufficient to derive a set of parameters for a typical cirrus cloud which may be used in the forward model.

The seasonal and latitudinal conditions which were studied were restricted to those for which there is model atmosphere climatology data available: March, at the equator and at 40°N, and December at 70°N (see section 2.4.2). Interpolating

between the elements of table 5.2, mean cloud top altitudes may be obtained for these three latitudes of 13.4 km, 9.6 km, and about 7.0 km respectively. The cloud centre will therefore be 0.75 km below the top in each case for the standard 1.5 km deep cloud.

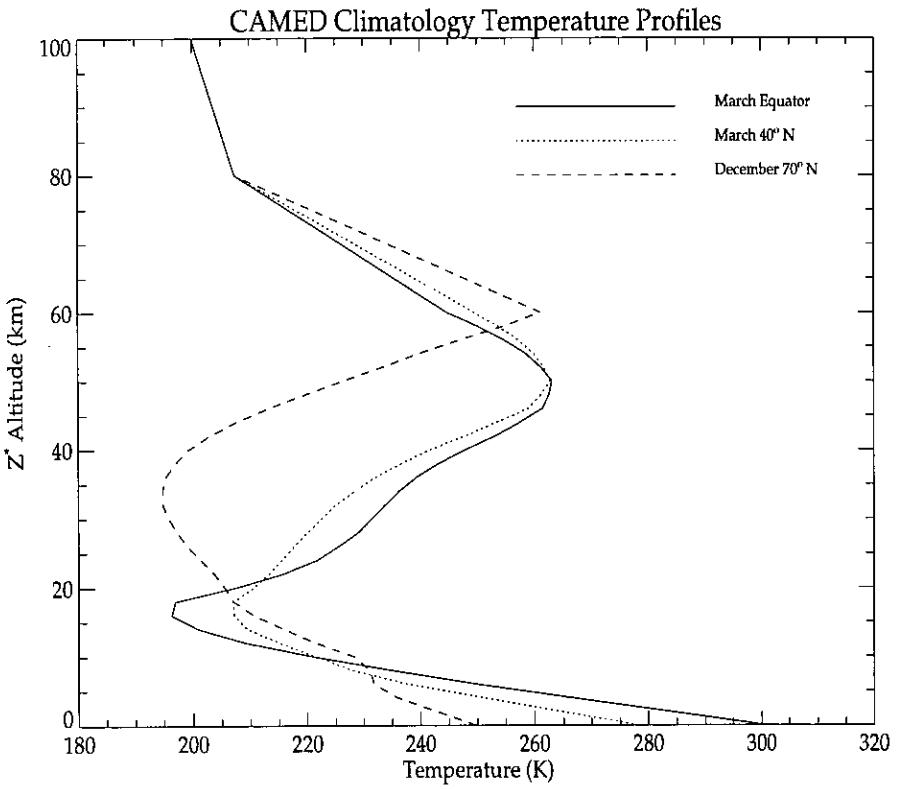

Figure 5.26: Vertical temperature profiles from the CAMED model atmosphere.

Figure 5.26 depicts the temperature profiles used in the CAMED model atmosphere (which has been described in chapter 2). From these profiles, the cloud centre altitudes can be roughly translated into typical cloud temperatures. Then, for each of the three latitude bands, the temperature may be used to define the ice water content where necessary. The mid- and high-latitudinal cirrus will typically be frontal in origin, while the equatorial cirrus will be due to tropical convective systems. So now typical clouds can be defined for each of the three latitudes in turn.

1. Firstly the high-latitudinal cloud (70°N), with a mean cloud midpoint height of 6.25 km, corresponds to a temperature of about 231 K, or −42°C. Obviously the temperature of the cloud varies throughout its depth, but to keep things simple I assume a uniform temperature (and therefore uniform microphysics) for the whole cloud. From equation 5.26, the mean IWC for a cloud at such a

temperature will be of order 0.004 gm^{-3}. The IWC can only be specified very approximately, given the nature of the temperature-IWC function. These parameters were fed into the model, and the cloud was included between 5.5 km and 7.0 km.

2. The same process was followed for the mid-latitudinal cloud at 40°N, with the cloud between 8.1 km and 9.6 km, at a temperature of −49°C, which corresponds to an IWC of about 0.002 gm^{-3}.

3. Finally, for the equatorial cloud, the base and height are 11.9 km and 13.4 km respectively, with a cloud midpoint temperature of −69°C. This is tropical convective cloud, and so the microphysics is different from that of the previous two cases. This temperature, −69°C, is the changeover point defined in section 5.4 between the 'cold' and 'warm' anvils derived from Knollenberg *et al* [1993]. For the purposes of this study I used the cold anvil. Therefore the temperature input to the model of the equatorial cirrus was changed slightly to −71°C, to put it into the cold anvil regime.

The standard model cloud parameters defined above are summarised in table 5.4.

	Equator	40°N	70°N
Cloud Top	13.4 km	9.6 km	7.0 km
Cloud Base	11.9 km	8.1 km	5.5 km
Temperature	−71°C	−49°C	−42°C
IWC	—	0.002 gm^{-3}	0.004 gm^{-3}

Table 5.4: Parameters for modelling an average cirrus cloud.

5.8 Chapter Summary

The simulation of cirrus cloud is now complete. A cirrus cloud at one of the specified latitudes 0°, 40°N, or 70°N, can be modelled according to its temperature, and if necessary its ice water content. Using the methods developed in this chapter, the raw size distribution can then be converted into a distribution of spheres which will hopefully mimic the scattering properties of the original distribution. A set of parameters has been defined to characterise an average cirrus cloud at each latitude.

The models developed in each of the chapters 2, 3, 4 and 5 were combined to produce a system which could simulate the influence which cirrus might be expected to exert on MLS tropospheric retrievals. In the next chapter the results of this combination of techniques are presented.

Chapter 6

Results

6.1 Introduction

It has been shown how the forward model calculates the microwave radiance from the atmosphere which would be observed by the EOS MLS. This forward model has been extended so that it is able to simulate approximately the scattering of microwave radiation by cirrus clouds. In this chapter, the effect of such scattering on the retrieval capabilities of the EOS MLS is investigated through the analysis of output from the forward model under various scattering conditions.

Before presentation of the results, the process of retrieval will be described at a basic level, to explain the way in which radiance measurements may be interpreted to give estimates of atmospheric composition, and therefore how errors in the measurements propagate into errors in the retrieval.

The first set of results presented introduces the regions of the microwave spectrum which will be observed by the EOS MLS, and demonstrates the nature of the information we expect to gain from observations at such frequencies. Then the influence functions are discussed, which provide a measure of the sensitivity of the observed radiances to changes in the atmospheric parameters that are being measured. Included in this discussion is a method of increasing measurement sensitivity by coarsening the resolution of the measurement grid. Finally the retrieval theory already developed is used to combine these influence functions with an estimate of the measurement error, to create profiles of the expected error in the retrieved quantities, and thus to determine the vertical range over which the retrieval is feasible. At this stage the scattering process is introduced to the model, to provide a second set of results which apply in the presence of cirrus cloud. The direct effect of the cloud on the observed radiance is demonstrated, as well as the consequences for the vertical range of the retrieval.

To conclude the chapter the most important results are identified and discussed.

6.2 Retrieval Theory

Retrieval is the process of deducing the atmospheric state from the microwave radiances measured by the MLS. The true profile of any given atmospheric parameter (the *state* profile) is a continuous function, and so a finite number of measurements[1] is not sufficient to determine the profile completely. The problem is ill-posed, and the solution is underconstrained, so there are in fact an infinite number of solution profiles which would produce the same set of measurements.

The problem may be constrained and simplified by *discretisation*, that is the representation of the solution profile by a finite number of coefficients. This may be done by expressing the continuous state profile $x(z)$ as a linear combination of *basis functions* $B_i(z)$ as follows:

$$x(z) = \sum_i x_i B_i(z) \tag{6.1}$$

The aim of the retrieval is then to determine the most probable values of the coefficients x_i for a given set of measurements.

The form of the basis functions is arbitrary, and the solution coefficients obtained by retrieval are unique only for the chosen form. For this thesis the continuous state profile was piecewise-linear, formed of interpolative line segments linking values of the atmospheric state sampled at each grid point. Such a profile may be represented by triangular basis functions of unit magnitude, each spanning two grid levels. The coefficients are then simply the point values of the continuous state profile at each level. This type of discretisation and linear representation is illustrated in figure 6.1. The solid curve is a smooth state profile, and the long-dashed line is a piecewise-linear representation of the state profile. The multiples of the triangular basis functions which can be linearly combined to form the piecewise-linear profile are shown alternately by the dotted and short-dashed lines.

The discretisation is not sufficient by itself to fully constrain the solution and make the problem well-posed, so a pre-determined *virtual measurement* is required to supplement the real measurements. The virtual measurement is a linear constraint of the same form as the real measurement. This concept will be discussed further in section 6.2.2.

The theory discussed in the remainder of this section is general and independent of the choice of basis functions. Since the measurements and the state profile coefficients are finite in number and discrete, vector and matrix notation may be used. Vectors will be denoted by bold lower-case characters, eg. $\mathbf{y}$, and matrices by bold upper-case, eg. $\mathbf{K}$.

[1] The word 'measurement' is used throughout this chapter to refer to the radiances observed by the MLS.

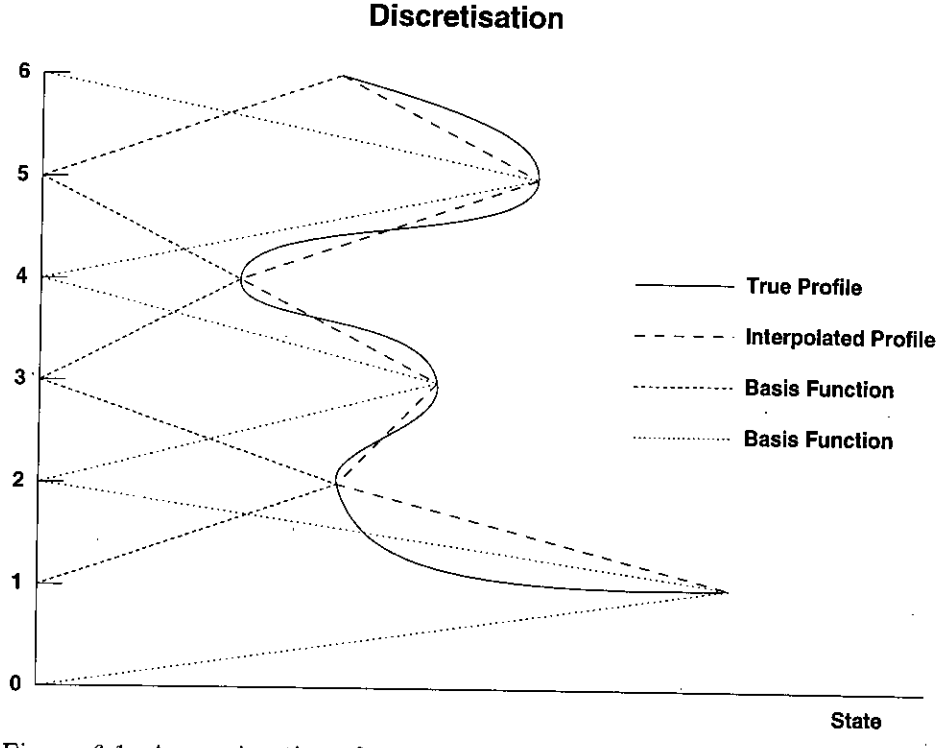

Figure 6.1: Approximation of a smooth profile by linear interpolation, and representation by a set of triangular basis functions.

6.2.1 The Forward Problem

The fundamental vectors are the *state vector* $\mathbf{x}$, which is the set of coefficients x_i that define the atmospheric state profile, and the *measurement vector* $\mathbf{y}$, which is the set of radiances which are observed. The measurement vector contains radiances from all the radiometer channels for all the pointing heights[2] examined.

The measurement vector is related to the state vector by the forward problem, expressed thus:

$$\mathbf{y} = F(\mathbf{x}, \mathbf{b}) + \boldsymbol{\epsilon} \tag{6.2}$$

where F is the *forward model*, which operates on $\mathbf{x}$ and a set of independent parameters $\mathbf{b}$ which are not retrieved but which affect $\mathbf{y}$. The final term, $\boldsymbol{\epsilon}$, is the noise error vector, each element of which is the random noise on the corresponding radiance in $\mathbf{y}$. In the case that there is no systematic error inherent in the measuring system, the mean of $\boldsymbol{\epsilon}$ over a large number of independent measurements will be the zero vector, and its statistical distribution will be characterised by a covariance matrix $\mathbf{S}_\epsilon$.

Small perturbations in $\mathbf{y}$ may be considered approximately linear with respect

[2]The *pointing height* is the tangent height of the line of sight along the central axis of the MLS antenna.

to perturbations in $\mathbf{x}$, so the two may be related as follows:

$$(\mathbf{y} - \overline{\mathbf{y}}) = \mathbf{K}(\mathbf{x} - \overline{\mathbf{x}}) \tag{6.3}$$

where $\overline{\mathbf{y}}$ and $\overline{\mathbf{x}}$ are linearisation vectors which are assumed to be close to the true values. The rows of the matrix $\mathbf{K}$ are the *influence functions*, defined by $\mathbf{K} = \partial F/\partial \mathbf{x}$. Since this is a partial derivative, and the second term in equation 6.2 has no explicit dependence on $\mathbf{x}$, it may also be stated that

$$\mathbf{K} = \frac{\partial \mathbf{y}}{\partial \mathbf{x}} \tag{6.4}$$

Equation 6.3 shows that the perturbation in $\mathbf{y}$ is a weighted mean of the perturbations in $\mathbf{x}$, with weights given by the rows of $\mathbf{K}$. For this reason the rows of $\mathbf{K}$ are also known as *weighting functions*.

6.2.2 The Inverse Problem

The inverse problem is the relationship between the estimate of the state vector, $\hat{\mathbf{x}}$, and the measurement vector $\mathbf{y}$. It is expressed thus:

$$\hat{\mathbf{x}} = I(\mathbf{y}, \mathbf{b}, \mathbf{c}) \tag{6.5}$$

where I is the *inverse model* or *retrieval*, $\hat{\mathbf{x}}$ is the retrieved set of estimates for the true state $\mathbf{x}$, and $\mathbf{c}$ is the set of parameters required by the retrieval which do not appear in the forward model. These extra parameters must include the virtual measurements which are required to constrain the problem.

A simple method of retrieval is *optimal estimation*, the determination of the most probable solution $\hat{\mathbf{x}}$ given a set of measurements $\mathbf{y}$ and a virtual measurement (or rather a virtual state) $\mathbf{x}_a$, called the *a priori* state. Strictly speaking the discretisation is itself an *a priori* constraint, but in this discussion the term is used only to refer to $\mathbf{x}_a$. The *a priori* state should be a realistic estimate of the true state $\mathbf{x}$, and will have an associated covariance $\mathbf{S}_a$ which represents the statistics of the deviation $(\mathbf{x}_a - \mathbf{x})$. Typically $\mathbf{x}_a$ would be a climatological average profile, with its associated statistical covariance.

In optimal estimation, the *a priori* state is combined as a weighted mean with the state derived from the measurements, to obtain a retrieval state $\hat{\mathbf{x}}$ for which the associated covariance $\hat{\mathbf{S}}$ is minimised. When the measurements are linearly related to the true state, as in equation 6.3, the resulting optimal solution is that given by Rodgers [1976]:

$$\hat{\mathbf{x}} - \overline{\mathbf{x}} = (\mathbf{S}_a^{-1} + \mathbf{K}^T\mathbf{S}_\epsilon^{-1}\mathbf{K})^{-1}(\mathbf{S}_a^{-1}[\mathbf{x}_a - \overline{\mathbf{x}}] + \mathbf{K}^T\mathbf{S}_\epsilon^{-1}[\mathbf{y} - \overline{\mathbf{y}}]) \tag{6.6}$$

where $\mathbf{S}_\epsilon$ is the covariance of the radiance measurements $\mathbf{y}$, and $\mathbf{K}^T$ is the transpose of $\mathbf{K}$. The linearisation vectors $\overline{\mathbf{x}}$ and $\overline{\mathbf{y}}$ are arbitrary, but are assumed to be close

enough to the true state and measurement vectors that deviations from them are linearly related. The form of equation 6.6 is slightly different from that given by Rodgers [1976], who assumes that $\mathbf{y}$ is linearly related to $\mathbf{x}$, not just for small deviations about a linearisation point.

The covariance $\hat{\mathbf{S}}$ associated with this optimal solution is given by Rodgers as

$$\hat{\mathbf{S}} = (\mathbf{S}_a^{-1} + \mathbf{K}^T \mathbf{S}_\epsilon^{-1} \mathbf{K})^{-1} \tag{6.7}$$

6.2.3 Error Analysis

The eventual aim of this study is to determine the error introduced into a given retrieval by the presence of cirrus. To evaluate this effect it is necessary to perform an error analysis on the inverse problem, in order to separate out the individual sources of error in the retrieved state. The procedure followed is that developed by Rodgers [1990].

The sources of error in the retrieval can be identified by a linearisation of the inverse model. Reconsider the inverse model given in equation 6.5, and substitute for $\mathbf{y}$ from equation 6.2:

$$\hat{\mathbf{x}} = I[F(\mathbf{x}, \mathbf{b}) + \epsilon, \hat{\mathbf{b}}, \hat{\mathbf{c}}] \tag{6.8}$$

where $\hat{\mathbf{b}}$ and $\hat{\mathbf{c}}$ are our best estimates of the model parameters. The measurements $\mathbf{y}$ are only truly represented by the forward model when the parameters $\mathbf{x}$ and $\mathbf{b}$ are the true values, which only nature 'knows'. In a forward model, these parameters are only known as estimates, and so errors are introduced to the retrieved quantities. It is expected that the estimated quantities will be close to the true values, so a linearisation may be performed to analyse the resulting errors. This is done below, firstly for $\mathbf{b}$.

By the first-order Taylor expansion of F about $\mathbf{b} = \hat{\mathbf{b}}$, equation 6.8 becomes

$$\hat{\mathbf{x}} = I\left[F(\mathbf{x}, \hat{\mathbf{b}}) + \frac{\partial F}{\partial \mathbf{b}}(\mathbf{b} - \hat{\mathbf{b}}) + \epsilon, \hat{\mathbf{b}}, \hat{\mathbf{c}}\right]$$

and then the subsequent first-order Taylor expansion of I about $\mathbf{y} = F(\mathbf{x}, \hat{\mathbf{b}})$ gives:

$$\hat{\mathbf{x}} = I[F(\mathbf{x}, \hat{\mathbf{b}}), \hat{\mathbf{b}}, \hat{\mathbf{c}}] + \frac{\partial I}{\partial \mathbf{y}}\left[\frac{\partial F}{\partial \mathbf{b}}(\mathbf{b} - \hat{\mathbf{b}}) + \epsilon\right] \tag{6.9}$$

At this point some definitions may be made to simplify the discussion. By analogy with the influence functions defined in section 6.2.1, we can define the *parameter influence functions* $\mathbf{K}_b = \partial F / \partial \mathbf{b}$ to represent the sensitivity of the measurement to the forward model parameters. Similarly, the sensitivity of the retrieved state to the measurements is represented by the *contribution function* $\mathbf{D}$, given by

$$\mathbf{D} = \frac{\partial I}{\partial \mathbf{y}} = \frac{\partial \hat{\mathbf{x}}}{\partial \mathbf{y}} \tag{6.10}$$

Finally, the first term of equation 6.9 can be represented by the *transfer function* T as follows:

$$I[F(\mathbf{x}, \hat{\mathbf{b}}), \hat{\mathbf{b}}, \hat{\mathbf{c}}] = T(\mathbf{x}, \hat{\mathbf{b}}, \hat{\mathbf{c}}) \tag{6.11}$$

The transfer function represents the way in which a state profile is altered as it is converted into a measurement by the forward model, and back again by the inverse model.

With these definitions in place, equation 6.9 becomes:

$$\hat{\mathbf{x}} = T(\mathbf{x}, \hat{\mathbf{b}}, \hat{\mathbf{c}}) + \mathbf{D}\mathbf{K}_b(\mathbf{b} - \hat{\mathbf{b}}) + \mathbf{D}\boldsymbol{\epsilon} \tag{6.12}$$

Now by the same method that has been used to linearise about $\hat{\mathbf{b}}$, I may be linearised about a suitable state vector $\overline{\mathbf{x}}$, to give:

$$\hat{\mathbf{x}} = T(\overline{\mathbf{x}}, \hat{\mathbf{b}}, \hat{\mathbf{c}}) + \mathbf{D}\mathbf{K}(\mathbf{x} - \overline{\mathbf{x}}) + \mathbf{D}\mathbf{K}_b(\mathbf{b} - \hat{\mathbf{b}}) + \mathbf{D}\boldsymbol{\epsilon} \tag{6.13}$$

Note that the linearisation state vector $\overline{\mathbf{x}}$ is not necessarily the same as that used in equation 6.3, since both are arbitrary.

Now subtracting the true state vector from each side of equation 6.13, and rearranging, the expected error in the retrieved state is found to be

$$\hat{\mathbf{x}} - \mathbf{x} = [T(\mathbf{x}, \hat{\mathbf{b}}, \hat{\mathbf{c}}) - \overline{\mathbf{x}}] + (\mathbf{D}\mathbf{K} - \mathbf{I})(\mathbf{x} - \overline{\mathbf{x}}) + \mathbf{D}\mathbf{K}_b(\mathbf{b} - \hat{\mathbf{b}}) + \mathbf{D}\boldsymbol{\epsilon} \tag{6.14}$$

where $\mathbf{I}$ is the unit matrix.

The terms enclosed in square brackets on the right hand side of equation 6.14 represent a systematic error due to bias in the inverse model. This bias may be evaluated and then offset from future calculated values, and so its effect may be neglected here. The remaining three terms represent three distinct sources of error.

- The first term, $(\mathbf{D}\mathbf{K} - \mathbf{I})(\mathbf{x} - \overline{\mathbf{x}})$, is the *smoothing error* which corresponds to those parts of the true profile that cannot be observed by the *measurement system* (the MLS itself combined with the retrieval method used). A smoothing error is a necessary consequence of discretisation. The covariance of this error is represented by

  $$\mathbf{S}_s = (\mathbf{D}\mathbf{K} - \mathbf{I})\mathbf{S}_x(\mathbf{D}\mathbf{K} - \mathbf{I})^T$$

  where $\mathbf{S}_x$ is the covariance of $(\mathbf{x} - \overline{\mathbf{x}})$.

- The second term is the *parameter error*, which represents the uncertainty in the retrieved state arising from the uncertainty in the parameters $\hat{\mathbf{b}}$ used in the forward model. If the uncertainty $(\mathbf{b} - \hat{\mathbf{b}})$ is characterised by a covariance $\mathbf{S}_b$, then the resulting covariance in the retrieved state is given by

  $$\mathbf{S}_p = \mathbf{D}\mathbf{K}_b\mathbf{S}_b\mathbf{K}_b^T\mathbf{D}^T$$

It will be shown later that the effect of cirrus extinction may be considered as a parameter error.

- The final term is the *measurement error*, caused by noise in the radiometer system. Ideally the error itself, ϵ, will average to zero, but there is an associated error covariance $\mathbf{S}_\epsilon$, which causes an error in the retrieval given by

$$\mathbf{S}_M = \mathbf{D}\mathbf{S}_\epsilon\mathbf{D}^T$$

The error analysis described up to this point is general to any linear inverse model, and may be applied specifically to the optimal estimation solution given by equations 6.6 and 6.7. Therefore the contribution function, defined in equation 6.10 may be found for optimal estimation by differentiating the right hand side of equation 6.6 with respect to $\mathbf{y}$, to give:

$$\mathbf{D} = \hat{\mathbf{S}}\mathbf{K}^T\mathbf{S}_\epsilon^{-1} \tag{6.15}$$

Using this definition the retrieval errors separated in equation 6.14 may be evaluated for the optimal estimation solution.

The three error contributions are independent, so the total covariance $\hat{\mathbf{S}}$ is the sum of the three covariances $\mathbf{S}_S$, $\mathbf{S}_P$, and $\mathbf{S}_M$. When relating this to the total covariance defined for the optimal estimation solution in equation 6.7, it should be borne in mind that there is no parameter error implied in the derivation of that solution, so $\hat{\mathbf{S}}$ excludes the contribution from $\mathbf{S}_P$.

Cirrus cloud is an unretrieved quantity which nevertheless influences the radiances calculated by the forward model. If it is not somehow included in the state vector, then it exists as a model parameter with an associated error. It is not readily quantifiable as a parameter, so the expression $(\mathbf{b} - \hat{\mathbf{b}})$ has no particular meaning, but its effect on the radiance (i.e. the difference $(\Delta\mathbf{y})_c$ between the radiance in its presence and that in its absence) may be written as

$$(\Delta\mathbf{y})_c = \mathbf{K}_b(\mathbf{b} - \hat{\mathbf{b}}) \tag{6.16}$$

and therefore the 'cloud parameter error' from equation 6.14 is given by:

$$(\Delta\hat{\mathbf{x}})_c = \mathbf{D}(\Delta\mathbf{y})_c \tag{6.17}$$

This expression will be used later in this chapter to quantify the effect that cirrus has on MLS retrievals. The retrievals affected will be in the troposphere, and in the next section the measurements which will be used to make these retrievals are discussed.

It is possible to devise a way of characterising a cirrus cloud such that it could be included in the state vector. For example, a discrete profile of its extinction

coefficient might be appended to $\mathbf{x}$, and a retrieval of the cloud could then be attempted. Such a technique would be unlikely to succeed, since the extinction due to cirrus does not provide a distinctive spectral signature which the retrieval would be able to identify. However, such a method may be effective in reducing the uncertainty associated with cirrus. The question of how to account for the presence of cirrus, whether in the forward model or in the inverse model, is addressed further in section 6.6.1.

6.3 Tropospheric Brightness Temperature Spectra

The proposed radiometer frequencies for the EOS MLS have been subject to frequent revision. The objective of the EOS MLS project is the measurement of various atmospheric parameters at certain altitudes, as detailed in chapter 1, and the choice of what frequencies to use to measure these parameters has been determined from the forward modelling results of Mark Filipiak. For the purposes of this study, three double-sideband measurements were chosen on the basis of suggestions by Filipiak to represent proposed tropospheric measurements to be made by the EOS MLS.

The selected bands will be referred to in the rest of this chapter as bands 1,2 and 3, and are specified as follows:

- Band 1: 203.3 ± 1.1 GHz, measuring tropospheric H_2O.
- Band 2: 239.7 ± 3.2 GHz, measuring tropospheric O_3.
- Band 3: 642.9 ± 6.6 GHz, also measuring tropospheric H_2O.

For each of the bands, brightness temperature spectra were produced for each of the latitude-season cases of the model atmosphere described in section 2.4.2, that is: the equator and 40°N during March, and 70°N during December. In this section, brightness temperature spectra are shown for the equatorial case only, as they are intended solely as an illustration of the general spectral characteristics of each band. The results are presented below for each band in turn.

6.3.1 Band 1 (H_2O) Spectra

Figure 6.2 shows the modelled brightness temperature spectrum across a 4 GHz band centred on 203.3 GHz, for a limb view of tangent height 15 km at the equator. The strongest lines within the band are labelled with the name of the chemical species that produced them, and the two sidebands of the EOS MLS measurement are marked by vertical dashed lines. In certain cases the labelling of the lines is not particularly useful; for instance the water line labelled in the centre of the plot is not distinguishable because it lies on the wing of the stronger ozone line. Similarly,

there is a peak near the centre of the upper sideband which is unlabelled, because it is due to a closely-spaced group of ClO lines rather than a single strong line.

Although the sidebands sit on the wings of the strong O_3 line in the centre of the spectrum, there is a larger contribution to the overall radiance from the water vapour continuum, and it is this contribution which is used to retrieve the H_2O mixing ratio.

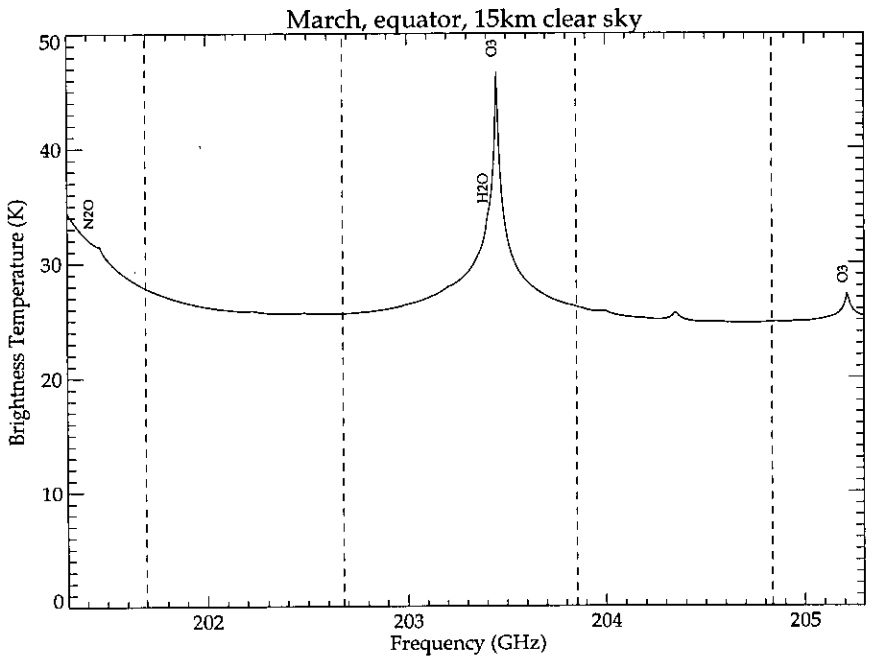

Figure 6.2: Brightness temperature spectrum around the 203.3 GHz radiometer centre at the equator, tangent height 15 km. Vertical dashed lines delimit the EOS MLS sidebands. The strongest spectral lines are labelled with chemical names.

By way of contrast, figure 6.3 shows the same spectrum for a limb view at a tangent height of 6 km. At such low altitudes and high pressures the ozone line is swamped beneath the large contributions from the water vapour continuum and from the wings of broadened nearby lines. The strong water line is again labelled, but it is not distinguishable from the surrounding continuum.

The radiance received from the radiometer's mixer is a double sideband measurement, so the output spectrum will be a sum of the two sideband brightness temperature spectra when they are folded on top of each other, as described in section 2.5. For this measurement both sidebands are providing useful information, because the measurement is based on the almost-flat H_2O continuum defined by equation 2.19. This is not the case for higher-altitude retrievals, which tend to be based upon a single spectral line which lies in one sideband, while the other sideband contributes a contaminant signal and is chosen such that it is as insensitive

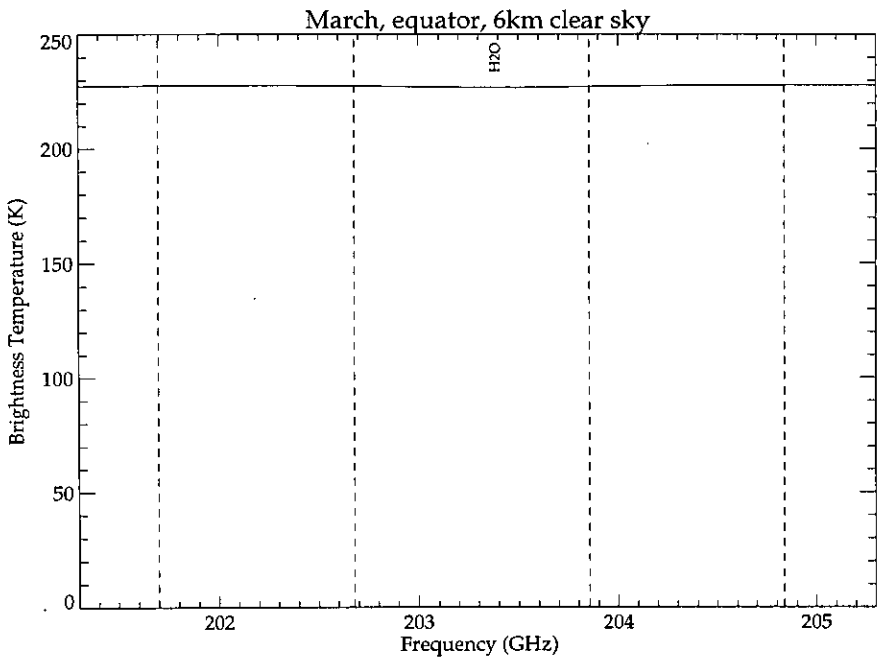

Figure 6.3: Brightness temperature spectrum around the 203.3 GHz radiometer centre at the equator, tangent height 6 km. Vertical dashed lines delimit the EOS MLS sidebands, strongest spectral lines are labelled.

as possible.

The double sideband measurement is shown in figure 6.4, at various heights in the troposphere. The brightness temperature spectrum is separated into the 21 channels which will be used by EOS MLS, with the radiance in each channel represented by a horizontal line segment of length equal to the filter width. However, the separate filters cannot be distinguished in this example since the spectrum is so flat, so the centres of the filters have been indicated by vertical bars on the 15 km spectrum.

6.3.2 Band 2 (O_3) Spectra

The brightness temperature spectrum around the 239.662 GHz radiometer is shown in figure 6.5 for a 15 km tangent height at the equator. Again, the principal emission lines are identified, and the sidebands of the radiometer are demarcated by the dashed lines.

The two sidebands span the troughs between two separate pairs of strong ozone lines, and the brightness temperature across these troughs is sensitive to changes in the ozone concentration in the upper troposphere, as will be demonstrated later. Once again, both sidebands are contributing a similarly shaped signal which is symmetrical in frequency, which means that when the two sidebands are folded on top of each other to produce the double-sideband response of the mixer, the

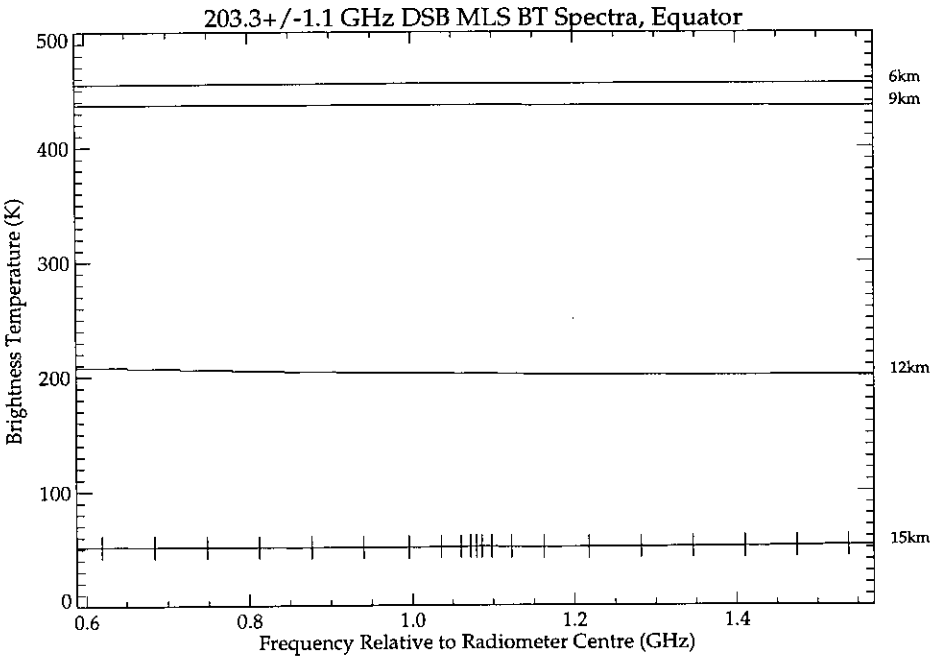

Figure 6.4: Filtered double sideband brightness temperature spectra for band 1 at the equator. Filter centres are indicated by vertical bars on the 15 km spectrum.

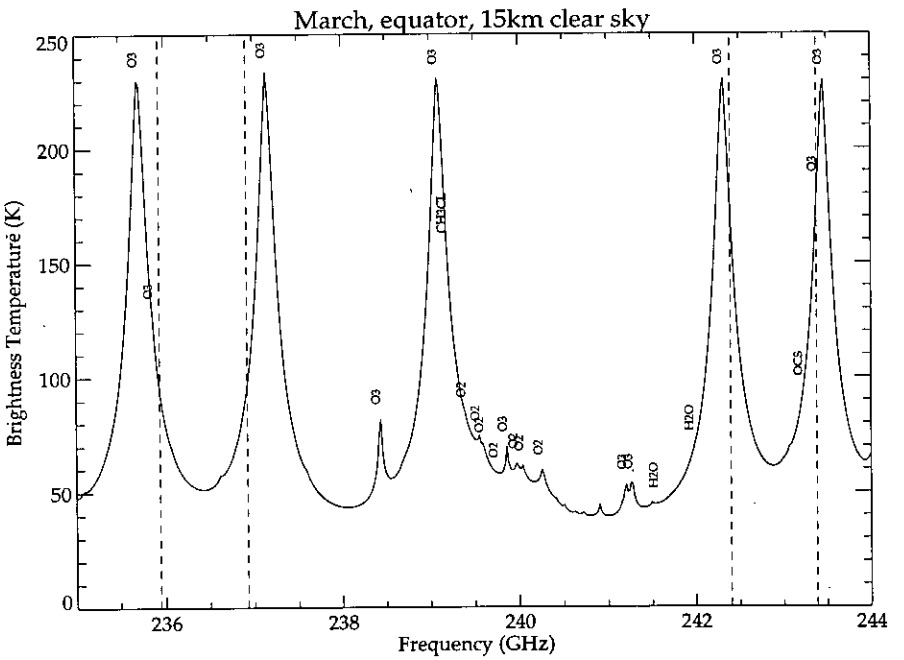

Figure 6.5: Brightness temperature spectrum around the 239.7 GHz radiometer centre at the equator, tangent height 15 km. Vertical dashed lines delimit sidebands, strongest spectral lines are labelled.

information content is enhanced rather than cross-contaminated. Figure 6.6 shows the filtered double-sideband measurement, for a number of heights through the troposphere at the equator. At the top of the troposphere there is some shape to the trough, which enhances the information content of the retrieval, but at lower altitudes the shape is swamped by the water-vapour continuum.

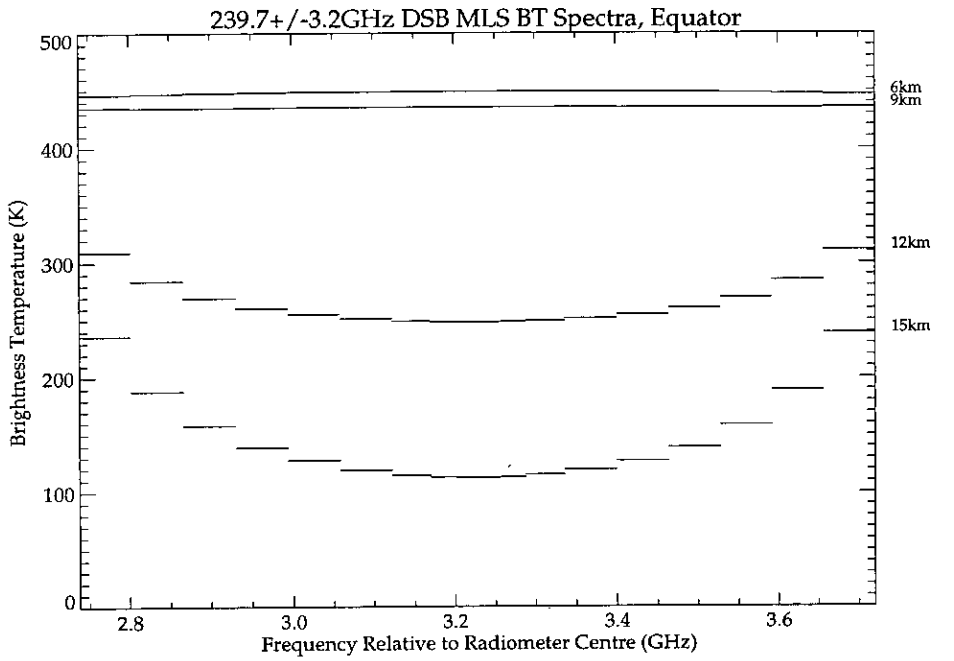

Figure 6.6: Filtered double sideband brightness temperature spectra for band 2 at the equator. The bandwidth of each filter is represented by a horizontal line segment.

6.3.3 Band 3 (H_2O) Spectra

The third and final prospective measurement would be made by a radiometer operating at a centre frequency of 642.85 GHz, with sidebands centred on 6.60 GHz on either side. The spectrum around this radiometer and the part which falls within the sidebands is depicted in figure 6.7, again for a tangent height near the top of the troposphere at 15 km, and at the equator. Some contamination of the sidebands is apparent: in the upper sideband there are two features, one of which is a weak ozone line at 649.137 GHz; and in the lower sideband there is a similar ozone line at 636.124 GHz, and a band of CH_3Cl lines just to the high frequency side of the band, which gives the spectrum an upward gradient towards that end.

The filtered double-sideband combination shown in figure 6.8 demonstrates that the shape of the filter bank effectively removes the lineshape information from those contaminant lines which lie away from the band centre, because they are averaged

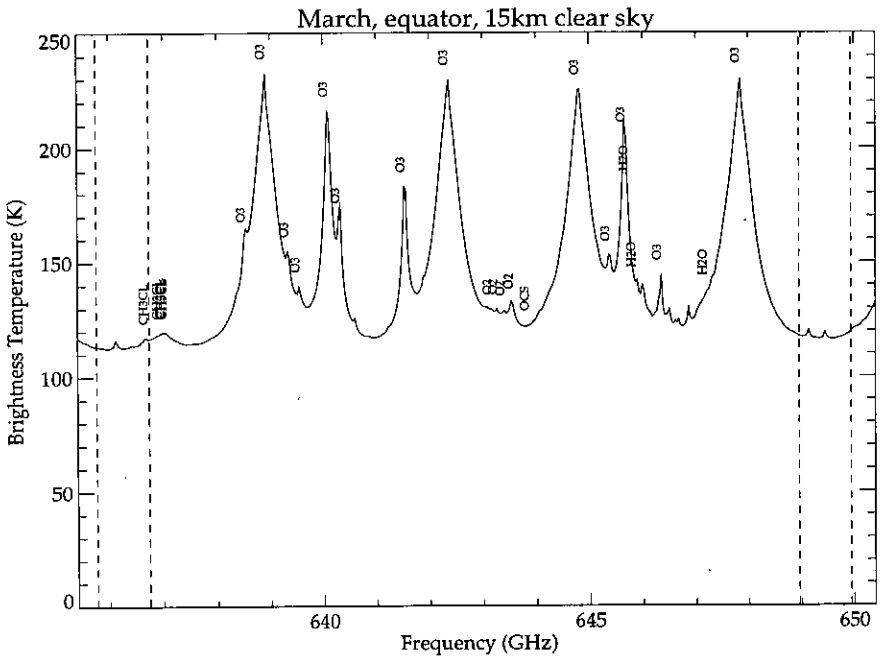

Figure 6.7: Brightness temperature spectrum around the 642.9 GHz radiometer centre at the equator, tangent height 15 km. Sidebands are delimited by vertical dashed lines. Strongest spectral lines are labelled.

over wide filters. The small feature in the centre of the upper sideband is resolved at the top of the troposphere, but it is of negligible size and becomes unresolved at lower altitudes.

6.4 Influence Functions

6.4.1 Introduction

The sensitivity of the observed brightness temperature spectra to the atmospheric parameters which we want to quantify is represented by the influence functions which were defined in section 6.2.1. These are calculated by equation 6.4, which in practice is evaluated by the following process. First, the forward model is used to produce filtered, double-sideband brightness temperature spectra for pointing heights spaced at 1 km intervals between the ground and 30 km. Then the input *state profile*, for example the profile of water vapour mixing ratio, is perturbed by 10% at the first level (corresponding approximately to an altitude of 1 km), and another 31 spectra are calculated. This process is repeated for each of the state level profiles up to the 30th. The elements of the influence function array are then calculated by dividing the change in brightness temperature of each measurement, ΔT_B, by the change in mixing ratio (or other state variable) Δr, which caused the

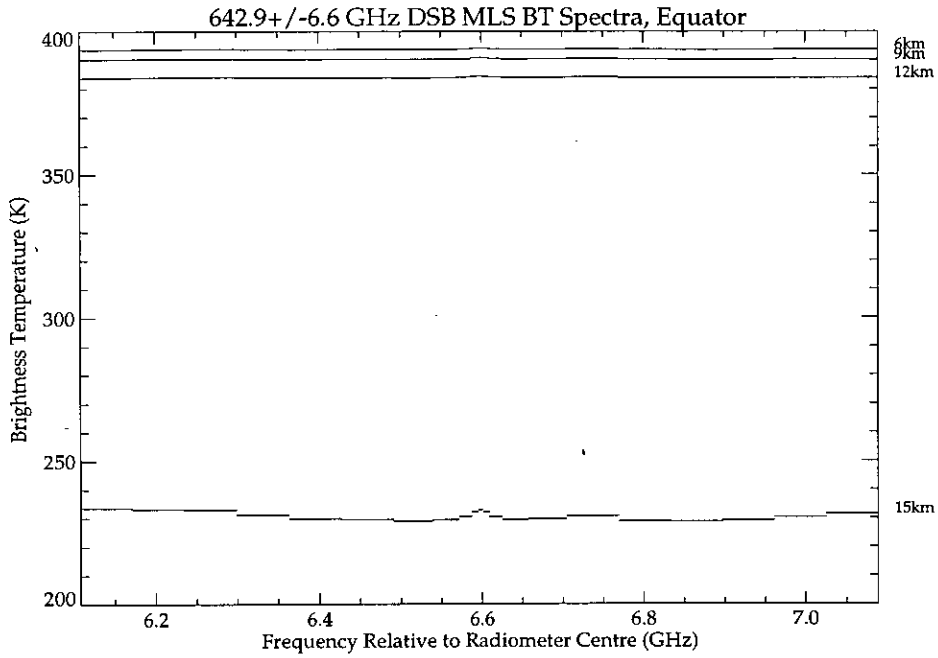

Figure 6.8: Filtered double sideband brightness temperature spectra for band 3 at the equator. The bandwidth of each filter is represented by a horizontal line segment.

change in brightness temperature. In this way the approximation is being made that

$$\frac{\partial T_{\mathrm{B}}}{\partial r} \simeq \frac{\Delta T_{\mathrm{B}}}{\Delta r} \tag{6.18}$$

which is assumed to hold for small changes in r. Since the brightness temperatures T_{B} are the elements of the measurement vector $\mathbf{y}$, and the mixing ratios r are the elements of the state vector $\mathbf{x}$, the ratio in equation 6.18 is equivalent to an element of the influence function matrix $\mathbf{K}$ as defined by equation 6.4.

The size of the perturbation in r is chosen as a trade-off between the need to have Δr as low as possible for the linear approximation to be safe, and the need to have a ΔT_{B} which is distinguishable above the numerical noise inherent in the model. A perturbation of 10% was found to be suitable through a process of trial and error.

The influence function matrix $\mathbf{K}$ is a two-dimensional matrix with a vertical axis corresponding to $\mathbf{y}$ (the *measurement axis*), and a horizontal axis corresponding to $\mathbf{x}$ (the *state axis*). Therefore it has a row, labelled j, for each measurement level, and a column, labelled i, for each retrieved state level (i.e. each perturbation level).

6.4.2 Changing the Resolution of Influence Functions

When a single element of the state vector is perturbed, the resulting perturbation of the piecewise-linear profile used in the forward model is triangular, because in effect a single triangular basis function is being perturbed (see figure 6.1). As described above, these perturbations were performed on state levels at pressure height[3] intervals of 1 km*, so $\mathbf{K}$ will have a column for each 1 km* level. In a manner of speaking, the information content of the measurement vector $\mathbf{y}$ is distributed amongst these 1 km* levels. Intuitively it can be seen that if this information is divided over fewer columns, the information content of each step must be larger in order to conserve the total information content for measurement j. Therefore, if the resolution on the state axis is made coarser, the influence functions will increase, i.e. the measurement is made more sensitive.

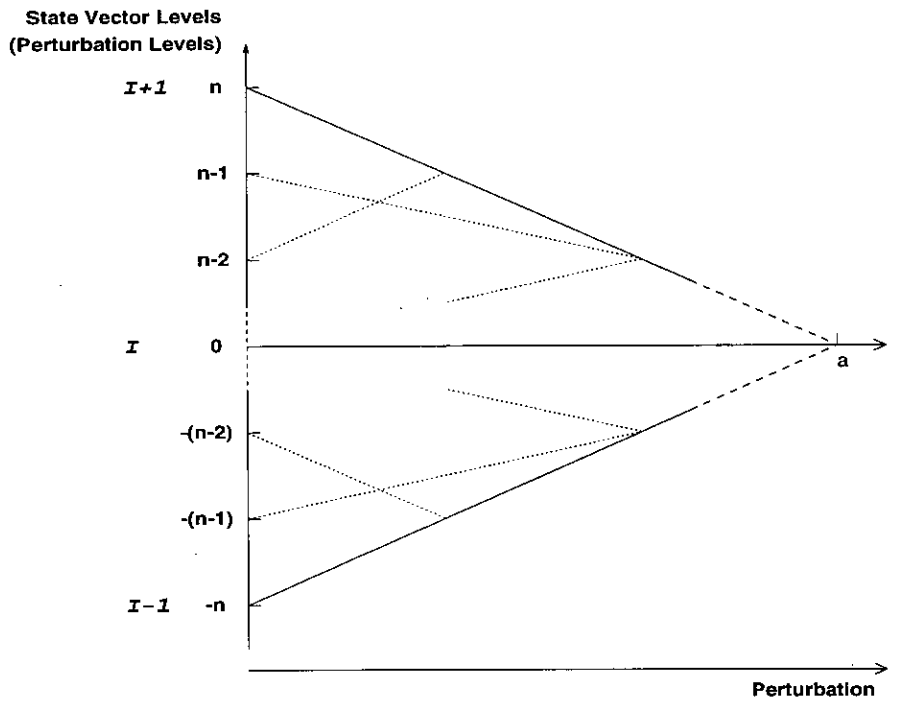

Figure 6.9: Triangular perturbation on an n km resolution grid, represented as a sum of 1 km perturbations.

In order to change the resolution of $\mathbf{K}$ such that it has a column for every n km* level (where n is some integer > 1), it is first necessary to calculate how an n km* perturbation is expressed in terms of 1 km* perturbations. Figure 6.9 shows a triangular perturbation represented by the function $A_I(z)$, which has magnitude a,

[3]The units km* are used here to indicate that the pressure height defined in section 2.4.2 is being used rather than the geophysical height.

base $2n$ km*, and is centred on an n km*-resolution grid level I. The dashed sections around level I denote an unspecified number of 1 km* state levels not shown, and the continuation of the triangular perturbation to its apex across these levels.

The function $A_I(z)$ may be represented by a linear combination of triangular 1 km* basis functions $B_i(z)$, in the same way as the state profile in equation 6.1. If $A_I(z)$ is sampled at 1 km* sub-levels, its value at sub-level i is the coefficient of the basis function $B_i(z)$ for that sub-level. The triangular functions denoted by dotted lines in figure 6.9 are the multiples of $B_i(z)$ which sum to form $A_I(z)$.

So, if the sub-levels are numbered from $-n$ to n and centred on zero as shown, then the large-scale perturbation is expressed as a sum of basis functions as follows:

$$A_I(z) = \sum_{i=-(n-1)}^{n-1} \left(1 - \frac{|i|}{n}\right) aB_i(z). \tag{6.19}$$

Now, since the n km* grid perturbation and the sum of 1 km* grid perturbations are equivalent, the net effect on the radiance at a given level j must be the same, and so we can express this overall radiance change as a sum of the influences of each of the component perturbations which make up the right-hand side of equation 6.19.

$$\Delta y_j[n \text{ km}^*, a, I] = \sum_{i=-(n-1)}^{n-1} \Delta y_j[1 \text{ km}^*, \alpha_i, i], \tag{6.20}$$

where the information in square brackets after each radiance term gives the scale of the perturbation (i.e. half the range over which the triangular perturbation is applied), its magnitude, and the level on which it is centred. The magnitudes α_i are the coefficients of $B_i(z)$ in equation 6.19.

It is assumed for optimal estimation that the measurement $\mathbf{y}$ is linear with respect to small changes in $\mathbf{x}$ about the linearisation state. This being the case, the change in radiance can be expressed as $\Delta y_j = A_I \times K_{jI}$, and so equation 6.20 can be written:

$$aK_{jI}[n \text{ km}^*] = \sum_{i=-(n-1)}^{n-1} \alpha_i K_{j(I+i)}[1 \text{ km}^*]. \tag{6.21}$$

Substituting the values of α_i from equation 6.19, and dividing out the common factor a (the magnitude of the original n km* perturbation A_I), we end up with the following relationship between the influence functions at n km* resolution, and those at 1 km* resolution:

$$K_{jI}[n \text{ km}^*] = \sum_{i=-(n-1)}^{n-1} \left(1 - \frac{|i|}{n}\right) K_{j(I+i)}[1 \text{ km}^*]. \tag{6.22}$$

It is clear that the influence functions at n km* resolution will be much larger than their 1 km* equivalents, and this is to be expected in terms of the calculation of

the influence functions. The change in radiance at level j will be appreciably larger for the same magnitude perturbation on a n km* grid, because in the forward model the state profile is changing over a $2n$ km* range, compared with 2 km* for the 1 km* grid.

6.4.3 Influence Function Results

The influence functions are a means to an end, since they are used to calculate the expected error in the retrieved state. By themselves they do not provide sufficient information to determine the quality of a particular retrieval. Therefore in this section I present only a few examples of influence functions from band 1, which illustrate the distinctive features of the vertical profile of sensitivity of the MLS.

Figure 6.10 shows a surface plot of the influence functions for channel 11 (the central filter) of the band 1 water vapour retrieval. All the channels have much the same influence function shape as that shown here, since the observed spectrum (shown in figure 6.4) has no particular shape. The y-axis of the plot represents the pointing height, that is, the tangent height of the central axis of the MLS antenna. Along the x-axis is the model atmosphere pressure height at which the state profile has been perturbed, in other words the level at which changes to the state vector are being retrieved. The z-axis represents the influence function. The peak of the plot corresponds to the maximum sensitivity of the radiance in this band to changes in H_2O, and lies at a pointing height of 13 km and a perturbation pressure height of 13 km*.

As described in the previous section, the sensitivity of measurements can be enhanced by reducing the resolution of the grid on which the retrieval is performed. The influence functions already discussed were calculated on a 1 km* resolution grid; in figure 6.11 the same set of functions are converted to a coarser 3 km* grid, resulting in a considerable increase in sensitivity. It is only by changing to coarser retrieval grids in this way that the signal-to-noise ratio of the measurements becomes large enough to allow retrieval in the troposphere, as will become clear in section 6.5.1.

The same influence functions that are shown as a surface in figure 6.11 are replotted as contours in figure 6.12. This shows more clearly the location of the peak of sensitivity, and demonstrates that the sensitive region extends well into the stratosphere. This plot may be compared to that of the influence functions for the same band and channel, but at a latitude of 70°N (during the winter), as shown in contour form in figure 6.13. The sensitive region in the latter case is located lower in the atmosphere. This suggests that despite the lower tropopause at high latitudes, the corresponding lowering of the sensitivity pattern of the MLS may mean that

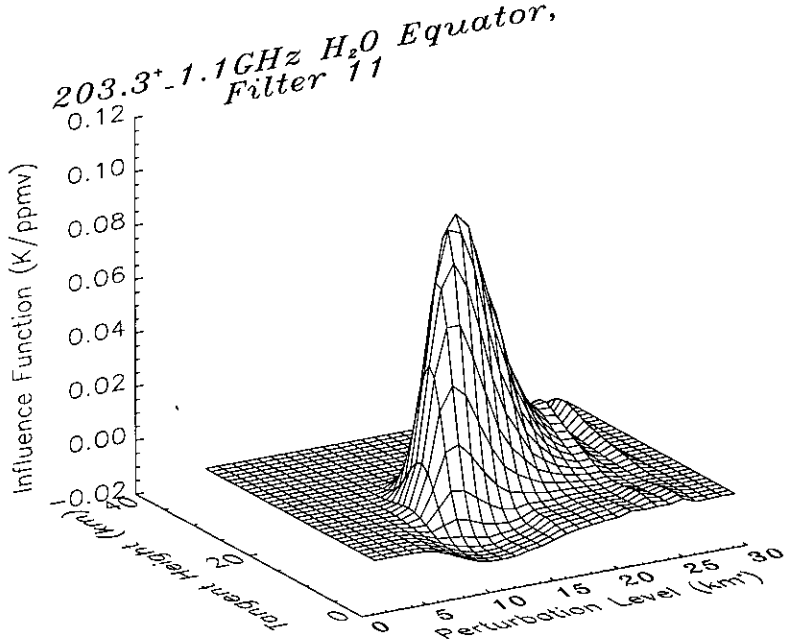

Figure 6.10: Influence functions for the central filter of the band 1 retrieval at the equator, at 1 km* resolution.

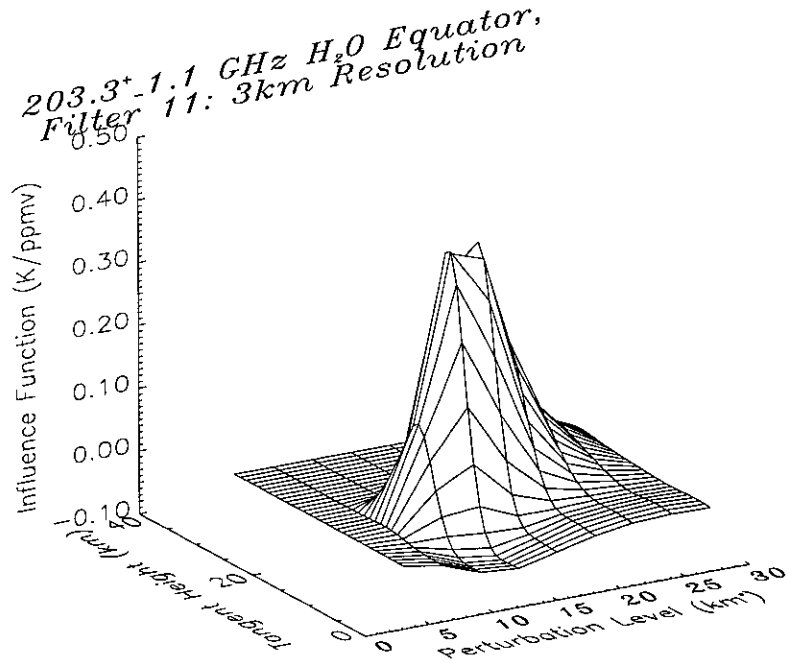

Figure 6.11: Influence functions for the central filter of the band 1 retrieval at the equator, converted to 3 km* resolution.

tropospheric retrievals are still possible. This suggestion is shown to be correct in the next section.

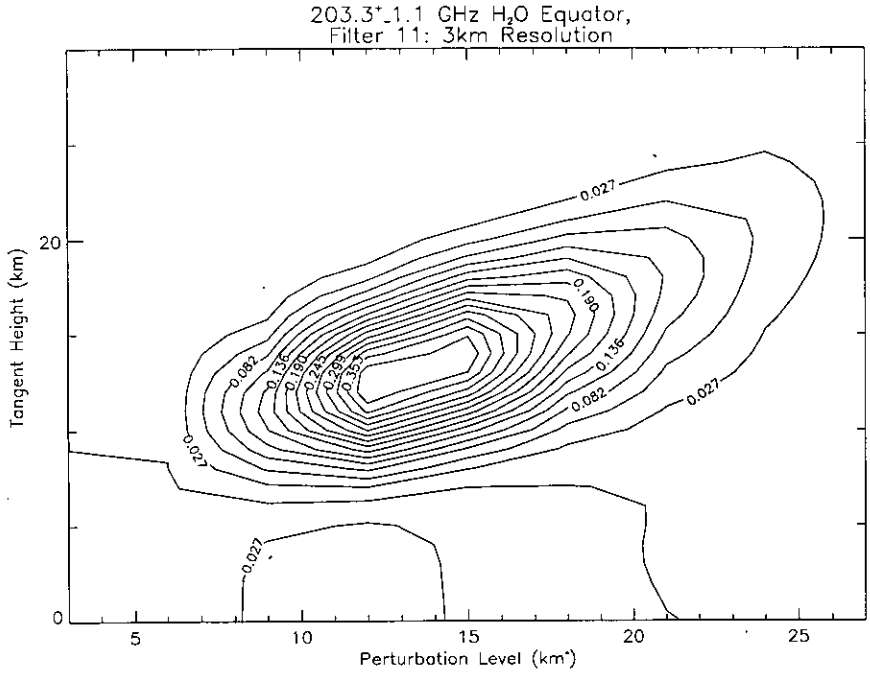

Figure 6.12: Influence functions as for previous figure, in contour form.

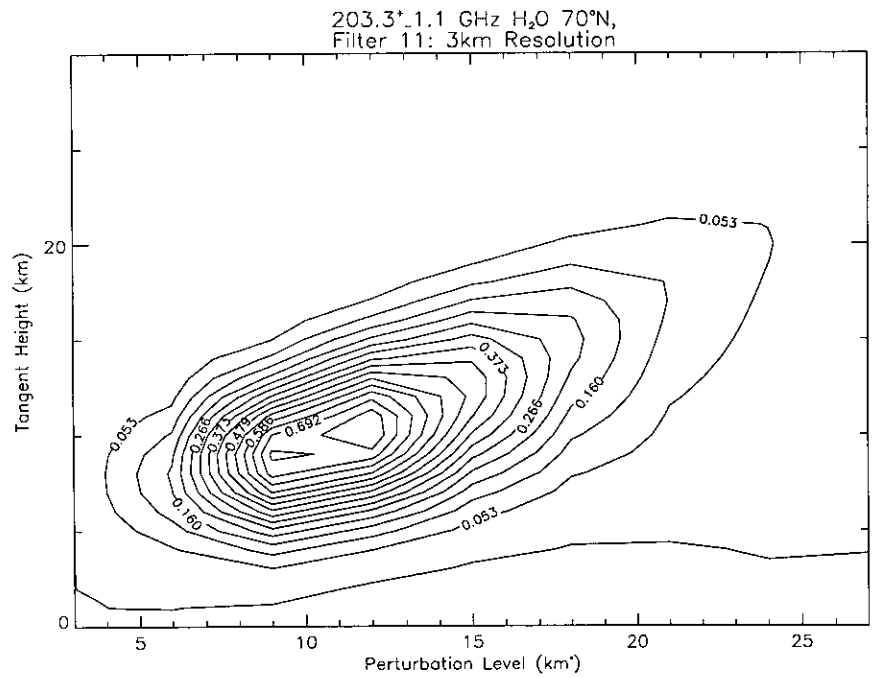

Figure 6.13: Influence functions for the central filter of the band 1 retrieval at 70°N, 3 km* resolution.

6.5 Retrieval Errors

6.5.1 Measurement Error Covariance

The true test of whether a set of measurements provides enough information for a retrieval comes from an analysis of the expected uncertainty in the retrieved state vector. The covariance matrix $\hat{\mathbf{S}}$ defined in equation 6.7 takes the form:

$$\hat{\mathbf{S}} = \begin{pmatrix} \sigma_1^2 & \sigma_{12} & \cdots \\ \sigma_{21} & \sigma_2^2 & \cdots \\ \vdots & \vdots & \ddots \end{pmatrix}$$

The values along the diagonal are the variances of the retrieved state variable at each level, and the square root of this variance is the standard deviation of the error on the retrieved value. The off-diagonal terms are the *covariances* between values of the state variable at different levels. Covariance is defined by the equation

$$\sigma_{ab} = \frac{1}{N}\sum_{i=1}^{N}(a_i - \overline{a})(b_i - \overline{b}) \tag{6.23}$$

where, in the case of $\hat{\mathbf{S}}$, a and b are the retrieved mixing ratios at two different levels. If a and b are independent, then $\sigma_{ab} \rightarrow 0$ as $N \rightarrow \infty$, because positive and negative deviations of a and b from their means are equally likely. However, the covariance $\sigma_{ab} \neq 0$ when a and b are *correlated*. This correlation may be positive, when the deviation $(a_i - \overline{a})$ is more likely to be associated with a deviation $(b_i - \overline{b})$ of the same sign, or negative when the deviations have opposite signs. In practice the off-diagonal terms in $\hat{\mathbf{S}}$ are not zero, in fact they are similar in magnitude to the variances themselves, indicating a very high degree of correlation between retrieval levels. This inter-correlation of levels may be diagnosed by finding the eigenvectors and eigenvalues of $\hat{\mathbf{S}}$, as shown by Rodgers [1990], but it was not felt that such information was of particular relevance to this study. Therefore only the diagonal of the covariance matrix has been used, providing a profile of the retrieval error variance, and therefore of the standard deviation, with which to ascertain the feasibility of retrieval at each level.

The covariance of the retrieved state vector is a combination of the covariance of the *a priori* data, $\mathbf{S}_a$, with that of the measurements, $\mathbf{S}_\epsilon$. Both of these matrices must be defined; the latter is considered first. The uncertainty in a given measurement of radiance is due to noise in the radiometer system. This noise originates within the radiometer, but it is convenient to consider it in terms of the brightness temperature arriving at the mixer which would produce a power output from the radiometer equal to the noise power. Such a brightness temperature is called the

equivalent input noise temperature of the receiver[4], T_{REC}. The values of T_{REC} which were used for the EOS MLS radiometers are presented in table 6.1. They are loosely based upon the values of Siegel [1992], and have been confirmed by Robert Jarnot [personal communication].

Frequency (GHz)	T_{REC} (K)
203	2500
239	3000
642	8500

Table 6.1: Receiver noise temperatures for the EOS MLS.

T_{REC} represents the noise inherent in the receiver, but does not account for the reduction of the input signal due to loss in the antenna system. For EOS MLS this loss is of the order of 1 dB [Filipiak, personal communication], so in order to produce a temperature T_{REC} at the mixer, the input temperature at the antenna must be LT_{REC}, where L is $\sim 10^{0.1}$ and is called the *optic loss factor*. A further contributor to the noise of the system is the emission from the antenna given by $(L-1)T_o$, where T_o is the ambient temperature. Since the MLS is space-borne, T_o will be very low, so the antenna emission is negligible compared with the receiver noise. Therefore the total noise temperature of the MLS system is represented by $T_{\text{SYS}} = LT_{\text{REC}}$.

The radiometric resolution of the measurement, that is the lowest brightness temperature change that can be resolved, is given by the root-mean-square level of fluctuation of the radiometer output. This is dependent on the mixer noise, the bandwidth $\Delta\nu$ of the particular channel under consideration, and the *integration time* τ, which is the period over which the MLS makes its measurement before changing its pointing direction. The expected integration time at the time of writing was 0.33 seconds [Filipiak, personal communication]. These factors are combined as follows to yield the radiometric resolution ΔT [Ulaby *et al* 1981, p.364,365].

$$\Delta T = \frac{T_{\text{SYS}}}{(\tau\Delta\nu)^{1/2}} \tag{6.24}$$

For a double-sideband measurement, the received spectral power is approximately doubled in the mixer because the two sidebands are folded on top of one another, as described in section 2.5. Now the values of T_{REC} tabulated in table 6.1 are single-sideband (SSB) temperatures, meaning they represent the temperature at the antenna which would cause a single sideband to deliver an output power equal to the noise. In the case of a double-sideband (DSB) system, since the input power

[4] Where 'receiver' refers to the mixer plus the spectrometers.

is doubled, $T_{\text{REC}}(\text{DSB}) \simeq T_{\text{REC}}(\text{SSB})/2$. The use of $T_{\text{REC}}(\text{DSB})$ in equation 6.24 would give the radiometric resolution of the measured value of the antenna temperature T_{A}. However, for the results presented in this section, the elements of the measurement vector $\mathbf{y}$ are the sums of the two sidebands, not their means, so the error in a particular element of $\mathbf{y}$ is the standard deviation of this summed radiance. To calculate this standard deviation, $T_{\text{REC}}(\text{SSB})$ was used in equation 6.24.

The diagonal elements of the covariance matrix for the measurement error $\mathbf{S}_\epsilon$ were defined by setting the diagonal elements equal to $(\Delta T)^2$ for each element of $\mathbf{y}$. Ideally there will be no interdependence between measurements in each channel and at different levels. This was assumed to be the case, so the off-diagonal elements of $\mathbf{S}_\epsilon$ were set to zero.

Now the *a priori* covariance needs to be determined. This might be defined in a similar manner to the measurement covariance, using the variances of a climatological average as the diagonal elements. However, in this study since there are no real measurements $\mathbf{y}$, a full retrieval of $\hat{\mathbf{x}}$ is not attempted; the aim is to determine the error characteristics of a hypothetical retrieval. Consequently the *a priori* state vector $\mathbf{x}_a$ has not been specified, and its covariance is similarly undefined. One approach would be to specify a likely *a priori* covariance and use it in the error analysis, but in order to retain greater generality, $\mathbf{S}_a$ was instead defined as a diagonal matrix with elements set to unrealistically high values (100 times the value of the atmospheric state being retrieved at that level). In this way the inverse of the matrix contains very small values, and so the retrieval covariance as calculated by equation 6.7 is heavily weighted towards the contribution from the real measurement covariance. Therefore the covariances predicted by this method are larger than those which would be achieved in a full retrieval where $\mathbf{x}_a$ and $\mathbf{S}_a$ were realistic. In the event that a measurement provides no information about the state, the retrieval covariance calculated in this way reverts to the *a priori* value and so acts as a flag to indicate the insensitive regions of the profile.

So, the retrieval error covariance matrix $\hat{\mathbf{S}}$ defined by equation 6.7 may now be calculated, since all the terms on the right-hand side of the equation have been defined: the covariance matrices $\mathbf{S}_\epsilon$ and $\mathbf{S}_a$ as described above, and the influence function matrix $\mathbf{K}$ as described in section 6.4. The diagonal of $\hat{\mathbf{S}}$ provides a profile of the retrieval error variance, and the square root of each of these variances is the standard deviation.

Examples of standard deviation profiles for the retrieval error in band 2 are shown in figure 6.14. This plot demonstrates the need to reduce the resolution of the retrieval grid in order to increase sensitivity, as described in section 6.4.2. Standard deviation profiles are shown for the band 2 retrieval at the equator, at

three different resolutions of the state vector: 1 km* (three-dot-dashed line), 2 km* (dashed line) and 3 km* (dash-dotted line). A profile of the volume mixing ratio (VMR) of ozone, the atmospheric state that is being retrieved, is plotted as a solid line on the same axes. It is clear that only by coarsening the resolution to 3 km* can the error be reduced in this case to a level which permits retrieval below the tropopause.

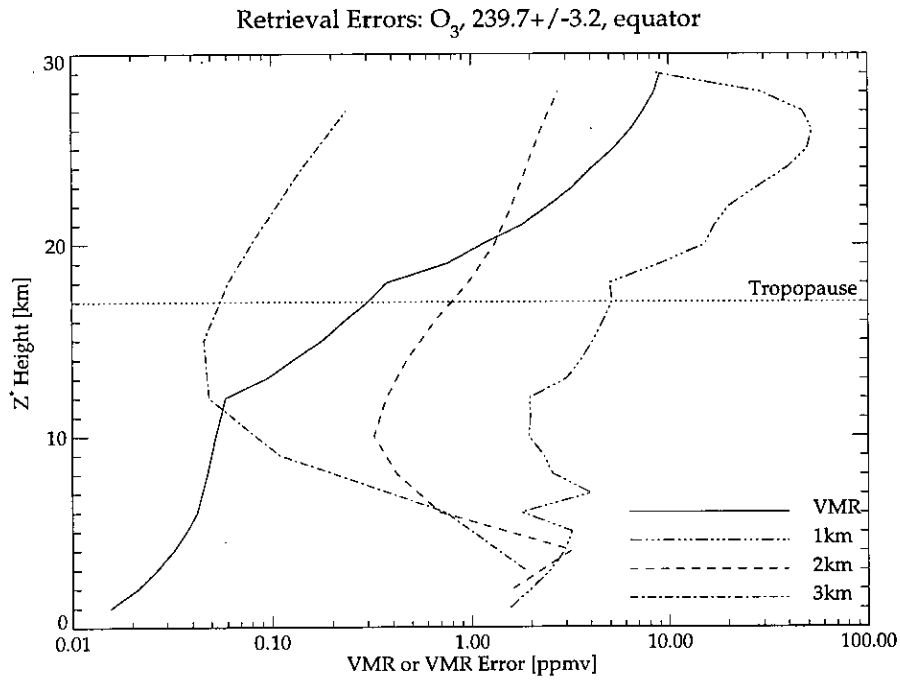

Figure 6.14: Reduction of errors by coarsening of the retrieval grid. Broken lines denote retrieval errors for various resolutions of the state vector. Solid line represents the volume mixing ratio (VMR) of O_3.

6.5.2 Dependence of Retrieval Error on Matrix Size

When equation 6.7 was used to calculate $\hat{\mathbf{S}}$, the size of the matrix elements was found to depend on the number of levels in the retrieved state vector, even when the region of atmosphere covered by one state vector was a subset of the other. This is illustrated in figure 6.15 below, which shows profiles of the standard deviation of retrieval error for band 2 at the equator, calculated with a 3 km* resolution of the state vector. In each case the measurement vector is the same, comprising all 21 channels, at each of 11 measurement heights from 10 km to 20 km. It is clear that as the matrix size increases, the standard deviation at a given level also increases. However, the standard deviation still represents the same retrieved quantity on the same resolution.

This effect can be understood by considering that each level of the ozone VMR

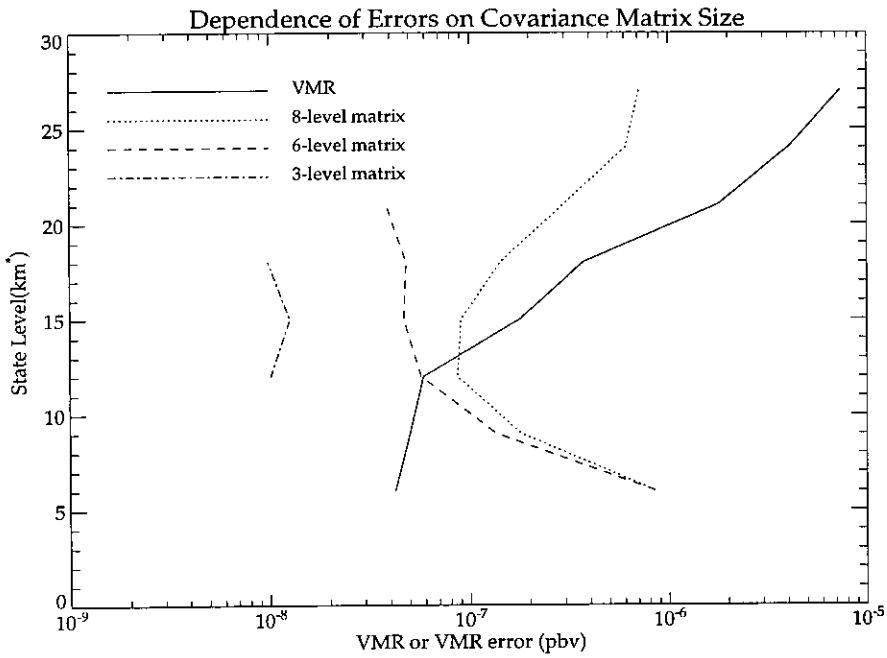

Figure 6.15: Profiles of standard deviation of retrieval error at 3 km* resolution, calculated using different matrix sizes, for the band 2 retrieval at the equator. The solid line represents the state which is to be retrieved (the VMR of O_3).

profile in the atmosphere is contributing to the radiance vector, even if that level is not included in the retrieved state vector. From equation 6.2 it can be seen that any factor which affects the radiance, but which is not retrieved, must be considered part of the model parameter vector $\mathbf{b}$. Therefore the unretrieved levels contribute a model parameter covariance $\mathbf{S}_P$ to the total covariance $\hat{\mathbf{S}}$. It has been shown in section 6.2.3 that the $\hat{\mathbf{S}}$ calculated by equation 6.7 does not include $\mathbf{S}_P$, and so the smaller the state vector, the greater the underestimate in the covariance.

In figure 6.15, as the size of the matrix increases, the retrieved standard deviation approaches its correct value as the ignored contribution from $\mathbf{S}_P$ falls. Therefore, rather than calculate $\mathbf{S}_P$, an 18-level state vector was used, at 3 km* resolution, to cover the atmosphere from the ground to 54 km*. This minimised the missing contribution from $\mathbf{S}_P$. The suitability of the 18-level state vector was tested by comparing the standard deviations that were obtained using it with those found using a 19-level vector. It was found that, for the first 9 levels of the state vector, the standard deviations from the 19×19 covariance matrix were identical (to 14 significant figures) to those obtained from the 18×18 matrix. Level numbers above 9 (27 km*) were not considered significant because the retrievals are intended to be tropospheric. Therefore the 18-level vector was used to produce all subsequent results.

6.5.3 Retrieval Error Results and Vertical Ranges

In this section a sample of vertical profiles of the standard deviation of retrieval error will be presented, which demonstrate the sensitivity of each band in the troposphere, and which therefore allow an estimation of the vertical range over which the retrieval is viable. In many cases the profiles will be presented in the next section in conjunction with profiles of cloud parameter error, in order to demonstrate the reduction in vertical range which may be caused by the scattering effect of cirrus. Therefore to save space only a few examples are presented here, in order to demonstrate the way in which the information may be used. All profiles are calculated on a resolution of 3 km*.

For band 1, figure 6.16 shows the standard deviation profile for the retrieval error at 40°N. The standard deviations are plotted as a percentage of the mixing ratio at each level, showing that the retrieval should be possible between 6 km and 12 km. Outside this vertical range the error in the retrieval is many times larger than the quantity being retrieved. In the case of levels above 12 km this is because the water vapour content is low, so changes in its concentration do not result in changes of radiance that give a sufficiently high signal-to-noise ratio for retrieval. For levels below 6 km, the problem is that there is too much water vapour; this means that the atmosphere is highly opaque, so that the majority of the radiation received by the MLS has come not from the tangent point, but from higher altitudes closer to the MLS along the line of sight. Therefore perturbations made at the tangent point do not result in detectable changes in the radiance, and the retrieval is not sensitive to these levels.

Moving north to 70°N, it was noted in section 6.4.3 that both the tropopause and the region of peak sensitivity of the MLS were lower in the atmosphere compared to lower latitudes. Figure 6.17 shows the retrieval error profile for band 1 at this latitude, and it is seen that the standard deviation at an altitude of 6 km is low enough in comparison to the mixing ratio to allow an accurate retrieval.

For the band 2 measurement, figure 6.18 shows a profile of standard deviation of the retrieval error at 40°N. In this case it is apparent that the retrieval is not possible in the mid-latitudinal troposphere because the region of peak sensitivity of the MLS is too high in the atmosphere. The standard deviation is about 20% at the tropopause itself which makes this an effective lower limit for the retrieval. The same behaviour is observed at 70°N, where again, it is not possible to retrieve ozone at this resolution.

The examples presented in this section are the final product of the process of converting the radiances calculated by the forward model into vertical ranges for each retrieval. In the next section these error profiles are presented for all three

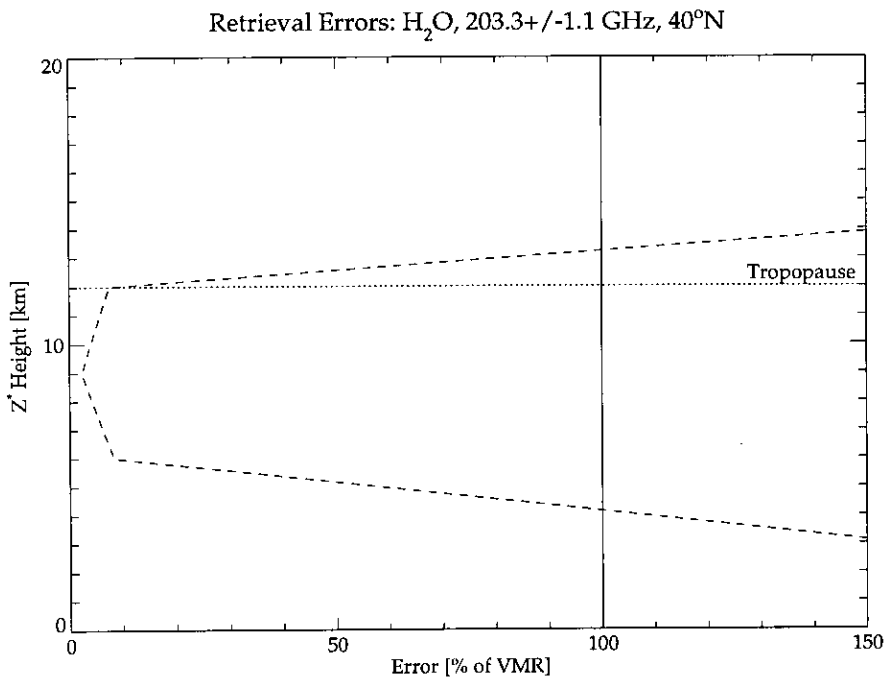

Figure 6.16: Errors for the 203.3 ± 1.1 GHz H_2O retrieval at 40°N, as a percentage of VMR.

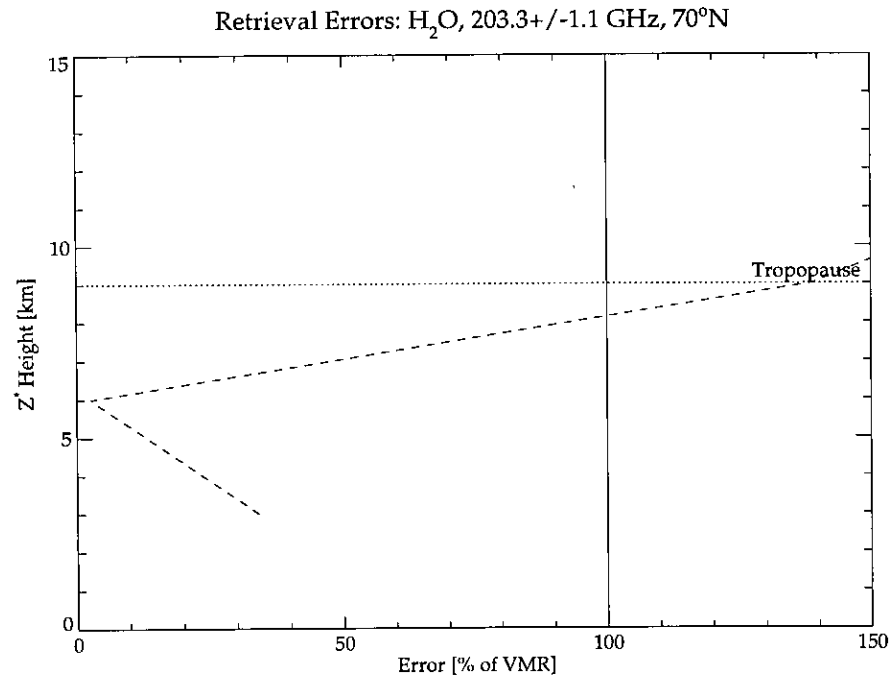

Figure 6.17: Errors for the 203.3 ± 1.1 GHz H_2O retrieval at 70°N, as a percentage of VMR.

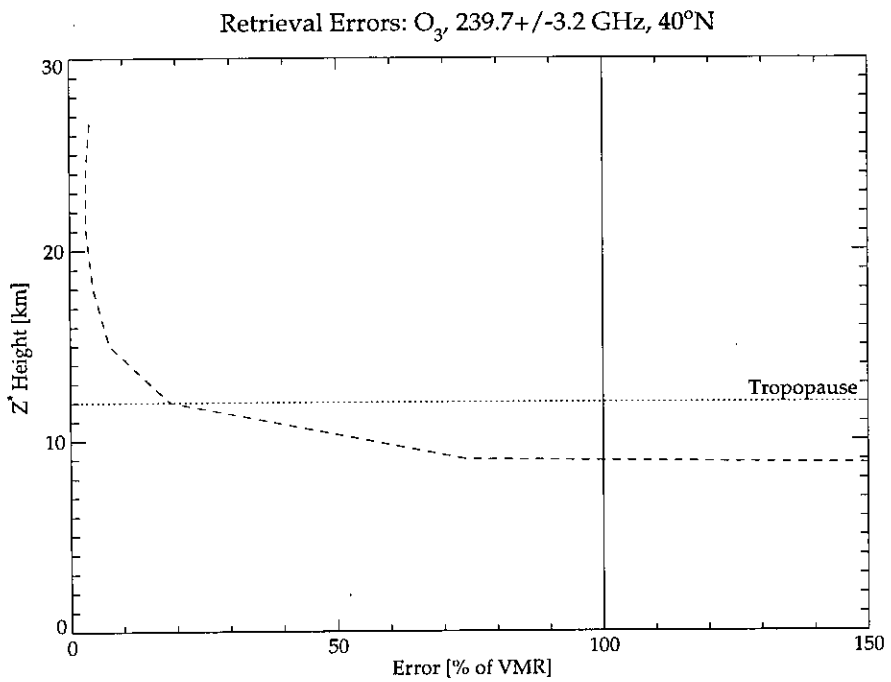

Figure 6.18: Errors for the 239.7 ± 3.2 GHz O_3 retrieval at 40°N, as a percentage of VMR.

of the bands, and are compared with the corresponding errors which arise in the presence of cirrus.

6.6 Effect of Cirrus Scattering

6.6.1 Introduction

The scattering effect of cirrus clouds leads to a degradation of the sensitivity of retrievals in two ways.

- The dominant effect is the *cloud parameter error* described in section 6.2.3 and given by equation 6.17, which is the error in the retrieval that will arise when the radiance is altered by the presence of clouds, and this alteration is not accounted for. It assumes that we do not know when clouds are affecting our measurements and treats the radiance change as if it were caused by a variation in the retrieved state. The solution of equation 6.17 requires calculation of the contribution function, which is in turn calculated by equation 6.15. As an example, figure 6.19 shows a single column of a contribution function matrix plotted as a profile. It illustrates the oscillatory nature of the function, a nature that is transferred to the cloud parameter error that the function is used to calculate. The cloud parameter error profiles in this section are plotted as absolute values.

- The second effect is the loss of sensitivity which occurs as a result of the cirrus scattering useful retrieval information out of the line of sight, which is called here the *information loss error*. The influence functions, and hence the standard deviation profiles, for each band were recalculated in the presence of cloud, in order to investigate the extent to which the retrieval will be degraded even if we are able to account for the radiance change caused by the cloud. This effect is more subtle and is only significant in certain cases, as will be seen.

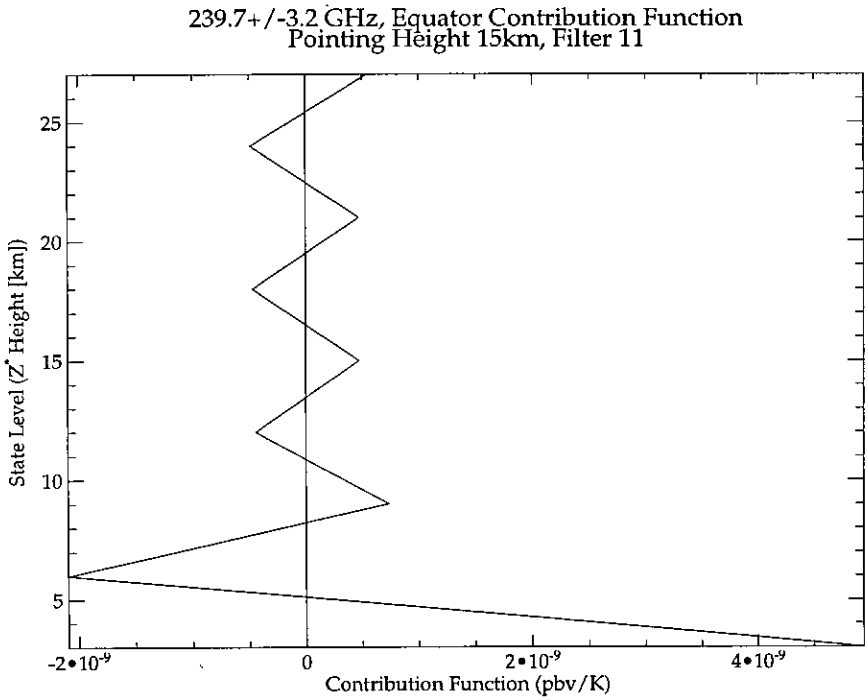

Figure 6.19: Contribution function **D** for the 239.7 ± 3.2 GHz O_3 retrieval at the equator: a single column corresponding to a pointing height of 15 km and the central filter.

The cloud parameter error defined above applies in the case that nothing is known of the state of cloudiness in the field of view. Retrievals in this case are made on the assumption that there is no cloud present, in which case any change in the observed radiance which results from the extinction due to cirrus will be unaccounted for and therefore be misinterpreted. By the same token, retrievals made in the absence of cirrus may only be trusted within the bounds of the cloud parameter error, since although they have not been affected by extinction, we have no way of knowing that. This represents the worst possible effect that cirrus could have on a retrieval, since it may be possible to account for its presence in other ways. One such method would be to try to retrieve the cloud itself from the radiance measurements, as was suggested in section 6.2.3. A more promising technique would

be to use simultaneous measurements from other instruments mounted on the same platform which are more suited to the detection of cirrus. The CHEM-1 platform that will carry the MLS is also expected to carry two infrared instruments: the High Resolution Dynamics Limb Sounder (HIRDLS) and the Tropospheric Emission Spectrometer (TES) [NASA 1995]. HIRDLS has as one of its mission objectives the detection of tropospheric cloud tops, so at the very least it should be able to determine when cirrus is present, and its data products may prove suitable for the retrieval of cloud ice water content. TES is not designed to observe clouds, but it operates at similar frequencies to HIRDLS and also combines limb-viewing and nadir-viewing capabilities, so its measurements may provide useful information for the location of cirrus.

At the simplest level, such complementary measurements could determine if any cloud was present, allowing confidence in those retrievals made under cloud-free conditions. More detailed measurements might provide microphysical data which could be used to simulate the cirrus in the forward model. In this case there would be an associated parameter covariance $\mathbf{S}_P$ arising from the uncertainty in the results provided by the other instrument, but the retrieval errors derived from this covariance would be considerably less than the cloud parameter errors described here.

6.6.2 Results

The set of parameters defined in section 5.7 to represent typical cirrus conditions at the equator, middle latitudes and high latitudes was introduced into the forward model to generate a set of radiance spectra for cloudy atmospheres. From these spectra, modified profiles of the standard deviation of the retrieval error were derived, together with profiles of the cloud parameter error, for comparison against the cloud-free profiles. The results are presented below for each band in turn. In each case up to three profiles are presented, these being:

1. The profiles of standard deviation of retrieval error, referred to as the 'retrieval errors'.

2. These same retrieval errors in the presence of the cirrus.

3. The cloud parameter errors due to the cirrus, as defined by equation 6.17.

As previously, the profiles are calculated on a resolution of 3 km*. A comparison with the same results calculated at 4 km* resolution (not presented here) showed that the cloud parameter errors were not altered sufficiently at the coarser resolution to affect the conclusions of this chapter.

Band 1 (H_2O)

In figure 6.20 the effect of scattering from cirrus crystals on the brightness temperature received by the MLS is shown for a tangent height of 12 km, which lies within the vertical range (11.9 km to 13.4 km) of a typical cirrus cloud at the equator. The brightness temperatures shown are double-sideband values, and are plotted against the frequency relative to the radiometer centre frequency of 203.3 GHz. The non-cloudy spectrum in this plot is the same as that plotted in figure 6.4, but on a larger vertical scale. This plot shows that the radiance is actually enhanced by the presence of the cirrus. This is because the high radiances which are incident on the cloud from below are scattered by the crystals into the line of sight. However, this scattered radiance does not contribute to the information about the tangent height which is required, and so the 'useful' brightness temperature may still be reduced by the cloud's presence.

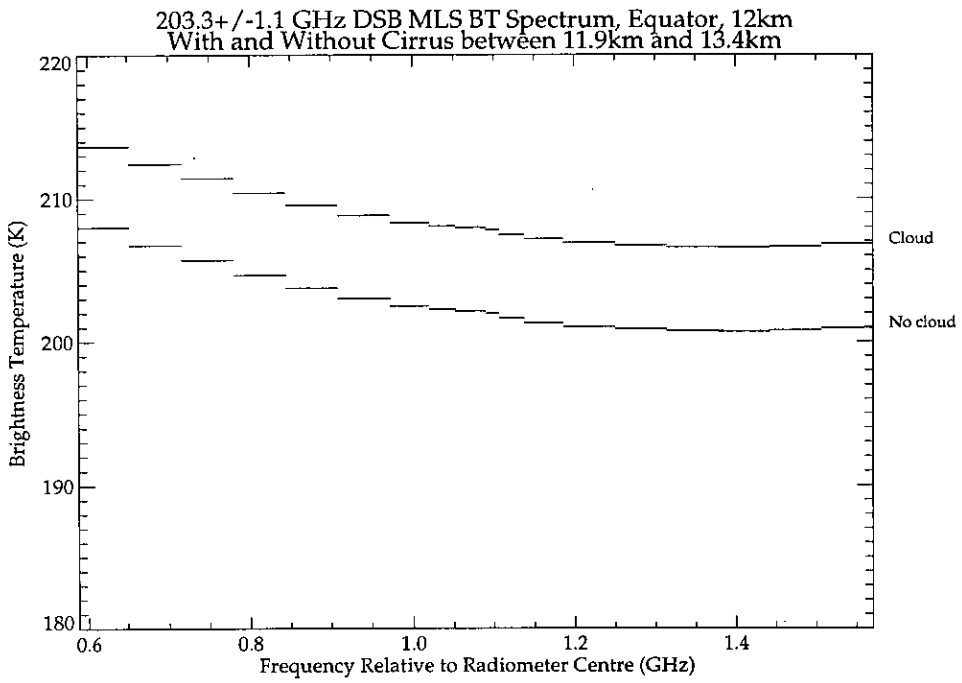

Figure 6.20: Radiance change at 203.3 ± 1.1 GHz associated with the presence of typical equatorial cirrus (base at 11.9 km, top at 13.4 km). A horizontal line segment represents the bandwidth of each filter.

In figure 6.21 the cloud-free retrieval errors for band 1 at the equator are plotted as a dashed line on the same axes as the corresponding cloud parameter errors (three-dot-dashed line) due to the presence of a typical equatorial cirrus cloud. The retrieval errors in the presence of cloud in this case were identical to the cloud-free case; in other words the information loss error due to the cirrus was negligible. This would suggest that the majority of the radiation scattered into the line of sight is

from levels close to the pointing level, and is therefore providing information for the retrieval. This is to be expected, given that the large crystals which are responsible for the majority of the scattering will scatter radiation in a narrow lobe about the forward direction (see figure 3.4).

The retrieval errors are sufficiently low to allow retrieval of H_2O between 6 km and 12 km: outside this vertical range the error is too large a proportion of the value being measured.

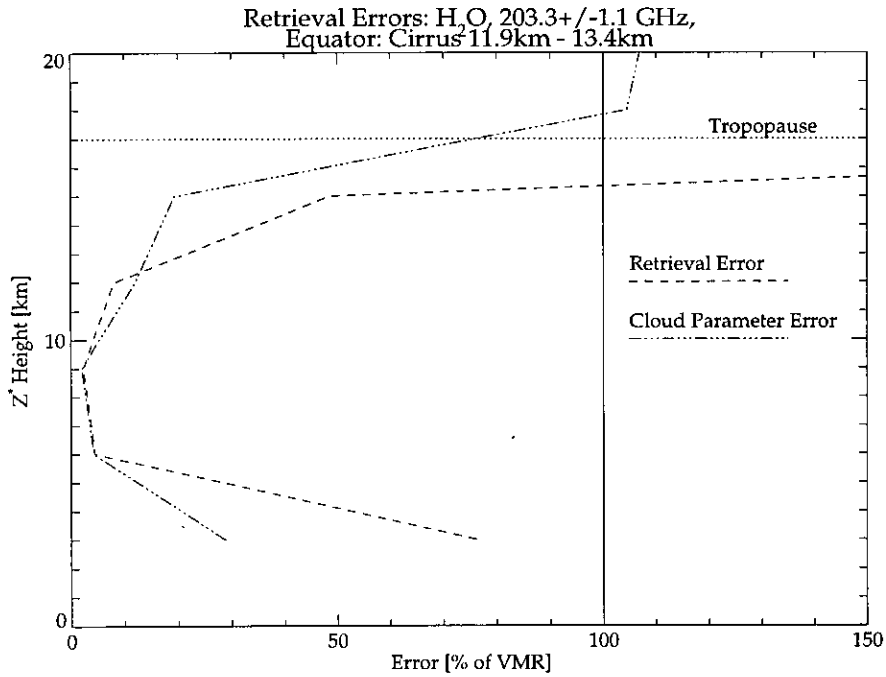

Figure 6.21: Errors for the band 1 H_2O retrieval at the equator, with and without typical cirrus (base at 11.9 km, top at 13.4 km).

The cloud parameter error arises when it is not possible to account for the presence of cirrus, in which case the change in brightness temperature seen in figure 6.20 will be interpreted by the retrieval as a change in the state profile. The profile of cloud parameter error for this band shows that the cloud does not cause serious problems; the retrieval is still possible between 6 km and 12 km, although the error will be slightly larger at 12 km as a result of the cloud. Note however, that the cloud parameter error is large above the tropopause, despite the fact that the cloud itself lies several kilometres below. This illustrates the way in which information is distributed about the retrieval levels by the contribution function. In this case the high cloud parameter error above the tropopause is inconsequential, since the retrieval is not possible there anyway.

The same type of plot for this retrieval at 40°N is shown in figure 6.22. The profile indicated by the dashed line is the same as that plotted previously in fig-

ure 6.16, and shows that the retrieval is possible over a vertical range from 6 km to the tropopause. It should be noted that the horizontal scale of this plot is considerably extended from that which was used for figure 6.16. The typical cirrus cloud for this latitude lies between 8.1 km and 9.6 km, in the middle of the vertical range of the retrieval. As at the equator, the information loss error due to the cloud is very small, so the retrieval error profile does not change appreciably in the presence of cirrus (and is therefore not reproduced here). The cloud parameter error shown by the three-dot-dashed line in figure 6.22 is a different matter. The error is never lower than 200%, and clearly in this case the cloud has rendered the whole retrieval infeasible.

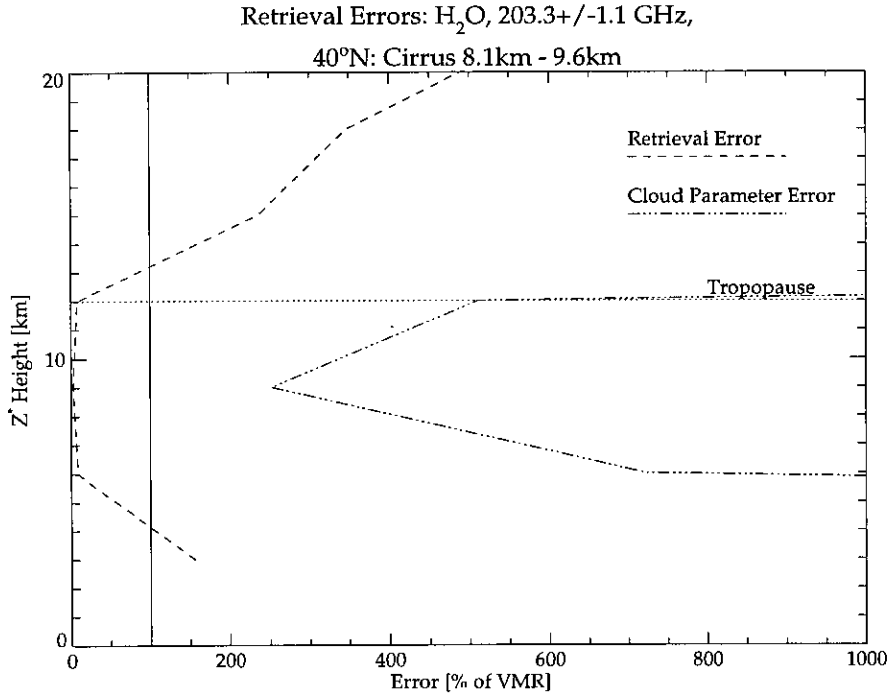

Figure 6.22: Errors for the band 1 H_2O retrieval at 40°N, with and without typical cirrus (base at 8.1 km, top at 9.6 km, IWC=0.002 gm^{-3}).

Finally for this band, the error profiles for the 70°N are given by figure 6.23. The retrieval error in the absence of cloud, which has already been shown in figure 6.17, is replotted here on an extended horizontal scale. In addition to this profile and the cloud parameter error profile, the retrieval error profile in the presence of cirrus is also shown, as a dot-dashed line. This shows the same sensitivity at the 6 km level as was the case in the absence of cirrus, but the 3 km error becomes very large, indicating a considerable degradation of the signal by the cloud. This degradation also leads to a large cloud parameter error, which is greater than 100% even at its lowest point, and so again the retrieval must be considered impossible in the

presence of such cirrus.

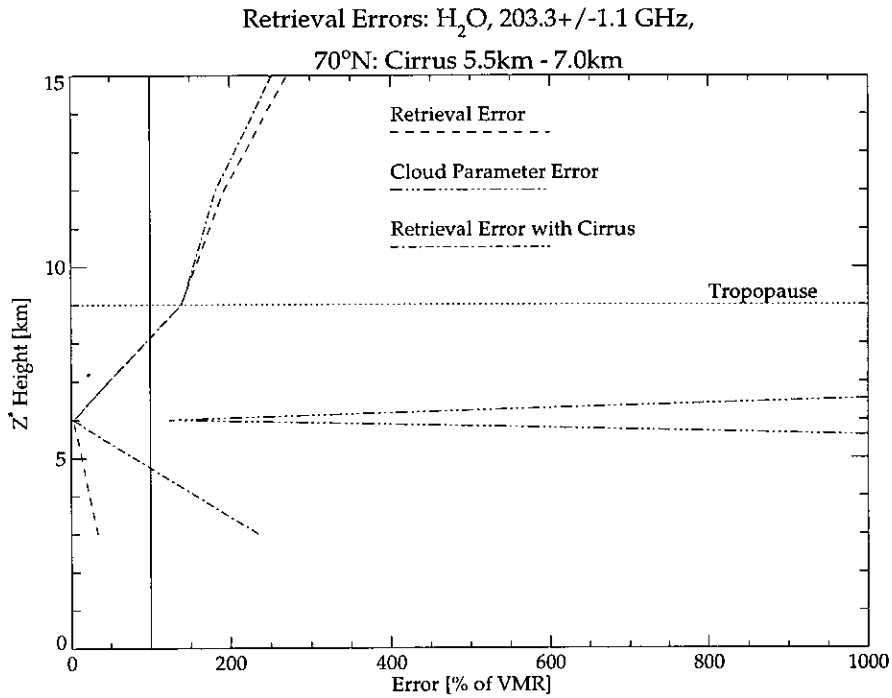

Figure 6.23: Errors for the band 1 H_2O retrieval at 70°N, with and without typical cirrus (base at 5.5 km, top at 7.0 km, IWC=0.004 gm^{-3}).

Band 2 (O_3)

The change in brightness temperature in band 2 at the equator caused by the presence of cirrus is shown in figure 6.24 for a tangent height of 12 km, which lies within the cloud. The cloud enhances the brightness temperature by about the same amount and for the same reasons as for band 1.

Retrieval errors and cloud parameter errors for the equator are shown in figure 6.25. The retrieval error profile shows that band 2 is really most suitable for the measurement of ozone in the lower stratosphere, and that tropospheric retrieval is only possible at 15 km and above, with poor accuracy. Figure 6.25 shows that the cirrus does not cause a significant further deterioration in this case. The retrieval error profile in the presence of cirrus is identical to the cloud-free profile shown here, and the cloud parameter error in the sensitive region above 15 km is small compared with the retrieval error.

However, in this case the most sensitive region of the retrieval is above the top of the standard cirrus cloud, which is at 13.4 km. The cloud heights used in this study are mean values, but individual occurrences of cirrus may be much higher or lower. Therefore it is instructive in this case to examine the effect of a higher cloud. For

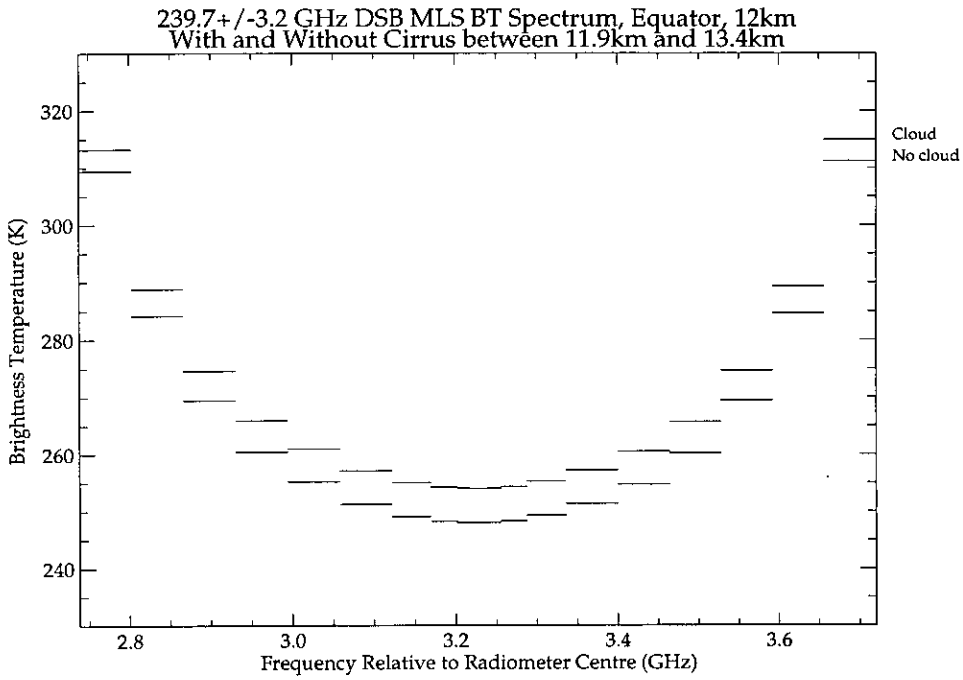

Figure 6.24: Radiance change at 239.7 ± 3.2 GHz associated with the presence of typical equatorial cirrus (base at 11.9 km, top at 13.4 km).

this purpose the calculations were repeated with a cirrus cloud of the same depth, 1.5 km, but with a midpoint at 15 km. The corresponding results are shown in figure 6.26, which shows that the cloud parameter error is high enough to prohibit a successful retrieval. Therefore in this case, although figure 6.25 shows that the retrieval is not badly affected by a typical cirrus cloud, the conclusion should be that *in the majority of cases* an individual retrieval at any given time will not be badly affected.

In the middle latitudes, band 2 is no longer suitable for the retrieval of tropospheric ozone, as was shown in figure 6.18, since it is only at the tropopause itself that the retrieval error becomes sufficiently low. This is well above the cloud top at 9.6 km, and so the information loss error will not make the retrieval any worse, and indeed the retrieval error profile is unchanged by the presence of cirrus. However, the cloud parameter error shown by figure 6.27 is substantial, even well above the tropopause, and renders even the retrieval at the tropopause impossible. This again demonstrates the influence of cirrus on retrieved quantities at levels well above the cloud top, as discussed previously with regard to figure 6.21.

No results are presented here for the 70°N retrieval. The deterioration of the retrieval accuracy continues with increasing latitude, and at 70°N no retrieval of ozone is possible in the troposphere, even in the absence of cloud.

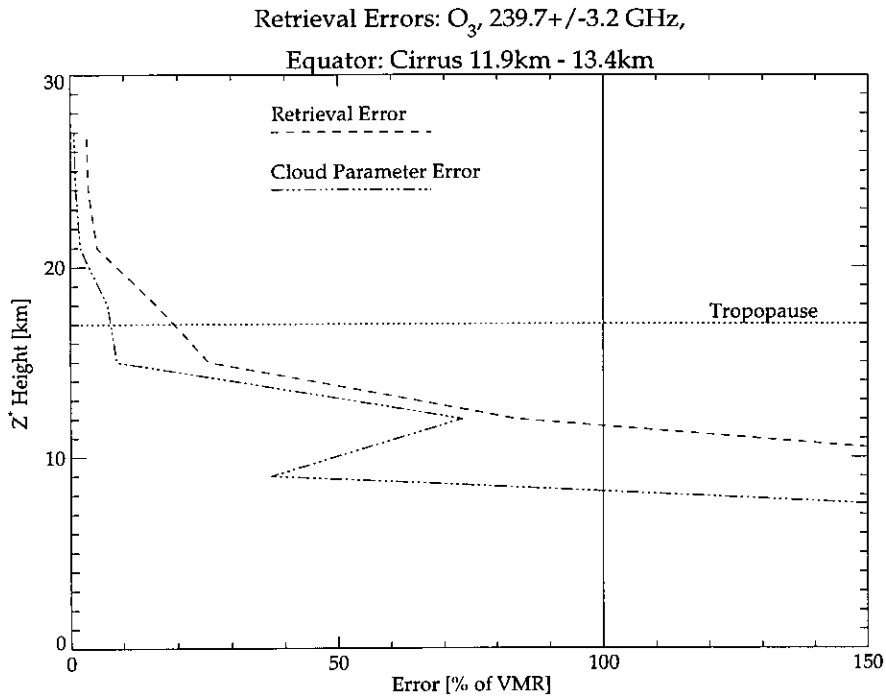

Figure 6.25: Errors for the band 2 O_3 retrieval at the equator, with and without typical cirrus (base at 11.9 km, top at 13.4 km).

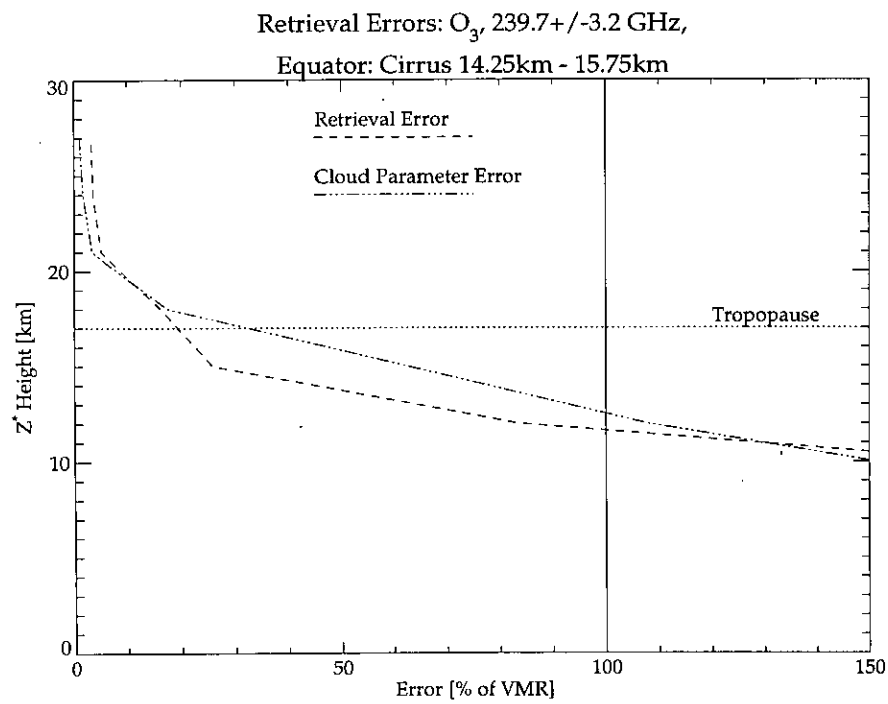

Figure 6.26: Errors for the band 2 O_3 retrieval at the equator, with and without typical cirrus (base at 14.25 km, top at 15.75 km).

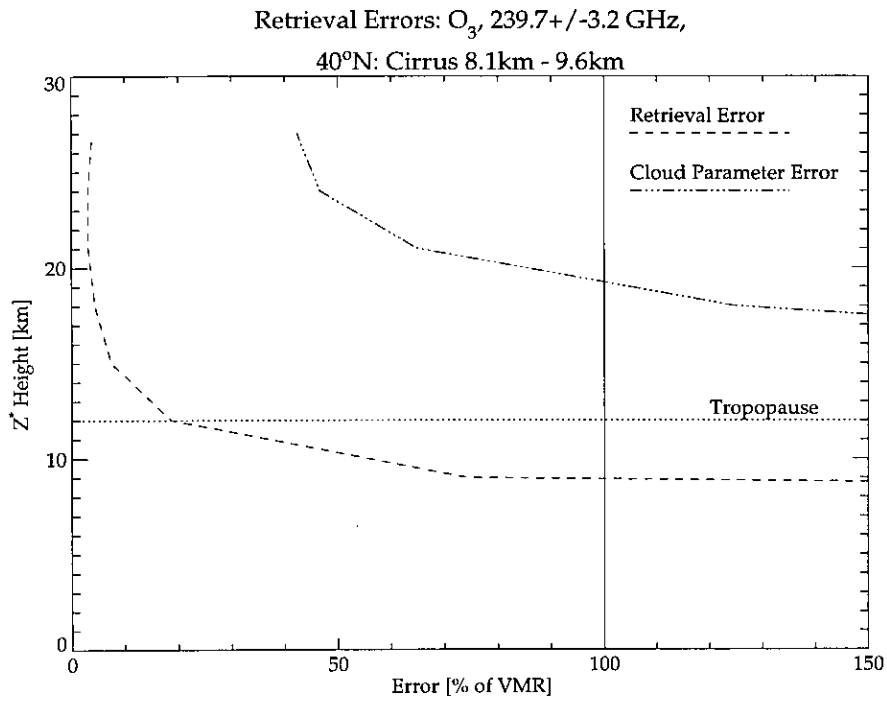

Figure 6.27: Errors for the band 2 O_3 retrieval at 40°N, with and without typical cirrus (base at 8.1 km, top at 9.6 km, IWC=0.002 gm^{-3}).

Band 3 (H_2O)

From the scattering theory developed in chapter 3, the extinction coefficient for band 3 is expected to be higher than for bands 1 and 2 since the frequency is considerably higher. For the same reason there will be a greater difference between the extinction coefficient and scattering coefficient for this band. These effects are evident in the comparison of double-sideband radiances for a pointing height of 12 km shown in figure 6.28. Although the absolute change in brightness temperature is similar to that of the other bands, in this case the cirrus causes the brightness temperature to be *reduced*, indicating that the attenuation by extinction is outweighing the augmentation by multiple scattering.

The greater level of extinction in this band leads to a significant information loss error. In figure 6.29, for the equator, the retrieval error profiles are shown both with and without cirrus, together with the cloud parameter error. At most levels the retrieval errors are similar, but at 9 km, the first grid level beneath the cloud, the retrieval error is doubled by the effect of the cirrus. The error remains sufficiently low to be considered an acceptable value for a successful retrieval, but the accuracy of the retrieval is seriously impaired. This example demonstrates that at high frequencies the presence of cirrus is not negligible with respect to the information content of the measured radiances.

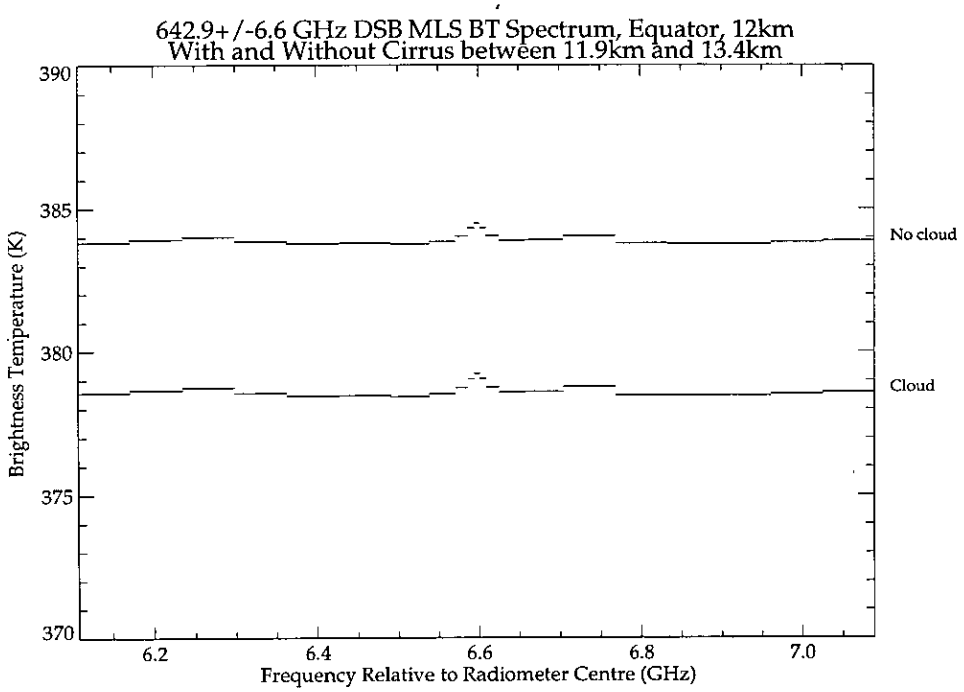

Figure 6.28: Radiance change at 642.9 ± 6.6 GHz associated with the presence of typical equatorial cirrus (base at 11.9 km, top at 13.4 km).

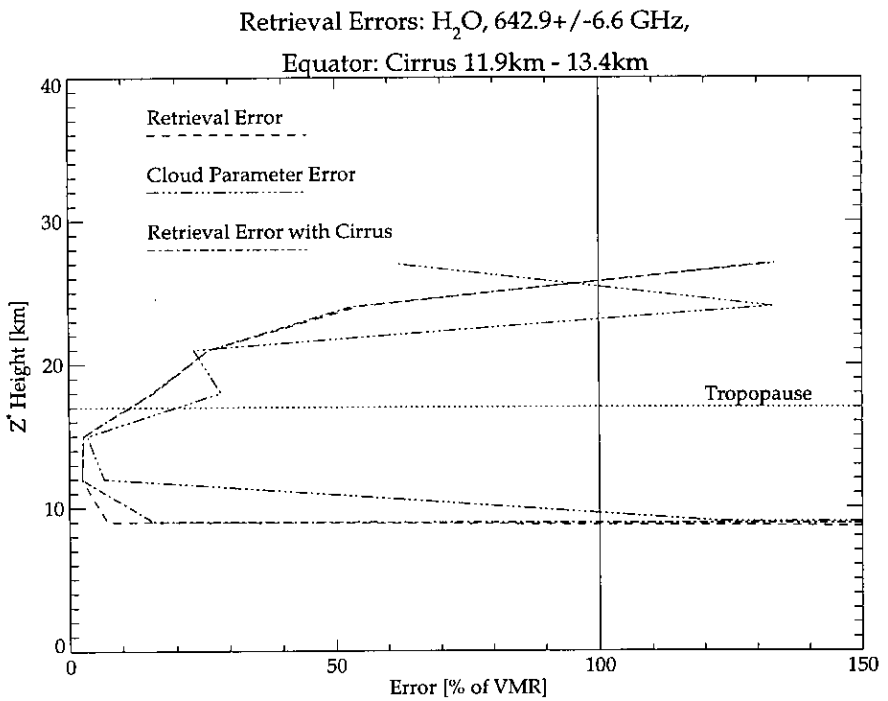

Figure 6.29: Errors for the band 3 H_2O retrieval at the equator, with and without typical cirrus (base at 11.9 km, top at 13.4 km).

In the event that the presence of cirrus cannot be accounted for, the information loss error is outweighed by the cloud parameter error. The retrieval errors plotted in figure 6.29 show that the retrieval is possible in a cloud-free atmosphere over a vertical range of 9 km to 15 km. However, the cloud parameter error at 9 km is over 100%, rendering the retrieval impossible at this level and reducing the vertical range to between 12 km and 15 km.

However, at 40°N no such problems arise. Figure 6.30 shows the error profiles for band 3 at this latitude. The vertical range of the retrieval obtained from this figure is between 9 km (where the error is about 20%) and the tropopause, and there is no significant information loss error which reduces this in the presence of the typical cirrus cloud. Furthermore, in contrast to the effect of the cloud parameter error on this band at the equator, at middle latitudes there is no significant degradation, presumably because the cloud is lower in the atmosphere and therefore lies partly beneath the lowest sensitive level.

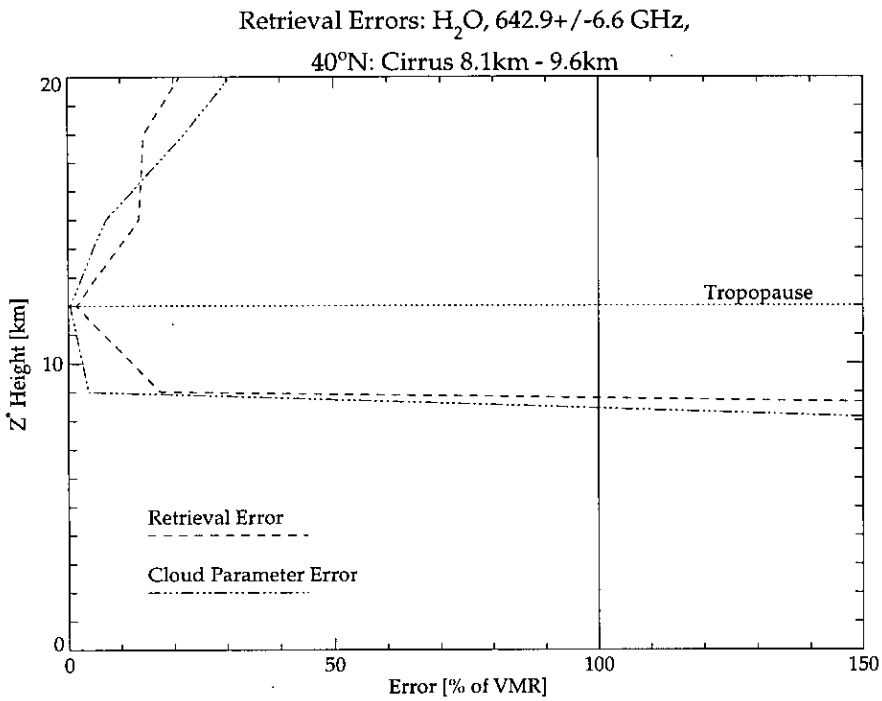

Figure 6.30: Errors for the band 3 H_2O retrieval at 40°N, with and without typical cirrus (base at 8.1 km, top at 9.6 km, IWC=0.002 gm^{-3}).

The final measurement considered was the band 3 retrieval at 70°N, and again the cloud does not prove detrimental to retrieval. The retrieval error profile is plotted only for the cloud-free case in figure 6.31, since the equivalent profile in the presence of cirrus is identical, and shows that the retrieval is accurate over a vertical range from 6 km to the tropopause and above. In addition, the cloud

parameter error profile shown on the same axes has a negligible uncertainty at 6 km, and remains lower than the expected retrieval error at levels above this into the stratosphere.

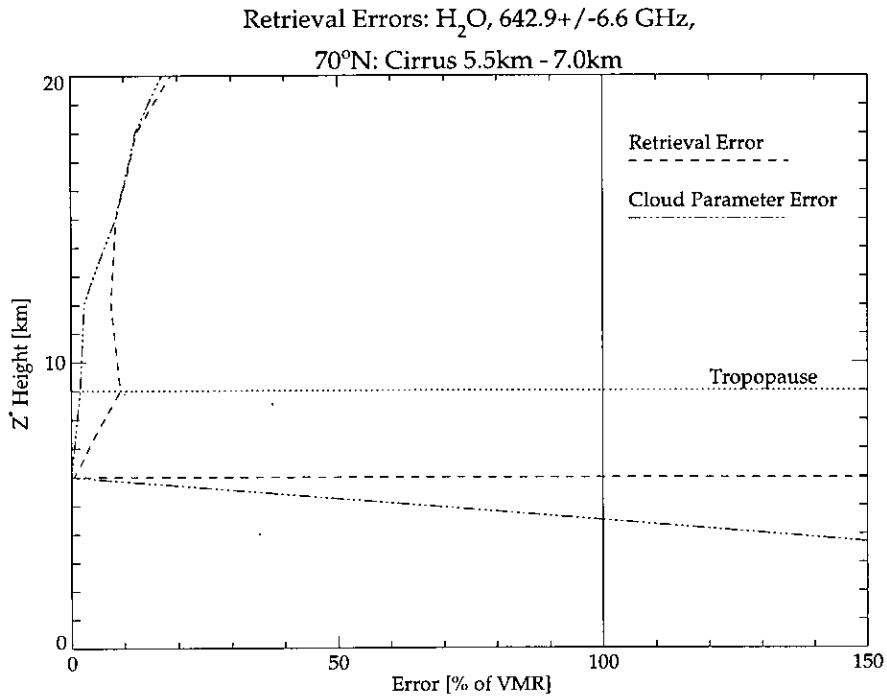

Figure 6.31: Errors for the band 3 H_2O retrieval at 70°N, with and without typical cirrus (base at 5.5 km, top at 7.0 km, IWC=0.004 gm^{-3}).

6.6.3 Sensitivity of Cloud Parameter Error to Changes in Extinction

In chapter 5 it was shown that the use of alternative techniques (specifically the equivalent-volume and discrete dipole approximations) for the modelling of extinction due to complex crystals can lead to widely differing results. In order to test the sensitivity of the calculated cloud parameter errors to the extinction coefficient of the cloud, the cloud parameter errors for band 1 at 40°N were recalculated using a cloud for which the extinction coefficient was one third of its normal value. This band and latitude were chosen because they are the most seriously affected by cloud, as shown by figure 6.22. The factor of one third is chosen as a rough estimate of the relative difference, averaged over all particle sizes, between the equivalent-area and discrete dipole approximations based upon the results of section 5.6.

The resulting cloud parameter error profile is shown in figure 6.32, together with the original, unreduced cloud parameter error profile, and the retrieval error profile. The cloud parameter error is reduced by approximately one third, indicating that the response of the cloud parameter error is roughly proportional to the change in

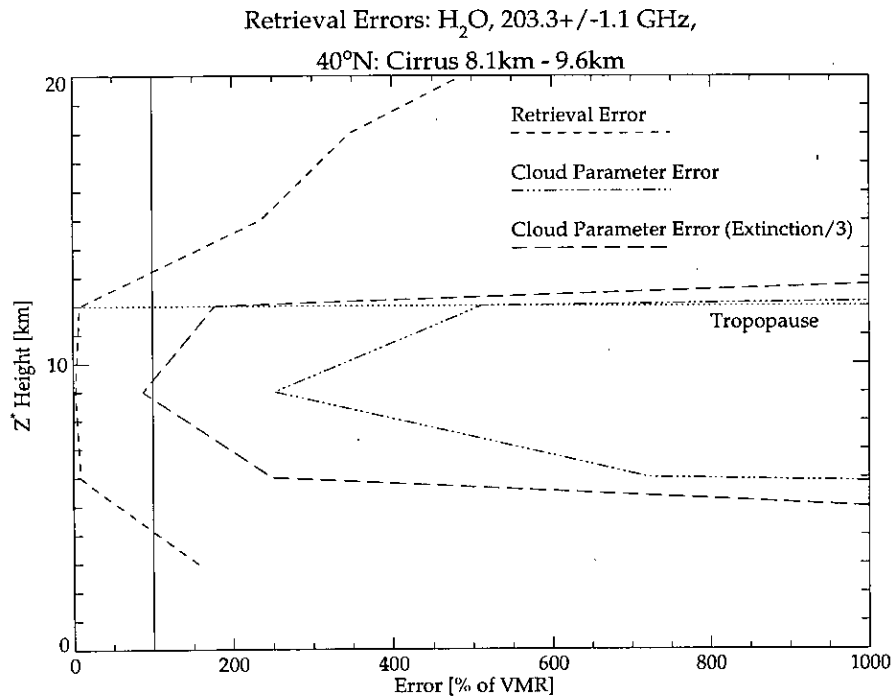

Figure 6.32: Errors for the band 1 H_2O retrieval at 40°N, with and without typical cirrus (base at 8.1 km, top at 9.6 km, IWC=0.002 gm^{-3}). The long-dashed line represents the cloud parameter errors when the extinction coefficient is divided by 3.

the extinction coefficient. However, it is also clear that the reduction is not sufficient to make the retrieval any more viable, since the error remains near or above 100% of the VMR across the sensitive region of the retrieval. If similar considerations are applied to the 70°N retrieval for band 1 shown in figure 6.23, the error will fall to 40% at its lowest point, which is still too large for a reliable retrieval. The same is true of the 9 km level of the band 3 retrieval at the equator.

Therefore although the equivalent-area sphere method may be overestimating the extinction, the degradation by cirrus of the retrievals discussed above is sufficiently serious that it would still render those retrievals unreliable even if the extinction coefficients were several times smaller.

6.7 Chapter Summary

In this chapter the forward model and the cirrus simulation described in previous chapters have been combined to determine the errors expected in retrieved tropospheric parameters, and to estimate the extent to which those errors are increased by the presence of cirrus. This has been achieved through an error analysis of the optimal estimation retrieval process, where cirrus is regarded as an unretrieved model parameter, and its corresponding error calculated accordingly.

Three bands have been identified as suitable for tropospheric retrieval, of which bands 1 and 3 were used for water vapour, and band 2 for ozone. It has been shown how the accuracy of these retrievals is improved by lowering the resolution of the state vector. Retrieval errors have been determined for the three bands by estimating the uncertainty in the measurement due to noise in the radiometer, and using this in the optimal estimation equations.

Finally, the influence of an average cirrus cloud on retrieved profiles of water vapour and ozone was systematically investigated. Band 2, at 239.7 ± 3.2 GHz, was the only measurement of ozone described. It is only at the equator that this can really be called a tropospheric measurement, and the findings of this chapter have indicated that cirrus is unlikely to be a problem for such a retrieval. At 40°N, cirrus wipes out the retrieval at the tropopause, which is very poor even in the absence of cirrus.

The susceptibility of the water vapour retrievals to cirrus degradation is highly dependent on latitude. For band 1 it has been demonstrated that the equatorial retrieval of H_2O is not seriously affected by the presence of cirrus, whereas at middle and high latitudes the cloud parameter error is so large that retrieval is rendered impossible.

Conversely, in band 3 for the middle and high latitude retrievals, no loss of information was found, and the cloud parameter errors at sensitive levels were insignificantly small. At the equator, however, there is a substantial increase in retrieval error due to information loss at 9 km, and the cloud parameter error at this level is so large that it restricts retrieval to levels at and above 12 km.

The sensitivity of these results to changes in the cloud extinction coefficient has also been determined, to assess the impact of changes in the assumptions made in the cirrus simulation.

In the next, and final chapter, I will recap the method which has been followed in this thesis, and summarise its principal findings, putting them into a global context.

Chapter 7

Conclusions

In this thesis I have attempted to determine the effect of typical cirrus clouds on retrievals made in the troposphere using a microwave limb sounder, specifically that to be launched as part of the Earth Observing System. There now follows a synopsis of how this objective has been achieved, and a summary of the principal results obtained. Following this, the implications for microwave limb sounding of the troposphere are discussed, in conjunction with a brief review of the global climatology of cirrus to put the results of the previous chapter into perspective. Weaknesses in the techniques that have been used are identified, to determine the reliability of the results, and to put them into context with similar studies by other authors.

7.1 Summary of the Thesis

In chapter 2, a forward model was described which simulated radiative transfer through a non-scattering atmosphere. The theory of molecular radiation which forms the basis for such a model has been discussed, and numerical methods have been described which were used to solve the equation of radiative transfer. In addition, the instrumental characteristics of the EOS MLS have been described, via the principles of microwave radiometry, to show how the forward model converts the radiance arriving at the MLS antenna into that which is actually measured in each of the spectrometer channels. The forward model has been validated by comparison with the output from several other independently-developed models.

Chapter 3 described a simple model of scattering, designed to calculate the scattering and extinction coefficients of a distribution of spherical particles. Mie theory was used to calculate the scattering efficiencies for a single sphere, and these results were extended for a polydispersion of such spheres. The process of incorporating such a representation of scattering into the forward model was described, and the effects of multiple scattering were estimated. This completed the development of

the forward model.

To represent cirrus clouds in the model it was necessary to understand their microphysical structure. Therefore chapter 4 consisted of a review of the extensive published literature on this subject, with the aim of determining both the size distribution and the shape distribution of the ice crystals in various forms of cirrus cloud. This required firstly some discussion of the two distinct forms of cirrus (frontal and convective) and the mechanisms of their formation. Then by collating the data from several different authors, the size and shape distributions were approximately parameterised according to cirrus type, temperature, and ice water content. Crystal shapes were classified into several commonly-occurring categories for the purpose of defining the shape distributions.

The cirrus particle distributions derived in chapter 4 were unsuitable for use in the forward model because the crystals were not spherical. Therefore these crystals were represented in the forward model by spheres of equivalent projected area. Chapter 5 described how the conversion was achieved, by representing each of the crystal shape classes as an idealised geometrical form. The scattering properties of the resulting equivalent-sphere distributions were used to help decide on the form of the large-particle tail of the distributions.

The validity of using equivalent-area spheres has been discussed, and it was recognised that an equivalent-volume method may have been more representative of the particles' scattering properties, particularly the extinction. A comparison of the two methods has been conducted, which showed that the equivalent-area method predicts extinction efficiencies a factor of ~ 2 larger than those of the equivalent-volume method.

Finally in chapter 6 the effect of the simulated cloud on retrieval was evaluated. The retrieval process was described, and three frequency bands were selected which were suitable for tropospheric retrievals in the absence of cloud. Then, through an error analysis of the inverse model, the error due to contamination by cirrus was calculated for each band. For the water vapour band at 203 GHz, the retrieval was found to be infeasible in the presence of cirrus at middle and high latitudes. The 642 GHz water vapour retrieval at the equator was still possible, but with a reduced vertical range. In all other cases studied, including the ozone retrieval in the 239 GHz band, the cloud was not a problem. It has been noted that the results assume that no account has been taken of the cirrus in the retrieval process, which would be the case if it were assumed that microwave measurements are unaffected by the presence of cloud. If the MLS measurements were supported by simultaneous, independent measurements of the cirrus, perhaps from an infrared instrument, the degradation caused by the cloud would be considerably reduced.

7.2 Geographical Distribution of Cirrus

The results of chapter 6 have demonstrated that under certain circumstances the presence of cirrus in the field of view of an MLS is likely to cause substantial uncertainty in the retrieved state. It is therefore important to determine how often, and in which geographical regions, cirrus will interfere with the retrievals of the EOS MLS.

On a global scale, Dowling and Radke's [1990] review of the results of a number of authors leads them to conclude that the global mean cirrus coverage is somewhere between 20% and 50%. One of the studies included in that review is that of Wylie and Menzel [1989], whose results (for North America only) are based upon over six million observations made over a period of two years. They find that between 20% and 30% of the observations indicate the presence of cirrus, and that the seasonal variation of the cirrus is low, suggesting that a considerable percentage of the cloud is continuously present. These results imply that cirrus is sufficiently prevalent to affect a considerable proportion of the measurements made by the EOS MLS.

A global climatology of cirrus is required to assess the geographical distribution of this problem. Satellite observations are the most effective way of providing the global scale of results that are required to produce such a climatology, and the two principal satellite studies of cirrus that have been reported are those of Barton [1983] and Woodbury & McCormick [1989].

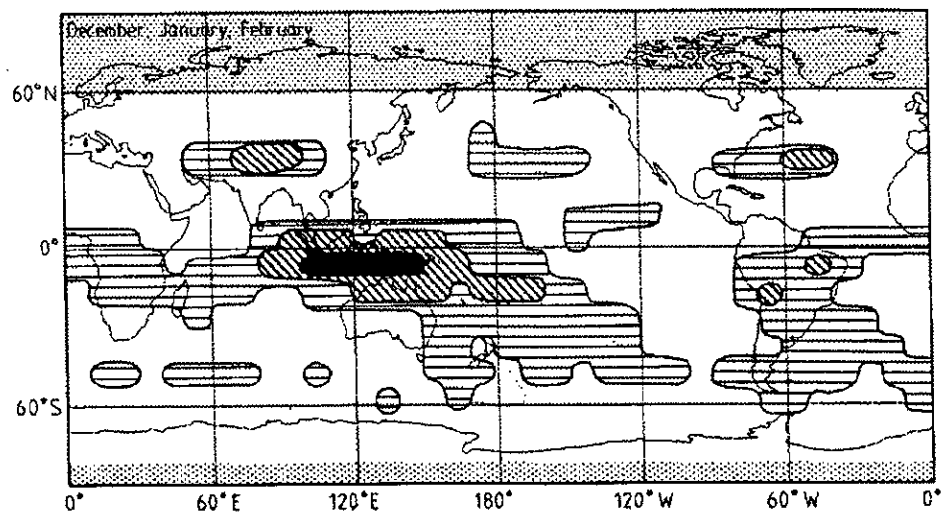

Figure 7.1: Distribution of high clouds for winter, from Barton [1983]. Dark area represents a greater than 60% frequency of cloud cover; diagonal lines – greater than 40%; horizontal lines – greater than 20%; clear – less than 20%. Shaded areas at top and bottom contain no observations.

Barton [1983] provides comprehensive maps of the global distribution of 'high

cloud', that is cloud whose top is above 6 km. In general this will be cirriform cloud, although it possible that some altostratus will be found at such heights [UKMO 1972]. The maps are produced from 2.5 years of continuous measurements from the *selective chopper radiometer* (SCR), which is a nadir-viewing infrared instrument on board the Nimbus 5 satellite. The data cover a latitude range that varies from between 40°N and 80°S in winter, to between 80°N and 40°S in summer. Barton's map for the Northern Hemisphere winter is reproduced here as figure 7.1. This map displays similar salient features to those for the other three seasons. The area of maximum cirrus coverage over south-east Asia corresponds to the tropical Asian monsoon which was discussed in section 4.2.1. The equatorial band of cirrus generation associated with the ITCZ is also apparent from this map.

Woodbury and McCormick [1986] have also produced a cirrus climatology, using measurements from SAGE. This is an infrared solar occultation device, which tracks the sun's disk through the limb of the Earth's atmosphere, and detects cirrus by measuring the absorption of the sun's radiance. The resulting cirrus climatology is based upon 34 months of these measurements, and covers a similar latitude range to that of Barton.

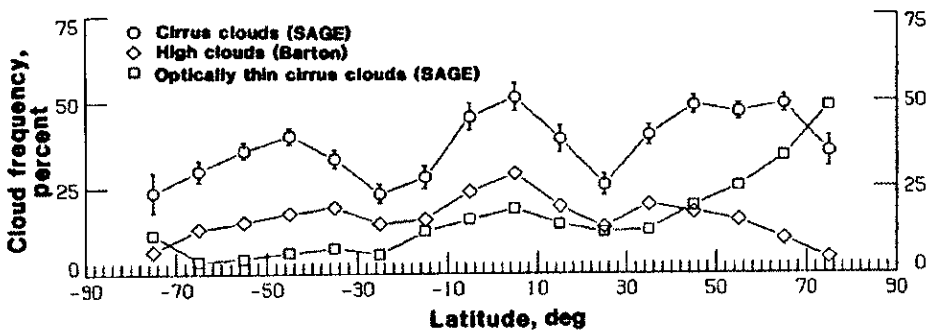

Figure 7.2: Zonal means of cirrus cloud frequency from 34 months of SAGE observations (from Woodbury and McCormick [1986]), compared with zonal means from Barton [1983].

As a limb viewer, SAGE has two major advantages over the nadir-viewing SCR. Firstly, it has high vertical resolution, allowing reliable classification of the cloud type according to its height. Secondly, a much longer section of its line of sight passes through the cirrus than is the case for a nadir view, so it is able to detect more tenuous and patchy regions of cirrus than the SCR. As a result of this greater sensitivity, the cirrus coverage derived from SAGE measurements is considerably greater than that found by Barton. This is illustrated in figure 7.2, which compares zonal averages of cirrus frequency[1] for the full 34 month period against equivalent

[1] Cirrus frequency is simply the number of observations which detect cirrus as a proportion of

zonal averages derived from Barton's results. The SAGE cirrus frequencies are generally double those measured by Barton.

The maps presented by Woodbury and McCormick show a geographical distribution which is consistent with that found by Barton, with a persistently high level of cirrus coverage in the Asian monsoon region and over the equatorial parts of South America and Africa. Conversely, the regions which remain the most clear of cirrus are the Eastern Pacific, the Sahara and Middle East, and the Southern Indian Ocean.

Clearly the cirrus is most prevalent in the tropics and it must be expected that most MLS measurements in this region will be looking through cloud. The typical equatorial cirrus cloud was found not to affect the retrievals in bands 1 and 2, but it must be expected that the reduction of the vertical range of the 642 GHz retrieval will apply in the majority of cases. Away from the tropics, cirrus is less prevalent, but it remains sufficient to affect a significant proportion of measurements. Figure 7.2 shows that Woodbury & McCormick's zonal means are at their minimum at 30° from the equator, but even at these latitudes the mean cirrus frequency is 25%. Therefore a similar proportion of the MLS retrievals in band 1 are likely to be affected by the serious degradation due to cirrus which was described in chapter 6.

Figure 7.3 represents a quantitative combination of Woodbury & McCormick's zonal means with the results of chapter 6. The cirrus frequencies plotted in figure 7.2 have been averaged into bins between the latitudes shown. Each of these bins corresponds to one of the latitudes, in either hemisphere, for which the results of chapter 6 were obtained; that is, 70°, 40° and 0°. Then the degradation of each retrieval was quantified by calculating the number of state vector levels for which the cloud parameter error exceeded 50% of the volume mixing ratio, as a percentage of the total number of levels which would be retrievable in the absence of cloud. The vertical axis of figure 7.3 is the product of the cloud frequency with this degradation factor, and therefore gives an idea of the percentage of the total retrieved levels in the troposphere which will be affected. This highlights the severity of the problem in the extra-tropical latitudes.

7.3 Reliability of Results

The procedure which has been followed in obtaining the results of this study has been simplified by the use of a number of assumptions and approximations of varying degrees of reliability. In this section, some of the most significant of these simpli-

the total number of observations. Both Barton and Woodbury & McCormick use this as a measure of cirrus coverage.

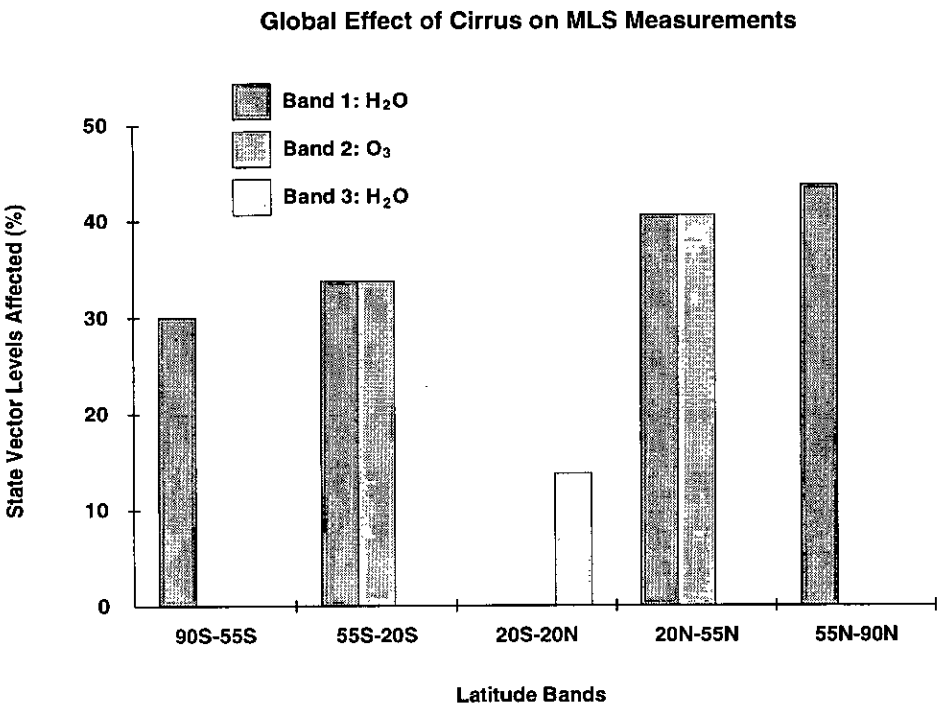

Figure 7.3: Percentage of retrieved state levels, in each of five latitude bands, for which the cloud parameter error due to cirrus exceeds 50% of the volume mixing ratio.

fications are listed, with a discussion of their possible importance to the results in each case.

Equivalent-Area Spheres: It has been explained in chapter 5 that the use of spheres of equivalent area may not be the most effective way to model the scattering properties of non-spherical particles. The equivalent-volume method has been suggested as an alternative, but in both cases the calculated phase function seems likely to be considerably different from its true value. This would lead to differences in the contribution from multiple scattering, although that is a less significant factor than extinction in terms of the degradation of retrievals.

Vagueness of the Habit Fractions: The estimated percentages of crystals occupying each habit are based upon a number of different sets of results which do not correspond well. In addition it has been shown that the scattering properties of a cloud are sensitive to changes in this habit distribution. Furthermore, the habits have been represented by regular geometrical forms, whereas in nature they are often irregular aggregations of simpler forms.

Poor Knowledge of Large Crystal Concentrations: The very largest crystals in a cirrus cloud are of the order of millimetres in dimension, and therefore they contribute significantly to the overall scattering. However, they exist at very low concentrations because they drop out of the cloud quickly, and so they are less well sampled than the smaller crystals. They therefore represent a considerable uncertainty in the calculated scattering and extinction coefficients of a cirrus cloud.

Computer-based simulation of the scattering caused by cirrus will always be limited by factors such as these, particularly the uncertainty in the habit distribution. It has been noted in chapter 5 that the techniques used by other authors in studies of cirrus scattering are based upon similar approximations to those used here, although an exception is the work of Evans and Stephens [1995a, 1995b], whose modelling technique is considerably more complex. A comparison has been made between their results and those produced by the equivalent-area model, which has shown that the latter produces extinction coefficients which may be several times larger than those of the former. This appears to have a proportional effect on the cloud parameter error, but the magnitude of that error for the degraded retrievals is such that even when the extinction coefficient is reduced by a factor of three, the retrievals remain impracticable.

It should also be noted that the results which have been presented were calculated for typical cirrus cloud at each latitude. The discussion in section 5.7 has shown that in certain cases, cirrus clouds may be many times thicker than the average depth of 1.5 km, and that ice water contents are also highly variable. It is clear that if a typical cirrus cloud can cause the degradation indicated by the results of this study, then a more extreme example may affect a greater proportion of the retrievals.

To fully assess the reliability of the methods used here, it will be necessary to combine the radiance data from a microwave limb sounder with independent measurements of the cloud's structure from instruments which use infrared or visible frequencies. In this way the actual effect which a cirrus cloud of known temperature and ice water content has on the received microwave radiances could be measured and compared with the prediction of a model.

Notwithstanding the limitations of the methodology which have been listed above, this thesis has demonstrated that cirrus clouds have the potential to disrupt microwave retrievals of the troposphere. The insensitivity of microwave measurements is cited as a principal strength of the MLS over higher-frequency instruments, and while this is the case in relative terms, it appears that cirrus ought not to be ignored completely.

Therefore the developers of MLS instruments, such as that on EOS, which are intended to make tropospheric retrievals, need to design a retrieval scheme which in some way incorporates the extinction effect of cirrus. This might be done by attempting to retrieve some cirrus parameters, such as temperature, IWC, or ice water path, as well as the chemical mixing ratios. Since cloud extinction produces very limited spectral information, it would be difficult to achieve a reasonably accurate retrieval of these parameters, but the process of incorporating them into the retrieval means that less of the radiance change due to the cirrus will be ascribed to changes in the chemical species, and the retrieval will therefore be more accurate. A more sophisticated option would be to use contemporaneous measurements from other instruments more suited to cirrus retrieval, to obtain a set of cirrus parameters which could be used to simulate the cloud's effect on the retrieval (using a scattering model such as the one used in the present study). In most of the cases examined in chapter 6 the information loss error has been small, so the majority of the degradation has been due to a misinterpretation of the small radiance change caused by cirrus extinction. If cirrus could be effectively accounted for in this way then the residual loss of information would be comparatively insignificant.

Appendix A

Derivation of Pressure as a Function of Height

The forward model needs to be able to calculate accurately the pressure at a given height and latitude, in order to construct its model atmosphere. This is done through the use of two approximations: the hydrostatic equation ($dp = -g\rho\ dz$) and the ideal gas equation ($p = nkT$).

The ideal gas equation may be rewritten as $p = \rho RT/M$, where M is the mass per mole and R is the gas constant, 8.31 $\mathrm{JK^{-1}mol^{-1}}$. Substituting the ρ derived from this equation into the hydrostatic equation gives an expression which can be integrated between levels z_i and z_{i+1} to yield the following relation between pressure and *geopotential*, Φ:

$$\int_{\ln p_i}^{\ln p_{i+1}} \frac{RT}{M} d(\ln p) = -(\Phi_{i+1} - \Phi_i) \tag{A.1}$$

where the geopotential Φ is defined by:

$$d\Phi = g\ dz \tag{A.2}$$

The temperature T and the mass per mole M in equation A.1 are quantities which vary with height, and therefore they are both functions of $\ln p$. The variation of M with height is sufficiently slow that it can be represented by the mean value $\overline{M} = (M_{i+1} + M_i)/2$. The temperature on the other hand may vary quickly with height, and so it is calculated at a given height by linear interpolation with respect to $\ln p$. If z_{i+1} and z_i are consecutive levels of the CAMED temperature profile, then the temperature T at an arbitrary height z between these levels is given by the linear function $T = a \ln p + b$, where p is the pressure at height z, and the constants are given by:

$$a = \frac{T_{i+1} - T_i}{\ln p_{i+1} - \ln p_i}$$

and

$$b = T_i - \left[\frac{T_{i+1} - T_i}{\ln p_{i+1} - \ln p_i}\right] \ln p_i$$

Now by substituting the interpolated temperature into equation A.1, the left-hand side may be analytically integrated between the levels to give:

$$\frac{R}{\overline{M}}\left[\frac{a(\ln p_{i+1})^2}{2}+b\ln p_{i+1}-\frac{a(\ln p_i)^2}{2}-b\ln p_i\right]=-(\Phi_{i+1}-\Phi_i) \qquad \text{(A.3)}$$

This equation was used to calculate the geopotential at each of the levels of the CAMED atmosphere, starting from an initial condition of $\Phi(z=0)=0$.

If $\ln p_{i+1}$ in equation A.3 is replaced by an arbitrary value $\ln p$, then the equation may be rearranged to form a quadratic in terms of $\ln p$. The positive root of this quadratic then gives $\ln p$ as a function of Φ, as follows:

$$\ln p=\frac{-b+\left[(a\ln p_i+b)^2-\frac{2a\overline{M}}{R}(\Phi-\Phi_i)\right]^{1/2}}{a} \qquad \text{(A.4)}$$

Φ_i is the geopotential at the first level immediately below a given geopotential Φ, and is obtained from the profile derived from equation A.3. It may be substituted into equation A.4 to calculate the pressure p corresponding to Φ.

Now if geopotential is related to height, it will be possible to calculate the pressure at any given height, and vice versa. Geopotential is related to height by equation A.2. Substituting for $g(z)$ in this equation using the inverse square law of gravitation, $g(z)=GM_e/(R_e+z)^2$, and integrating the result, we get:

$$\Phi=\frac{g_o R_e z}{R_e+z} \qquad \text{(A.5)}$$

where $g_o=GM_e/R_e^2$.

A final factor to take into account is the variation with latitude of both the Earth's radius R_e, and the gravitational acceleration at sea-level, g_o. This may be accounted for by redefining R_e as the *effective radius* of the Earth, according to the definition provided by List [1968, p.218] as follows:

$$R_e=\frac{2g_o}{-(\partial g/\partial z)_{z=0}} \qquad \text{(A.6)}$$

Use of the effective radius in equation A.5 ensures that the calculated geopotential is consistent with the gravitational acceleration at sea-level, and with the vertical gradient of the gravitational acceleration at sea-level, at each latitude. Values of g_o and $(\partial g/\partial z)_{z=0}$ are tabulated against latitude by List [1968, p.218,488].

To summarise, the combination of the equations A.5 and A.4 may be used to calculate the pressure p given a height z, while conversely equation A.5 may be inverted and used with equation A.3 to find the height corresponding to a given pressure.

References

Arfken, G. ; *Mathematical Methods for Physicists* (3rd edition) ; Academic Press 1985

Armstrong, B.H., and R.W. Nicholls ; *Emission, Absorption and Transfer of Radiation in Heated Atmospheres* ; Pergamon Press 1972

Arnott, W.P., Y.Y. Dong, J. Hallett & M.R. Poellot ; Role of Small Ice Crystals in Radiative Properties of Cirrus: A Case Study, FIRE II, November 22, 1991 ; *Journal of Geophysical Research* ; Vol.99, No.D1, p.1371 ; 1994

Auer, A.H. and D.L.Veal ; The Dimension of Ice Crystals in Natural Clouds ; *Journal of the Atmospheric Sciences* ; Vol.27, p.919 ; 1970

Bader, M.J., G.S. Forbes, J.R. Grant, R.B.E. Lilley, A.J. Waters (editors) ; *Images in Weather Forecasting* ; Cambridge University Press 1995

Barton, I.J. ; Upper Level Cloud Climatology from an Orbiting Satellite ; *Journal of the Atmospheric Sciences* ; Vol.40, p.435 ; 1983

Bennetts, D.A. and M. Ouldridge ; An Observational Study of the Anvil of a Winter Maritime Cumulonimbus Cloud ; *Quarterly Journal of the Royal Meteorological Society* ; Vol.110, p.85 ; 1984

Borovikov, A.M., L.I. Gaivoronskii, E.G. Zak, V.V. Kostarev, I.P. Mazin, V.E. Minervin, A.Kh. Khrgian, S.M. Schmeter ; *Cloud Physics* ; Israel Programme for Scientific Translations, Jerusalem 1963

Burch, D.E. and D.A. Gryvnak ; Continuum Absorption by H_2O Vapor in the Infrared and Millimeter Regions (in *Atmospheric Water Vapor*, editors A. Deepak, T.D. Wilkerson, L.H. Ruhnke) ; Academic Press 1980

Burden, R.L. and J.D. Faires ; *Numerical Analysis* (4th edition) ; PWS-Kent 1989

Cess, R.D., G.L. Potter, J.P. Blanchet, G.J. Boer, A.D. Del Genio, M. Déqué, V. Dymnikov, V. Galin, W.L. Gates, S.J. Ghan, J.T. Kiehl, A.A. Lacis,

H. Le Treut, Z-X. Li, X-Z. Liang, B.J. McAvaney, V.P. Meleshko, J.F.B. Mitchell, J-J. Morcrette, D.A. Randall, L. Rikus, E. Roeckner, J.F. Royer, U. Schlese, D.A. Sheinin, A. Slingo, A.P. Sokolov, K.E. Taylor, W.M. Washington, R.T. Wetherald, I. Yagai, M-H. Zhang ; Intercomparison and Interpretation of Climate Feedback Processes in 19 Atmospheric General Circulation Models ; *Journal of Geophysical Research* ; Vol.95, No.D10, p.16601 ; 1990

Dagg, I.R., G.E. Reesor, J.L. Urbaniak ; Collision Induced Microwave Absorption in N_2, CH_4 and N_2-Ar, N_2-CH_4 Mixtures at 1.1 and 2.3 cm^{-1} ; *Canadian Journal of Physics* ; Vol.52, No.9, p.821 ; 1974

Dagg, I.R., G.E. Reesor, J.L. Urbaniak ; Collision Induced Absorption in N_2, CO_2, and H_2 at 2.3 cm^{-1} ; *Canadian Journal of Physics* ; Vol.53, No.18, p.1764 ; 1975

Dagg, I.R., G.E. Reesor, M. Wong ; A Microwave Cavity Measurement of Collision-Induced Absorption in N_2 and CO_2 at 4.6 cm^{-1} ; *Canadian Journal of Physics* ; Vol.56, No.8, p.1037 ; 1978

Dagg, I.R., A. Anderson, S. Yan, W. Smith ; Collision-Induced Absorption in Nitrogen at Low Temperatures ; *Canadian Journal of Physics* ; Vol.63, No.5, p.625 ; 1985

Deirmendjian, D. ; *Electromagnetic Scattering on Spherical Polydispersions* ; American Elsevier 1969

Deshler, T., D.J. Hoffman, B.J. Johnson, W.R. Rozier ; Balloonborne Measurements of the Pinatubo Aerosol Size Distribution and Volatility at Laramie, Wyoming During the Summer of 1991 ; *Geophysical Research Letters* ; Vol.19, No.2, p.199 ; 1992

Deshler, T., B.J. Johnson, W.R. Rozier ; Balloonborne Measurements of Pinatubo Aerosol During 1991 and 1992 at 41°N; Vertical Profiles, Size Distribution, and Volatility ; *Geophysical Research Letters* ; Vol.20, No.14, p.1435 ; 1993

Dickerson, R.E. ; *Molecular Thermodynamics* ; W.A. Benjamin 1969

Disselkamp, R.S., S.E. Anthony, A.J. Prenni, T.B. Onasch, M.A. Tolbert ; Crystallization Kinetics of Nitric Acid Dihydrate Aerosols ; *The Journal of Physical Chemistry* ; Vol.100, No.21, p.9127 ; 1996

Dowling, D.R. and L.F. Radke ; A Summary of the Physical Properties of Cirrus Clouds ; *Journal of Applied Meteorology* ; Vol.29, p.970 ; 1990

Dozier, J ; Looking Ahead to EOS: The Earth Observing System ; *Computers in Physics* ; p.248, May/June 1990

Drayson, S.R. ; Rapid Computation of the Voigt Profile ; *Journal of Quantitative Spectroscopy & Radiative Transfer* ; Volume 16, p.611 ; 1975

Elliott, W.P., and D.J. Gaffen ; On the Utility of Radiosonde Humidity Archives for Climate Studies ; *Bulletin of the American Meteorological Society* ; Vol.72, No.10, p.1507 ; 1991

Evans, K.F., G.L. Stephens ; Microwave Radiative Transfer through Clouds Composed of Realistically Shaped Ice Crystals. Part I: Single Scattering Properties ; *Journal of the Atmospheric Sciences* ; Vol.52, No.11, p.2041 ; 1995(a)

Evans, K.F., G.L. Stephens ; Microwave Radiative Transfer through Clouds Composed of Realistically Shaped Ice Crystals. Part II: Remote Sensing of Ice Clouds ; *Journal of the Atmospheric Sciences* ; Vol.52, No.11, p.2058 ; 1995(b)

Flowers, B.H. and E. Mendoza ; *Properties of Matter* ; John Wiley 1970

French, A.P., and E.F. Taylor ; *An Introduction to Quantum Physics* ; Van Nostrand Reinhold 1978

Gaut, N.E., and E.C. Reifenstein III; Interaction Model of Microwave Energy and Atmospheric Variables ; Technical Report #13 ; Environmental Research and Technology, Inc., Waltham, Mass. ; 1971

Gedzelman, S.D. ; *Atmospheric Circulation Systems* (chapter 1 in *Handbook of Applied Meteorology*, editor D.D. Houghton) ; John Wiley 1985

Gordy, W., W.V. Smith, R.F. Trambarulo ; *Microwave Spectroscopy* ; John Wiley 1953

Gow, M.M. ; *A Course in Pure Mathematics* ; English Universities Press 1960

Grant, I.S. and W.R. Phillips ; *Electromagnetism* ; John Wiley 1975

Griffith, K.T., S.K. Cox, R.G. Knollenberg ; Infrared Radiative Properties of Tropical Cirrus Clouds Inferred from Aircraft Measurements ; *Journal of the Atmospheric Sciences* ; Vol.37, p.1077 ; 1980

Gunn, K.L.S. and T.W.R. East ; The Microwave Properties of Precipitation Particles ; *Quarterly Journal of the Royal Meteorological Society* ; Vol.80, p.522 ; 1954

Hall, J.T. ; Attenuation of Millimeter Wavelength Radiation by Gaseous Water ; *Applied Optics* ; Vol.6, No.8, p.1391 ; 1967

Harwood, R.S., J. Kinnersley, J.A. Pyle ; CAMED-theta Two-Dimensional Model (in *The Atmospheric Effects of Stratospheric Aircraft: Report of the 1992 Models and Measurements Workshop*) ; NASA Reference Publication 1292 ; Vol.1, p.70 ; 1993

Heriot-Watt University, RAL, Edinburgh University ; *EOS Microwave Limb Sounder Draft Executive Summary* ; November 1994

Herzberg, G. ; *Atomic Spectra and Atomic Structure* (2nd Edition) ; Dover 1945

Heymsfield, A.J. ; Cirrus Uncinus Generating Cells and the Evolution of Cirriform Clouds. Part I: Aircraft Observations of the Growth of the Ice Phase ; *Journal of the Atmospheric Sciences* ; Vol.32, p.799 ; 1975

Heymsfield, A.J. ; Precipitation Development in Stratiform Ice Clouds: A Microphysical and Dynamical Study ; *Journal of the Atmospheric Sciences* ; Vol.34 p.367 ; 1977

Heymsfield, A.J. ; The Characteristics of Graupel Particles in Northeastern Colorado Cumulus Congestus Clouds ; *Journal of the Atmospheric Sciences* ; Vol.35, p.284 ; 1978

Heymsfield, A.J. ; Ice Particles Observed in a Cirriform Cloud at $-83°C$ and Implications for Polar Stratospheric Clouds ; *Journal of the Atmospheric Sciences* ; Vol.43, No.8, p.851 ; 1986(a)

Heymsfield, A.J. ; Ice Particle Evolution in the Anvil of a Severe Thunderstorm during CCOPE ; *Journal of the Atmospheric Sciences* ; Vol.43, No.21, p.2463 ; 1986(b)

Heymsfield, A.J. ; Microphysical Structures of Stratiform and Cirrus Clouds (chapter 4 in *Aerosol-Cloud-Climate Interactions*, editor P.V. Hobbs) ; Academic Press 1993

Heymsfield, A.J. and L.J. Jahnsen ; Microstructure of Tropopause Cirrus Layers ; *Proceedings of the 6th Conference on Aerospace and Aeronautical Meteorology* ; El Paso, Texas, 12-15 November 1974 ; American Meteorological Society 1974

Heymsfield, A.J. and R.G.Knollenberg ; Properties of Cirrus Generating Cells ; *Journal of the Atmospheric Sciences* ; Vol.29, p.1358 ; 1972

Heymsfield, A.J., K.M. Miller and J.D. Spinhirne ; The 27–28 October 1986 FIRE IFO Cirrus Case Study: Cloud Microstructure ; *Monthly Weather Review* ; Vol.118, No.11, p.2313 ; 1990

Heymsfield, A.J. and C.M.R. Platt ; A Parameterisation of the Particle Size Spectrum of Ice Clouds in Terms of the Ambient Temperature and the Ice Water Content ; *Journal of the Atmospheric Sciences* ; Vol.41, No.5, p.846 ; 1984

Hobbs, P.V., S. Chang, J.D. Locatelli ; The Dimensions and Aggregation of Ice Crystals in Natural Clouds ; *Journal of Geophysical Research* ; Vol.79, No.15, p.2199 ; 1974

Holton, J.R. ; *An Introduction to Dynamic Meteorology* (3rd Edition) ; Academic Press 1992

Houghton, J.T. ; *The Physics of Atmospheres* (2nd Edition) ; Cambridge University Press 1986

van de Hulst, H.C.; *Light Scattering by Small Particles* ; Dover 1981

Iaquinta, J., and P. Personne ; Theoretical Scattering Function of Bullet Rosette Ice Crystals ; *Fifth ICE/EuCREx Workshop*, Clermont-Ferrand, France ; p.143 ; 1992

Iaquinta, J., H. Isaka, P. Personne ; Scattering Phase Function of Bullet Rosette Ice Crystals ; *Journal of the Atmospheric Sciences* ; Vol.52, No.9, p.1401 ; 1995

IFE (Institute of Remote Sensing), University of Bremen, Germany ; *ESA Intercomparison Campaign of Forward Calculations – Report of Step 2* ; Vols. I & II ; 1994

IFE (Institute of Remote Sensing), University of Bremen, Germany ; *ESA Intercomparison Campaign of Forward Calculations – Final Report* ; Vols. I & II ; 1995

Illari, L. ; The Quality of Satellite Precipitable Water Content Data and their Impact on Analysed Moisture Fields ; *Tellus* ; Vol.41A, No.4, p.319 ; 1989

Intrieri, J.M., G.L. Stephens, W.L. Eberhard, T. Uttal ; A Method for Determining Cirrus Cloud Particle Sizes Using Lidar and Radar Backscatter Technique ; *Journal of Applied Meteorology* ; Vol.32, No.6, p.1074 ; 1993

Jarnot, R.F., and R.E. Cofield ; *Microwave Limb Sounder (MLS) Instrument Calibration Report* ; Version 1.0 ; NASA 1991

Jasperson, W.H., G.D. Nastrom, R.E. Davis, J.D. Holdeman ; Variability of Cloudiness at Airline Cruise Altitudes from GASP Measurements ; *Journal of Climate and Applied Meteorology* ; Vol.24, No.1, p.74 ; 1985

Jensen, E.J., O.B. Toon, D.L. Westphal, S. Kinne, A.J. Heymsfield ; Microphysical Modelling of Cirrus : 1. Comparison with 1986 FIRE IFO Measurements ; *Journal of Geophysical Research* ; Vol.99, No.D5, p.10421 ; 1994

Johnson, L.W. and R.D. Riess ; *Numerical Analysis* (2nd edition) ; Addison-Wesley 1982

Kelly, K., A.F. Tuck, T. Davies ; Wintertime Asymmetry of Upper Tropospheric Water Vapour Between the Northern and Southern Hemispheres ; *Nature* ; Vol.353, No.6341, p.244 ; 1991

Kilsby, C.G., D.P. Edwards, R.W. Saunders, J.S. Foot ; Water-Vapour Continuum Absorption in the Tropics: Aircraft Measurements and Model Comparisons ; *Quarterly Journal of the Royal Meteorological Society* ; Vol.118, p.715 ; 1992

King, M.D. and Harshvardhan ; Comparative Accuracy of Selected Multiple Scattering Approximations ; *Journal of the Atmospheric Sciences* ; Vol.43, No.8, p.784 ; 1986

Kinne, S., O.B. Toon, G.C. Toon, C.B. Farmer, E.V. Browell, M.P. McCormick ; Measurements of Size and Composition of Particles in Polar Stratospheric Clouds from Infrared Solar Absorption Spectra ; *Journal of Geophysical Research* ; Vol.94, No.D14, p.16481 ; 1989

Knollenberg, R.G., A.J. Dascher, D. Huffman ; Measurements of the Aerosol and Ice Crystal Populations in Tropical Stratospheric Cumulonimbus Anvils ; *Geophysical Research Letters* ; Vol.9, No.6, p.613 ; 1982

Knollenberg, R.G., K. Kelly, J.C. Wilson ; Measurements of High Number Densities of Ice Crystals in the Tops of Tropical Cumulonimbus ; *Journal of Geophysical Research* ; Vol.98, No.D5, p.8639 ; 1993

Krupp, C. ; Holographic Measurements of Ice Crystals in Cirrus Clouds during the International Cirrus Experiment ICE 1989 ; *ICE/EuCREx Report on the Fourth Workshop at the Meteorological Office College*, Reading, UK ; Editors R.W. Saunders & P.R.A. Brown 1991 ; p.58 ; 1991

Lacis, A.A., D.J. Wuebbles, J.A. Logan ; Radiative Forcing of Climate by Changes in the Vertical Distribution of Ozone ; *Journal of Geophysical Research* ; Vol.95, No.D7, p.9971 ; 1990

Legleau, H. ; Simulation of a Realistic Cloud Field on the AMSU Measurements (in *Microwave Remote Sensing of the Earth System*, editor A. Chedin) ; A. Deepak 1989

Lenoble, J. (editor) ; *Radiative Transfer in Scattering and Absorbing Atmospheres : Standard Computational Procedures* ; A. Deepak 1985

Liebe, H.J. ; A Nemesis for Millimeter Wave Propagation (in *Atmospheric Water Vapor*, editors A. Deepak, T.D. Wilkerson, L.H. Ruhnke) ; Academic Press 1980

Lindzen, R.S. ; Some Coolness Concerning Global Warming ; *Bulletin of the American Meteorological Society* ; Vol.71, No.3, p.288 ; 1990

Liou, K-N. ; Influence of Cirrus Clouds on Weather and Climate Processes: A Global Perspective ; *Monthly Weather Review* ; Vol.114 p.1167 ; 1986

List, R.J. ; *Smithsonian Meteorological Tables* (6th edition) ; Smithsonian Institution Press 1968

Logan, J.A., M.J. Prather, S.C. Wofsy, M.B. McElroy ; Tropospheric Chemistry: A Global Perspective ; *Journal of Geophysical Research* ; Vol.86, No.C8, p.7210 ; 1981

Ma, Q. and R.H. Tipping ; Water Vapor Continuum in the Millimeter Spectral Region ; *Journal of Chemical Physics* ; Vol.93, No.9, p.6127 ; 1990

Magono, C. and C.W. Lee ; Meteorological Classification of Natural Snow Crystals ; *Journal of the Faculty of Science, Hokkaidô University* ; Series VII, Vol.II, No.4, p.321 ; 1966

Mathews, J.H. ; *Numerical Methods for Computer Science, Engineering, and Mathematics* ; Prentice-Hall 1987

Matrosov, S.Y., T. Uttal, J.B. Snider, R.A. Kropfli ; Estimation of Ice Cloud Parameters from Ground-Based Infrared Radiometer and Radar Measurements ; *Journal of Geophysical Research* ; Vol.97, No.D11, p.11567 ; 1992

McCormick, M.P. ; SAGE Aerosol Measurements: Vol. III – January 1, 1981 to November 1981 ; NASA Ref. Publ. 1173, 2/87, NASA, Langley Research Centre, Hampton, Virginia ; 1987

McIntosh, D.H. and A.S. Thom ; *Essentials of Meteorology* ; Wykeham 1969

Mitchell, D.L. ; A Model Predicting the Evolution of Ice Particle Size Spectra and Radiative Properties of Cirrus Clouds. Part I: Microphysics ; *Journal of the Atmospheric Sciences* ; Vol.51, No.6, p.797 ; 1994

Mitchell, D.L. and W.P. Arnott ; A Model Predicting the Evolution of Ice Particle Size Spectra and Radiative Properties of Cirrus Clouds. Part II: Dependence of Absorption and Extinction on Ice Crystal Morphology ; *Journal of the Atmospheric Sciences* ; Vol.51, No.6, p.817 ; 1994

Moody, J.L., S.J. Oltmans, H. Levy II, J.T. Merrill ; Transport Climatology of Tropospheric Ozone: Bermuda, 1988–1991 ; *Journal of Geophysical Research* ; Vol.100, No.D4, p.7179 ; 1995

Mugnai, A. and E.A. Smith ; Radiative Transfer to Space Through a Precipitating Cloud at Multiple Microwave Frequencies. Part I: Model Description ; *Journal of Applied Meteorology* ; Vol.27, No.9, p.1055 ; 1988

Muller, B.M., H.E. Fuelberg, X. Xiang ; Simulations of the Effects of Water Vapor, Cloud Liquid Water, and Ice on AMSU Moisture Channel Brightness Temperatures ; *Journal of Applied Meteorology* ; Vol.33, p.1133 ; 1994

Munro, R. ; *Middle Atmosphere Water Vapour* (Ph.D. Thesis) ; University of Oxford 1991

NASA ; 1995 MTPE EOS Reference Handbook (editors G. Asrar and R. Greenstone) ; NASA 1995

Ono, A ; The Shape and Riming Properties of Ice crystals in Natural Clouds ; *Journal of the Atmospheric Sciences* ; Vol.26, p.138 ; 1969

Penkett, S.A., I.S.A. Isaksen, D. Kley ; A Program of Tropospheric Ozone Research (TOR) (in *Tropospheric Ozone*, editor I.S.A. Isaksen) ; Reidel 1988

Pickett, H.M., R.L. Poynter, E.A. Cohen ; *Submillimeter, Millimeter, and Microwave Spectral Line Catalogue* ; JPL Publication 80-23, Rev. 3 ; 1992

Pilsbury, R.K. ; *Clouds and Weather* ; Batsford 1969

Platt, C.M.R. and A.C. Dilley ; Remote Sounding of High Clouds IV: Observed Temperature Variations in Cirrus Optical Properties ; *Journal of the Atmospheric Sciences* ; Vol.38, p.1069 ; 1981

Platt, C.M.R., J.D. Spinhirne and W.D. Hart ; Optical and Microphysical Properties of a Cirrus Cloud: Evidence for Regions of Small Ice Particles ; *Journal of Geophysical Research* ; Vol.94, No.D8, p.11151 ; 1989

Pollack, J.B. and J.N. Cuzzi ; Scattering by Nonspherical Particles of Size Comparable to a Wavelength: A New Semi-Empirical Theory and its Application to Tropospheric Aerosols ; *Journal of the Atmospheric Sciences* ; Vol.37, No.4, p.868 ; 1980

Prabhakara, C., R.S. Fraser, G. Dalu, Man-Li C. Wu, R.J. Curran ; Thin Cirrus Clouds: Seasonal Distribution over Oceans Deduced from Nimbus-4 IRIS ; *Journal of Applied Meteorology* ; Vol.27, No.4, p.367 ; 1988

Press, W.H., S.A. Teukolsky, W.A. Vetterling, B.P. Flannery ; *Numerical Recipes in FORTRAN* (2nd edition) ; Cambridge University Press 1992

Prinz, B. ; Ozone Effects on Vegetation (in *Tropospheric Ozone*, editor I.S.A. Isaksen) ; Reidel 1988

RAL, Heriot-Watt University, Edinburgh University ; *EOS Microwave Limb Sounder Review* ; May 14, 1993

Ramanathan, V., and W. Collins ; Thermodynamic Regulation of Ocean Warming by Cirrus Clouds Deduced from Observations of the 1987 El Niño ; *Nature* ; Vol.351, No.6321, p.27 ; 1991

Raval, A. and V. Ramanathan ; Observational Determination of the Greenhouse Effect ; *Nature* ; Vol.342, No.6251, p.758 ; 1989

Raychaudhuri, A.K., S. Banerji, A. Banerjee ; *General Relativity, Astrophysics, and Cosmology* ; Springer-Verlag 1992

Read, W.G., J.W. Waters, D.A. Flower, L. Froidevaux, R.F. Jarnot, D.L. Hartmann, R.S. Harwood, R.B. Rood ; Upper-Tropospheric Water Vapour from UARS MLS ; *Bulletin of the American Meteorological Society* ; Vol.76, No.12, p.2381 ; 1995

Reber, C.A., C.E. Trevathan, R.J. McNeal, M.R. Luther ; The Upper Atmosphere Research Satellite (UARS) Mission ; *Journal of Geophysical Research* ; Vol.98, No.D6, p.10643 ; 1993

Rice, J.R. ; *Numerical Methods, Software and Analysis* ; McGraw-Hill 1983

Rind, D., E.W. Chiou, W. Chu, J. Larsen, S. Oltmans, J. Lerner, M.P. McCormick, L. McMaster ; Positive Water Vapour Feedback in Climate Models Confirmed by Satellite Data ; *Nature* ; Vol.349, p.500 ; 1991

Rind, D., E.W. Chiou, W. Chu, S. Oltmans, J. Lerner, J. Larsen, M.P. McCormick, L. McMaster ; Overview of the Stratospheric Aerosol and Gas Experiment II

Water Vapour Observations: Method, Validation, and Data Characteristics ; *Journal of Geophysical Research* ; Vol.98, No.D3, p.4835 ; 1993

Rodgers, C.D. ; Retrieval of Atmospheric Temperature and Composition from Remote Measurements of Thermal Radiation ; *Reviews of Geophysics and Space Physics* ; Vol.14, p.609 ; 1976

Rodgers, C.D. ; Characterization and Error Analysis of Profiles Retrieved from Remote Sounding Measurements ; *Journal of Geophysical Research* ; Vol.95, No.D5, p.5587 ; 1990

Rosenkranz, P.W. ; Interference Coefficients for Overlapping Oxygen Lines in Air ; *Journal of Quantitative Spectroscopy & Radiative Transfer* ; Vol.39, No.4, p.287 ; 1988

Rothman, L.S., R.R. Gamache, A. Goldman, L.R. Brown, R.A. Toth, H.M. Pickett, R.L. Poynter, J-M. Flaud, C. Camy-Peyret, A. Barbe, N. Husson, C.P. Rinsland, M.A.H. Smith ; The HITRAN Database: 1986 Edition ; *Applied Optics* ; Vol.26, No.19, p.4058 ; 1987

Rothman, L.S., R.R. Gamache, R.H. Tipping, C.P. Rinsland, M.A.H. Smith, D.C. Benner, V.M. Devi, J-M. Flaud, C. Camy-Peyret, A. Perrin, A. Goldman, S.T. Massie, L.R. Brown, R.A. Toth ; The HITRAN Molecular Database: Editions of 1991 and 1992 ; *Journal of Quantitative Spectroscopy & Radiative Transfer* ; Vol.48, p.469 ; 1992

Rudman, S.D., R.W. Saunders, C.G. Kilsby, P.J. Minnett ; Water-Vapour Continuum Absorption in Mid-Latitudes: Aircraft Measurements and Model Comparisons ; *Quarterly Journal of the Royal Meteorological Society* ; Vol.120, p.795 ; 1994

Sassen, K., and K-N. Liou ; Scattering of Polarized Light by Water Droplet, Mixed Phase and Ice Crystal Clouds. Part I: Angular Scattering Patterns ; *Journal of the Atmospheric Sciences* ; Vol.36, No.5, p.838 ; 1979

Sassen, K., D.O'C. Starr and T. Uttal ; Mesoscale and Microscale Structure of Cirrus Clouds: Three Case Studies ; *Journal of the Atmospheric Sciences* ; Vol.46, p.371 ; 1989

Sassen, K., N.C. Knight, Y. Takano, A.J. Heymsfield ; Effects of Ice-Crystal Structure on Halo Formation: Cirrus Cloud Experimental and Ray-Tracing Modeling Studies ; *Applied Optics* ; Vol.33, No.21, p.4590 ; 1994

Schanda, E. ; *Physical Fundamentals of Remote Sensing* ; Springer-Verlag 1986

Schnell, R.C., S.C. Liu, S.J. Oltmans, R.S. Stone, D.J. Hofmann, E.G. Dutton, T. Deshler, W.T. Sturges, J.W. Harder, S.D. Sewell, M. Trainer, J.M. Harris ; Decrease of Summer Tropospheric Ozone Concentrations in Antarctica ; *Nature* ; Vol.351, No.6329, p.726 ; 1991

Shimazaki, T. ; *Minor Constituents in the Middle Atmosphere* ; Terra Scientific Publishing 1985

Siegel, P. ; Radiometers ; in *A Cost-Constrained MLS for EOS, Volume I: Science and Technical* ; NASA Goddard Space Flight Centre ; 1992

Stackhouse, P.W. and G.L. Stephens ; A Theoretical and Observational Study of the Radiative Properties of Cirrus : Results from FIRE 1986 ; *Journal of the Atmospheric Sciences* ; Vol.48, No.18, p.2044 ; 1991

Starr, D.O'C. and D.P. Wylie ; Synoptic Conditions Producing Cirrus During the FIRE Cirrus IFO ; in *FIRE Science Results 1988* ; NASA 1988

Stephens, G.L., S.C. Tsay, P.W. Stackhouse Jr., P.J. Flatau ; The Relevance of the Microphysical and Radiative Properties of Cirrus Clouds to Climate and Climatic Feedback ; *Journal of the Atmospheric Sciences* ; Vol.47, No.14, p.1742 ; 1990

Stone, N.W.B., L.A.A. Read, A. Anderson, I.R. Dagg, W. Smith ; Temperature-Dependent Collision-Induced Absorption in Nitrogen ; *Canadian Journal of Physics* ; Vol.62, No.4, p.338 ; 1984

Stone, R.S., J.R. Key and E.G. Dutton ; Properties and Decay of Stratospheric Aerosols in the Arctic Following the 1991 Eruptions of Mount Pinatubo ; *Geophysical Research Letters* ; Vol.20, No.21, p.2359 ; 1993

Sun, Z. and K.P. Shine ; Studies of the Radiative Properties of Ice and Mixed-Phase Clouds ; *Quarterly Journal of the Royal Meteorological Society* ; Vol.120, p.111 ; 1994

Takano, Y. and K-N. Liou ; Solar Radiative Transfer in Cirrus Clouds. Part I: Single Scattering and Optical Properties of Hexagonal Ice Crystals ; *Journal of the Atmospheric Sciences* ; Vol.46, No.1, p.3 ; 1989

Toon, O.B., R.P. Turco, J. Jordan, J. Goodman, G. Ferry ; Physical Processes in Polar Stratospheric Ice Clouds ; *Journal of Geophysical Research* ; Vol.94, No.D9, p.11359 ; 1989

Toon, O.B., M.A. Tolbert, B.G. Koehler, A.M. Middlebrook, J. Jordan ; Infrared Optical Constants of H_2O Ice, Amorphous Nitric Acid Solutions, and Nitric Acid Hydrates ; *Journal of Geophysical Research* ; Vol.99, No.D9, p.25631 ; 1994

Torres, O., Z. Ahmad, J.R. Herman ; Optical Effects of Polar Stratospheric Clouds on the Retrieval of TOMS Total Ozone ; *Journal of Geophysical Research* ; Vol.97, No.D12, p.13015 ; 1992

Twomey, S., *Atmospheric Aerosols* ; Elsevier 1977

UKMO (UK Meteorological Office) ; *The Meteorological Glossary* (5th edition) ; HMSO 1972

Ulaby, F.T., R.K. Moore, A.K. Fung ; *Microwave Remote Sensing: Active and Passive* (Volume 1: *Fundamentals and Radiometry*) ; Addison-Wesley 1981

Urbaniak, J.L., I.R. Dagg, G.E. Reesor ; Collision Induced Microwave Absorption in N_2, CH_4 and CF_4 in the Gaseous and Liquid Phases ; *Canadian Journal of Physics* ; Vol.55, No.6, p.496 ; 1977

Van de Berg, L., A. Pyomjamsri, J. Schmetz ; Monthly Mean Upper Tropospheric Humidities in Cloud-Free Areas from METEOSAT Observations ; *International Journal of Climatology* ; Vol.11, No.8, p.819 ; 1991

Van Vleck, J.H., and V.F. Weisskopf ; On the Shape of Collision-Broadened Lines ; *Reviews of Modern Physics* ; Vol.17, p.227 ; 1945

Vivekanandan, J., J. Turk, V.N. Bringi ; Ice Water Path Estimation and Characterization Using Passive Microwave Radiometry ; *Journal of Applied Meteorology* ; Vol.30, No.10, p.1407 ; 1991

Vouk, V. ; Projected Area of Convex Bodies ; *Nature* ; Vol.162, p.330 ; 1948

Wang, W-C., N. Dak Sze, G. Molnar, M. Ko, S. Goldenberg ; Ozone-Climate Interactions Associated with Increasing Atmospheric Trace Gases (in *Tropospheric Ozone*, editor I.S.A. Isaksen) ; Reidel 1988

Wang, P-H., M.P. McCormick, P. Minnis, G.S. Kent, G.K. Yue, K.M. Skeens ; A Method for Estimating Vertical Distribution of the SAGE II Opaque Cloud Frequency ; *Geophysical Research Letters* ; Vol.22, No.3, p.243 ; 1995

Warren, S.G. ; Optical Constants of Ice from the Ultraviolet to the Microwave ; *Applied Optics* ; Vol.23, No.8, p.1206 ; 1984

Waters, J.W. ; *Absorption and Emission by Atmospheric Gases* (section 2.3 in *Methods of Experimental Physics*, editor M.L. Meeks, 12B – Radio Astronomy) ; Academic Press 1976

Waters, J.W. ; *A Proposal for the Earth Observing System Microwave Limb Sounder* ; Volume 1 ; JPL 1988

Waters, J.W. ; *Absorption and Emission by Atmospheric Gases* (Revision 1.0) ; Microwave Limb Sounder Technical Note ; JPL 1990

Weinman, J.A. ; The Effect of Cirrus Clouds on 118-GHz Brightness Temperatures ; *Journal of Geophysical Research* ; Vol.93, No.D9, p.11059 ; 1988

Wielicki, B.A., J.T. Suttles, A.J. Heymsfield, R.M. Welch, J.D. Spinhirne, M-L.C. Wu, D.O'C. Starr, L. Parker, R.F. Arduini ; The 27–28 October 1986 FIRE IFO Case Study: Comparison of Radiative Transfer Theory with Observations by Satellite and Aircraft ; *Monthly Weather Review* ; Vol.118, No.11, p.2356 ; 1990

WMO ; *Atmospheric Ozone 1985 – WMO Global Ozone Research and Monitoring Project Report No. 16* ; World Meteorological Organisation 1985

Woodbury, G.E. and M.P. McCormick ; Zonal and Geographical Distribution of Cirrus Clouds Determined from SAGE Data ; *Journal of Geophysical Research* ; Vol.91 No.D2 p.2775 ; 1986

Wu, M-L.C. ; Determination of Cloud Ice Water Content and Geometrical Thickness Using Microwave and Infrared Radiometric Measurements ; *Journal of Climate and Applied Meteorology* ; Vol.26, No.8, p.878 ; 1987

Wylie, D.P. and W.P. Menzel ; Two Years of Cloud Cover Statistics Using VAS ; *Journal of Climate* ; Vol.2, p.380 ; 1989

Yamashita, A. ; On the Trigonal Growth of Ice Crystals ; *Journal of the Meteorological Society of Japan* ; Vol.51 No.5 p.307 ; 1973

Zemansky, M.W. and R.H. Dittman ; *Heat and Thermodynamics* (6th edition) ; McGraw-Hill 1981

List of Personal Communications and Affiliations

Mark Filipiak ; Department of Meteorology, University of Edinburgh, Scotland, UK.

Andrew Heymsfield ; National Centre for Atmospheric Research, Boulder, Colorado, USA.

Robert Jarnot ; Jet Propulsion Laboratory, California Institute of Technology, Pasadena, California, USA.

Peter Jonas ; Atmospheric Physics Research Group, Department of Physics, UMIST, Manchester, UK.

William Read ; Jet Propulsion Laboratory, California Institute of Technology, Pasadena, California, USA.